Fast energy relaxation in the afterglow of a nanosecond capillary discharge in nitrogen/oxygen mixtures

Nikita Lepikhin

NNT : 2017SACLX087

THESE DE DOCTORAT
DE
L'UNIVERSITE PARIS-SACLAY
PREPAREE A
L'ECOLE POLYTECHNIQUE

ÉCOLE DOCTORALE N° ED 572

Ondes et Matière

Spécialité de doctorat : Physique des plasma

Par

M Nikita Lepikhin

Fast energy relaxation in the afterglow of a nanosecond capillary discharge in nitrogen/oxygen mixtures

Thèse présentée et soutenue à Palaiseau, le 7 décembre 2017:

Composition du Jury :

M S. Pasquiers, Directeur de Recherche, CNRS-LPGP, Président du Jury
M G. Dilecce, Senior Researcher, CNR-Institute of Nanotechnology, P.Las.M.I. Lab., Rapporteur
M E. Robert, Directeur de Recherche, CNRS-GREMI, Rapporteur
M N. Sadeghi, Directeur de Recherche émérite, CNRS-LiPhy, Examinateur
M L. Perfetti, Professeur, École polytechnique, Examinateur
Mme S. Starikovskaia, Directrice de Recherche, École polytechnique, Directrice de thèse
M N. Popov, Leading scientific researcher, Skobeltsyn Institute of Nuclear Physics, Co-Directeur de thèse

Contents

Acknowledgements

I would like to express my respect and gratitude to my supervisor Svetlana Starikovskaia and my co-supervisor Nikolay Popov. It was pleasure to learn low-temperature plasma physics from the leading experts in this field. I am grateful to Svetlana Starikovskaia for the experimental skills I have acquired and her wise advices that helped a lot to solve the issues appeared during the work. I am thankful to Nikolay Popov for fruitful discussions and deep understanding of the plasma kinetics I have gained. I am happy to work in the team, where both experimental and numerical plasma studies are coupled and complement each other.

I am very thankful to Giorgio Dilecce from CNR-Institute of Nanotechnology (P.Las.M.I. Lab.) and Eric Robert from University of Orleans (GREMI), who accepted to be reviewers of my Thesis. I am also grateful to all members of the Jury: Stephane Pasquiers from University Paris Sud (LPGP), Nader Sadeghi from Grenoble Alps University (LiPhy) and Luca Perfetti from Ecole Polytechnique (LSI).

I would like to thank Sergey Stepanyan, who first told me about the Laboratory of Plasma Physics in Ecole Polytechnique and his work there. I also would like to thank Andrey Klochko, who introduced me to the topic and transmitted his knowledge about the nanosecond capillary discharge. I thank Yifei Zhu for discussions and for invaluable assistance in manuscript preparation. I also would like to thank Georgy Pokrovskiy, who assisted me in the experiments and obtained a part of the experimental results during his master internship. I am thankful to our collaborators Sergey Zyryanov and Dmitry Lopaev from Moscow State University for friendship and invaluable help in the automation of experiments.

I am grateful to Ali Mahjoub for the technical advices, his help in the modification of the experimental setup and development of the new one. Also I would like to thank him for companionship and wise advices concerning broad aspects of everyday life.

I thank Bruno Dufour for his invaluable contribution to the implementation of the ideas and projects. I am also thankful to Philippe Auvray for his advices in technical questions.

I also would like to thank our administrative team Cherifa Ighoud, Catherine Jegu, Marilyne Bazin and Edouard Bouchet for their help.

I thank my friend Sergey Shcherbanev. His company brightened up the work and everyday life significantly. I am also thankful to him for the introduction to the experimental techniques used in the laboratory.

I am very thankful to my sweetheart Sofya Maslovskaya, who fills my life with meaning and supports me. I am happy that I met you.

I would like to thank my family and especially my parents. I am very grateful to them for upbringing, help and priceless advices. I also appreciate that they approve my decisions concerning the life path. I love you! And thank you very much one more time!

Résumé de thèse

Le travail était axé sur la cinétique du plasma nanoseconde dans les conditions de dépôt d'énergie spécifique élevée aux champs électriques réduits élevés.

Les mesures des paramètres électriques de la décharge capillaire nanoseconde ont montré que la plupart de l'énergie est déposée à la plasma en présence des champs électriques réduits élevés, 100-350 Td. L'énergie spécifique totale déposée est également élevée, jusqu'à 1 eV/molécule. Il a été montré par modélisation cinétique numérique que la fraction totale des atomes et des molécules d'azote excités est de 5-7% de la densité initiale du gaz. Dans ces conditions, la probabilité d'interaction entre les particules excitées et/ou les particules chargées augmente et change la cinétique dans la décharge et dans la post-luminescence. Dans ce cas, l'applicabilité de toute technique spectroscopique doit être analysée en tenant compte de la production et de la dépopulation supplémentaires des niveaux étudiés. En particulier, il a été montré que la technique des mesures de champ électrique basé sur la population relative de la $N_2(C^3\Pi_u)$ et de la $N_2^+(B^2\Sigma_u^+)$ n'est pas valide dans les conditions de décharge capillaire nanoseconde à la pression modérée.

Le plasma de longue durée de vie a été observé expérimentalement dans l'azote pur: à une densité d'électrons typique de $N_e = 9 \cdot 10^{14}$ cm^{-3} pendant l'impulsion de la décharge, les valeurs de densité électronique observées après la décharge, par exemple 200 ns et 600 ns plus tard, sont égal à 10^{14} cm^{-3} et $0.4 \cdot 10^{14}$ cm^{-3}, respectivement. Une désintégration de densité électronique pareille a été observée numériquement. Il a été montré par comparaison des résultats expérimentaux avec les résultats des calculs numériques que les réactions de l'ionisation associative entre les états excités de l'azote moléculaire maintiennent la élevée densité électronique dans la post-luminescence. Par conséquent, le degré élevé d'excitation électronique dû au dépôt d'énergie spécifique élevée a été confirmé, puisque ces réactions ne sont efficaces que pour une densité élevée des espèces excitées. La longue désintégration du plasma a été également observée expérimentalement et numériquement dans les mélanges azote:oxygène. Dans ce cas, l'existence du plasma de longue durée de vie s'explique par la recombinaison lente ion-électron impliquant l'ion O_2^+, qui est un

ion positif dominant dans les conditions données selon les calculs numériques.

Le dépeuplement des espèces excitées dans la post-luminescence tôt de la décharge capillaire nanoseconde dans l'azote pur et les mélanges azote:oxygène a été étudié. Il a été montré que la désintégration des états excités, en particulier des états $N_2(C^3\Pi_u, v = 0)$ et $N_2(B^3\Pi_g)$, est anormalement vite. Les études détaillées dans le cas de l'azote pur ont démontré que le processus de collision additionnel qui n'est normalement pas pris en compte dans les modèles de cinétique développés pour les décharges à faible énergie spécifique est responsable de l'extinction de l'état $N_2(C^3\Pi_u, v = 0)$. Ce processus est les collisions super-élastiques entre les $N_2(C^3\Pi_u, v = 0)$ et les électrons:

$$N_2(C^3\Pi_u) + e \rightarrow N_2(X^1\Sigma_g^+, A^3\Sigma_u^+, B^3\Pi_g, ...) + e.$$

Les estimations des constantes de vitesse de désexcitation collisionnelle du $N_2(C^3\Pi_u)$, $N_2(B^3\Pi_g)$, $N_2^+(B^2\Sigma_u^+)$ et du $N_2(A^3\Sigma_u^+)$ par électrons ont été effectués. Les constantes de vitesse de l'extinction par les électrons estimées sont $k_e^{N_2(C)} \approx 10^{-7}$ cm^{3}s^{-1}, $k_e^{N_2(B)} \approx 2.2 \cdot 10^{-8}$ cm^{3}s^{-1}, $k_e^{N_2^+(B)} \approx 10^{-7}$ cm^{3}s^{-1} et $k_e^{N_2(A)} \approx 1.8 \cdot 10^{-10}$ cm^{3}s^{-1} à la température électronique $T_e \approx 0.8$ eV typique pour la post-luminescence selon les calculs numeriques. Un bon accord entre les résultats expérimentaux et les résultats de la modélisation cinétique de la décroissance d'intensité d'émission en utilisant les constantes de vitesse de réaction suggérées a été démontré sur l'exemple de l'état $N_2(C^3\Pi_u, v = 0)$.

Distribution radiale des espèces excitées a été étudiée expérimentalement pour obtenir le profil initial de la densité électronique qui est nécessaire pour la modélisation numérique 1D fiable de la décharge capillaire nanoseconde et la comparaison correcte des résultats des calculs numériques avec l'expérience. Il a été démontré que le maximum de la densité électronique est situé hors de l'axe du tube capillaire dans l'azote pur. On a également observé que la distribution de la densité électronique initiale est sensible à la composition du gaz: même 1% du d'ajout d'oxygène modifie le profil radial initial de la densité électronique.

Chauffage rapide du gaz en azote pur et mélanges N_2:O_2 a été étudié experimentalement et numériquement en utilisant des profils de densité électronique initiale mesurés expérimentalement entant que données d'entrée. L'augmentation de température élevée à l'échelle de temps de centaines de nanosecondes a été obtenue. Le rôle significatif de désexcitation collisionnelle des atomes de $N(^2D)$ dans le chauffage rapide du gaz dans l'azote pur a été clairement démontré. Sur la base de la comparaison des résultats expérimentaux des mesures de dynamique de température du des gaz avec les résultats de la modélisation numérique, un nouveau processus qui conduit au chauffage du gaz rapide intensif dans l'azote pur a été

proposé: réaction de pooling entre les molécules $N_2(B)$

$$N_2(B) + N_2(B) \rightarrow N_2^* + N_2(X^1\Sigma_g^+, v) \rightarrow N_2(B, v) + N_2(X^1\Sigma_g^+, v) + \varepsilon,$$
$$N_2(B) = N_2(B^3\Pi_g, W^3\Delta_u, B'^3\Sigma_u^-), \varepsilon = 5 \text{ eV},$$

avec la constante de vitesse $k \approx 4 \cdot 10^{-10}$ cm^3s^{-1}. Malgré les nombreux schémas cinétiques largement utilisés pour la description du chauffage rapide du gaz dans l'azote pur et les mélanges azote: oxygène, ce processus n'a jamais été mentionné auparavant. Le mécanisme de chauffage du gaz dans ce processus est supposé d'être similaire au mécanisme de chauffage dans la réaction de pooling entre les molécules $N_2(A^3\Sigma_u^+)$ utilisé dans la plupart des modèles de chauffage rapide du gaz dans le plasma d'azote.

Il a été montré que dans les conditions de dépôt d'énergie spécifique élevée à des champs électriques réduits élevés, la réaction de pooling entre les molécules $N_2(B)$ joue un rôle clé dans le chauffage rapide du gaz dans l'azote pur. L'accord entre les calculs numériques de la dynamique du chauffage rapide du gaz pour des mélanges de N_2:O_2 avec 1, 10 et 20 % de O_2 et les résultats expérimentaux des mesures de température du gaz a également été démontré.

Enfin, on peut conclure: l'ensemble de données expérimentaux obtenues - le profil du champ électrique réduit, l'énergie déposée, la désintégration du plasma, l'évolution temporelle des profils radiaux des espèces excitées, la dynamique temporelle de la densité du $N_2(C^3\Pi_u, v{=}0)$ et la dynamique de la température du gaz - est décrite de manière adéquate par le modèle cinétique incluant l'extinction des espèces excitées par les électrons et la réaction de pooling entre les molécules $N_2(B)$.

Abstract

Nanosecond discharges are widely used as a source of non-thermal plasma in a variety of applications: surface treatment, plasma medicine, plasma flow control, plasma assisted ignition and combustion. High reduced electric field in the nanosecond discharges provides efficient excitation of the electronic states of atoms or molecules. At relatively low specific deposited energy the excited species mostly interact with background gas. The "classical" plasma kinetics is developed mainly on this assumption. Increasing of the specific energy deposited during nanosecond discharge leads to increase of the probability of interaction of excited and charged species between each other, which changes the plasma kinetics dramatically. The main aim of the present work was to investigate, how plasma kinetics changes at the conditions of high specific energy deposition at high reduced electric fields. The nanosecond capillary discharge was used as an experimental tool. The measurements were performed for pure nitrogen and nitrogen:oxygen mixtures.

The thesis contains 10 chapters. In Chapter 1 the literature review is given. The main features of the nanosecond discharges are discussed and explained from the point of view of physical kinetics. The main applications of non-equilibrium plasma produced by nanosecond discharges are listed. The fast gas heating, playing the key role in a number of applications is reviewed; the experimental and numerical approaches are given. The fast ionization waves and discharges in thin tubes are discussed. The peculiarities of the development of these discharges are described.

In Chapter 2 the main aim of the present work and corresponding tasks are formulated.

In Chapter 3 the description of the nanosecond capillary discharge setup used in the experimental program is given, as well as the description of the experimental equipment. The main experimental techniques are described. The calculation of the spectral sensitivity of the spectral system required for the correction of the relative intensity of the measured spectra is performed. Calibration procedure for the capacitive probe is presented. The parameters required for the electric potential value reconstruction based on the signal from the capacitive probe are obtained. The

experimental and mathematical techniques for measuring of the radial distribution of excited species are presented.

In Chapter 4 the most important characteristics of the discharge are given. Electric parameters of the discharge are measured: the applied voltage, the electric current, the electric field and the energy deposition. It is shown that the value of the reduced electric field, as well as the specific deposited energy are high, that corresponds to the initial problem formulation. The spectra of the optical emission from the discharge are presented. It is demonstrated that spectral data can not be explained in the framework of "classical" plasma kinetics.

In Chapter 5 a brief description of the kinetic model used in the numerical calculations is given. The validation of the kinetic scheme based on the comparison of the calculated waveform of the electric field with the experimentally measured one is performed. The high excitation and ionization degrees in the nanosecond discharge are confirmed.

In Chapter 6 the electron density in the discharge pulses is measured. The plasma decay is studied by the measurements of the electron density in the afterglow of the discharge. The comparison of the calculated electron density profile in the afterglow and the experimentally measured one is done. The processes controlling the plasma decay are determined and analyzed.

In Chapter 7 depopulation of excited molecules on the example of $N_2(C^3\Pi_u)$ state of molecular nitrogen is studied in nitrogen:oxygen mixtures. The processes responsible for depopulation of excited species in the afterglow of the nanosecond discharge at high specific deposited energy at high reduced electric field are discussed.

In Chapter 8 the radial distribution of the excited species is investigated. The validity of the used technique is discussed. The experimental results and results of numerical 1D calculations are presented as well. The distributions of excited species at different gas compositions are compared and discussed.

In Chapter 9 the experimental and numerical study of the processes responsible for fast gas heating in pure nitrogen and in nitrogen:oxygen mixtures in the afterglow of nanosecond capillary discharge is performed. The peculiarities of the fast gas heating at conditions of the nanosecond discharge at high specific deposited energy at high reduced electric field are discussed. The modifications of traditionally used kinetic schemes are proposed.

In Chapter 10 the results are summarized. The contribution of the present work is discussed. The perspectives and the plans of the future work are given as well.

Chapter 1

Literature review

1.1 Nanosecond discharges and their key features. Main applications.

The discharges at given pressure and given gas composition can be classified by a number of characteristics: the applied voltage, the electric field, electric current and the energy deposition. However, the most important characteristic is the reduced electric field E/N (with an electric field E and a gas density N), since it determines the electron energy distribution function (EEDF) [1]. The EEDF controls the electron energy branching through internal degrees on freedom of atoms/molecules. It is directly follows from the fact that excitation extremely depends on the electron energy (or the electron temperature), and that higher electric field provides higher electron temperature.

The EEDF can be obtained from velocity distribution function of electrons $f(t, \mathbf{r}, \mathbf{v})$. The $f(t, \mathbf{r}, \mathbf{v})$ is defined so that $f d\mathbf{r} d\mathbf{v}$ is number of electrons at a time instant t in element of phase volume $d\Gamma = d\mathbf{r}d\mathbf{v} = dxdydz \cdot dv_x dv_y dv_z$, where $\mathbf{r} = \{x, y, z\}$ is space coordinate and $\mathbf{v} = \{v_x, v_y, v_z\}$ is the velocity [2,3]. The evolution of the $f(t, \mathbf{r}, \mathbf{v})$ in the electric field $\mathbf{E}$ is described by Boltzmann's equation [3]

$$\frac{\partial f}{\partial t} + \mathbf{v} \cdot \nabla f - \frac{e}{m} \mathbf{E} \cdot \nabla_v f = C[f], \tag{1.1}$$

where e is the elementary charge, m is the electron mass, ∇_v is the velocity gradient operator, C corresponds to the rate of change in f due to collisions. The common way to solve (1.1) is to use two-term approximation [2, 3]. This requires spatially

uniform the electric field and collision probabilities. In this case the electric field is the axis of the symmetry in velocity space and f varies along the $\mathbf{E}$ only, i.e. f is the function of the velocity magnitude v, the angle θ between the velocity and the electric field, and the position along the electric field z: $f = f(t, v, z, \theta)$. In this case f can be represented as expansion over Legendre polynomials of $cos\theta$, typically two first terms are used

$$f(t, v, z, \theta) = f_0(t, v, z) + f_1(t, v, z)cos\theta, \tag{1.2}$$

with isotropic $f_0(t, v, z)$ and anisotropic $f_1(t, v, z)$ parts of $f(t, v, z, \theta)$.

It was shown in [4] that in nitrogen this approximation is valid even at high reduced electric fields up to 1500 Td (1 Td= 10^{-17} V $\cdot$ cm^2). An additional confirmation of the result [4] is given in Fig. 1.1 taken from [5]. Excitation rate coefficient of $N_2(C^3\Pi_u)$ state from the ground state of molecular nitrogen and the ionization rate of the ground state of molecular nitrogen were calculated by BOLSIG+ [3] software using two-term approximation for solution of the Boltzmann's equation. It is seen that the results of calculations [5] are in good agreement with the experimental results [4] in the range 100 Td $< E/N <$ 1100 Td. Thus, the usage of this approximation is possible in nitrogen at E/N up to 1100 Td.

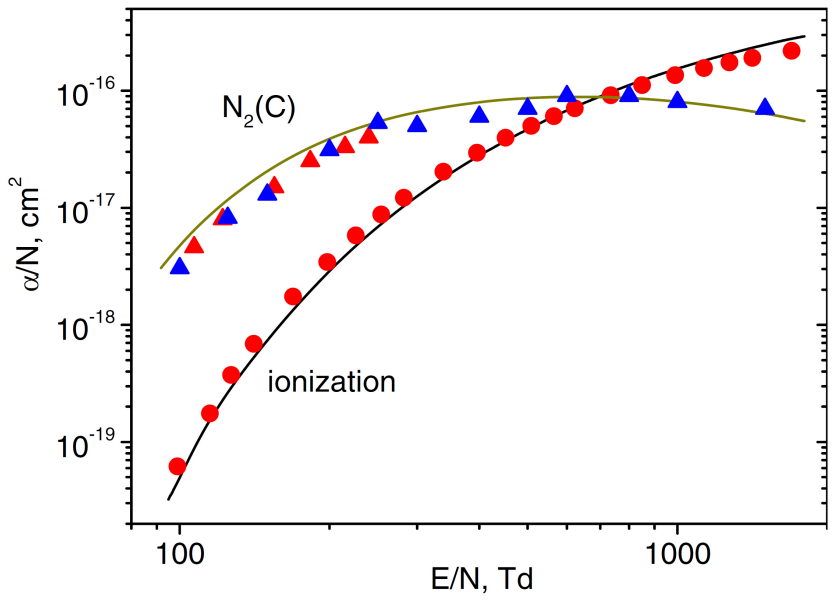

Figure 1.1 – Excitation rate coefficient of $N_2(C^3\Pi_u)$ state and the rate coefficient of ionization in nitrogen as functions of reduced electric field. Solid curves are the results of the calculations using BOLSIG+ [3] software. Symbols are the experimental data from [4] and references therein. The figure is taken from [5].

The solution of the Boltzmann's equation (i.e. EEDF) provides an important information of the energy branching in the discharge. The energy branching calculated for different gas compositions [6] is presented in Fig. 1.2. One can see from the figure that in air, for example, at relatively low reduced electric fields $E/N \lesssim 100$ Td the excitation of vibrational states of molecular oxygen and molecular nitrogen takes place, as well as rotational excitation. At higher E/N excitation of electronic states of N_2 dominates (triplet states at $E/N < 500$ Td, and singlet states at 500 Td $< E/N <$ 1000 Td). Further increase of the E/N ($>$ 1000 Td) leads to energy transfer to gas ionization.

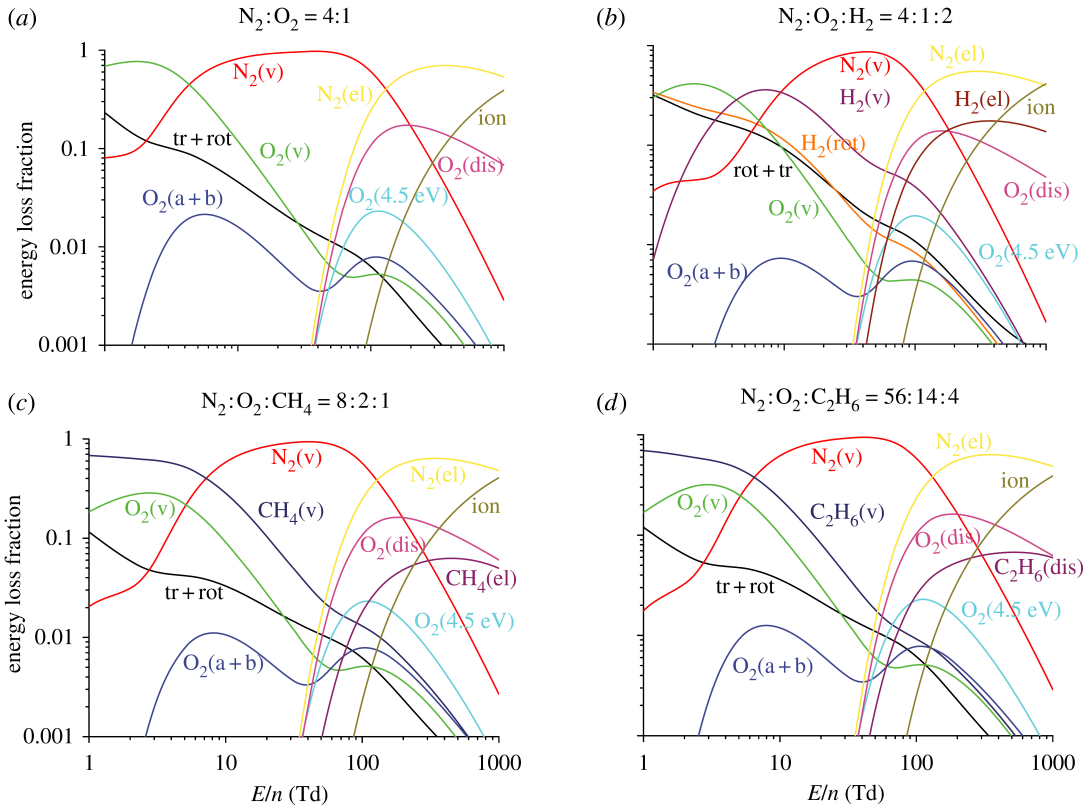

Figure 1.2 – Electron energy branching through molecular degrees on freedom as a function of E/N. (a) Air; (b) hydrogen–air; (c) methane–air; (d) ethane–air stoichiometric mixtures. tr + rot, sum of translational and rotational excitation; v, vibrational excitation; el, electronic excitation; ion, ionization; dis, dissociation; a + b, sum of electronic excitation of singlet 'a' and 'b' states of molecular oxygen. The figure is taken from [6].

The nanosecond discharges are characterized by relatively high reduced electric fields (hundreds of Td) [7–13] and, thus, are extremely efficient for excitation of electronic degrees of freedom. The non-equilibrium plasma produced by the nanosecond discharges is used in wide range of applications.

The highly reactive plasma can be successfully used in medical applications. They include living tissue sterilization and sterilization of non-living objects, non-thermal plasma assisted blood coagulation, plasma assisted wound healing and tissue regeneration, plasma assisted treatment of various diseases. Papers concerning the interaction of plasma or plasma generated products with living cells are discussed in details in the reviews [14–21]; the examples of the nanosecond plasma sources for medical applications can be found in [22, 23].

Non-equilibrium nanosecond plasma can be also used for ignition and/or combustion. According to [24], the main goals for plasma usage are the following: reduction of the ignition delay time, stabilization of the flame, slow fuel oxidation, ignition and flameholding, sustaining uniform ionization in supersonic flows. The control of deflagration-to-detonation transition [6] also should be noticed. The results of experimental research in plasma assisted ignition/combustion are summarized in the reviews [6, 25]. In Fig. 1.3 the results [24] of numerical studies of the stoichiometric ethylene-air mixtures ($P = 60$ Torr) ignition by experimentally validated kinetics model are presented.

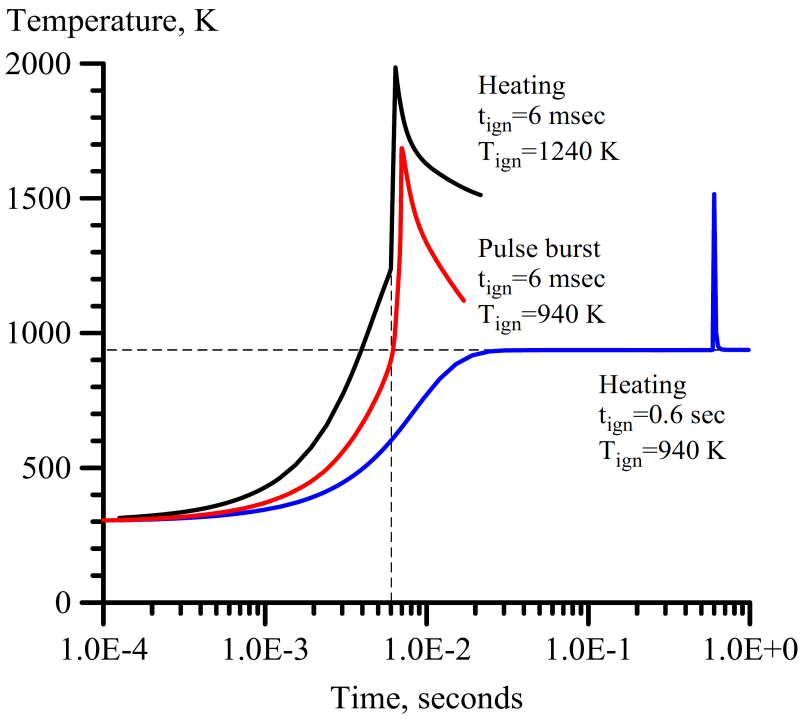

Figure 1.3 – Temperatures of a stoichiometric ethylene-air mixture ignited by a nanosecond pulse burst at $\nu = 50$ kHz (red curve) and by equilibrium heating: for the same ignition temperature (blue curve) and for the same ignition delay time (black curve). $P = 60$ Torr. The figure is taken from [24].

The ignition delay time and the ignition temperature can be obtained from the temperature-time plots for repetitively plasma ignition ($\nu = 50$ kHz, FWHM 25 ns, 20 kV) and ignition by steady-state heat source. The regime of the steady-state heating leading to ignition at the same temperature as at plasma ignition shows the delay time equal to 600 ms (blue curve), which is two order of magnitude longer then 6 ms corresponding to plasma assisted ignition (red curve), see Fig. 1.3. When the ignition times are the same, the ignition temperature with plasma (red curve) is 300 K lower than at equilibrium heating (black curve). Thus, non-equilibrium plasma can efficiently facilitate ignition of combustible mixtures.

The influence of the non-equilibrium plasma on the ignition/combustion simplistically can be reduced to two main effects: heating of the gas [5, 26–28] leading to increase of the chemical reaction rate constants, which generally yield to the Arrhenius equation, and/or production of the active species (radicals and excited molecules) [7, 29–32] leading to accelerating of chain reactions development. However, the influence of these two effects is difficult to separate. The roles of the effects were compared in [33], for example.

In [33] the kinetics of ignition of hydrocarbons by nanosecond discharge was studied experimentally and numerically in oxygen:argon mixtures. The discharge was initiated by high voltage pulses with the amplitude in range 100-160 kV (on the electrode) and the voltage rise rate of tens kilovolts per nanosecond behind the shock-wave reflected from the end plate of the shock-tube. The scheme of the experimental setup is presented in Fig. 1.4. The shock waves with different parameters were used to create different initial conditions (a pressure and a temperature).

The ignition delay times were measured and calculated numerically for the set of the initial conditions. The autoignition delay time τ_a (ignition without the discharge) was compared with the ignition delay time τ_d in the case of ignition by the discharge to demonstrate the influence of the nanosecond discharge. The examples of the experimental results and the results of the numerical calculations are presented in Fig. 1.5. The initial temperature was in the range 1370-1850 K for autoignition delay time measurements and 1180-1560 K for the plasma assisted ignition studies at the initial gas densities ranges $(0.6 - 2.6) \cdot 10^{18}\text{cm}^{-3}$ and $(0.6 - 2.6) \cdot 10^{18}\text{cm}^{-3}$, respectively. It is clearly seen that nanosecond discharge decreases the ignition delay time in about one order of magnitude.

To compare relative roles of the gas heating and the radicals produced in the nanosecond discharge, the temperature increase due to the energy released in the discharge was included in the model. The calculated numerically ignition delay times for C_2H_6:O_2:Ar (2:7:81) mixture at different assumption about the gas heating value are presented in Fig. 1.6.

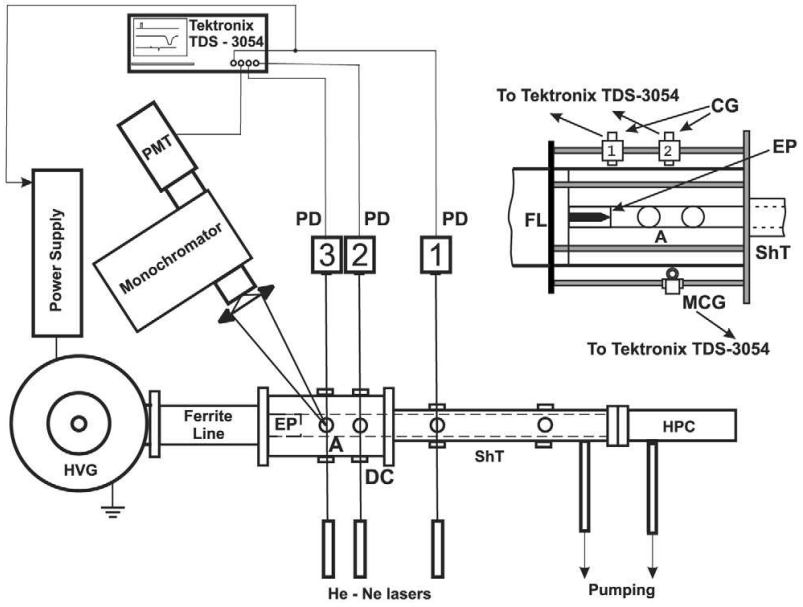

Figure 1.4 – Scheme of the experimental setup: DC, discharge cell; A, cross-section of measurement; EP, end plate; HPC, high pressure cell; HVG, high-voltage generator; ShT, shock tube; PD, photodiodes; PMT, photomultiplier; CG, capacitive gauge; MCG, magnetic current gauge. The insert gives the discharge cell on an enlarged scale. The figure is taken from [33].

(a) (b)

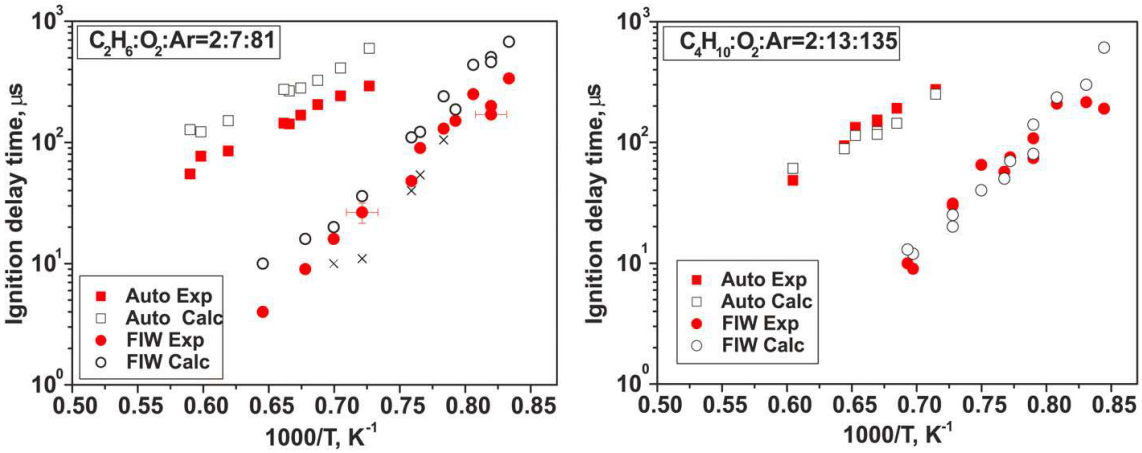

Figure 1.5 – The ignition delay time for autoignition (squares) and ignition with nanosecond discharge (circles). Filled symbols are the experimental results, open symbols are the results of the numerical calculations. (a) C_2H_6:O_2:Ar (2:7:81) mixture, (b) C_4H_{10}:O_2:Ar (2:13:135) mixture. The figures are taken from [33].

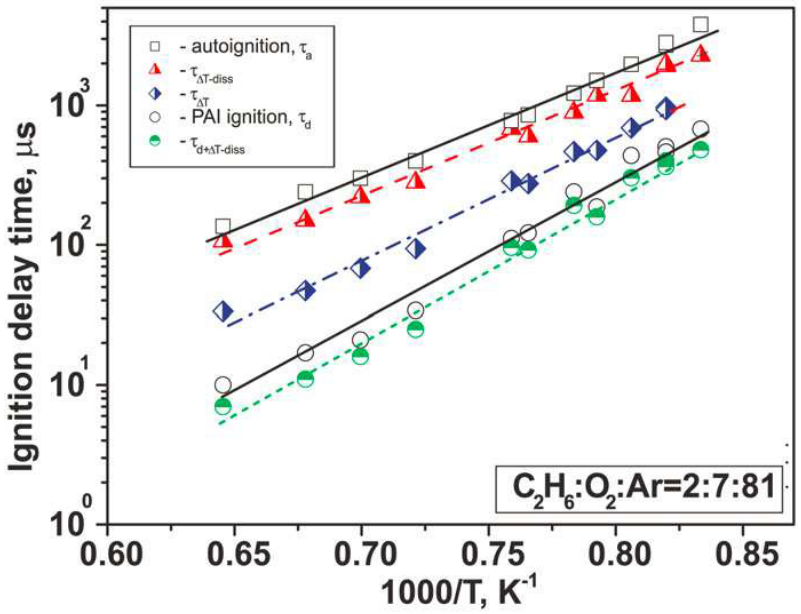

Figure 1.6 – The ignition delay times calculated numerically at different assumption about the gas heating value and the effect of the radicals produced in the discharge, see the text. The figure is taken from [33].

The square empty symbols correspond to autoignition delay time τ_a. The red symbols correspond to the ignition delay time, $\tau_{\Delta T-diss}$, calculated in assumption that all deposited discharge energy after deduction of radicals production energy is rapidly converted to the gas heating, the effect of radicals is neglected. One can see that heat release due to discharge decreases the ignition delay time comparing the autoignition. The blue symbols denote the ignition delay time, $\tau_{\Delta T}$, calculated in assumption that all deposited discharge energy is rapidly converted to the gas heating, the influence of the radicals is neglected. At this assumption the gas heating is overestimated, as a consequence, the influence on the ignition delay time in this case is much stronger. The empty circles denote the ignition delay time τ_d in the case when only the effect of radical is taken into account, the gas heating is neglected. The green symbols are the results of numerical calculations of the ignition delay time, $\tau_{d+\Delta T-diss}$, in the assumption of the gas heating due to deposited energy after subtraction of radicals production energy, the effects of the radicals included in the model. In this case the ignition delay time is the lowest. Thus, it can be concluded that both gas heating and the radicals production decrease ignition delay time, but the influence of the radicals produced by the non-thermal plasma is much more significant at the presented conditions.

To illustrate the influence of the non-thermal plasma on the ignition, the time evolution of the main components are presented in Fig. 1.7 for the autoignition and the plasma assisted ignition. One can see that large number of the radicals produced

in the nanosecond discharge leads to much faster decomposition of the hydrocarbons and chain-reactions development causing the faster ignition.

(a) (b)

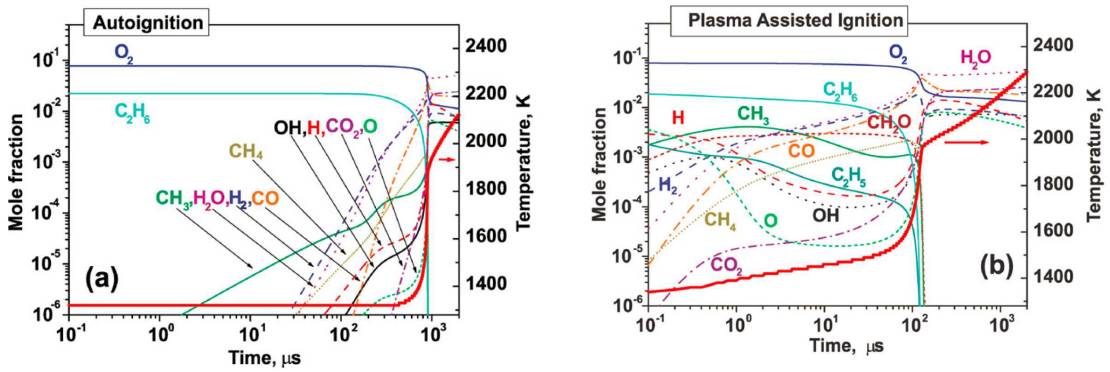

Figure 1.7 – Time evolution of the mole fractions of main components of the C_2H_6:O_2:Ar (2:7:81) mixture. (a) autoignition, (b) plasma assisted ignition. The gas temperature evolution is presented by thick red line. The initial temperature is 1318 K, the initial pressure is 0.6 bar. The figures are taken from [33].

If in the plasma assisted ignition/combustion the dominant role of the non-equilibrium plasma is the active radical production, in plasma flow control, which is another nanosecond plasma application, the influence of the plasma is non-chemical. Main flow perturbations caused by plasma can be identified according to the review [34]: (1) low-speed near-surface jets generated by electro-hydrodynamic interaction (ion wind); (2) spanwise and streamwise vortices formed by both electro-hydrodynamic and thermal effects; (3) weak shock waves produced by rapid heating in pulsed discharges on sub-microsecond time scale; and (4) near-surface localized stochastic perturbations, on sub-millisecond time. The nanosecond discharges can be especially efficient in control of high speed flows, since the characteristic time scale of the discharge and the post-discharge processes is much shorter than the time of flow-plasma interaction and acoustic time scale. Thus, they can be used in repetitively pulse mode accumulating the effects of a single shot discharge to increase the final impact on the flow. One of the main mechanisms of interaction of the nanosecond discharge with the flow is the fast heat release leading to compressive waves [35–39]. The compressive waves were studied by phase-locked schlieren imaging of the post-discharge in [39]. The dielectric barrier discharge (DBD) actuator was used. The discharge was initiated by positive polarity pulses (peak voltage up to 20 kV, pulse duration 50-100 ns FWHM) in atmospheric pressure quiescent air. The formation and propagation of the compressive wave due to fast gas heating

are clearly seen in Fig. 1.8. The temperature was measured by emission spectroscopic technique. The temperature rise $\Delta T = 80 \pm 50$ K at time scale ≈ 200 ns after the single discharge pulse was observed. The similar effect has been observed numerically, see, for example, [40].

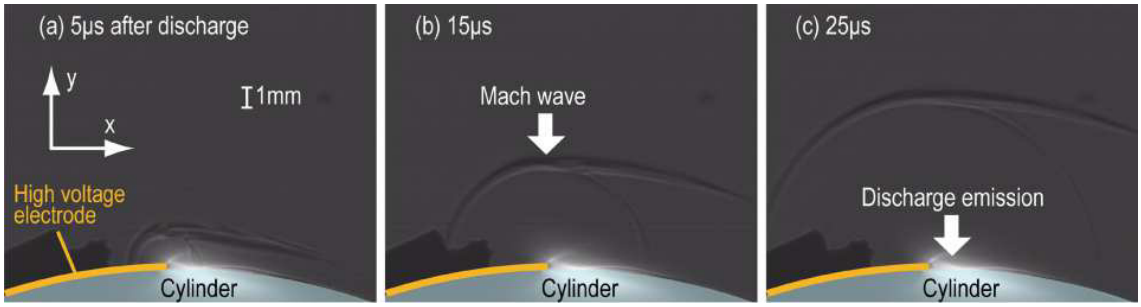

Figure 1.8 – Phase-locked schlieren images of a compression wave generated by a nanosecond pulse discharge for several time delays after the discharge pulse, from 5 μs to 25 μs. Positive polarity pulses, peak voltage is about 11 kV, pulse duration ≈ 100 ns FWHM), atmospheric pressure quiescent air. Images are taken from a direction parallel to the cylinder axis. The figure is taken from [39].

The interaction of the nanosecond-pulse-driven actuator with the airflow can be more complex than at quiescent air. It was studied by Schlieren visualization in [41], for example. The dielectric barrier discharge (DBD) was initiated in air by high voltage pulse with amplitude 10 kV and 40 ns rise time and 100 ns width. The DBD was initiated in the leading edge of the airfoil, see Fig. 1.9(a). The discharge impact in the quiescent air is rather similar to the described above. The pressure wave is produced by the heat release, see Fig. 1.9(b).

In the air flow (20 ms^{-1}) the heat release can impact the dynamic of the gas by another way. Experiments [41] showed that at the very beginning the pressure wave is produced as in the quiescent air at time scale of 0.01 ms, see Fig. 1.10(a). The dark color of the image in the region corresponding to the discharge area indicates that gas density decreases due to the gas heating causing a pressure wave. Further, when the pressure wave has passed, at time scale 0.2-0.5 ms the region with high gas density (the bright region in the image) is observed near the upper side of the foil, see Fig. 1.10(b) and Fig. 1.10(c), i.e. the gas density increases along the shear layer. In Fig. 1.10(b) the low-density region flowing downstream along the airfoil surface is seen (highlighted by the dashed ellipse). This low-density region is the gas, which has been heated by the discharge. Starting from 0.5 ms, Fig. 1.10(c), this region breaks into two heated zones denoted as (i) and (ii) in Fig. 1.10(d). The structure (i) flows along the shear layer with the flow speed. The approximately circular

(a) (b)

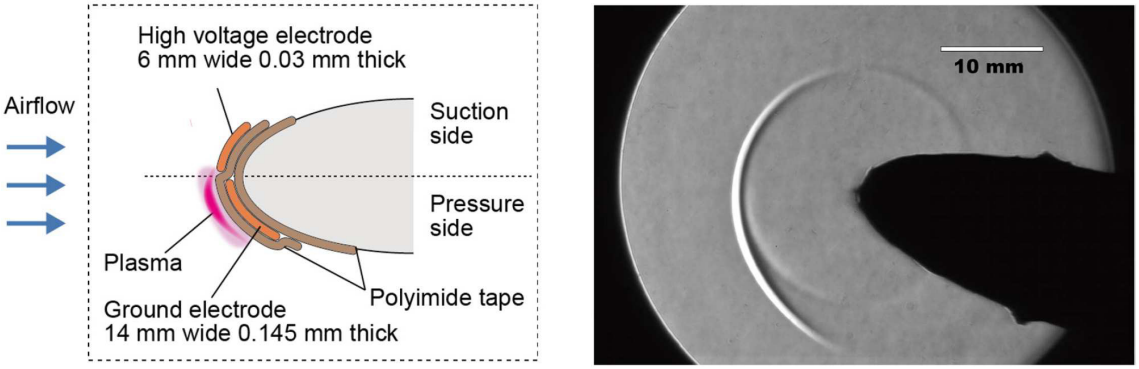

Figure 1.9 – (a) Schematic view of the electrode configuration viewed from spanwise direction. (b) The pressure wave in quiescent air at 30 μs after the discharge near the leading edge of the airfoil. The amplitude of the high voltage pulse is 10 kV, the rise time is 40 ns and the pulse width is 100 ns. The figures are taken from [41].

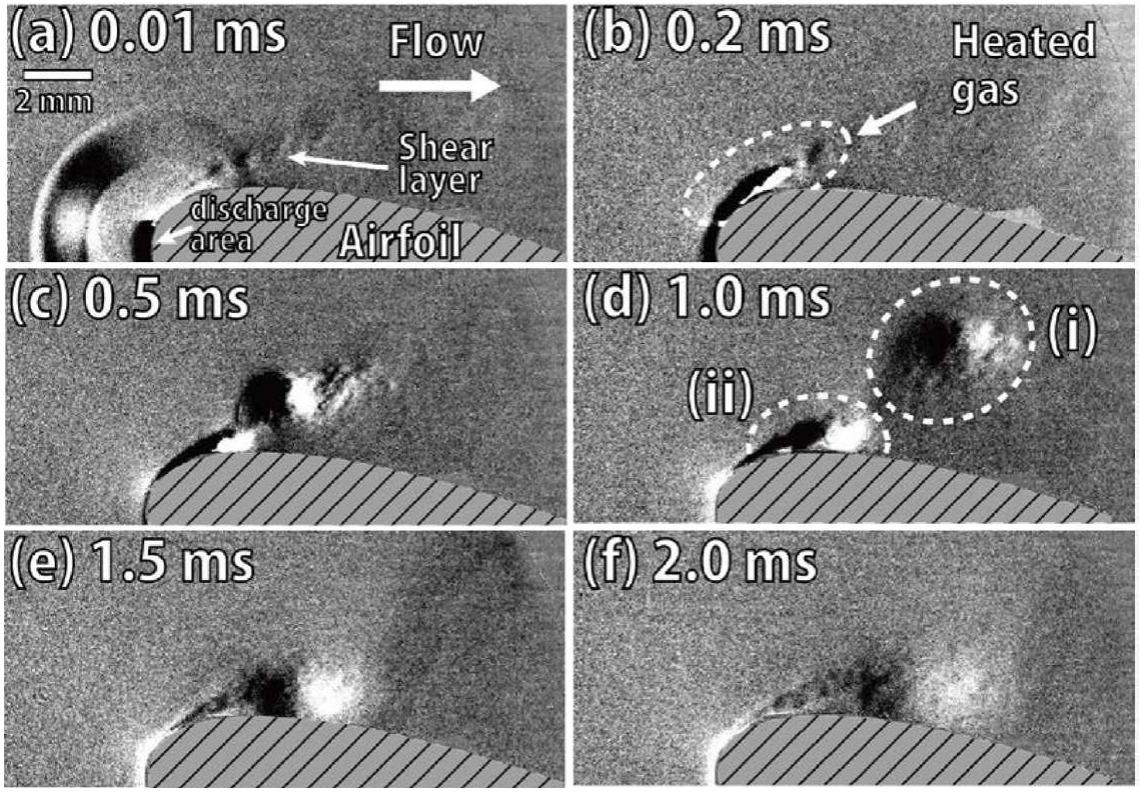

Figure 1.10 – Temporal variations of Schlieren images of airflow (20 ms^{-1}) near the airfoil after the pulsed discharge. The angle of attack is 22 degrees. The figure is taken from [41].

structure (ii), in contrast, moves slowly along the airfoil surface. At the repetitively mode operation of the nanosecond DBD plasma actuator (ns-DBDPA) the heated zone (i) becomes diffusive and approaches the airfoil surface. The effect is enhanced at each new discharge pulse. Finally, it was shown [41] for the angle of attack of 16 degrees that continuous ns-DBDPA operation leads to the attachment of the air flow to the airfoil surface with a transition time about 10 ms. After 10 ms the flow is in a quasi-steady state. At the angle of attack of 22 degrees (corresponding to the Fig. 1.10) the effect is unstable, the flow separates from the airflow and reattaches to it repeatedly. Nevertheless, the influence of the nanosecond discharge is clearly seen. Finally, the authors conclude that thermal perturbations on the sub-millisecond time scale due to gas heating are more important than pressure waves at the described conditions.

Thus, one can see that non-thermal plasma produced in the nanosecond discharges can be used in wide range of applications. Starting with living cells/tissues treatment, where low temperature of the non-equilibrium plasma is the key feature, continuing with plasma assisted ignition/combustion, where the active radical production is complemented by the gas heating due to energy deposited in the gas during the discharge, and ending with plasma flow-control, where the fast and significant temperature rise is one of the most important way of flow interaction, and the radical chemistry is omitted. However, the radical production and the gas heating due to the nanosecond discharges are coupled. This interrelationship is reviewed in more details in the next section. The methods and techniques of the fast gas heating studies are discussed as well.

1.2 Fast gas heating

The term *fast* gas heating (FGH) [5] means the gas heating occurs at times much less than those of VT relaxation, or VV′ exchange.

Initially, fast gas heating has been observed in microwave discharges in air and nitrogen, see, for example, [42], where the heating has been studied at pressures 10 Torr and 30 Torr at reduced electric field $E/N \approx 100$ Td. It was concluded that measured abnormal high heating rate can not be explained by relaxation of the vibrational energy of the molecules. It was proposed that the heating is caused by relaxation of the electronic energy of the excited species.

With development of nanosecond discharge techniques the same observation became possible at higher E/N. The observations of the gas heating can be performed at direct gas temperature measurements by optical emission spectroscopy [28,43–46] or by laser techniques [36,47,48], see also the review [49] and references therein; or by

indirect measurements, for example, shock-wave front propagation dynamics [50,51] or gas density dynamics measurement by interferometry [52]. However, last two methods can be less precise, since they are affected by sufficient influence of the gas-dynamics perturbations [5]. The laser techniques are very precise, but require rather complex experimental equipment. The optical emission spectroscopy is rather precise and simple in the same time. Thus, the spectroscopic temperature dynamics measurements are usually more preferable, and are widely used for validation tests of kinetic models developed to describe the mechanism of fast gas heating. It has been chosen as an experimental method of temperature measurements in the present Thesis. Further, the examples of the results of fast gas heating investigations obtained with this technique are discussed.

The spectroscopic temperature measurements are usually based on the rotational structure of the molecular nitrogen emission bands. The details of the technique are presented in the review [53]. In [45, 46] the rotational temperature of molecular nitrogen was measured and compared with synthetic spectrum calculated numerically using SPECAIR [54] software. The measurements of fast gas heating were performed in preheated air (1000 K) at atmospheric pressure. The discharge parameters are the following: pulse duration 10 ns, voltage amplitude 5.7 kV, repetition rate 10 kHz, pip-to-pin geometry with 4 mm gap, leading to reduced electric field value $E/N \leq 250$ Td. In Fig. 1.11 the example of measured and calculated spectra of (0-2) transition of the second positive system of molecular nitrogen is given [46]. One can see that this technique allows to measure the rotational temperature of excited species with rather high precision.

The results [45] of temperature evolution measurements during the discharge pulse are presented in Fig. 1.12. One can see the fast rise of the temperature during the discharge pulse (20 ns): from initial temperature of 1000 K to 2400 K. It is important to note that the time interval during which the measurements of the rotational temperature correspond to the gas temperature is limited, since it is required that $N_2(C^3\Pi_u)$ state is populated from lower electronic state by direct electron impact. After the pulse end (20 ns) the electric field is zero and $N_2(C^3\Pi_u)$ state is formed by the pooling reaction between metastable states of molecular nitrogen [55, 56]

$$N_2(A^3\Sigma_u^+, v) + N_2(A^3\Sigma_u^+, v') \rightarrow N_2(C^3\Pi_u) + N_2. \tag{1.3}$$

Authors [45] emphasize this fact by the red two-pointed arrow in Fig. 1.12. The applicability of the method of the temperature measurements based on $N_2(C^3\Pi_u)$ state emission at conditions of the Thesis will be discussed in details in Section 9.1.

The temperature rise during the discharge pulse presented in Fig. 1.12 is about 1400 K during 20 ns, which is rather high. Typically, in the experiments the final temperature rise due to fast gas heating is lower, or the heating rates are slower

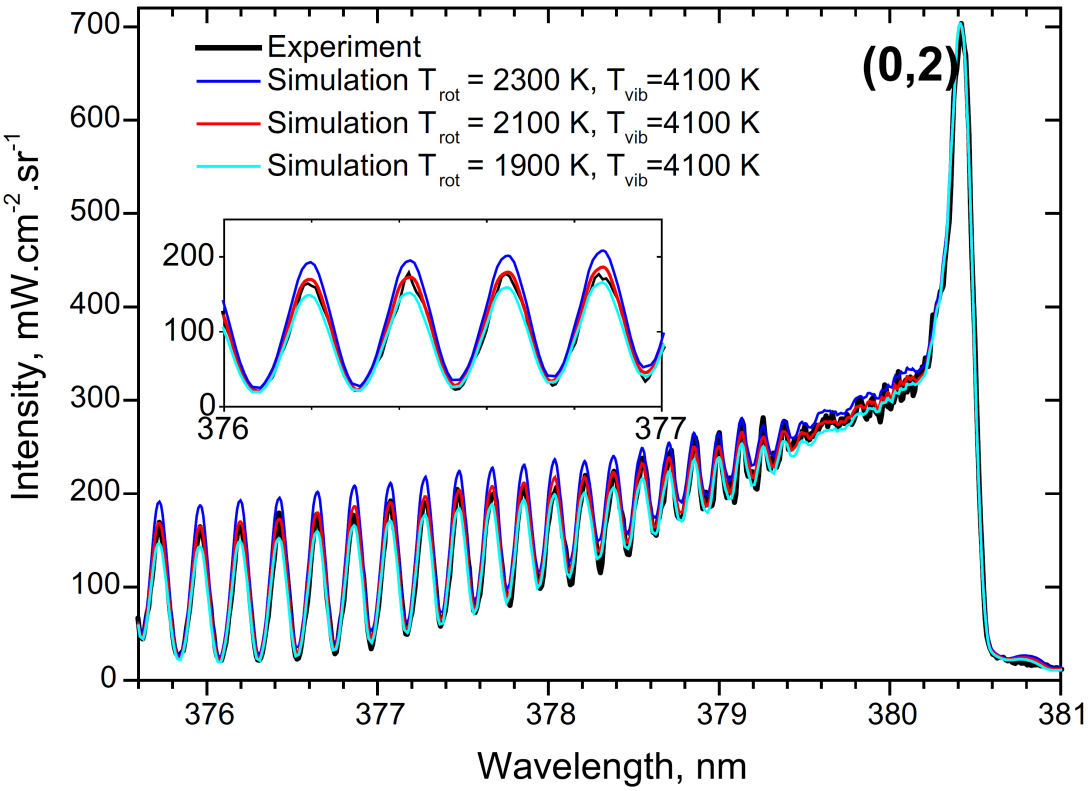

Figure 1.11 – Measured and calculated spectra of (0-2) transition of the second positive system of molecular nitrogen. The figure is taken from [46].

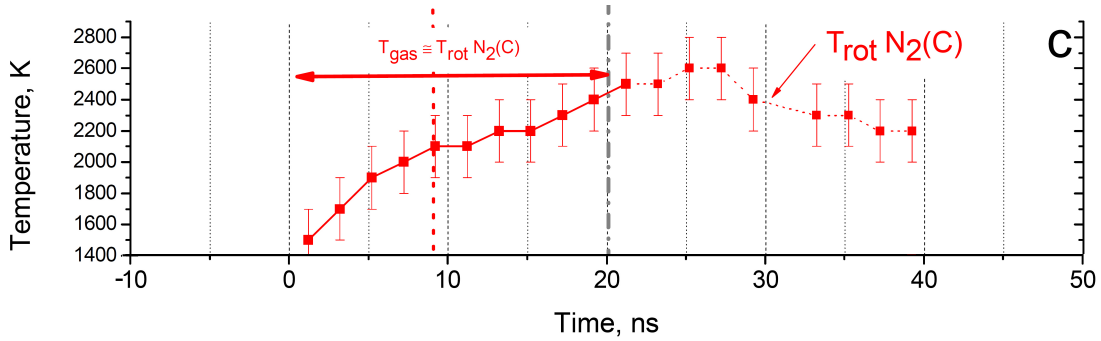

Figure 1.12 – The rotational temperature of $N_2(C^3\Pi_u)$ state during the discharge and early afterglow. The figure is taken from [45].

(however, the rates are still faster than VT relaxation, or VV′ exchange), due to conditions different from the conditions of [45, 46]. For example, in [57] the two stages of heating due to nanosecond discharge (pin-to-plane streamer in dry air at atmospheric pressure, 32 kV pulse amplitude and duration ≈ 200 ns FWHM) were observed: fast stage at times $t \leq 1$ μs and slow one at time scale of hundreds of microsecond. The total heating ΔT was low, about 22-26 K [5]. However, the

dynamics of gas density measured in the experiment was successfully used for the kinetic model validation developed in [5], which will be discussed further.

The kinetic models of the fast gas heating in nitrogen-oxygen plasma are presented in [5,26–28]. The model [5,26,27] was validated for a broad range of reduced electric fields using experimental results. The good agreement of the calculation results with the results of the experiments confirms that energy relaxation from the electronic degrees of freedom of excited species is the heating source at time scale much less than those of VT relaxation, or VV′ exchange. The main processes leading to gas heating in air described in the model [5] are: (i) dissociation of nitrogen and oxygen molecules by electron impact, (ii) quenching of the electronically excited states of nitrogen molecules by oxygen molecules, (iii) quenching of the excited atoms $O(^1D)$, (iv) ion-molecule reactions, reactions of electron-ion and ion-ion recombination. The ratio between energy release through the different channels is function of the reduced electric field. The contribution of different processes in the fast gas heating was calculated in [5] for air at pressure 760 Torr, see Fig. 1.13. One can see that at fields $E/N \leq 200 - 300$ Td the dominant processes are quenching of $N_2(C^3\Pi_u)$ and $N_2(B^3\Pi_g)$ states by molecular oxygen and quenching of $O(^1D)$ atoms, total contribution more than 70% [5]. At high reduced electric fields ionization become sufficient, see Fig. 1.2, and the heating due to charged particles becomes dominant.

One of the most important parameters for the nanosecond discharge applications is the value of the energy spent to the fast gas heating. Several corresponding parameters can be introduced [5,26]: the fraction of the discharge energy converted to the gas heating

$$\eta_R = \frac{W_R}{j \cdot E \cdot N}, \tag{1.4}$$

where W_R is the gas heating rate in chemical reactions, j and E are the current density and the electric field in the discharge, respectively, N is the gas density; the fraction of the discharge energy spent to electronic excitation/ dissociation/ionizations of molecules η_q; and the fraction η_E of the energy spent to electronic excitation/dissociation/ ionizations of molecules converted to the gas heating calculated as

$$\eta_E = \frac{\eta_R}{\eta_q} \tag{1.5}$$

In general case, the detailed kinetic studies are required to calculate η_R and η_E, that is rather complex task. However, for nitrogen:oxygen mixtures it was shown [5, 26] that η_R and η_E are the functions of the reduced electric field only. The value η_R sufficiently increases with E/N, while the value η_E is almost constant and equal to $30 \pm 3\%$. Since the values η_R and η_E are functions of E/N, it makes them extremely convenient for studies of plasma and plasma applications in air and

nitrogen-oxygen mixtures. Using η_R and η_E it is enough to know only E/N and the total value of the discharge energy to predict the amount of the energy going to the gas heating. The precise kinetics calculations are not required to estimate the gas heating in this case.

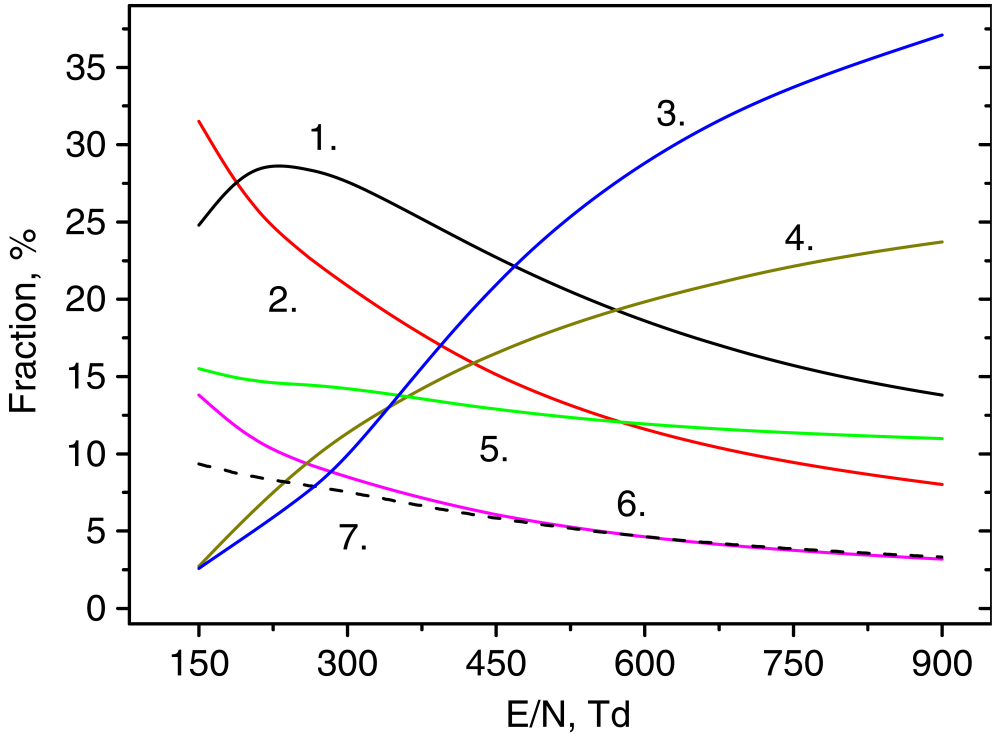

Figure 1.13 – Calculated contribution of different processes in the fast gas heating in air at $P = 760$ Td as function of reduced electric field. Curve (1) quenching of $N_2(C^3\Pi_u)$ state by molecular oxygen, (2) quenching of $N_2(B^3\Pi_g)$ state by molecular oxygen, (3) reactions involving charged particles, (4) dissociation of N_2 by electron impact and following quenching of $N(^2D)$ atoms, (5) quenching of $O(^1D)$ atoms by molecular nitrogen, (6) dissociation of O_2 by electron impact, (7) quenching of $N_2(A^3\Sigma_u^+)$ and $N_2(a'^1\Sigma_u^-)$ states by molecular oxygen. The figure is taken from [5].

However, as will be demonstrated in Chapter 9, for pure nitrogen these values also depend on the specific deposited energy or on the initial gas temperature. It is caused by the strong temperature dependence of the rate constant of the process

$$N(^2D) + N_2 \rightarrow N(^4S) + N_2(v), \tag{1.6}$$

which influences on the fast gas heating significantly, since, as it was shown in [58], up to 90% of excitation energy of $N(^2D)$ atoms (2.35 eV) goes to the gas heating and less than 10% goes to vibrational excitation of molecular nitrogen. According to the

results of calculations [59], the rate constant of this process significantly increases with gas temperature

$$k_{(1.6)}(T) = 4.52 \cdot 10^{-14} \cdot T^{0.68} \cdot exp\Big(- \frac{1438}{T} \Big) \text{ cm}^3\text{s}^{-1}. \quad (1.7)$$

The significant influence of quenching of excited nitrogen atoms on the fast gas heating in pure nitrogen was demonstrated in [60]. The discharge was initiated at room temperature and 100 Torr pressure by 10 kV high voltage pulse 100 ns in duration between two sphere-shape electrodes. The gas temperature was equal to about 500 K at 5 μs, i.e. the temperature rise was only 200 K. It was concluded based on the comparison of the numerical results with the experimental results of the temperature measurements that 20% of nitrogen atoms generated in the discharge are in N(^{2}D) state. However, the data about molecular nitrogen dissociation by electron impact obtained in [61] show that predissociation to N(^{2}D) + N(^{4}S) fragments is the primary mechanism of N_2 dissociation. Thus, the fraction of the nitrogen atoms generated in the discharge in N(^{2}D) state obtained in [60] can be underestimated. Consequently, this leads to uncertainty in the determination of the role of the quenching of the N(^{2}D) atoms in the fast gas heating. The influence of the quenching of excited nitrogen atoms can be clearly demonstrated at higher temperatures due to strong temperature dependence of the rate constant (1.7) of the reaction (1.6). Thus, higher temperatures are required to investigate the mechanism of the fast gas heating in pure nitrogen precisely. To obtain higher temperatures, the higher specific energy deposition and higher excitation degree are required.

The fast ionization wave (FIW) is characterized by high reduced electric fields, which provide high excitation degree leading to intense fast gas heating. To obtain high specific energy deposition, the discharge in the capillary tube can be used. The current density in the main discharge phase after the fast ionization wave propagation is increased significantly in this case. For example, it was shown [62, 63] that high temperatures up to 3000 K can be obtained at microsecond time scale by the nanosecond capillary discharge with fast ionization wave at high specific energy deposition up to 1 eV/molecule in air. This experimental tool has been chosen for the experimental program of the Thesis. In the next section the fast ionization waves and the discharges in long and capillary tubes are reviewed.

1.3 Fast ionization waves. Discharges in thin dielectric tubes.

The fast ionization waves have been studied for a long time, since its discovery in 1893 [64]. The FIWs can be initiated in free space (see review [8] and references

therein), and in large volumes at low pressure [65, 66]. The FIW in the last case propagates quasi-spherically producing rather uniform distribution of the excited species [66].

However, classical configuration of the discharge cell for the FIW studies is a long discharge tube surrounded by a metal cylindrical screen. The discharge cell is connected to the generator of high-voltage nanosecond pulses by coaxial transmission line. The high-voltage electrode installed inside the tube is connected to the central conductor of the coaxial line, the metal screen is connected to the shielding of the coaxial line. Thus the discharge cell is a continuation of the coaxial transmission line. The schematic view of the discharge cell with FIW propagating inside is shown [8] in Fig. 1.14.

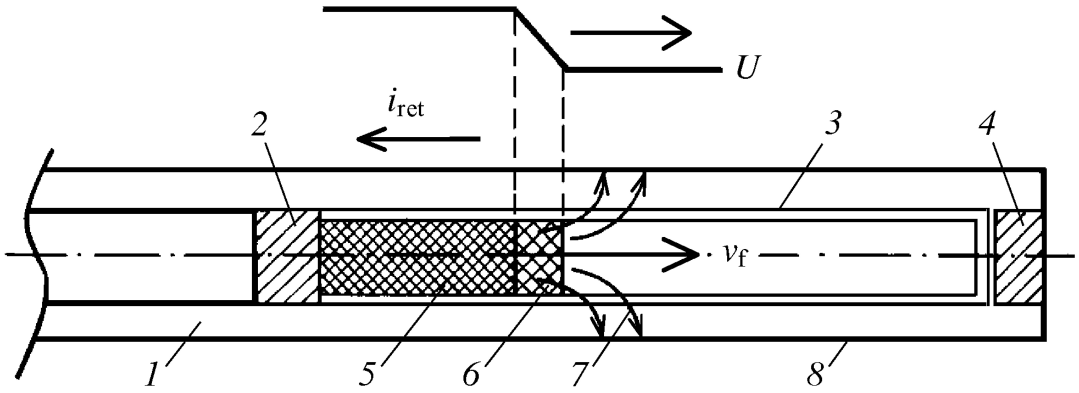

Figure 1.14 – Schematic view of the long tube discharge cell for the FIW studies. Coaxial transmission line (1) connected to the high-voltage electrode (2), installed in the discharge tube (3); low-voltage electrode (4). High-conductivity plasma column follows the wave front (6) propagating from the left to right with velocity v_f. The electric field force lines (7) close on the cylindrical metal screen (8). i_{ret} is the return current in the metal screen flowing in opposite direction relative to the wave front, U is the potential distribution in the wave front. The figure is taken from [8].

Fast ionization waves in long tubes are used both for plasma studies and for applications. One of the main advantages of the FIW is a high excitation degree of electronic degrees of freedom. The high energy deposition is no less important feature. Varying the geometry of the discharge cell presented in Fig. 1.14, the gas pressure and the high voltage pulse parameters, one can obtain very efficient absorption of the energy of the electric pulse by the discharge tube: higher than 80% in the first pulse, and almost 100%, if all subsequent re-reflections between discharge cell and high voltage generator are taken into account [67, 68]. Therefore,

the FIWs are especially useful for applications. For example, FIW in nitrogen or air can be used as high power laser UV source [8, 69–72]. It should be noted that high probability of the laser effect at high nitrogen excitation degree can influence the results of excited species decay measurements, see Section 7.2.1.

The fast ionization wave propagates as wave of charging of the capacitance formed by the tube and the metal screen. The best way to illustrate the FIW propagation is to plot the electric field dynamics at different distances x from the high voltage electrode using the capacitive probe (CP) moving along the tube (or using a number of CPs installed at different x). The example of the measurements of the electric field dynamics is presented in Fig. 1.15 [73]. The nanosecond discharge was initiated in the glass tube of inner diameter 1.75 cm and 60 cm length filled with air at $P = 8$ Torr. The tube was surrounded by the coaxial metal screen with the radius of 6 cm. The negative polarity high voltage pulse with the peak-pulse amplitude in the HV cable equal to $U = -15.5$ kV, the rise time equal to 3 ns and the pulse duration equal to 25 ns was applied to the flat HV electrode. The electric field in the FIW front is rather high and equal to ≈ 5 kV/cm (or ≈ 2000 Td at $P = 8$ Torr and $T = 300$ K), see Fig. 1.15. It should be noted that in Fig. 1.15 the longitudinal component of the electric field is presented, since the electric field is calculated as a derivative of the electric potential on the tube surface measured by the capacitive probe. The radial component of the electric field is not detected is this case. The electric current is closed on the metal screen by the displacement current during the FIW propagation, thus, the radial component of the electric field is dominate in the FIW front, see (7) in Fig. 1.14. Therefore, the total electric filed in the FIW front is even higher than the value 2000 Td presented in Fig. 1.15. It is seen in Fig. 1.15 that FIW front propagates from the HV electrode along the tube with velocity ≈ 40 mm/ns.

The FIW always starts from the high voltage electrode regardless the pulse polarity [8, 74]. However, there is the principal difference between the FIWs produced by negative and positive high voltage pulses, which can be important. The point is that at negative polarity pulses the high-energy electrons accelerated in the high electric field in the FIW front move ahead the fast ionization wave front and do not influence the EEDF behind the FIW front. In contrast to the negative polarity discharge, in positive polarity discharge the high-energy electrons heated in the FIW front are "injected" into the plasma volume. In this case the EEDF behind the front is affected by the high-energy electrons and becomes non-local. The high-energy part of the electron energy distribution function is overpopulated. The difference in the FIWs at negative and positive polarities was demonstrated in [74], for example. The temporal electric field profile measured by the capacitive probe was compared with the one measured by the spectroscopic method. The discharge was initiated in a

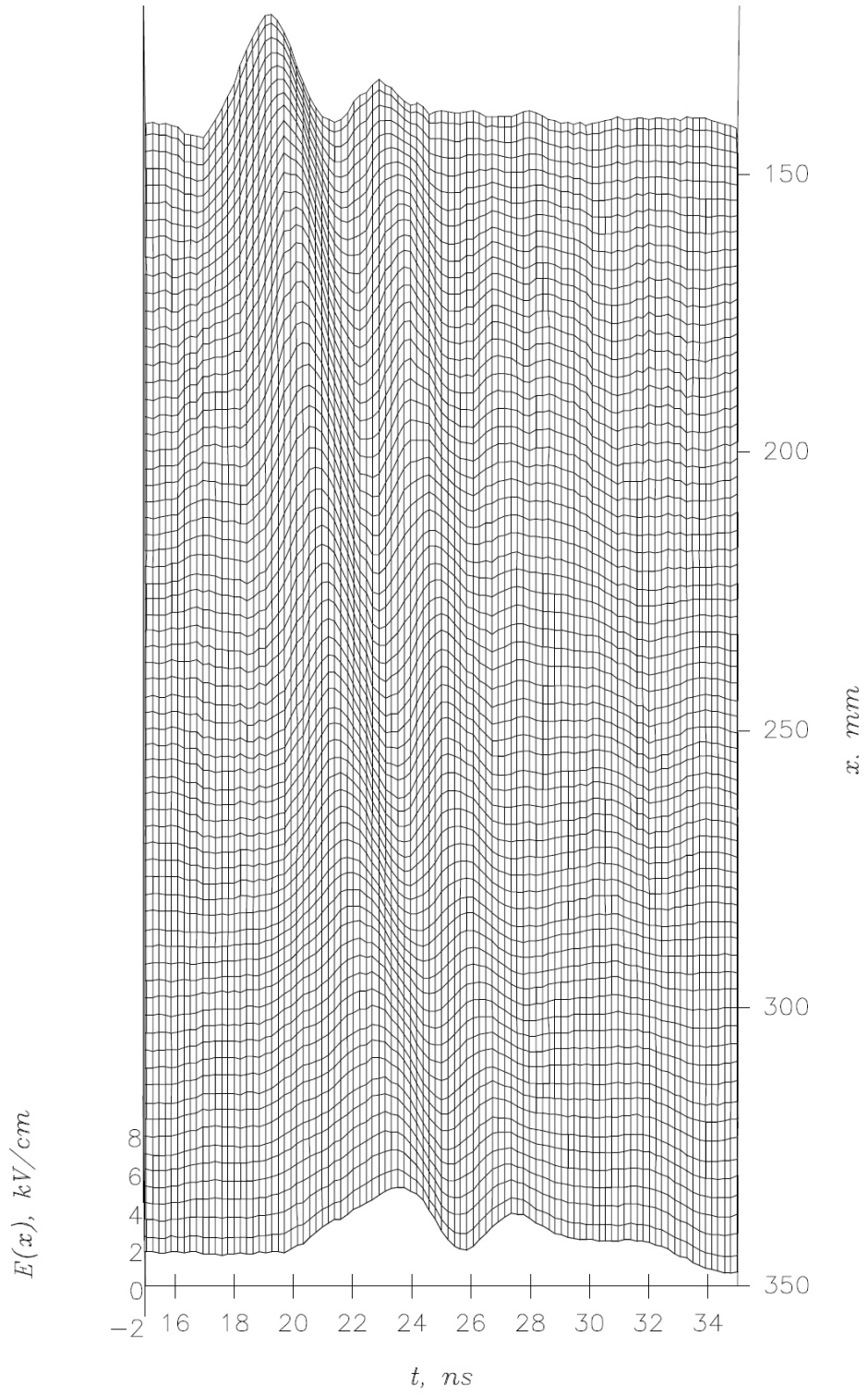

Figure 1.15 – Electric field dynamics at different distances x from the high-voltage generator in the glass tube of inner diameter 1.75 cm and 60 cm length. Air, $P = 8$ Torr; negative polarity, the peak-pulse amplitude in the HV cable is $U = -15.5$ kV, the rise time is 3 ns, the pulse duration is 25 ns. The figure is taken from [73].

quartz tube, of inner diameter, 17.5 mm, outer diameter, 21.5 mm, and length, 600 mm, filled with pure nitrogen at $P = 5$ Torr by high voltage pulses of 13.5 kV amplitude, 25 ns duration and 6 ns rise time. The spectroscopic method was based on the measurements of the intensities of the first negative system (FNS) and the second positive system (SPS) of molecular nitrogen. The rates of the population by electron impact $Y(x,t)$ were measured and compared for the $N_2(C^3\Pi_u, v = 0)$ and $N_2^+(B^2\Sigma_u^+, v = 0)$ states. The $Y(x,t)$ was defined as:

$$Y(x,t) = \frac{\partial I}{\partial t} + k_q[\mathrm{N_2}]\mathrm{I} + \frac{\mathrm{I}}{\tau}, \tag{1.8}$$

where I is the intensity of the transition, k_q is the quenching rate constant, τ is the lifetime of the energetic level, $[N_2]$ is the background gas density. It was assumed that there is no self-absorption and the densities of the $N_2(C^3\Pi_u, v = 0)$ and $N_2^+(B^2\Sigma_u^+, v = 0)$ states are proportional to the intensities of corresponding optical transitions. The ratio of the excitation rates $Y_C(x,t)$ and $Y_B(x,t)$ is function of the reduced electric field value, since

$$\frac{Y_C(x,t)}{Y_B(x,t)} = \frac{k^C(E/N)}{k^B(E/N)}, \tag{1.9}$$

where $k^C(E/N)$ and $k^B(E/N)$ are the rate constants of the excitation by the electron impact. The ratio $k^C(E/N)/k^B(E/N)$ was pre-calculated using the BOLSIG software [75] in the expected reduced electric field range. The electric field value measured by spectroscopic technique is sensitive to the EEDF, since $k^C(E/N)$ and $k^B(E/N)$ depend on the EEDF. The electric field measurements by the capacitive probe do not require any assumption about EEDF and can be used as a reference. The results of E/N measurements by two different techniques are presented in Fig. 1.16.

One can see that at negative polarity the results of the measurements by two different techniques are rather similar. At positive polarity, the difference between the electric field profiles measured by capacitive probe and spectroscopic technique is significant. The electric field measured on the basis of the spectroscopic data is overestimated comparing with the CP data in the FIW front. It should be commented that the overestimation is not caused by the fact that only longitudinal component of the electric field is measured by the capacitive probe, since at negative polarity the overestimation is not pronounced. Authors conclude [74] that the difference between the electric field profiles obtained by CP and the spectroscopic data is due to EEDF non-locality behind the wave front at positive polarity. As was mentioned above, at positive polarity high-energy electrons move inside the plasma. Moreover, E/N in the wave front is higher at positive polarity, see Fig. 1.16, thus, electrons gain higher energy in the wave front and perturb the EEDF more signifi-

cantly. Additionally, the EEDF relaxation is longer in the case of positive polarity, since the difference between energies of electrons gaining energy in the FIW front and behind it is higher than at negative polarity. Indeed, E/N behind the front of positive FIW is lower than E/N behind the front at negative polarity, consistently, the mean energy of the thermalized electrons is lower too. Therefore, it can be concluded that the possible EEDF non-locality behind the wave front should be taken into account, especially, at positive polarity high voltage pulses. The estimations of the EEDF relaxation should be done, if the local approximation is used.

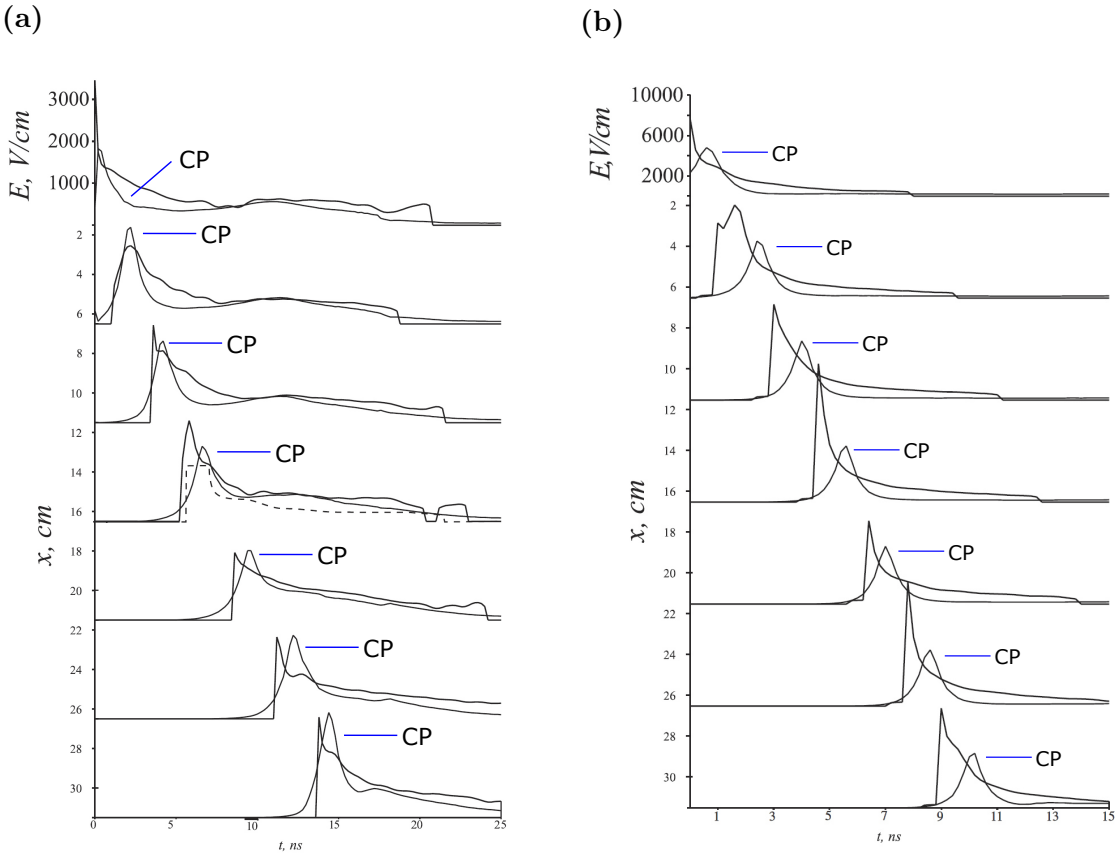

Figure 1.16 – Dynamic of the electric field measured by the capacitive probe (CP) and the spectroscopic technique (see text): (a) negative polarity, (b) positive polarity. Pure nitrogen at $P = 5$ Torr, high voltage pulses of 13.5 kV amplitude, 25 ns duration and 6 ns rise time. The original figures are taken from [74].

The influence of the non-locality on the results of kinetic studies is not critical, if the most energy is deposited (when the most part of excited species is produced) after the FIW front passing; for example, if the high current stage follows the FIW front propagation. In Fig. 1.17 the results of the measurements of the electric field, the electric current and the power deposited in the discharge in different cross-sections of the quartz discharge tube are presented [76]. The discharge was initiated in

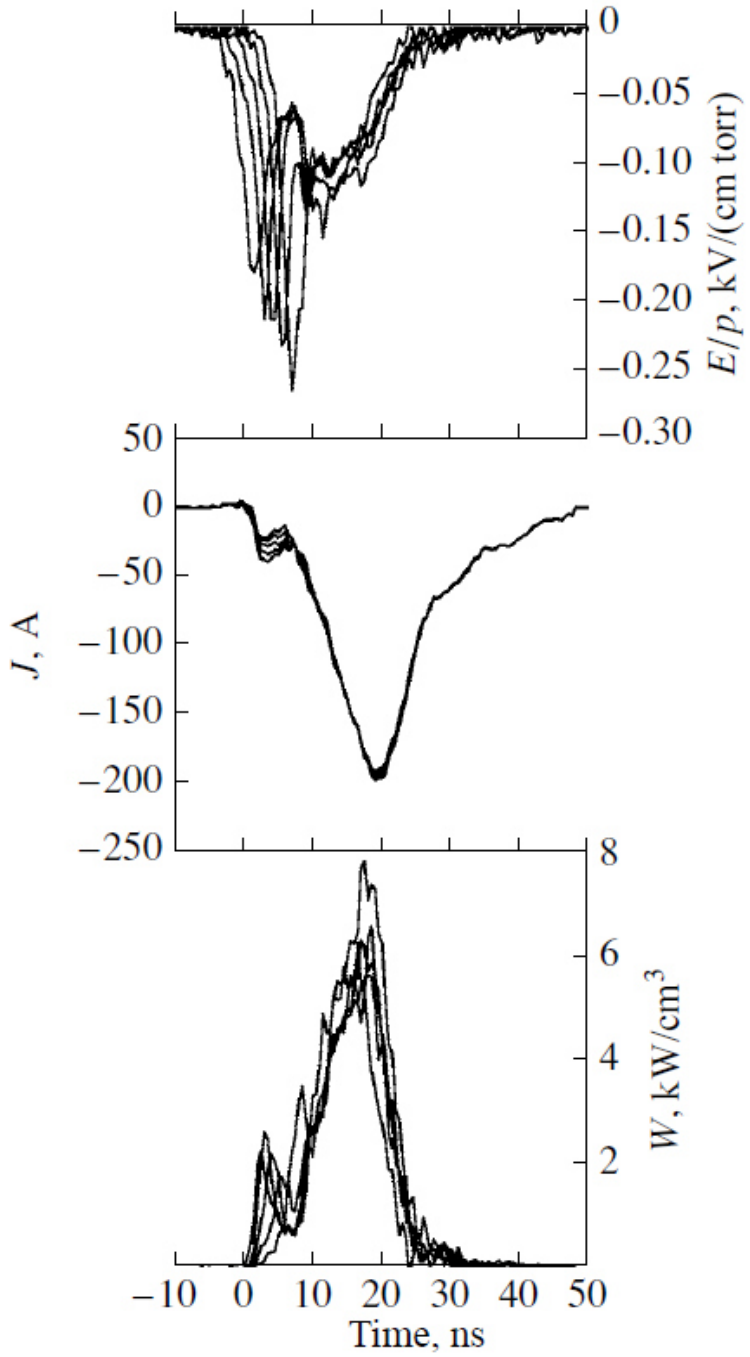

Figure 1.17 – The electric field, the electric current and the power deposited in the discharge in different cross-section of the discharge tube (the distances from HV electrode are 0.0, 3.6, 7.2, 10.8, 14.4 and 18 cm at total tube length of 20 cm). The discharge is initiated in a methane-air stoichiometric mixture at $P = 6.05$ Torr by negative voltage pulses with an amplitude equal to 11 kV, pulse duration of 25 ns and rise time of 5 ns. The figure is taken from [76].

a methane-air stoichiometric mixture by negative voltage pulses with an amplitude equal to 11 kV, pulse duration of 25 ns and rise time of 5 ns. One can see in Fig. 1.17 that the deposited power is high when the FIW has already passed, the discharge gap is closed and the high electric current flows. It also should be noted that the waveform of the electric current and electric field are the same in the different cross-sections of the tube when the gap is closed. Thus, the discharge is rather uniform along the tube. This is another advantage of this type of the discharges both from the point of view of applications, and from the research point of view as well.

As it was mentioned above (Fig. 1.17), after the FIW reaches the low-voltage electrode, the inter-electrode gap is closed and the electric current starts to flow. The distribution of the current density in the cross-section of the tube at this stage depends on the initial electron density distribution in the tube cross-section formed during propagation of the front of the fast ionization wave. At given high-voltage pulse characteristics the initial distribution of the current density determines following discharge development and electron density, and, consequently, final energy deposition, as well as the densities of the excited species.

The initial electron density profile formed by FIW depends on the number of factors: high voltage pulse characteristics, pressure, gas composition, as well as the discharge cell geometry. For example, in [77] the influence of the high voltage pulse polarity and the gas pressure on the discharge structure was studied in the tube with length 50 cm and diameter 1.8 cm by ICCD imaging (without reconstruction of the emission radial distribution). The ICCD images of the discharge are presented in Fig. 1.18.

It is extremely important to note that observed distribution of intensity, in fact, is a result of direct Abel transform of the real radial distribution of the emission, since the light is collected from the entire plasma volume. In another words, the image is a projection of the emission distribution on the plane of the ICCD matrix. The cross-section of the plasma volume is a circle. The plot of the projection of the circle with a uniform emission distribution is a parabola with maximum in the point corresponding to the tube axis. The result of the Abel transform of the thin ring with the radius r is two peaks on the projection at a distance r from the point corresponding to the tube axis position. The Abel transform is discussed in more details in Section 3.2.4 of the Thesis. Taking all this into account it is seen in Fig. 1.18 that at $P = 2$ Torr at positive polarity the radial distribution is more uniform, while at negative polarity the maximum of the emission is out of the axis of the tube. At higher pressure $P = 8$ Torr both distributions have the maximums out of axis of the tube, but at positive polarity the distribution seems to be more flat. The quantitative analysis of the distributions requires additional studies, but this is beyond the scope of the literature review.

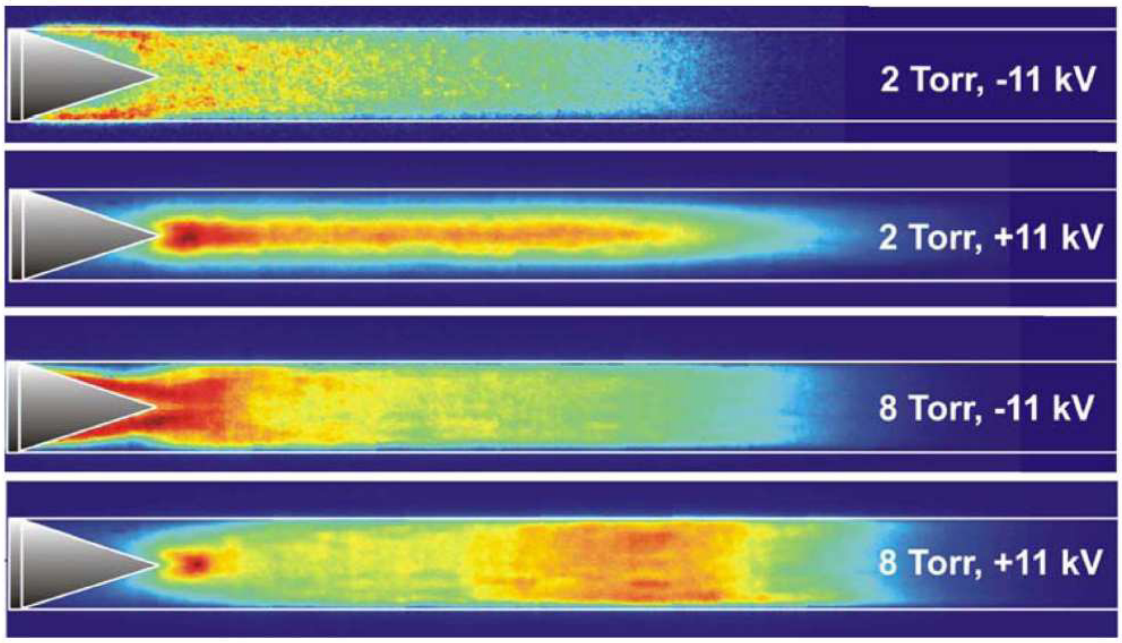

Figure 1.18 – The ICCD images of the nanosecond discharge in air in long tube (length 50 cm, diameter 1.8 cm) at different pressures and high voltage pulse polarities . Emission of the second positive system of molecular nitrogen in the spectral range $300 - 800$ **nm, ICCD gate 1 ns. The figure is taken from [77].**

The different emission distributions in the discharge tube (in a rectangular geometry) due to different discharge conditions and different gases were observed in [78, 79]. The discharge was initiated by high voltage pulses with peak voltage of 10-30 kV, pulse duration of 50-100 ns, and rate of voltage rise up to 1 kV/ns. The results [79] of ICCD imaging of the discharge in pure nitrogen and dry air at pressure $P = 10$ Torr are presented in Fig. 1.19. Here, the discharge tube has the rectangular cross-section (22 mm×13.5 mm outside dimension with 1.75 mm thick walls), thus the image almost directly corresponds to the real distribution of the emission in the tube, without significant influence of the Abel transform. It is clearly seen that in pure nitrogen at positive polarity, see Fig. 1.19(a), at low repetition rate the discharge propagates near the walls. Increase of the repetition rate leads to transformation of the discharge to the volumetric mode. At the repetition rate $\nu = 1 - 4$ kHz the emission occupies the entire volume of the tube. Further increase of frequency slightly decreases intensity of the emission in the central region. At negative polarity, see Fig. 1.19(b), at $\nu = 1$ kHz the most intensive emission observed in the narrow channel in the center of the tube. Increase of the frequency (above 2 kHz) leads to the discharge transformation to the volume-filling mode.

The tubular structure of the discharge, see Fig. 1.19(a), is explained by the seed

electron production near the tube walls. The calculations [78], where the same discharge was studied, show that higher electron density near the walls is caused by increase of the electric field near the wall due to the jump in dielectric permittivity, as well as by electron emission from the walls due to UV irradiation. The narrow channel with the most intensive emission in the center of the tube at negative polarity, see Fig. 1.19(b), is caused by electrons accelerated in the FIW front and moving in the direction of the wave.

(a) N_2, positive polarity

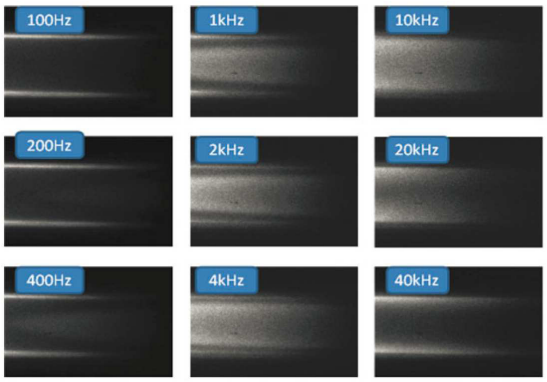

(b) N_2, negative polarity

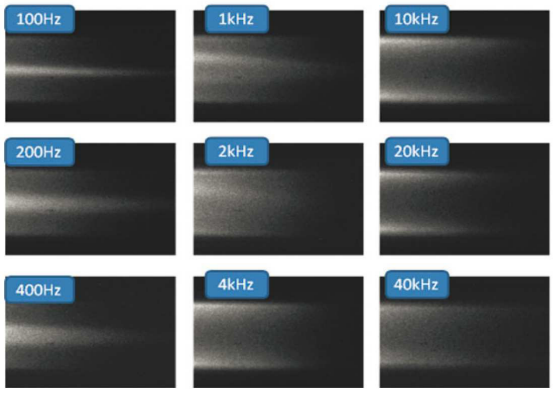

(c) Air, positive polarity

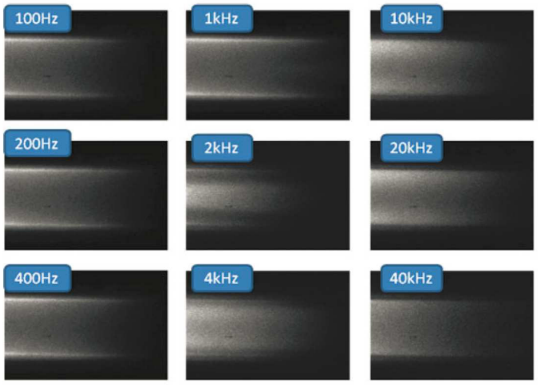

(d) Air, negative polarity

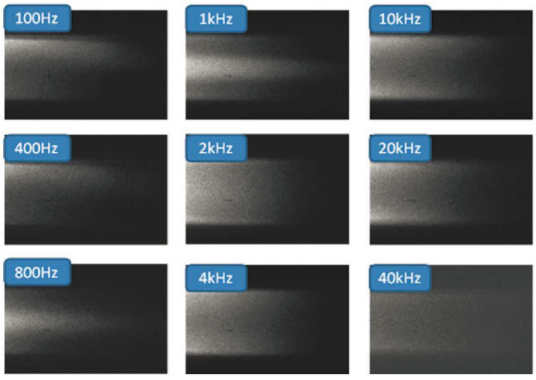

Figure 1.19 – ICCD images of FIW front at different pulse repetition rates at pressure $P = 10$ Torr in nitrogen (a, b) and dry air (c, d) for positive (a, c) and negative (b, d) polarity pulses. FIW propagates left to right. Camera gate is 4 ns. The figures are taken from [79].

The competing effect leading to the volumetric mode of the discharge is the increase of the residual electron density in the tube volume resulting in more intensive electron production in the tube volume during the wave propagation. In [79] the increase of the residual electron density in the tube volume was caused by higher repetition rates of the discharge both at negative and positive polarities, see Fig. 1.19(a) and Fig. 1.19(b). In dry air, see Fig. 1.19(c) and Fig. 1.19(d), the discharge struc-

ture depends on the polarity and the repetition rate frequency in the same way as the structure of the discharge in pure nitrogen. However, the non-uniformity of the discharge across the tube is noticeably reduced. The reason of the reducing of the transverse non-uniformity in the dry air comparing to the discharge in pure nitrogen is not discussed in details in [79]. It is only noted that according to the electric parameters measurements and estimations, the electron attachment and kinetics of the negative ions are not playing a significant role in the development of the ionization wave front. The influence of the admixtures of molecular oxygen on the discharge structure will be discussed in Chapter 8.

The nanosecond discharge development in the capillary tubes was studied in [80–83]. In [80] the numerical calculations in 2D geometry were performed for atmospheric pressure discharge (pin-to-plane geometry) placed in the capillary tubes. The following parameters of the tube were varied: the tube diameter R_{tube}, the dielectric permittivity of the wall ε_r, and the photo-emission coefficient of the wall γ_{ph}. The calculation of the streamer in free space was performed as a reference case as well. The discharge propagates in free space with rather constant speed, the maximum plasma channel diameter is about 600 μm, the maximum of the electron density and the maximum of the electric field value are on the axis of the symmetry, the electron density distribution is convex, see Fig. 1.20(a).

Firstly, the discharge in free space was compared with the discharge at the radial geometry constraint. To separate two effects (the geometrical constraint and the electric field perturbation due to jump of the relative dielectric permittivity on the wall surface), the calculations were performed at $\varepsilon_r = 1$. The tube diameter was set to be equal 100 μm and 300 μm. The results are presented in Fig. 1.20(b) and Fig. 1.20(c). One can see that the discharge development changes even at $\varepsilon_r = 1$. At $R_{tube} = 100$ μm, see Fig. 1.20(b), the maximum of the electric field is located near the wall surface. The electron density profile is rather flat in contrast to the convex profile in the discharge in free space, see Fig. 1.20(a). The discharge in the tube at $R_{tube} = 100$ μm propagates 2.4 times faster than in free space. The increase of the tube diameter up to $R_{tube} = 300$ μm, see Fig. 1.20(c), leads to higher non-uniformity. The electron density distribution is concave, the maximum is out of axis. The maximum of the electric field is located near the wall surface; the maximum value is lower than in 100 μm tube. The results for the different tube diameters are summarized in the Table 1.1(a). The discharge propagation is influenced by the presence of the tube in the case when the tube diameter is less or equal to the diameter of the streamer in the free space. With the increase of the tube diameter (1) the non-uniformity of the electron density distribution increases, (2) streamer becomes slower, (3) the maximum value of the electric field decreases, (4) the maximum value of the electron density decreases.

Table 1.1 – Discharge characteristics (a) in tubes with different radii R_{tube}, $\varepsilon_r = 1$, voltage is 9 kV; (b) in tubes with different values of ε_r, voltage is 6 kV, $R_{tube} = 100$ μm; (c) in tubes with different values of γ_{ph}, voltage is 9 kV, $R_{tube} = 100$ μm, $\varepsilon_r = 1$. t_f is the time of the discharge propagation between electrodes; n_e, max and $n_e(r = 0)$ are the maximum electron density value and the electron density value on the axis, respectively; E_{max} and $E(r = 0)$ are the maximum electric field value and the electric field value on the axis, respectively. The values are taken in middle of the inter-electrode gap ($x = 2.5$ mm). The tables are taken from [80].

(a)

R_{tube}, μm	t_f, ns	$\frac{n_e,max}{n_e(r=0)}$	n_e, max	E_{max}, kV/cm	$E(r = 0), kV/cm$
100	5.7	2.8	$5.5 \cdot 10^{14}$	300	220
300	8.4	100	$2.2 \cdot 10^{14}$	180	80
600	14.2	1000	$1.6 \cdot 10^{14}$	140	50
700	13.6	1	$3.2 \cdot 10^{13}$	110	110
w/o tube	13.6	1	$3.5 \cdot 10^{13}$	110	110

(b)

ε_r	t_f, ns	$\frac{n_e,max}{n_e(r=0)}$	n_e, max	E_{max}, kV/cm	$E(r = 0), kV/cm$
1	13.3	2.9	$3.7 \cdot 10^{14}$	230	170
2	13.7	5.5	$5.0 \cdot 10^{14}$	290	160
5	17.0	11.9	$5.7 \cdot 10^{14}$	340	135
10	22.9	16.2	$5.0 \cdot 10^{13}$	390	115

(c)

γ_{ph}	t_f, ns	$\frac{n_e,max}{n_e(r=0)}$	n_e, max	E_{max}, kV/cm	$E(r = 0), kV/cm$
0	5.7	2.5	$5.6 \cdot 10^{14}$	310	220
$5 \cdot 10^{-4}$	5.7	6.6	$7.4 \cdot 10^{14}$	315	185
$5 \cdot 10^{-3}$	5.5	90	$8.0 \cdot 10^{14}$	285	130
$1 \cdot 10^{-1}$	6.3	1000	$4.1 \cdot 10^{14}$	200	90

The influence of the dielectric permittivity of the tube wall was studied [80] in the tube with $R_{tube} = 100$ μm at 6 kV voltage pulse. It is seen from Fig. 1.21(a) and Fig. 1.21(b) that at higher ε_r the non-uniformity of the electron density distribution is more pronounced, the discharge structure becomes tubular at high ε_r. The results for the different ε_r values are summarized in the Table 1.1(b). With the increase of the dielectric permittivity (1) streamer becomes slower, (2) the maximum value of

the electric field increases, (3) the maximum electron density increases.

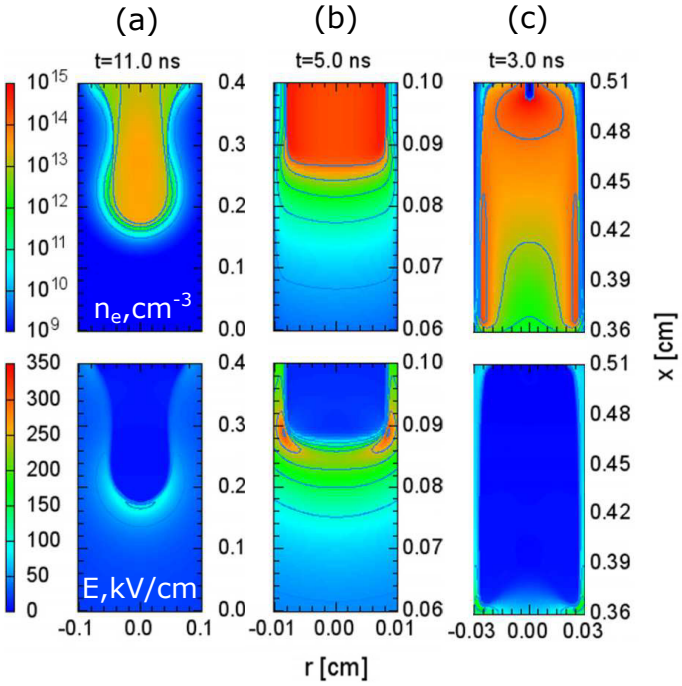

Figure 1.20 – The electron density (top line) and the electric field (bottom line) for the discharges (a) in free space, (b) in tube with $R_{tube} = 100$ μm and $\varepsilon_r = 1$, (c) in tube with $R_{tube} = 300$ μm and $\varepsilon_r = 1$. The voltage is 9 kV. The figure is composed based on the figures taken from [80].

It also can be noted that the electron density distribution is also influenced by the voltage amplitude, see Fig. 1.20(b) and Fig. 1.21(a). The only difference in the figures is voltage amplitude, lower voltage leads to higher non-uniformity.

The results discussed above were obtained without taking into account photo-emission due to UV irradiation of the wall. The influence of the photo-emission on the discharge development was studied for the tube with $R_{tube} = 100$ μm and $\varepsilon_r = 1$ at 9 kV pulse. It is seen from the comparison of the Fig. 1.20(b) and Fig. 1.21(c) that photo-emission ($\gamma_{ph} = 5 \cdot 10^{-4}$) increases non-uniformity of the electron density distribution, the discharge is more tubular. The results for the different γ_{ph} values are summarized in Table 1.1(c). The non-uniformity of the electron density distribution increases with the photo-emission dramatically.

Summarizing the results of numerical calculations [80] presented above, one can conclude that the presence of the capillary tube influences on the discharge development by three independent ways: (1) geometrical restriction of the discharge, (2) electro-dynamical perturbation due to jump of dielectric permittivity on the wall boundary, (3) fast production of electrons near the wall by photo-emission due to UV irradiation of the wall surface. Increasing of the corresponding parameters: R_{tube}

(while it is less than diameter of the streamer in free space), ε_r and γ_{ph} leads to more tubular structure of the discharge.

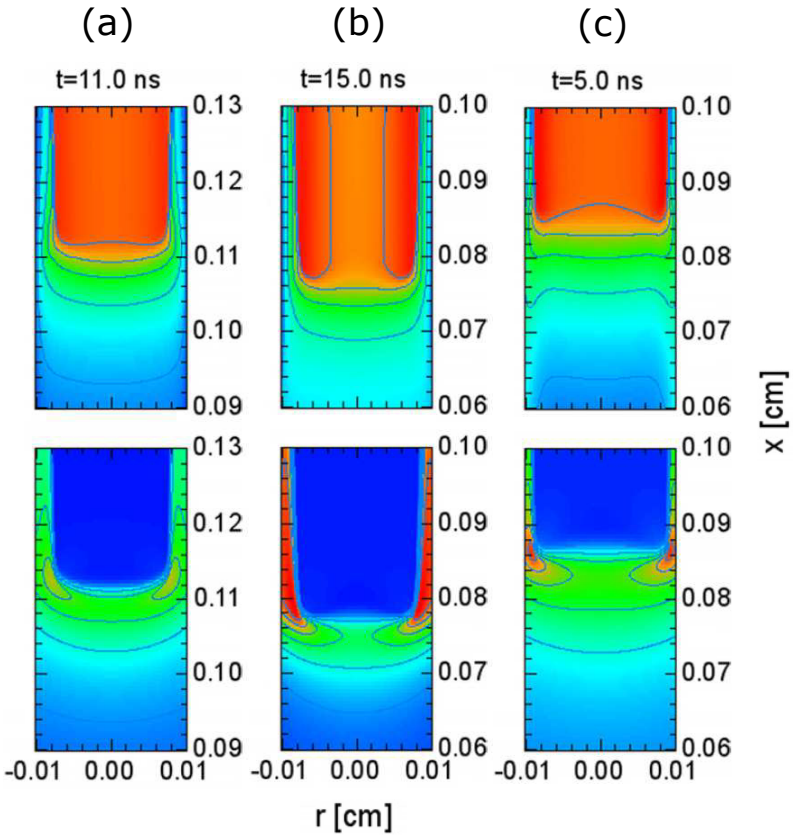

Figure 1.21 – The electron density (top line) and the electric field (bottom line) for the discharges in tube with $R_{tube} = 100$ μm. The voltage amplitude 6 kV (a) $\varepsilon_r = 1$, (b) $\varepsilon_r = 5$; (c) the voltage amplitude 9 kV with $\varepsilon_r = 1$ and photo-emission coefficient $\gamma_{ph} = 5 \cdot 10^{-4}$. The figure is composed based on the figures taken from [80].

The discharge configuration discussed above was studied experimentally and numerically in [82]. It was confirmed that discharge propagates faster in the tubes than in the free space, which means that presence of the tube facilitates discharge development. It was confirmed experimentally that in the tube with larger diameter the discharge has tubular structure, see Fig. 1.22. The increase of the discharge propagation velocity in the thin tubes was also observed in [81].

The propagation of the fast ionization wave front in the quartz capillary tube of 1.7 mm internal diameter similar to one used in the present work was studied in [9]. The discharge was initiated by the 9.8 kV high voltage pulse with duration equal to 35 ns and 4 ns rise time in synthetic air at 27 mbar. The two-dimensional numerical calculations showed that the electric field has rather high radial component near the wall surface in the FIW front and behind the front, see Fig. 1.23.

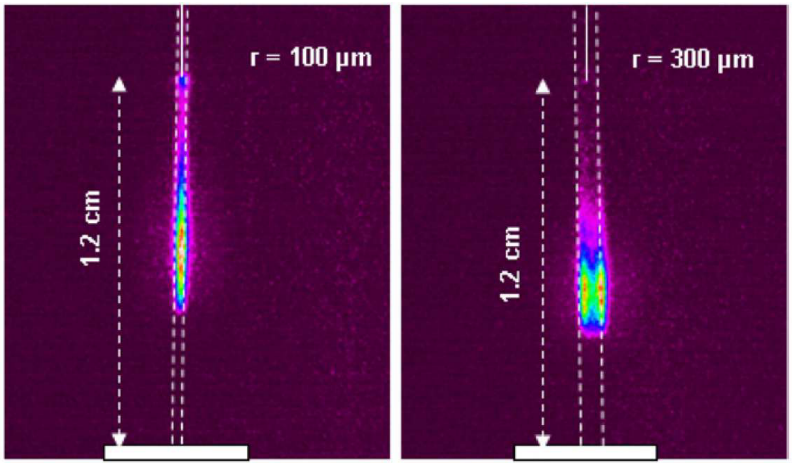

Figure 1.22 – Experimental images of the discharge in the glass tubes with $R_{tube} = 100$ μm and $R_{tube} = 300$ μm integrated over 1 ns. The voltage amplitude is 15 kV. The figure is taken from [82].

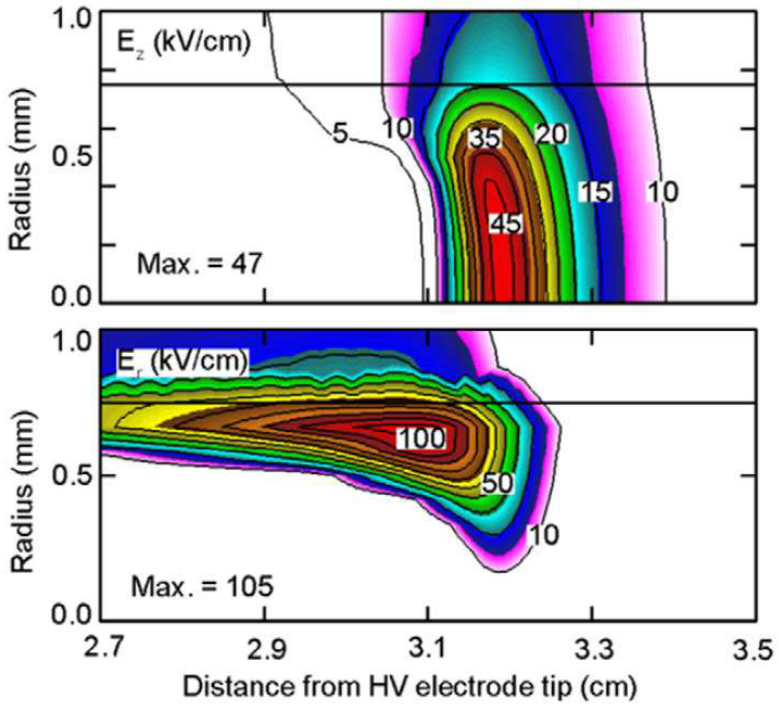

Figure 1.23 – The longitudinal and radial components of the electric field in the fast ionization wave front in the quartz capillary tube of 1.7 mm internal diameter similar to one used in the present work calculated in 2D geometry. The original figure is taken from [9].

Thus, one can see that distribution of the electron density and the value of the electric field can be strongly non-uniform during the discharge development both for relatively low pressures and for the atmospheric pressure. As was shown above, the

configuration of the electron density (or electric field) distribution in the front of the fast ionization wave or in the streamer head is a function of a number of independent parameters such as polarity and amplitude of the high voltage pulse, diameter of the tube, material of the tube (dielectric permittivity and photo-emission coefficient), repetition rate, pressure and gas composition. Therefore, it is difficult to predict the initial distribution *a priori*, and it is required to investigate it at given discharge conditions. The knowledge of the electron density radial distribution and, consequently, the radial distribution of the excited species can be important for applications. For example, for the atmospheric pressure plasma streams (PAPS) and the plasma bullets formed and/or propagated in the dielectric tubes [84–88]. These discharges can be used in the plasma medicine or plasma surface treatment at ambient air. The radial distribution of the charge carriers, excited or active species at the outlet of the tube used for plasma formation can determine the dynamics of the plasma bullet interaction with the ambient air due to, for example, different shape or area of the plasma-ambient air interface. For the present Thesis it is extremely important to know the initial distribution of electron density, since the further discharge development and energy deposition are determined by the initial electron density profile, which, in turn, affects the main observed effects, for example, the fast gas heating. Moreover, the knowledge of distribution of electron density or excited species is required for correct comparison of results of numerical calculations and experiment results, which gives integral (or averaged) values. The initial electron density distribution in the discharge studied in the Thesis is investigated in Chapter 8.

Chapter 2

Problem formulation

As it was demonstrated in the literature review, nanosecond discharges are characterized by high reduced electric fields. High reduced field leads to efficient excitation of electronic degrees of freedom of the gas. The non-equilibrium plasma produced in nanosecond discharges is a highly reactive medium. The various applications of the nanosecond discharges require plasma kinetic models valid in wide range of conditions. Existing kinetic models demonstrate a good agreement between the results of the numerical calculations and the experimental results in a broad range of the reduced electric fields. However, typically the specific energy deposition in the discharges used for the development and validation of the kinetic models is rather low. At relatively low specific deposited energy, the excited species mostly interact with a background gas. Increase of the specific energy deposited in the plasma during nanosecond discharge leads to increase of the probability of interaction of excited and/or charged species between each other changing the plasma kinetics dramatically. Therefore, the plasma kinetics models developed for nanosecond discharges with low specific energy deposition, which further in the text is referred as "classical" plasma kinetics, can be not applicable in this case.

The main aim of the present work is to study, on the basis of detailed experiments accompanied by numerical modeling, kinetics of nanosecond plasma at high reduced electric field and at high specific deposited energy, using the nanosecond capillary discharge as an experimental tool. The discharge in pure nitrogen and in nitrogen:oxygen mixtures is studied. The following tasks should be solved.

1) To measure the main electric parameters of the nanosecond capillary discharge: applied voltage, electric current, electric field and specific deposited energy. To

measure the electron density in the discharge and to study plasma decay at the time scale of hundreds of nanoseconds.

2) To study temporal behavior of densities of main excited species by analysis of the optical emission from the discharge and the afterglow. To investigate the influence of the high excitation degree due to high specific energy deposition on the plasma kinetics. To determine the main processes not typical for the classical plasma kinetics and to evaluate a possible impact of the observed processes.

3) To investigate initial radial distribution of the electron density required for reliable 1D numerical modeling of the nanosecond capillary discharge and for correct comparison of the results of the numerical calculations with the experiment. To trace the dynamics of the radial distribution of the excited species in the discharge and early afterglow.

4) To measure dynamics of the gas temperature. On the basis of comparison of the experimental measurements and the numerical calculations, to improve the traditionally used kinetic schemes of the fast gas heating in air, pure nitrogen and nitrogen with small oxygen admixtures.

Chapter 3

Experimental setup and experimental techniques

In this Chapter the description of the experimental setup and used experimental techniques is given.

3.1 Experimental setup

The experimental program of the present work was performed using nanosecond capillary discharge. The discharge was initiated in the quartz capillary tube with the internal diameter of 1.5 mm and the external one of 3.45 mm, some experiments were performed in the tube with internal and external diameters equal to 1.7 mm and 3.0 mm, respectively. The schematic view of the discharge cell is presented in Fig. 3.1.

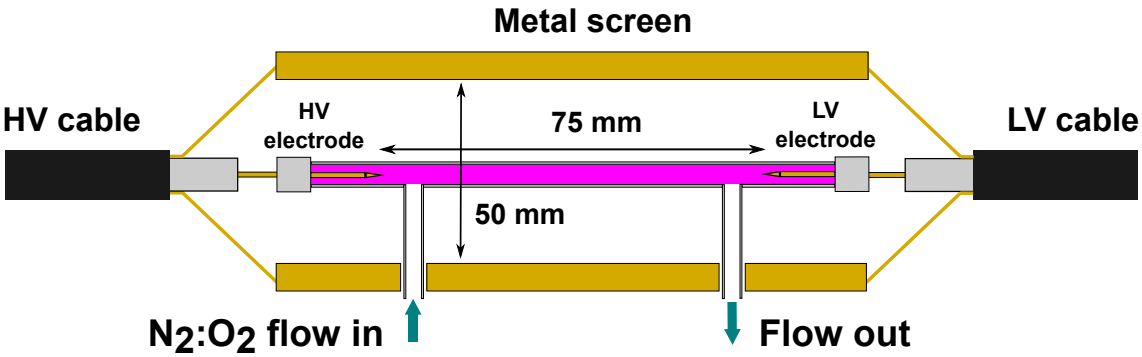

Figure 3.1 – Schematic view of the discharge cell used in the experiments.

The technical drawings are given in Fig. 3.4. It should be noted that some experiments were performed with the electrode configuration from [63] called "stabilized electrode system" in that work.

The pin-shape electrodes installed from the ends of the capillary tube are connected to the central wires of two high voltage coaxial cables RG213. The high-voltage electrode is connected to the high voltage generator via HV cable, the low-voltage electrode is not grounded and is connected to the LV cable under floating potential. The rectangular (48 mm×60 mm) metal screen surrounding the capillary tube is connected to the shielding of both HV and LV cables. Thus, one can say that the discharge cell is installed in the break of the high voltage cable.

The gas flow system is schematically presented in Fig. 3.2. The gas flow in the discharge tube is carried out by two side tubes soldered in the wall of the capillary and connected to the gas flow system by flexible tubes. The pure nitrogen and synthetic air from Air Liquid with admixtures < 5.5 ppm are used for the experiments. The gas bottles are connected to the discharge tube through two flow controllers (Brooks Instrument 5850TR). The flow controllers maintain the total constant flow rate equal to $Q = 50$ sccm. The time of gas renewing at given pressure P and temperature T can be estimated as

$$t_{renew} = \frac{V}{Q[\text{sccm}]} = \frac{T_0}{T}\frac{P}{P_0}\frac{\pi r^2 l}{Q[\text{cm}^3/\text{min.}]} \approx 4 \text{ ms}, \tag{3.1}$$

where r is the radius of the tube, l is the tube length and $P_0 = 101325$ Pa with temperature $T_0 = 273$ K denote pressure and temperature at the standard conditions. The repetition rate 10 Hz used in the experiments is much lower than $1/t_{renew} = 250$ Hz, then one can be sure that each new discharge does not depend on the previous one.

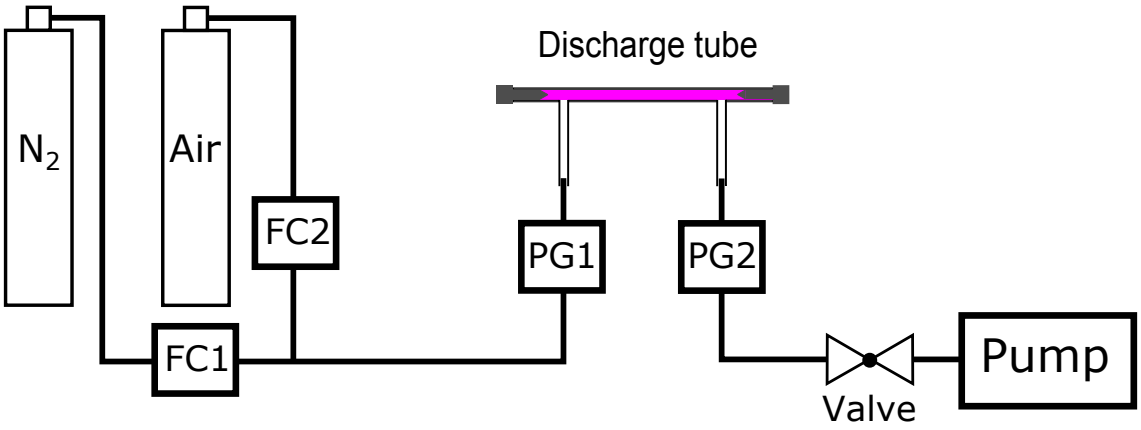

Figure 3.2 – Schematic view of the gas flow system used in the experiments. FC is a flow controller, PG is a pressure gauge.

The pressure in the tube is measured as a mean value of readings of two capacitive-type CMR 362 pressure gauges from Pfeiffer Vacuum installed upstream and downstream. It was shown early [63] by numerical solving of a weakly compressible Navier-Stokes equation in the capillary geometry including the gas inlets that the pressure drop is linear along the capillary tube. Thus, a mean value of readings of two pressure gauges indicates the pressure in the middle of the capillary tube, where all basic measurements are performed. It is valid, since the flow resistance of the capillary tube is much higher than flow resistance of flexible tubes using for gas pumping, and pressure drop in the supply tubes is negligible.

The general scheme of the experimental setup and the main experimental equipment are presented in Fig. 3.3. The triggering generator (TG) BNC 575 is used to command the high voltage generator (HVG) FPG 12-1NM (FID GmbH). Low-voltage synchronization pulse, produced by HVG before the high-voltage pulse, is used to trigger the ICCD camera. Other experimental equipment is triggered by the signal detected by back current shunts (BCSs). Corresponding experimental techniques are discussed in the next section.

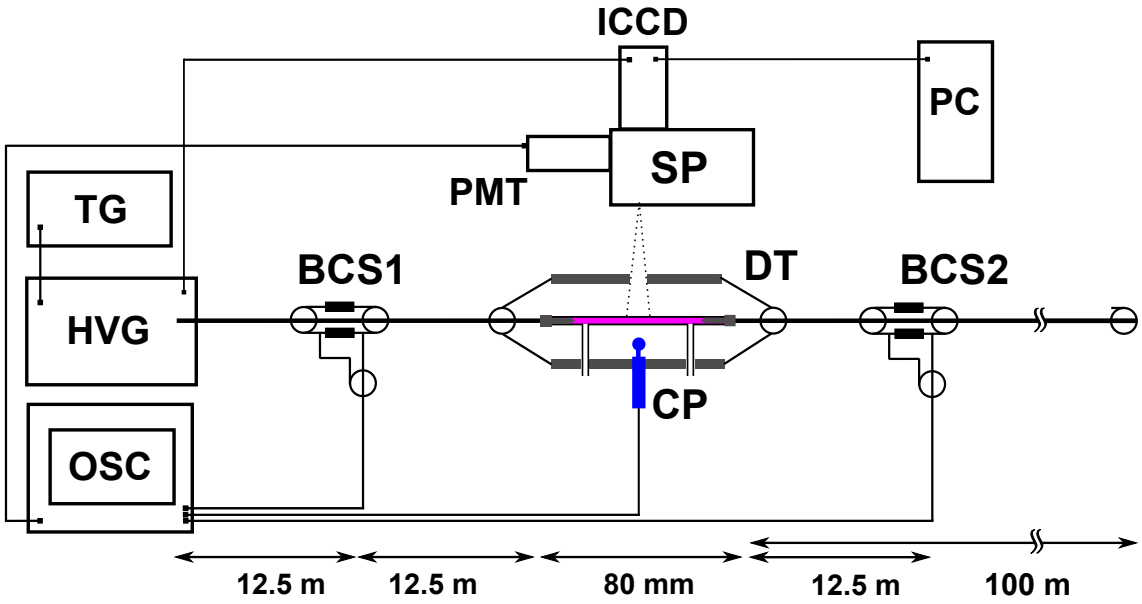

Figure 3.3 – A general scheme of the experimental setup with the main experimental equipment. TG is triggering generator, HVG is high voltage generator, OSC is oscilloscope, BCS is back current shunt, CP is capacitive probe, DT is discharge tube, PMT is photomultiplier tube, ICCD is intensified charge-coupled device (camera), SP is spectrometer, PC is personal computer.

(a)

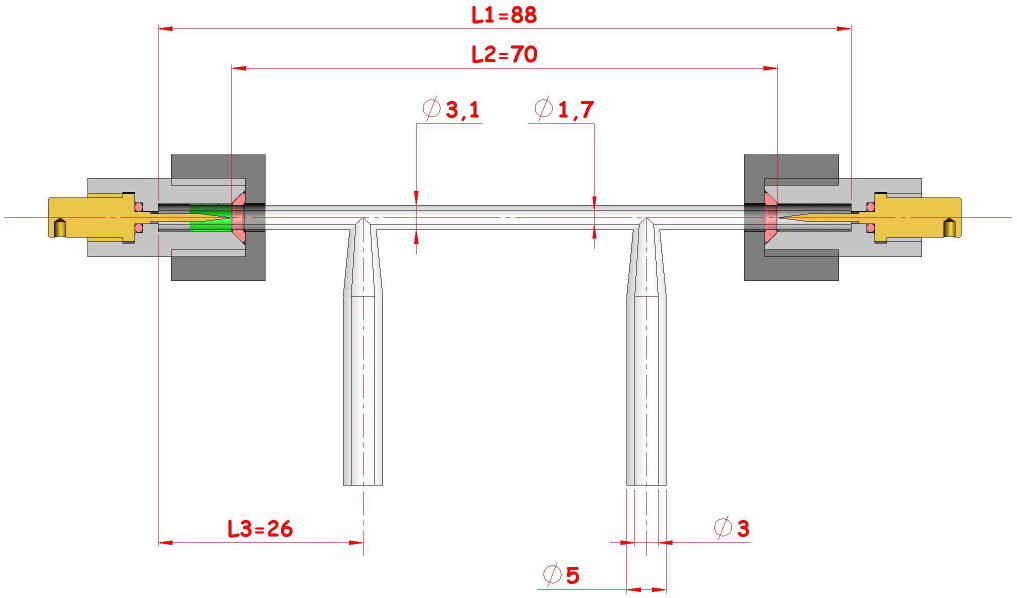

(b)

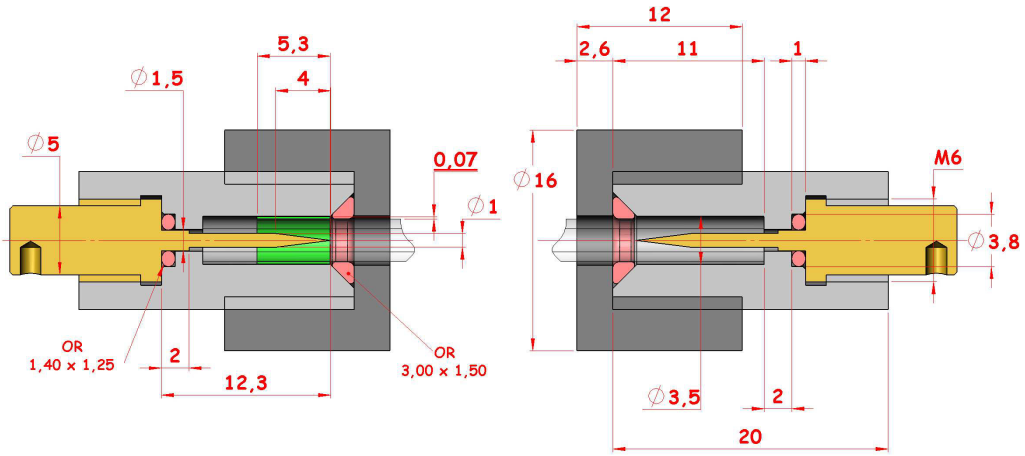

Figure 3.4 – The technical drawings of the discharge cell. (a) Quartz tube with attached electrode assemblies, $L1$ is the length of the discharge tube, $L2$ is the distance between the tips of electrode, $L3$ is the distance between end of the discharge tube and the place of the gas inlet tube connection. (b) The high-voltage (left) and low-voltage electrode (right) assemblies: brass electrodes (yellow), PVC holders (light and dark gray), silicon O-rings (pink), copper foil strip around the tube (green) is used to facilitate the discharge initiation. The figures are prepared with the help of Ali Mahjoub, design engineer, Laboratory of Plasma Physics, Ecole Polytechnique.

3.2 Experimental techniques

3.2.1 Optical emission spectroscopy

Optical emission spectroscopy (OES) is one of the most powerful experimental tools in plasma physics. It can be used to obtain a large number of plasma parameters. The optical spectrum of the discharge emission contains information about plasma composition, thus, the optical emission spectroscopy can be used for analytical purposes [89]. The spectra can be used for plasma species density measurements in absolute or relative units. The temporal evolution of the emission of the given excited specie (even in arbitrary units) can be used for quenching rates measurements [90–92]. The relative intensities of emission of two excited species (one of them is a reference with known density) can be used for absolute density measurements by actinometry technique [63, 93–96]. The ratio between intensities of a set of optical transitions of excited atoms can be used for electron temperatures and electron energy distribution function measurements [97]. The broadening of the atomic lines [54, 98, 99] or atomic ion lines [100] due to Stark effect can be used for electron density measurements. The structure of the molecular bands in the spectrum can be used for rotational and vibrational temperature measurements [53, 54]. The ratio of the intensities of the first negative system (FNS) of molecular nitrogen and the second positive system (SPS) of molecular nitrogen can be used for electric field measurements [74, 101, 102].

One of the most important parameters of the spectral system is spectral resolution. For example, the transitions in the spectrum or the rotational temperature of excited state can be determined by fitting of experimentally measured spectrum by one calculated one, see Fig. 1.11. Theoretically calculated spectrum is a set of delta-functions. However, real spectrum lines are always broadened by natural broadening, Doppler effect and mostly by slit function of used spectral system. To take last one into account the simulated spectrum is usually convoluted with trapezoidal function or with slit function measured experimentally.

The spectrum of any atomic line, for example, Ar of Hg recorded with the spectral system can be used as a slit function. Fig. 3.5 presents Hg line measured to get slit function. The light of Argon/Mercury low-pressure discharge lamp was collected by the UV Fused Silica lens (75 mm focal length) to the entrance slit (100 μm) of the spectrograph with 500 mm focal length (Acton SP-2500i, Princeton Instruments). Grating 2400 l/mm provided dispersion 0.7 nm/mm or 0.009 nm/pixel. The light was detected by ICCD camera (PI-MAX 4 1024i, Princeton Instruments).

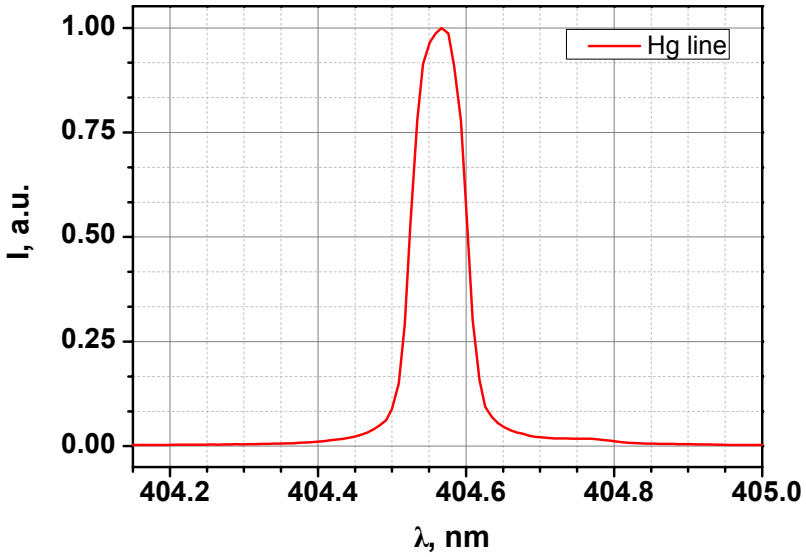

Figure 3.5 – Mercury line as a slit function of the used spectral system.

From Fig. 3.5 it is clearly seen that the resolution of the system is equal to 0.08 nm FWHM. To use the profile of a measured atomic line as a slit function, it is necessary to analyze other possible broadenings. In discharge and the afterglow, gas temperature increases significantly due to fast gas heating. FWHM of the line broadening by Doppler effect can be calculated as [103]

$$\Delta\lambda_D = 7.16 \cdot 10^{-7} \lambda_0 (T[K]/\mu[\mathrm{g} \cdot \mathrm{mol}^{-1}]), \tag{3.2}$$

where λ_0 is wavelength of the transition, μ is molar mass of the emitting particle. For $\lambda_0 = 337.1$ nm with molar mass $\mu = 28$ g$\cdot$mol^{-1} for nitrogen it gives $4 \cdot 10^{-4}$ nm at $T = 300$ K, and $1.25 \cdot 10^{-3}$ nm at $T = 3000$ K. Even at $T = 3000$ K the Doppler broadening is much lower than measured 0.08 nm FWHM of Hg atomic line. Thus, we can neglect the Doppler broadening at any gas temperature.

The measured apparatus function of the spectral system (profile of Hg line) was used as a function in Chapter 9 of the present work, while simulating discharge spectra by SPECAIR software [54].

Another important parameter of the spectroscopic system, which extremely impact on the results of the measurements, is the sensitivity of the system on the different wavelength. The sensitivity of the spectral system is determined by (i) transmission of the optical elements (filters, lenses, optical fibers, mirrors, etc.) used to collect the light; (ii) quantum efficiency of the diffraction gratings installed in the spectrograph; (iii) quantum efficiency of the light detector. To obtain the absolute sensitivity of the spectral system the absolutely calibrated light source is required. The relative sensitivity can be calculated analytically using the specifications of the equipment. The quantum efficiency of the diffraction gratings installed

in the 500 mm focal length spectrograph Acton SP-2500i (Princeton Instruments) used in the present work are given in Fig. 3.6(a) [104]. The quantum efficiency of the ICCD camera PI-MAX 4 1024i (Princeton Instruments) used as the light detector is presented in Fig. 3.6(b) [104]. Finally, calculated spectral sensitivity of the combination of the spectrometer Acton SP-2500i and the ICCD camera PI-MAX 4 1024i is presented in Fig. 3.6(c). The obtained curves are used to correct obtained spectra, which have been perturbed by the non-uniformity of the spectral sensitivity.

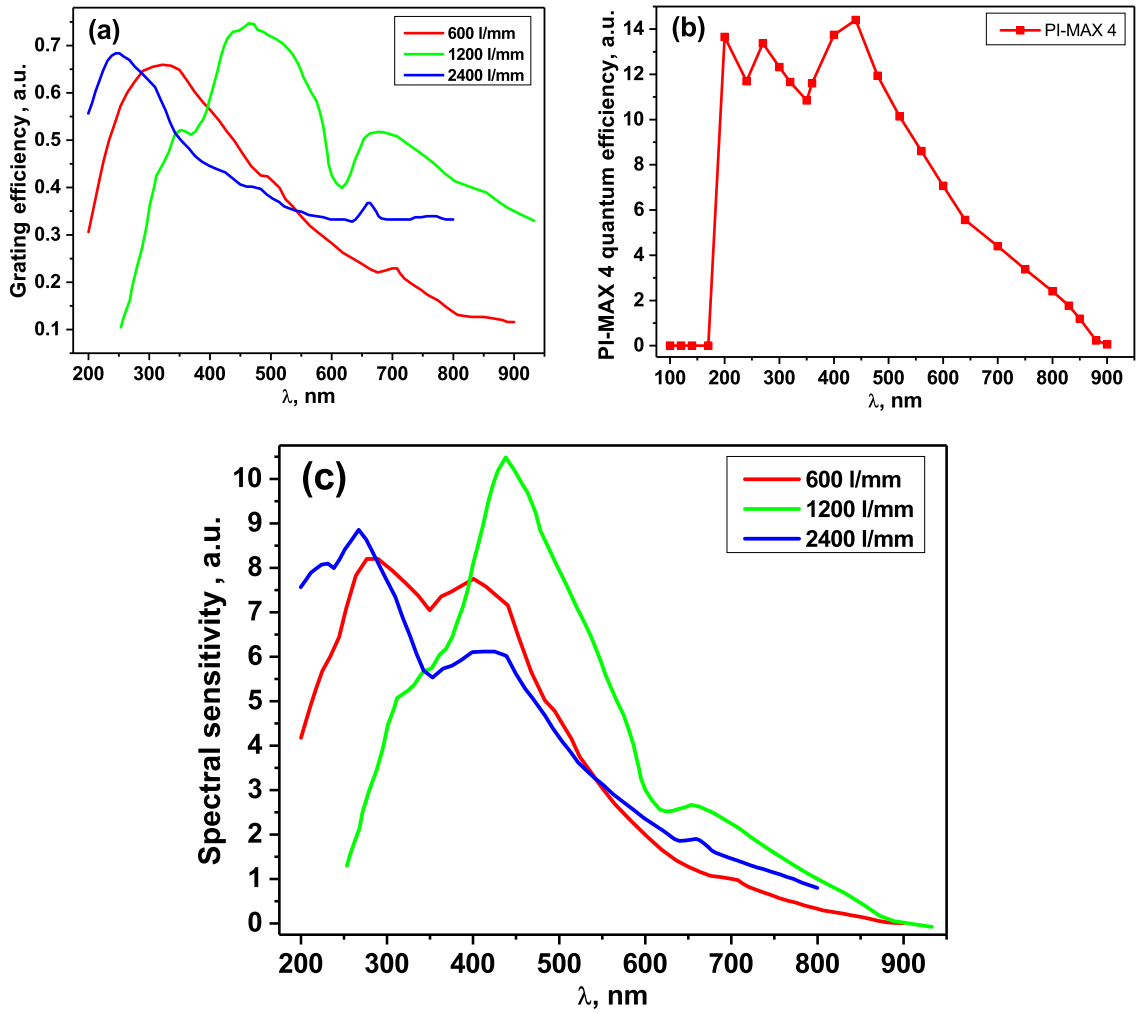

Figure 3.6 – (a) The quantum efficiency of the gratings used in the experiments. Red curve corresponds to the grating with 600 lines per millimeter (l/mm) and blaze 300 nm, green curve denotes the grating with 1200 l/mm and blaze 500 nm, blue line is for the grating with 2400 l/mm and blaze 240 nm. (b) The quantum efficiency of the ICCD camera PI-MAX 4 1024i. (c) Spectral sensitivity of the combination of the spectrometer Acton SP-2500i and the ICCD camera PI-MAX 4 1024i. The data are from [104].

3.2.2 Back current shunts

The current and voltage in the high voltage cable are measured by two custom–made calibrated back current shunts installed 12.5 m before and after the discharge tube (BCS1 and BCS2). The back current shunt consists of a set of low-inductive parallel resistors (KOA Speer CF1/2C2R2J) soldered into the cable shield break. When the high voltage pulse propagates in the cable, the current flowing in the shielding of the cable is equal to the current in the central wire of the cable I, but they have opposite directions. The voltage drop on the BCS made of n equivalent resistors with the impedance R each in this case can be written as

$$U_{BCS} = \frac{IR}{n}. \tag{3.3}$$

The signal from BCSs is registered by LeCroy WaveRunner 64Xi-A 600 MHz oscilloscope (OSC). Since typical values of U_{BCS} can reach tens of volts, the attenuators are used on the input channels of the OSC to avoid its over-range. If the attenuator reduces the signal in K_{att} times, the detected value of the voltage drop on the BCS registered by oscilloscope is equal to

$$U_{OSC} = \frac{U_{BCS}}{K_{att}} = \frac{IR}{nK_{att}}. \tag{3.4}$$

From (3.4) it follows that the value of the current in the central wire of the high voltage cable can be calculated as

$$I = U_{OSC}\frac{n}{R}K_{att}. \tag{3.5}$$

The voltage between the central wire and the shielding of the cable can be calculated using the Ohm's law for the long transmission lines: $U = IZ$, where $Z = 50$ Ohm is the wave resistance of the used high voltage cable.

The back current shunts are installed 12.5 m before and after the discharge tube to avoid the superposition of signals propagating in the cable. For example, the pulse incident on the discharge cell and the pulse reflected from the discharge cell due to the impedance mismatching. Indeed, the coefficient of reflection of the high voltage pulse propagating in the cable with impedance Z from the load with impedance R can be written as

$$K_U = \frac{R - Z}{R + Z}. \tag{3.6}$$

There are to limit cases. At infinite load $R = \infty$, $K_U = 1$ and high voltage pulse reflects from the load completely with the same polarity. If the load is characterizes by zero load (short circuit) $R = 0$, $K_U = -1$ and high voltage pulse reflects from the load completely with the opposite polarity. The impedance of the discharge cell is finite and high $R \geq Z$, thus, the voltage pulse reflects partially with the same

polarity. To separate the two pulses, the distance between BCS and the point of reflection should be longer than half of the part of the cable "occupied" by the signal. The voltage pulse with full width τ occupies the part of the cable with the length $V\tau$, where $V = c/\sqrt{\varepsilon} = 0.2$ m/ns is the velocity of the electromagnetic wave propagations in the cable with the vacuum light speed c and the dielectric permittivity $\varepsilon = 2.25$ of the insulator in the cable (polyethylene). For pulse with $\tau = 60$ ns, which is typical for present research, the corresponding length is 12 m, thus the incident and reflected pulses are separated with factor of safety 2.

The example of the signals obtained with BCS1 installed between the high voltage generator and the discharge cell is presented in Fig. 3.7. The pulse 1 is the pulse incident on the discharge cell, the pulse 2 is the reflection from the discharge cell with high impedance. One can see that the pulses are separated, in agreement with the above description. According to (3.6), the polarity of the voltage pulse is the same, as incident one has. However, the pulse 2 propagates in the high voltage cable in opposite direction in comparison with the pulse 1, thus, the sign of the detected voltage is inversed. The characteristics of the high voltage pulses measured by BCSs are discussed in more details in Chapter 4, Section 4.1.1.

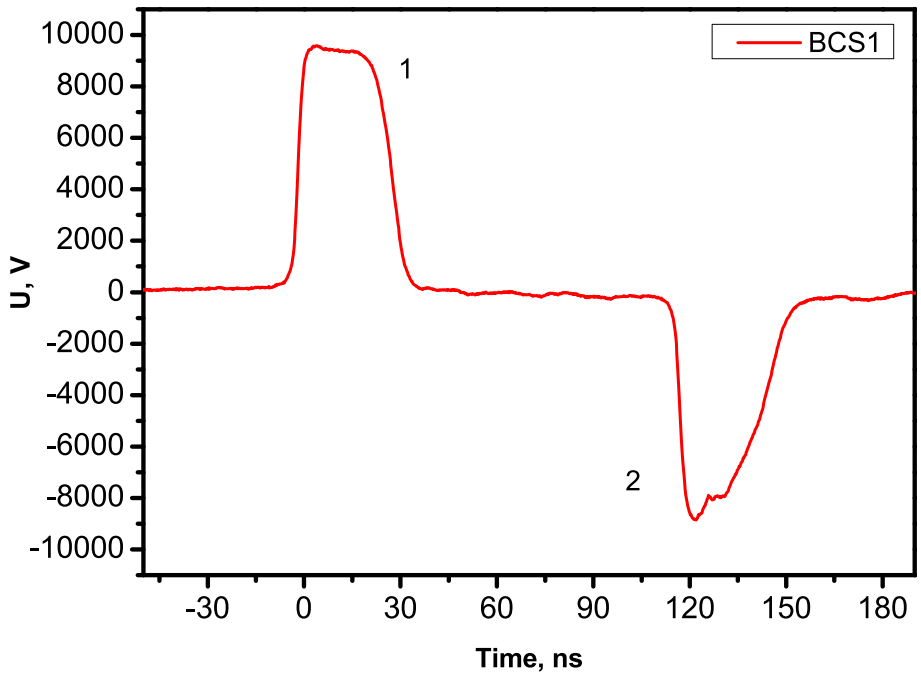

Figure 3.7 – The signal from BCS1. Peak 1 is the high voltage pulse incident on the discharge cell, pulse 2 is its reflection from the discharge cell.

3.2.3 Capacitive probe

The capacitive probe technique is widely used in the FIW studies [8, 9, 63, 73, 74, 76, 78, 79], see Fig. 1.15, for example. The capacitive probe (CP) is the capacitive divider, installed near the discharge tube surface. The equivalent electric scheme is presented in Fig. 3.8.

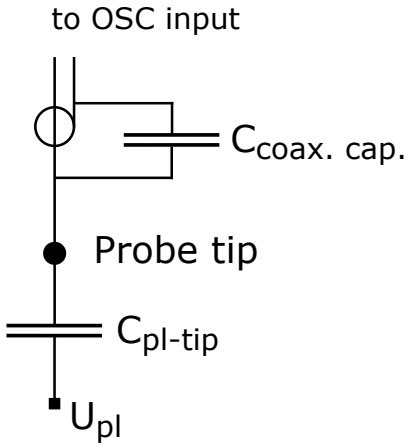

Figure 3.8 – The equivalent electric scheme of the capacitive probe. U_{pl} is the electric potential in the plasma, the capacitor C_{pl-tip} denotes the electric capacitance between the probe tip and the plasma, $C_{coax.cap.}$ is the coaxial capacitor: the lead is connected to the probe tip and the central wire of the coaxial cable going to the input channel of the oscilloscope (OSC), the cylindrical body is connected to the shielding of the cable.

The probe tip is connected to the central wire of the coaxial signal cable going to the input channel of the oscilloscope (OSC) through the lead of the coaxial capacitor with the capacitance $C_{coax.cap.}$. The cylindrical body of the capacitor is connected to the shielding of the signal cable with impedance $Z = 50$ Ohm. When the electric potential in the plasma changes, the electric current flows through the coaxial cable to charge the capacitance between the probe tip and the plasma. Therefore, the potential of the probe tip $U_{probe}(t)$ is measured by the oscilloscope, and, thus, the potential in the plasma at any time instant $U_{pl}(t)$ can be reconstructed. From the electric circuit presented in Fig. 3.8 it follows that

$$U_{pl}(t) = A_{CP}\Big(U_{probe}(t) + \frac{1}{\tau_{CP}}\int_0^{t'} U_{probe}(t')dt'\Big), \tag{3.7}$$

where $A_{CP} = 1 + C_{coax.cap.}/C_{pl-tip}$ is the amplitude response of the probe and $\tau_{CP} = A_{CP}ZC_{pl-tip}$ is the time response of the probe. However, C_{pl-tip} is usually unknown, and the calibration procedure is required.

To calibrate the capacitive probe the following procedure [63] has been performed. The copper wire of 1 mm diameter was inserted in the discharge tube and

connected to the electrodes. Since the resistance of copper is low, there is no significant voltage drop over the wire. Thus, the potential of the wire can be assumed to be equal to the potential of the HV electrode. The values of the parameters A_{CP} and τ_{CP} are varied until the good agreement between the waveform of the potential measured by back current shunts and by the capacitive probe is achieved. The results of the calibration is presented in Fig. 3.9. The obtained capacitive probe parameters are $A_{CP} = 24112$ and $\tau_{CP} = 23$ ns.

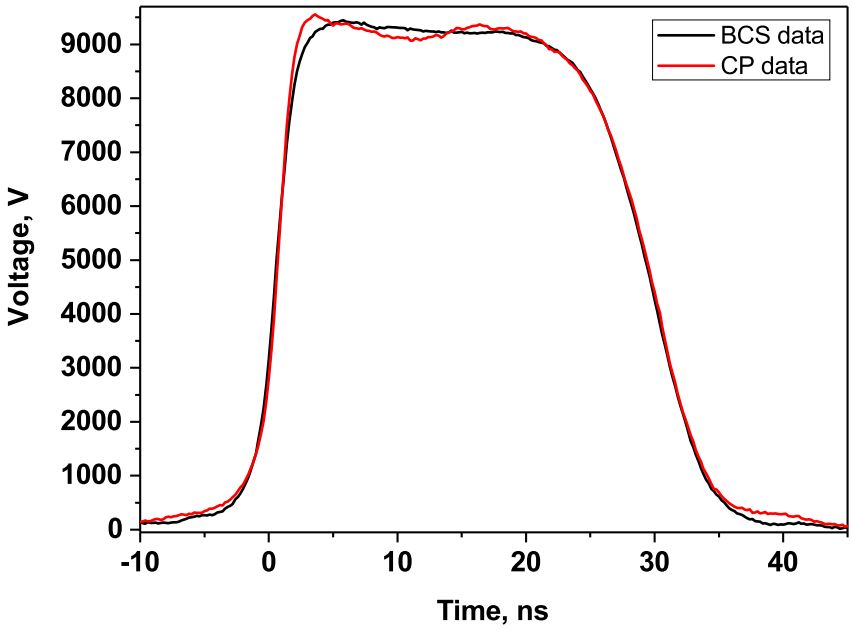

Figure 3.9 – The capacitive probe calibration procedure. Black curve is the waveform of electric potential of the copper wire inside the quartz tube measured by the back current shunts, red curve is the waveform reconstructed from the signal measured by the capacitive probe.

However, since the copper wire diameter is less than the diameter of the plasma channel (internal radius of the tube), the additional correction of the potential value is required. The corresponding electrostatic problem was solved in [63] by 3D numerical modeling for the same discharge cell configuration used for the electric field measurements. It was found that for the cross-section of the measurements (in the middle of the discharge tube) the correction factor is equal to 0.87, i.e. the real electric potential in the plasma is 0.87 times lower than (3.7) gives for the configuration with copper wire.

The electric potential in the plasma $U_{pl}(x,t)$ as function of the distances x from the high voltage electrode can be measured at different x moving the probe along the discharge tube. The longitudinal electric field in this case can be calculated as $E = -\partial U_{pl}(x,t)/\partial x$. The electric potential value was measured in a mesh of points

x_i with $\Delta x = 1$ mm step.

To increase the signal to noise ratio the electric field in the point with index k was calculated as averaged value over N_{av} neighboring points. The electric field is calculated as

$$E(x_k) = -\frac{U_k^+ - U_k^-}{d}, \tag{3.8}$$

where U_k^+ is the value of the electric potential averaged over points $x_{k+1}, ..., x_{k+N_{av}}$ and U_k^- is the value of the electric potential averaged over points $x_{k-N_{av}}, ..., x_{k-1}$:

$$\begin{aligned} U_k^+ &= \frac{\sum_1^{N_{av}} U(x_{k+i})}{N_{av}}, \\ U_k^- &= \frac{\sum_1^{N_{av}} U(x_{k-i})}{N_{av}}, \end{aligned} \tag{3.9}$$

and $d = (N_{av} + 1)\Delta x$ is the distance between the points corresponding to the averaged values U_k^+ and U_k^-. Finally, the electric field is expressed as

$$E(x_k) = \frac{\sum_1^{N_{av}} U(x_{k-i}) - U(x_{k+i})}{N_{av}(N_{av} + 1)\Delta x}. \tag{3.10}$$

The calculation are performed with $N_{av} = 10$, that gives rather smooth electric field waveform. The scheme illustrating averaging process is presented in Fig. 3.10.

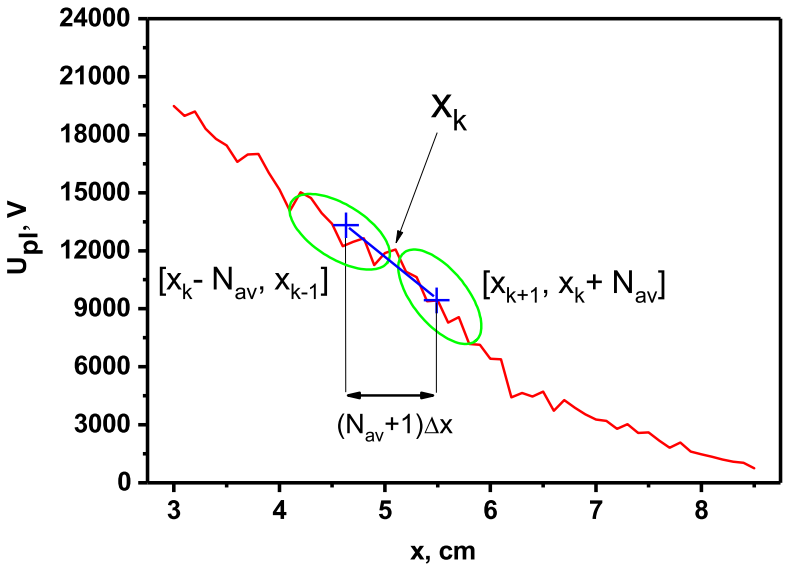

Figure 3.10 – The scheme illustrating calculation of the electric field. Red curve is the electric potential distribution. The electric field is calculated as a slope (blue line) between two points (blue crosses), which are potentials averaged over two groups of points with $x \in [x_{k-N_{av}}, x_{k-1}]$ and $x \in [x_{k+1}, x_{k+N_{av}}]$ denoted by green ellipses.

3.2.4 Reconstruction of radial distribution of excited species

Mathematical procedure

To obtain any information about the discharge structure, an ICCD camera with an optical system is required. In general, if the image of the discharge is obtained by a lens or an objective, the collected data can not be directly treated as a spatial distribution of the excited species. The problem is that plasma is a volumetric object, and the emission reaching the detector is a set of photons from different regions of the discharge. In other words, the signal is integral. The idea is illustrated by Fig. 3.11 (a), where light beams coming from different volumes reach the same point on the ICCD matrix.

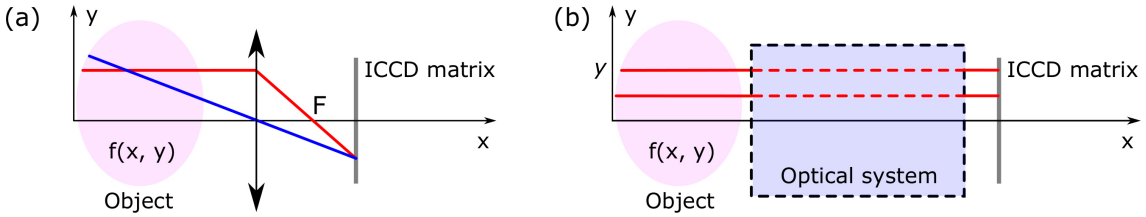

Figure 3.11 – (a) Schematic illustration of the light collection, non-correct for reconstruction of distribution of light sources. Red and blue lines represent light beams passed by different optical paths, but reaching the detector in the same point. (b) Schematic illustration of the light collection, correct for reconstruction of distribution of light sources. Each pixel of ICCD matrix collects light only from one of parallel beams going from the object.

If each pixel of ICCD matrix somehow collects light only from one of parallel beams going from the object, the image is the optical projection of the volumetric light source on the plane of the detector, see Fig. 3.11 (b). In this case, the signal can be considered as a result of integral Abel transform [105].

For two-dimensional case mathematically it can be written as

$$F(y) = \int_{-\infty}^{+\infty} f(x, y)dx, \tag{3.11}$$

where y is a position of the light beam parallel to the x axis, $f(x, y)$ is distribution of the light source intensity in plasma, $F(y)$ is the intensity distribution on the detector.

The capillary discharge in the middle of the discharge gap can be considered as an axially symmetric light source. For axially symmetric distribution, with $f(x, y) = f(r)$ one can write

$$F(y) = 2\int_y^\infty \frac{f(r)rdr}{\sqrt{r^2-y^2}}, \tag{3.12}$$

here the expressions $r = \sqrt{x^2+y^2}$ with $dx = rdr/\sqrt{r^2-y^2}$ were used, as well as the fact that $f(r)$ is an even function with respect to x.

In the case of axially symmetric distributions, it is possible to reconstruct the initial radial distribution profile of the light source intensity using the inverse integral Abel transform, which can be written as

$$f(r) = 1\frac{1}{\pi}\int_r^\infty \frac{dF}{dy}\frac{dy}{\sqrt{y^2-r^2}}. \tag{3.13}$$

However, the formula (3.13) is valid only if the initial profile $f(r)$ drops to zero more quickly than $1/r$.

As it was discussed in the Literature Review, the radial distribution of electron density in the nanosecond capillary discharge can be not only decreasing slower than $1/r$, but even increasing from center of the tube to the periphery of the plasma. Since the excitation of species is proportional to electron density during the discharge, the assumption that the distribution of sources of light emission drops to zero more quickly than $1/r$ seems to be incorrect in the case of nanosecond discharge. Thus the formula (3.13) is non-valid in this case, and another procedure is required to reconstruct the distribution of excited species in the plasma channel.

The following way of data treatment is proposed. If the radial distribution of excited species emitting light can be represented as polynomial of the order n of the radius $r \in [0, R_0]$ with radius of the plasma channel R_0:

$$f(r) = a_0 + a_1 r + a_2 r^2 + ... + a_n r^n, \tag{3.14}$$

the integral Abel transform of this polynomial can be written as

$$F(y) = 2\left[a_0\int_y^{R_0}\frac{rdr}{\sqrt{r^2-y^2}} + a_1\int_y^{R_0}\frac{r^2dr}{\sqrt{r^2-y^2}} + a_2\int_y^{R_0}\frac{r^3dr}{\sqrt{r^2-y^2}} + ...a_n\int_y^{R_0}\frac{r^{n+1}dr}{\sqrt{r^2-y^2}}\right], \tag{3.15}$$

or as

$$F(y) = a_0 I_1(y) + a_1 I_2(y) + a_2 I_3(y) + ... + a_n I_{n+1}(y), \tag{3.16}$$

with

$$a_i I_{i+1}(y) = a_i\int_y^{R_0}\frac{r^{i+1}dr}{\sqrt{r^2-y^2}} \tag{3.17}$$

for $i = 0..n$.

Functions $I_i(y)$ depend only on the geometry of the plasma channel, namely only on R_0, and can be pre-calculated. To increase the precision, the integrals are used in analytical form. Pre-calculation of $I_i(y)$ were performed using the Wolfram Alpha engine [106].

This gives possibility to use the integrals as basic functions for decomposition of $F(y)$ in the series over $I_i(y)$ (3.16) by least square method (LSM method) [107]. The coefficients a_i in the decomposition (3.16) substituted in (3.14) give the initial radial distribution of the excited species in the plasma channel. This method does not impose any restrictions on the profile form and can be used for treatment of experimental data with unknown *a priori* behavior of the profile of excited species. The only assumption, as was indicated before, is the axial symmetry of the plasma.

The proposed method was realized numerically by the Fortran programming language. Preliminarily results showed that it is required to use a piecewise definition of $f(r)$ at least on two segments $[0, R_0/2]$ and $(R_0/2, R_0]$ to reduce numerical oscillations. The procedure should be started from the external region of plasma, since by definition (3.12), the value of $F(y)$ depends only on profile $f(r)$ in segment $[y, R_0]$. Thus the following algorithm was used in the Fortran code:

1. The basis functions $I_i(y)$ are pre-calculated for each point y.

2. The profile $f(r)$ is piecewise defined on k segments with boundaries $0, R_1, ..., R_k$, where $R_k = R_0$.

3. On the segment $[R_{k-1}, R_k]$ the coefficients a_i^k are determined using LSM method directly with $F(y)$.

4. For internal segment j the results of previous calculations (set of $a_i^k, a_i^{k-1}, ..., a_i^{j+1}$) are used to subtract the part of $F(y)$ determined by segments $[R_j, R_k]$. In other words, for internal segments experimentally measured profile is corrected by subtracting of Abel transform of $f(r)$ on segments $j + 1, ..., k$ where the problem has been already solved.

5. The Items 3 and 4 are repeated until all segments are treated.

6. The curve $F(y)$ is calculated using complete set of $a_i^k, a_i^{k-1}, ..., a_i^1$ to compare it with initial experimental profile to estimate correctness and precision.

7. The radial distribution $f(r)$ is calculated as (3.14) using complete set of $a_i^k, a_i^{k-1}, ..., a_i^1$ values.

The validation of the code was performed using an analytical expression for Abel transform for uniform emitting circle with the unit amplitude intensity ($f(r) = 1$). In this case the "experimental" profile on the detector is

$$F(y) = 2\int_{y}^{R_0} \frac{rdr}{\sqrt{r^2 - y^2}} = 2\sqrt{R_0^2 - y^2}. \tag{3.18}$$

This profile was used as an input for the code. The results of calculations are presented in Fig. 3.12. The difference between the result of reconstruction and the initial profile $f(r) = 1$ is negligible.

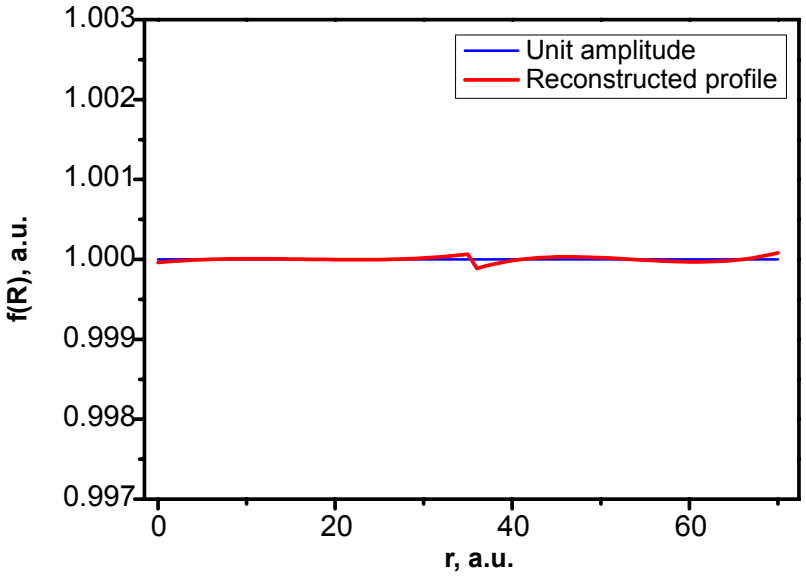

Figure 3.12 – Reconstructed constant intensity distribution $f(r) = 1$ with the input profile given by (3.18)

Influence of the quartz wall of the capillary tube on the light beam propagation

With described above schematic optical scheme (Fig. 3.11 (b)), one can collect light beams parallel to the optical axis with impact parameter denoted as y. For plasma in free space without the surrounding quartz tube, this light beam corresponds to the chord in the plasma cross-section at the distance y from the center. However, there are refractions and reflections on internal and external walls of the tube changing the direction of the beam. First, the influence of the refractions is considered. The influence of the partial reflections on these walls will be discussed below. The quartz is considered as a transparent medium with a refractive index higher than the refractive index of air.

To understand the influence of the refraction on the tube boundaries one can make simple geometric construction, schematically presented in Fig. 3.13. By the

theorem of the reversibility of rays it is possible to consider that the beam goes from the detector into the capillary tube.

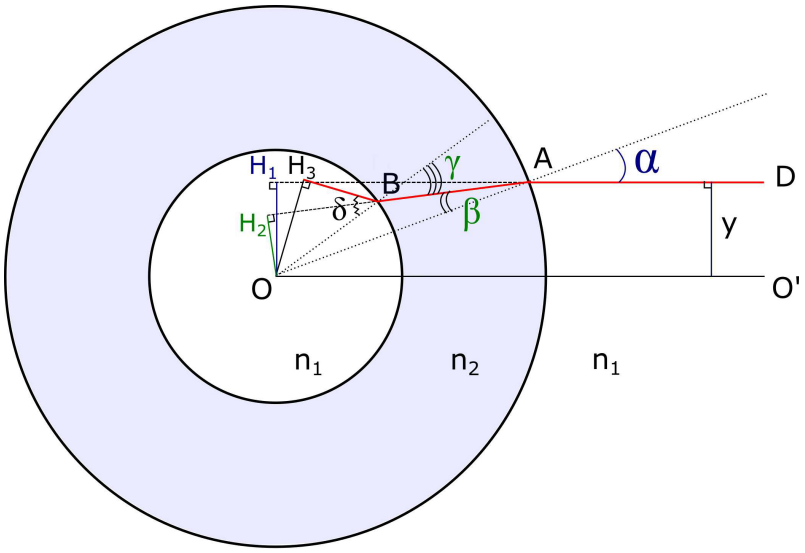

Figure 3.13 – Cross-section of the capillary tube. Geometric construction shows influence of the refractions on the surface of the walls of the capillary tube. Red line represents trajectory of the light beam. The refractive indexes of the free space and the quartz are denoted as n_1 and n_2, respectively.

The light beam with impact parameter y relative to optical axis $OO\prime$ enters the capillary tube in the point A. The angle of incidence is the angle between the ray OA and the beam AD and is equal to α. From the triangle $\triangle OAH_1$ it follows that

$$sin\alpha = \frac{OH_1}{OA} = \frac{y}{OA}. \tag{3.19}$$

According to the Snell's law, the angle of refraction $\angle OAH_2 = \beta$ is connected with the angle of incidence by equation

$$sin\beta = \frac{n_1}{n_2} sin\alpha. \tag{3.20}$$

With (3.19) it gives

$$sin\beta = \frac{n_1}{n_2}\frac{y}{OA}. \tag{3.21}$$

It also can be expressed from the triangle $\triangle OAH_2$ as

$$sin\beta = \frac{OH_2}{OA}. \tag{3.22}$$

Finally, (3.21) and (3.22) give

$$OH_2 = \frac{n_1}{n_2} y. \tag{3.23}$$

From the triangle $\triangle OAH_1$ it follows that

$$sin\gamma = \frac{OH_2}{OB}. \tag{3.24}$$

For $\angle OBH_3 = \delta$ the Snell's law, (3.24) and (3.23) give

$$sin\delta = \frac{n_2}{n_1} sin\gamma = \frac{n_2}{n_1}\frac{OH_2}{OB} = \frac{n_2}{n_1}\frac{n_1}{n_2}\frac{y}{OB} = \frac{y}{OB}. \tag{3.25}$$

From the triangle $\triangle OBH_3$ one can write

$$sin\delta = \frac{OH_3}{OB}. \tag{3.26}$$

Comparison of (3.25) and (3.26) gives

$$OH_3 = y. \tag{3.27}$$

Thus, refractions on the surfaces of the wall of the capillary tube changes only the direction of the beam, but the impact parameter stays the same. So, the emission from the capillary tube parallel to the optical axis can be considered as emission from the plasma channel fixed in the free space without any wall, and this emission can be used to reconstruct the distribution of the excited species. However, here the influence of partial reflections has not be included. To discuss it another geometric construction is presented in Fig. 3.14.

First of all, one can consider reflection on the internal surface of the quartz wall. The light source in the point H_1 emits the light beam H_1K, which is reflected on the internal wall surface as beam KF with $\angle OKA = \angle FKO$. Since $OF = OK = OA$, as radii of the internal circle and $\angle OKA = \angle FKO$ the isosceles triangles $\triangle OFK$ $\triangle OKA$ are equal, and consequently, $OH = OH_1$. It means that reflections on the internal wall surface are the chords remote at the same distance from the center O, so all further reasonings about the trajectory of the beam inside the wall are valid for the reflections also.

To investigate the beam propagation in the wall including partial reflections one can consider the light source in the point H_1 emits the light beam H_1A, which is refracted on the internal wall surface and propagates further as beam AB. Let us construct two additional angles $\angle BON = \angle NOD = \angle MOB$ and show that the light beam trajectory corresponds to segments BC and CD. Since $OB = OD$ as radii of the external circle, $OA = OC$ as radii of the internal circle and $\angle BON = \angle NOD = \angle MOB$, it is valid that $\triangle OAB = \triangle OBC = \triangle OCD$, as triangles with two sides with the same length and with equal included angle. Thus,

$\angle ABO = \angle OBC = \angle CDO$. Here first equality means that BC is reflection of the beam AB. It is also valid that $\angle BCO = \angle OCD = \angle OAB$, consequently, $\angle BCN = \angle NCD = \angle MAB$. First equality means that CD is reflection of the beam BC. Thus, it is proved that light beam trajectory correspond to broken line $ABCD$. It is also important that since $\angle MAB = \angle BCN$, the segment CL constructed as a refraction of BC (with Snell's law) is a chord remote at the same distance from the center O as initial light beam H_1A. It follows from the facts that $\angle H_1AO = \angle OCH_2$ and that $OA = OC$ as radii of the internal circle, which means that right triangles $\triangle OH_1A$ and $\triangle OH_2C$ are equal, consequently, $OH_1 = OH_2$.

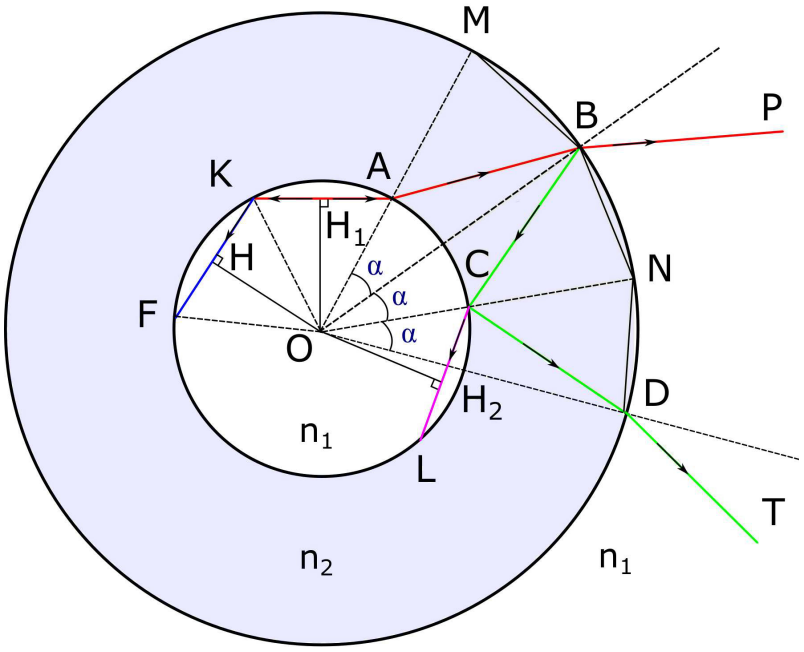

Figure 3.14 – Cross-section of the capillary tube. Geometric construction shows influence of the reflections on the surface of the wall of the capillary tube. Red line represents the main trajectory of the light beam. Green line shows the beam reflected from the surface of the wall of the capillary tube. Magenta line corresponds to the beam entering the internal volume from the volume of the quartz wall. The blue line illustrates reflection from the internal surface of the wall. The refractive indexes of the free space and the quartz are denoted as n_1 and n_2, respectively.

It should be noted that beams BP and DT go out of the external wall at the same angle. Also, since $OH_1 = OH_2$ and $\angle ABO = \angle CDO$ one can see that further trajectory of the beam will repeat described one. This and the fact, that very first

reflection on the internal surface of the wall is the same chord, mean that energy of the initial beam BP is distributed between number of "parasitic" output beams starting from different points of the external surface at equal angles to it.

At first sight, it is in contradiction with previous result about the influence of the refraction on the quartz wall. It was shown that refractions on the surfaces of the wall of the capillary tube changes only the direction of the beam, but the impact parameter stays the same. And it was concluded that the emission from the capillary tube parallel to the optical axis can be considered as emission from the plasma channel fixed in the free space without any wall.

However, in axially symmetric approximation, there is the ring of equal elementary light sources with radius equal to OH_1. Trajectories of the beams from another point of this ring as the same, as was discussed with Fig. 3.14, but with turn on some angle relative the point O. This means that for each "parasitic" beam like DT there is position of the light source on the ring, at which "parasitic" beam will coincide with the main beam BP. So, summation of emission of all light sources on the ring compensates the loses of energy of main beam BP, and it propagates as in case without any reflections on the surface of the wall.

Finally, it is concluded that in axially symmetric approximation the emission parallel to the optical axis can be considered as emission from the plasma channel fixed in the free space without any wall.

Optical scheme

To collect the light beams parallel to the optical axis, the optical scheme presented in Fig. 3.15 was used. The optical scheme consists on the two collecting lenses installed con-focally with the pin-hole diaphragm in the focus point. The idea is that the beams non-parallel to the optical axis are focused out of the diaphragm aperture and do not pass further. The narrow band filter allows to observe only a given wavelength range, so the emission of only one chosen excited specie can be collected. The filter is installed after the lenses system, because the best performance of the filters based on a thin film Fabry-Perot Interferometer is achieved in the parallel beams normal to the filter surface. From the Fig. 3.15 one can see that the ratio f_1/f_2 is a zoom factor. At $f_1/f_2 < 1$ the image linear size will be longer than the size of the object, at $f_1/f_2 > 1$ the image will be smaller than the object. First case can be applied to increase the spatial resolution in f_2/f_1 times, but the signal amplitude in this case drops in $(f_1/f_2)^2$ times, since the image is 2D. The opposite situation at $f_1/f_2 > 1$ is applied to increase signal amplitude in $(f_1/f_2)^2$ times (and the signal to noise ratio as a consequence), but the spatial resolution decreases in f_2/f_1 times. Since the signal value depends on the ratio between the focal distances

quadratically, and spatial resolution depends on the same ratio only linearly, in the present thesis the case with intensity gain was chosen.

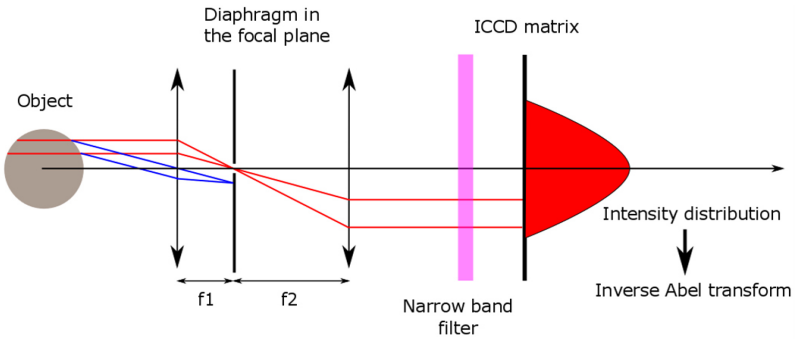

Figure 3.15 – The optical scheme used for measurements of distribution of excited species in the nanosecond capillary discharge. Red lines illustrate beams parallel to the optical axis, which can pass the diaphragm and reach the detector. Blue lines illustrate beams non-parallel to the optical axis, which are filtered

Two one inch in diameter Uncoated UV Fused Silica Plano-Convex Lenses from Thorlabs with focal distances $f_1 = 150$ mm and $f_2 = 75$ mm were used, thus energy gain was equal to 4 and spatial resolution was about 23 μm, the aperture of the pin-hole diaphragm was 300 μm, the narrow band filter with central wavelength 340 nm and band FWHM=10 nm was used to study the distribution of $N_2(C^3\Pi_u, v' = 0)$ by measuring the emission of $N_2(C^3\Pi_u, v' = 0) \rightarrow N_2(B^3\Pi_g, v'' = 0)$ transition. The images were acquired by ICCD camera (PiMax-4 1024i from Princeton Instruments) with a gate 1 ns or 2 ns.

Chapter 4

Discharge characteristics

In this Chapter the most important characteristics of the discharge are given.

4.1 Electric parameters of the discharge

The discharges at moderate pressure at given gas composition can be classified by a number of characteristics, but the most important are the applied voltage, the energy deposition, the electric field, and the electric current. They determine the discharge development and plasma kinetics in the discharge and in the afterglow.

The applied voltage is characterized by four main parameters, namely: (i) polarity (positive or negative), (ii) amplitude, (iii) rise time (typically, time during which the voltage reaches the $0.9V_{max}$ from $0.1V_{max}$ value, where V_{max} is the maximum amplitude) and (iv) pulse duration, usually given as FWHM. The polarity determines the breakdown process and the discharge development, since the direction of movement of electrons and ions depend on the polarity. At positive polarity, electrons move to the high voltage electrode, positive ions move in the gas volume from the electrode. At negative polarity, electrons are emitted from the electrode and move to the gas bulk, positive ions move to the electrode. This influences on the EEDF formations, see Fig. 1.16 and the corresponding discussion. The amplitude of the applied pulse controls both the electric field during the breakdown and the electric field during the current pulse, when the gap between electrodes is closed. Its typical value for nanosecond discharges is few tens of kilovolts. The rise time is an extremely important parameter determining the electrical field during the breakdown stage. The electrical field is higher at faster voltage rise. Rise time for

nanosecond discharges has typical value of few nanoseconds. The high voltage pulse width determines duration of the energy deposition stage.

The energy deposition itself determines plasma kinetics, excitation and ionization degree in the plasma, temperature dynamics. That is more important, it is conditions at which the energy was deposited: reduced electric field. The electric field value determines the electron energy branching, see Fig. 1.2. High electric field provides excitation of the electronic degrees of freedom. The excitation degree is higher at higher electron density at given electric field, i.e. is depends on the electric current value.

Further, the results of measurements of main characteristics of the nanosecond capillary discharge are presented.

4.1.1 Applied voltage and transmitted current

The applied voltage and transmitted current waveforms were measured by back current shunts (BCSs). The details of this measurements technique are given in Section 3.2.2. Typical voltage waveform measured by BCS1 installed in the high voltage cable is presented in Fig. 4.1.

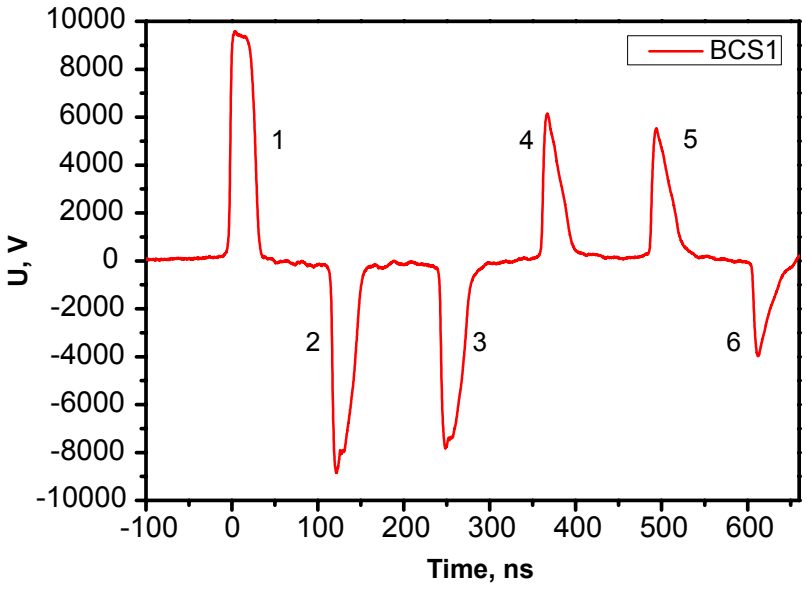

Figure 4.1 – Measured electric parameters of the nanosecond capillary discharge. Signal from BCS1. Three pairs of the incident from the high voltage generator and reflected from the discharge cell pulses: (1-2), (3-4) and (5-6).

Here pulse denoted by 1 (incident pulse) corresponds to the pulse coming from the high voltage generator. The generator produces only one high voltage pulse with the following characteristics: the amplitude is 9.3 kV, the rise time is 4 ns, the pulse

width is 30 ns FWHM, see Fig. 4.1 and Fig. 4.2. This pulse arrives the discharge cell and partially reflects due to mismatching between the impedances of the load (discharge cell) and the impedance of the high voltage cable, $Z = 50$ Ohm. The reflection of high voltage pulse from the discharge cell propagates back to the high voltage generator and is registered by the BCS1 again. This signal (reflected pulse) corresponds to the pulse 2 in Fig. 4.1. This voltage pulse has the same polarity as pulse 1, but it propagates in opposite direction, thus the sign of the signal is changed. Since the impedance of the output of the used high voltage generator is switched to zero after the high voltage pulse production, the pulse 2 is reflected from the generator with inverse polarity. This pulse denoted 3 can be considered as a new incident pulse, with the reflection from the discharge cell, 4. Described process repeats one more time. Thus, one can see in Fig. 4.1 three pairs of the incident and reflected pulses: 1-2, 3-4 and 5-6. The time between pulses in each pair, for example, 1 and 2 registered by BCS1 is defined by the cable length between BCS1 and the discharge cell. This time can be extracted from the oscillogram by shifting of inverted reflected pulse until its first front coincides with the first front of the incident one. The result of this procedure is presented in Fig. 4.2.

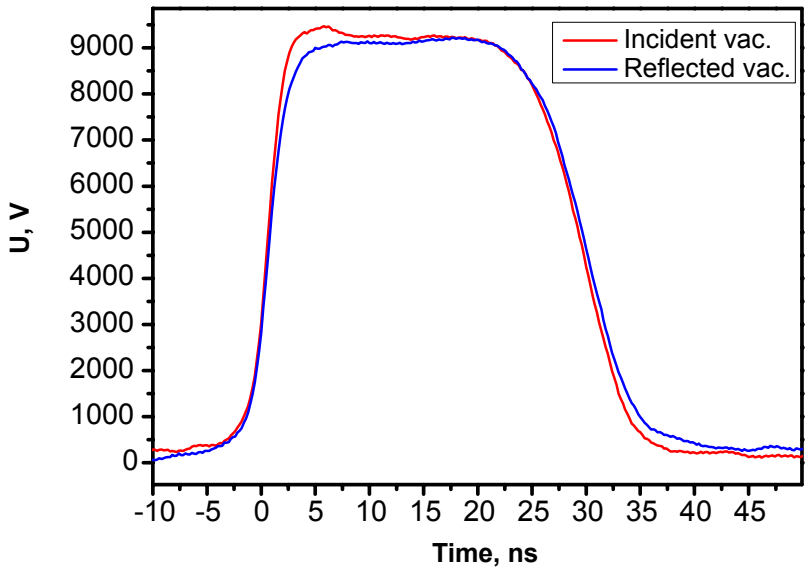

Figure 4.2 – The incident pulse superimposed with inverse reflected one shifted by $2\tau_1 = 118.6$ ns (vacuum configuration).

Here the incident pulse is superimposed with inverse reflected one shifted by 118.6 ns. The high voltage pulse has reflected from the discharge cell pumped to low pressure ($\approx 10^{-3}$ mbar), it allows avoiding any perturbations due to current transmission through the inter-electrode gap. This configuration is called "vacuum" further in the text. The measured time 118.6 ns corresponds to double distance between BCS1 and the discharge cell, thus, for the signal it takes $\tau_1 = 59.3$ ns to propagate from

BCS1 to the discharge cell. This value will be used for the synchronization of the measurements. One can see that falling front of the reflected pulse slightly differs from the falling front of the incident pulse. This is caused by dispersion in the high voltage cable. Higher frequencies attenuate more intensively during the signal propagation. It causes spreading of the high voltage pulse, which can be represented as a wave pack with different frequencies. The higher frequencies correspond to higher values of time derivatives, i.e. rise and falling fronts of the pulse. The slight difference in the waveforms of incident and reflected pulses just after the first front is caused by charging of the capacitance of electrode system.

The same procedure without any load on the end of the cable allows to obtain the value of attenuation coefficient. The reflected signal should be multiplied by some coefficient to get the amplitude equal to the amplitude of the incident pulse. It is square of the attenuation coefficient, since the signal propagates the double length between BCS1 and the discharge cell. For the cable used in the experiments it was found that the signal decays to the value $k_d = 0.975$ during propagation from the BCS1 to the discharge cell. Thus, the incident pulse of the initial amplitude should be multiplied by k_d value, since it is measured before the attenuation takes place. The reflected one should be multiplied by $1/k_d$, since it is measured after the attenuation occurs. The same procedure for the low–voltage cable with BCS2 gives the same value of attenuation, since the back current shunts 1 and 2 are installed at the same distance from the discharge cell in high-voltage and low-voltage cables, respectively.

Another information obtained from Fig. 4.1 is the time between two consecutive incident pulses 1 and 3, or 3 and 5. To calculate this time interval the signal from the BCS1 is shifted until the pulse 2 superimposes with the pulse 3. This time shift equal to 126.6 ns corresponds to the double length of the cable between BCS1 and the high voltage generator. Finally, sum of this time and $2\tau_1$ (corresponding to double length between BCS1 and the discharge cell) gives the time delay between two consecutive incident pulses equal to 245.2 ns.

Three pairs of high voltage pulses in Fig. 4.1 separated by 245.2 ns correspond to three current pulses transmitted through the plasma. The typical waveforms of the transmitted pulses are presented in Fig. 4.3.

One can see that the delay between the rising fronts of the pulses II and III is equal to the obtained delay between two consecutive incident pulses equal to 245.2 ns. The time between rising fronts of pulses I and II is slightly shorter, since in the first pulse, at the early stage of the discharge, during the FIW propagation from the high–voltage to low–voltage electrode, current flowing through plasma can not be registered by BCS2 installed in the low-voltage cable, since this current closes to the metal screen by displacement current. Thus, the first pulse really

starts early, then the signal of the BCS2 rises. This will be discussed additionally when the synchronization of the transmitted pulse with incident and reflected ones is described.

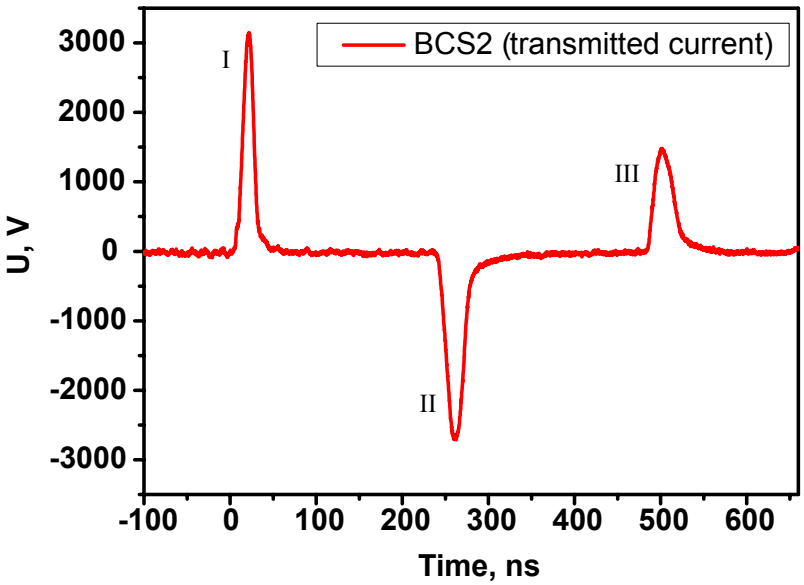

Figure 4.3 – Measured electric parameters of the nanosecond capillary discharge. Signal from BCS2. Three transmitted current pulses I, II and III corresponding to three pairs of pulses incident from the high voltage generator and reflected from the discharge cell: 1-2, 3-4 and 5-6 in Fig. 4.1, respectively.

It is obvious, that the signals for incident, reflected and transmitted pulses are registered by oscilloscope at different time instants, since it takes time for signal to propagate between the discharge cell and BCSs. The incident and reflected pulses can be synchronized by the method presented above, see Fig. 4.2. To synchronize the transmitted pulse with the incident and reflected ones one can use the following method. In the first approximation, the difference between incident and reflected pulses corresponds to electric current going to the discharge cell. However, as it was mentioned above during discussion of Fig. 4.2, during the FIW propagation the current closes to the metal screen by displacement current, also some part of the current is spent to charge the capacitance of the electrode system and does not flow through the plasma. Thus, the current flowing from the high voltage electrode can be more correctly calculated as a difference between the reflected pulse at vacuum configuration (blue curve in Fig. 4.2) and reflected pulse measured during the discharge. Finally, to synchronize the signal from the BCS2 with the BCS1, the signal from BCS2 should be shifted until the signal superimposed with the difference of the reflected pulse in vacuum configuration and the reflected pulse

measured during the discharge. The method of synchronization of BCS1 and BCS2 is illustrated by Fig. 4.4. Here, one can see the step on the blue curve (difference of two reflected pulses), which is absent on the signal from the BCS2 (green curve). It corresponds to the current flowing from the HV electrode, but not reaching the LV electrode, since the current in the FIW front is closed on the metal screen by displacement current, that was mentioned above. Finally, the signal from the BCS2 is shifted to 122 ns to synchronize the BCS2 signal with the signal from BCS1. This time interval corresponds to the sum of the times of signal propagation from the back current shunts to the discharge cell in the high voltage cables τ_1 and τ_2 with the difference of the times of the signal propagation from the back current shunts to the oscilloscope in the BNC cables:

$$\tau_1 + \tau_2 + (l'_2 - l'_1)/v = 122 \text{ ns}, \tag{4.1}$$

where l'_1 and l'_2 are the lengths of the BNC signal cables between the oscilloscope and BCS1 or BCS2, respectively, $v = 20$ cm/ns is the velocity of signal propagation in the cables. For BCS2 τ_2 can be measured by the same procedure as for BCS1 (see Fig. 4.2). It gives $\tau_2 = 62.5$ ns. Thus, the signal passes the distance equal to the difference of the lengths of the BNC cables between the back current shunts and the oscilloscope in only 0.2 ns.

4.1.2 Electric field

The longitudinal electric field can be measured by two different independent methods. The first method, based on BCS technique, is to calculate the electric field as a difference of potentials on the high–voltage and the low–voltage electrodes ΔU divided by the inter-electrode distance d: $\Delta U/d$. The potential on the high–voltage electrode is equal to $U_{inc} + U_{ref}$ according to the transmission lines theory, the potential on the low–voltage electrode is equal to U_{tr}. Finally, the electric field is calculated as

$$E = \frac{U_{inc} + U_{ref} - U_{tr}}{d}, \tag{4.2}$$

with $d = 75$ mm. The distance d is slightly longer than the distance between tips of the electrodes (70 mm) indicated in Fig. 3.4, since it is assumed that electric current flows not only between tips of the electrodes, but between the entire cone surfaces of the electrodes. The results of the electric field measurements with BCS technique for the first current pulse of 65 A in pure nitrogen at 27 mbar is presented in Fig. 4.5.

This method is valid only when the discharge gap is closed, i.e. the electrodes connected by plasma channel, and the transmitted current flows. Thus, it does

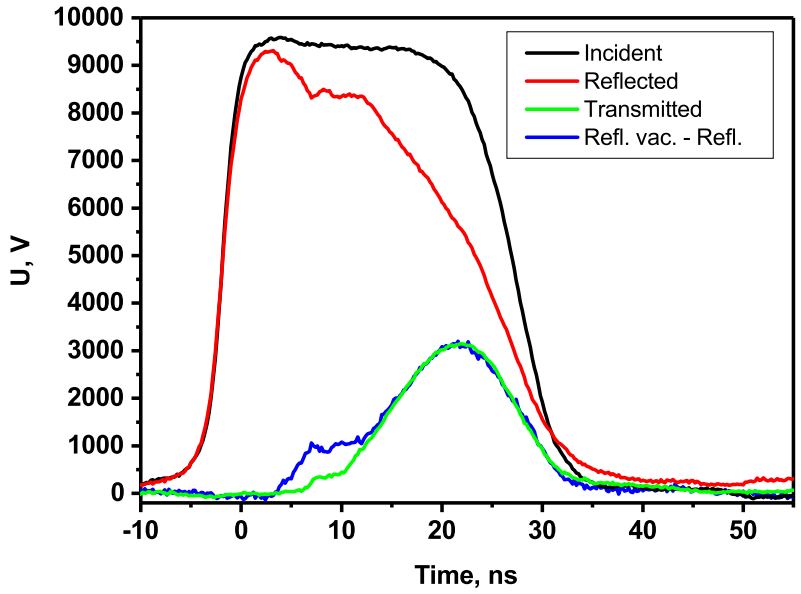

Figure 4.4 – Typical voltage waveforms corresponding to the first pulse incident from the high–voltage generator (black curve), reflected from HV electrode (red curve) and transmitted through the discharge cell (green) pulses measured by the back current shunts 1 and 2. The synchronization of the signals from BCS1 and BCS2 is performed by superposing of transmitted pulse with difference of reflected pulse in vacuum configuration and the reflected pulse during the discharge (magenta curve). The signal from BCS2 is shifted to 122 ns.

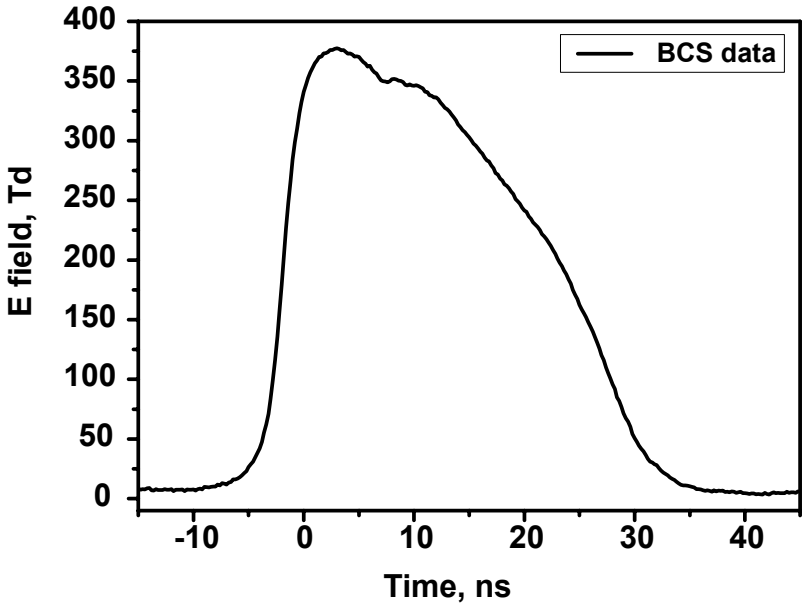

Figure 4.5 – The longitudinal electric field measured by BCS technique. First pulse, pure nitrogen, 27 mbar, $I_{tr} = 65$ A.

not resolve FIW. To resolve FIW structure, the Capacitive Probe (CP) technique is required. The details of this measurements technique are given in Section 3.2.3. The CP is used to measure the electric potential in the capillary tube as a function of time and longitudinal coordinate x. The longitudinal electric field is calculated as a gradient of the electric potential along the tube.

The results of the electric potential measurements for the current pulse of 65 A in pure nitrogen at 27 mbar are presented in Fig. 4.6 for different time instants. The longitudinal electric field calculated as the derivative of the electric potential over the space coordinate x along the tube at point $x = 55$ mm (the middle of the tube) is presented in Fig. 4.7. Here the green curve is the result of the measurements by capacitive probe, black curve is back current shunt data from Fig. 4.5, the red curve is scaled black one used for the synchronization of CP and BCS data. Synchronization of the current measured by BCS technique and of the electric filed measured by a capacitive probe is a very important issue. The technique illustrated by Fig. 4.7 was suggested in [9,63] providing a synchronization with the accuracy of data sampling, 0.2 ns in our case. The idea is the following. At the beginning of the pulse before FIW starts, there is no plasma (free charges are absent). The electric field in this case is the Laplace field produced by HV electrode. This field is detected by capacitive probe as well. The dynamics of this field determined by $U_{inc} + U_{ref}$, which corresponds to the BCS data while $U_{tr} = 0$, see (4.2). Thus, the curve for the electric field measured by BCS scaled by some coefficient can be superimposed with the CP data. The CP data should be shifted until it is in superimposition with scaled BCS curve, see Fig. 4.7.

Synchronized electric field clearly illustrate the development of the fast ionization wave in the capillary tube. The maximum of $E(t)$ waveform corresponds to the FIW front passing through the cross–section of measurements. In the FIW front, there are two factors leading to a noticeable underestimate in the field measurements. First, the electric current in the FIW front is closed by the displacement current to the metallic screen surrounding the capillary. The direction of the electric field in the front is mainly radial, while the capacitive probe gives the longitudinal electric field. Second, the duration of a sharp peak of the electric field in the FIW front does not exceed $2 - 3$ nanoseconds (FWHM). For the conditions of the present experiments, a typical length of the FIW front, $2 - 4$ cm, is only two times higher than a typical half–width of the sensitivity function of the capacitive detector, approximately equal to the distance between the detector and capillary tube axis [76]. So the value of 650 Td is not an exact value, although it can be used for the estimations and clearly demonstrates that the electric field in the FIW front is extremely high.

With the electrical field temporal profile shown in Fig. 4.7 it is easy to interpret electrical potential behavior presented in Fig. 4.6. Before the voltage pulse is applied

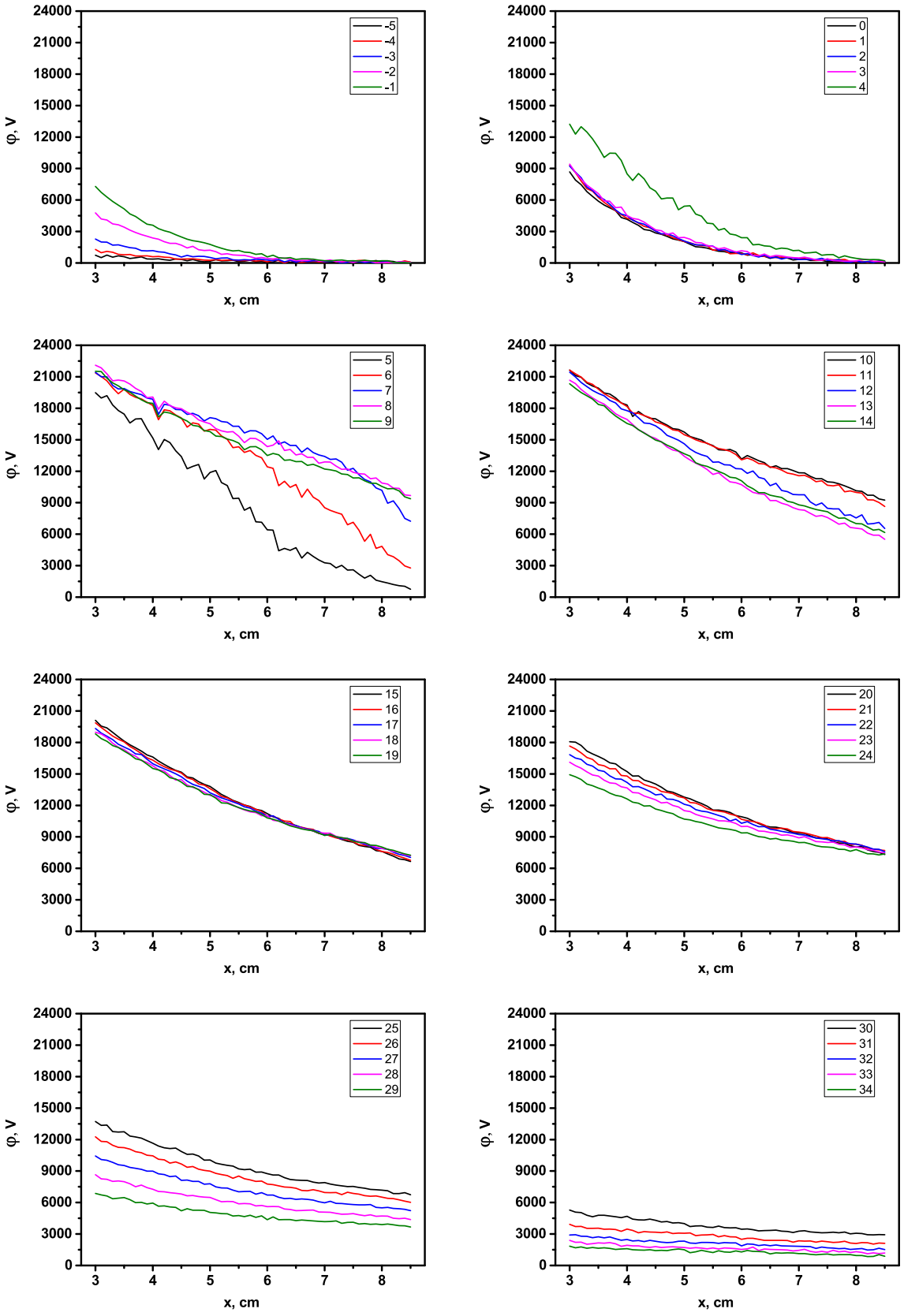

Figure 4.6 – The electric potential in the capillary tube as a function of the longitudinal coordinate at different time instants. Pure nitrogen, 27 mbar, $I_{tr} = 65$ A.

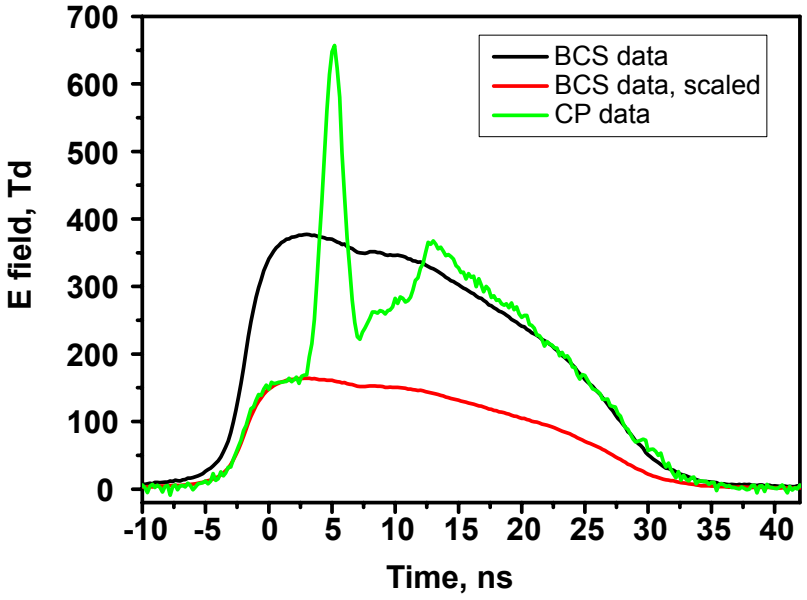

Figure 4.7 – The longitudinal electric field measured by CP technique (green curve) and by BCS technique (black curve). The red curve used for synchronization of CP data with BCS measurements is a scaled data obtained by BCS technique, see the text. First pulse, pure nitrogen, 27 mbar, $I_{tr} = 65$ A.

to the high voltage electrode, the electric potential at any point along the tube is equal to zero. The period from -5 ns to -1 ns corresponds to arrival of the high voltage pulse to the electrode and increasing of the voltage. As it was mentioned above, Laplace field during this period is a function of the voltage on the electrode $U_{inc} + U_{ref} \approx 2U_{inc}$. From 0 ns to 3 ns the distribution of the electric potential along the tube does not change, since the voltage on the high-voltage electrode has reached the plateau. Laplace field is constant during this period, see Fig. 4.7. The FIW starts only after 3 ns, the corresponding curve (4 ns) differs from other curves for previous time instants (3 ns in Fig. 4.6). The gradient of the electric potential increases in this moment, since the FIW propagates. Consequently, in the electric field temporal profile (green curve in Fig. 4.7), one can see the sharp rise in this moment. The FIW reaches LV electrode after 7 ns. Further, the establishment of the transmitted current takes place. During this stage the reverse wave is observed on the potential distribution. It is seen (Fig. 4.6) at $11 - 14$ ns, where the wave of potential decreasing propagates from the LV electrode side (higher x values) to the HV electrode side (lower x values), which cause increasing of the electric field value. After 14 ns the potential distribution slightly changes, which is observed as a "rotation" of the potential distribution curve. Then the voltage on the HV electrode starts to decrease, and the potential value decays on the HV electrode side. One can

see in Fig. 4.7, that BCS data and CP data are in perfect agreement starting from the time instant equal to 22 ns. This time moment corresponds to the maximum value of the transmitted current. It can be explained by the assumption, that in this moment the electron density reaches the value, which is enough to consider the plasma as a conductive channel.

The results of the electric field measurements for the second and third pulses are presented in Fig. 4.8. In the second and third pulses there is no FIW, since the gap between the electrodes has already been closed by the plasma produced during the first pulse or second pulse, respectively. The electric potentials corresponding to the electric fields shown in Fig. 4.8 are presented in Fig. 4.9 and Fig. 4.10.

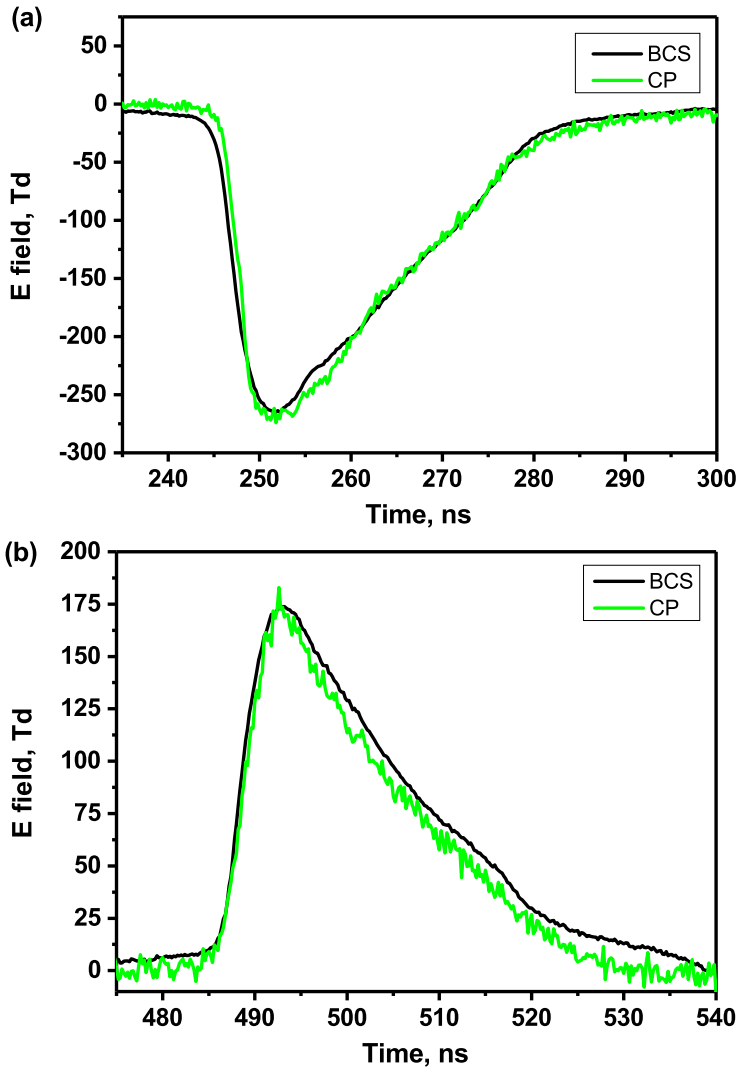

Figure 4.8 – The longitudinal electric field measured by CP technique (green curve) and by BCS technique (black curve). (a) Second pulse, (b) third pulse pure nitrogen, 27 mbar, $I_{tr} = 65$ A in the first pulse.

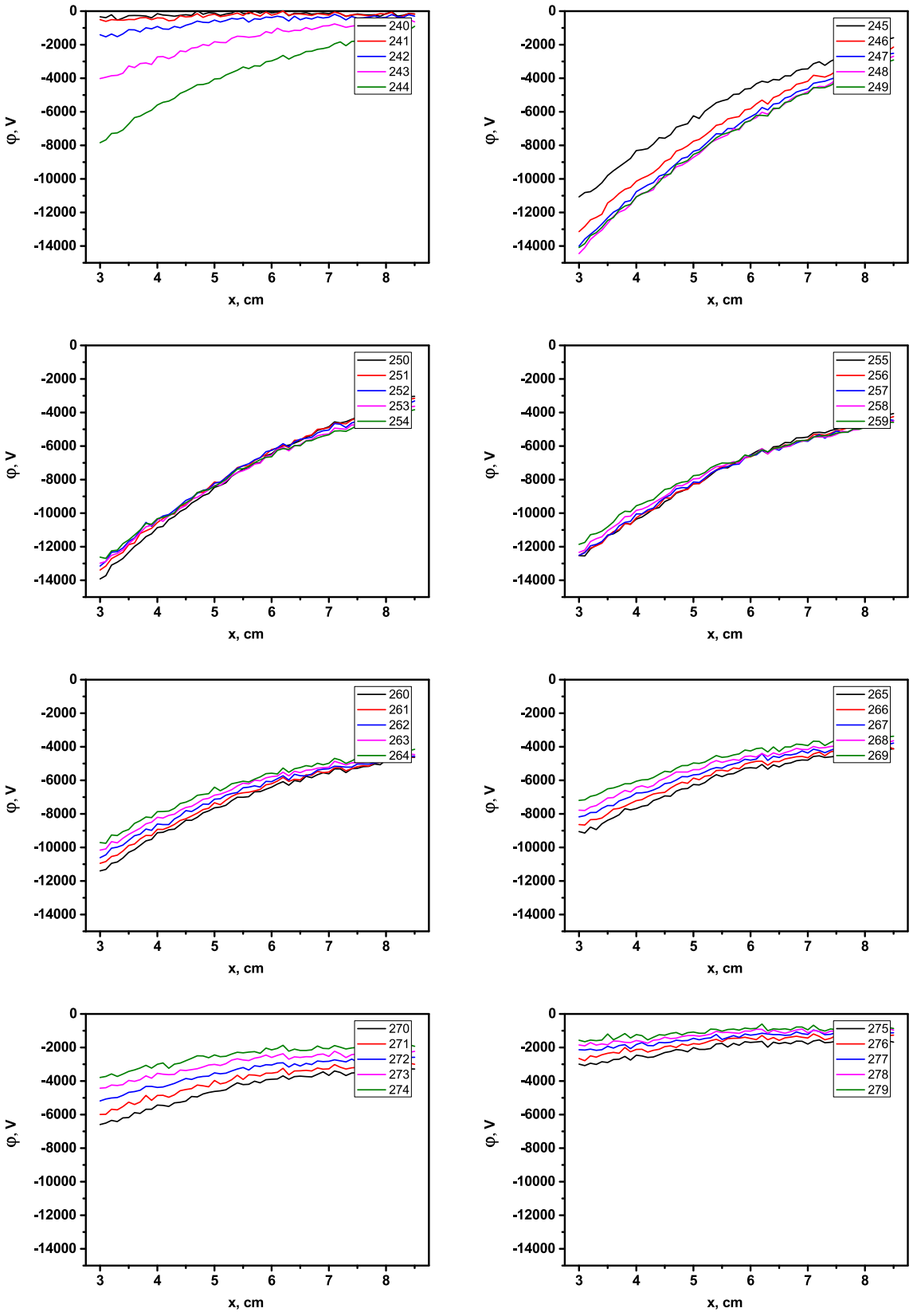

Figure 4.9 – The electric potential in the capillary tube as a function of the longitudinal coordinate at different time instants. Second pulse, pure nitrogen, 27 mbar, $I_{tr} = 65$ A in the first pulse.

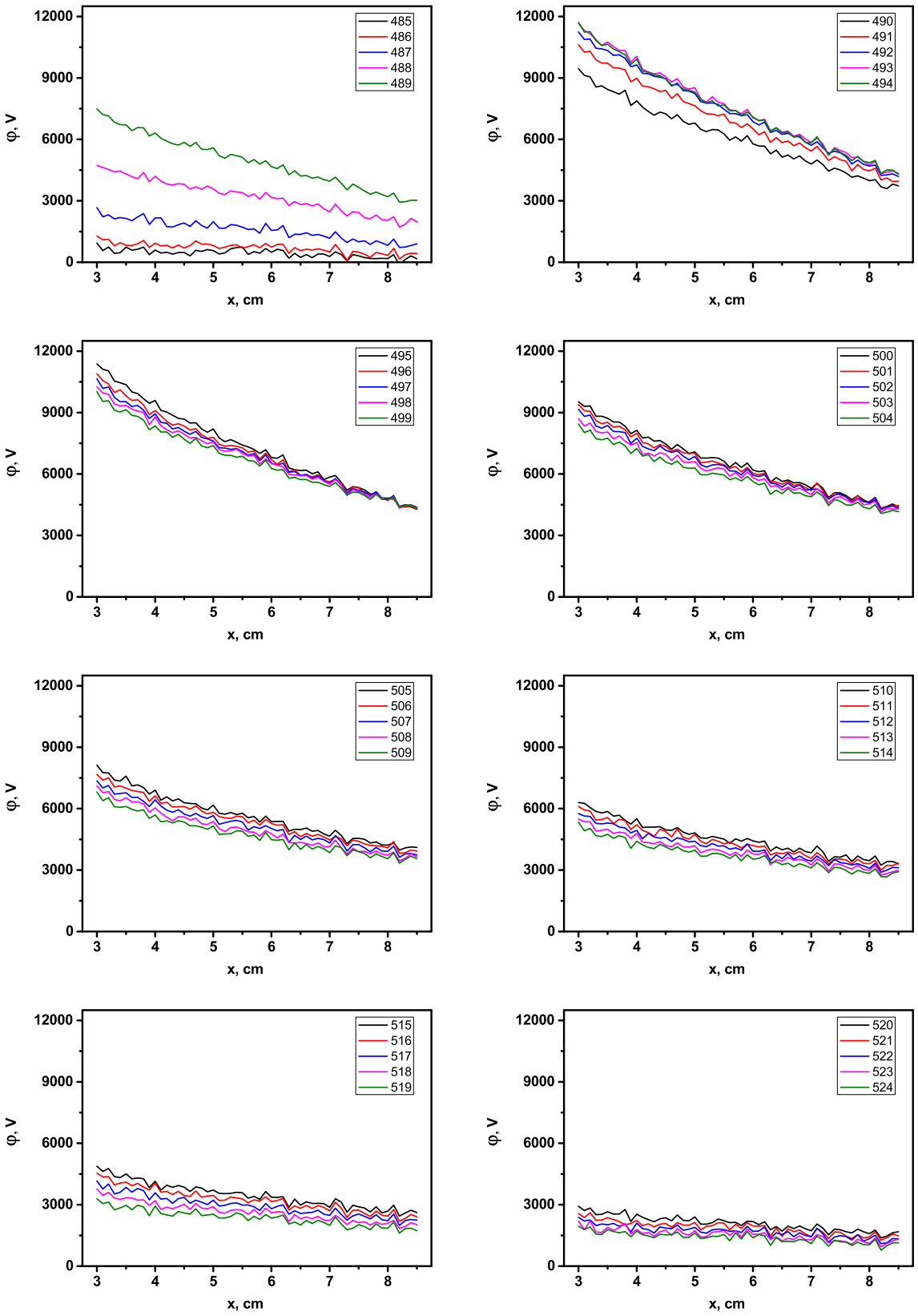

Figure 4.10 – The electric potential in the capillary tube as a function of the longitudinal coordinate at different time instants. Third pulse, pure nitrogen, 27 mbar, $I_{tr} = 65$ A in the first pulse.

4.1.3 Deposited energy

Energy deposited to the discharge in each pulse can be calculated from the signals obtained by the back current shunts. The power passing through the cross-section of the high voltage cable at the time instant t is equal to $U^2(t)/Z$, where $U(t)$ is amplitude of the high voltage pulse and Z is the wave resistance of the cable. In the absence of the plasma (at vacuum configuration, for example), the energy delivered by high voltage pulse W_{inc} coming from the HV generator reflects almost completely ($W_{ref.vac}$), but some part of energy goes to charging of the electrode system capacity W_{cap}:

$$W_{inc} = W_{ref.vac} + W_{cap}, \tag{4.3}$$

where

$$W_{inc} = \frac{1}{Z}\int_{t_0}^{t_{pulse}} U_{inc}^2(t)dt \tag{4.4}$$

and

$$W_{ref.vac} = \frac{1}{Z}\int_{t_0}^{t_{pulse}} U_{ref.vac}^2(t)dt. \tag{4.5}$$

Finally, for W_{cap} one can write

$$W_{cap} = \frac{1}{Z}\int_{t_0}^{t_{pulse}} (U_{inc}^2(t) - U_{ref.vac}^2(t))dt. \tag{4.6}$$

At the presence of plasma the energy balance is the following:

$$W_{inc} = W_{ref} + W_{tr} + W_{cap} + W_{dep}, \tag{4.7}$$

where W_{dep} is energy deposited in the plasma,

$$W_{ref} = \frac{1}{Z}\int_{t_0}^{t_{pulse}} U_{ref}^2(t)dt \tag{4.8}$$

and

$$W_{tr} = \frac{1}{Z}\int_{t_0}^{t_{pulse}} U_{tr}^2(t)dt \tag{4.9}$$

are the energies reflected from the discharge cell and transmitted through plasma to the low-voltage cable, respectively. Thus, for W_{dep} one can write

$$W_{dep} = \frac{1}{Z}\int_{t_0}^{t_{pulse}} (U_{ref.vac}^2(t) - U_{ref}^2(t) - U_{tr}^2(t))dt. \tag{4.10}$$

Here (4.6) and (4.7) were used. The integrand (including $1/Z$) is the instantaneous power deposited in plasma. The specific deposited energy can be calculated as $\omega = W_{dep}/(NV)$, where N is the gas density, $V = 0.1325$ cm^3 is the tube volume.

The instantaneous power and energy deposited in the plasma for 27 mbar of pure nitrogen at transmitted current 65 A in the first pulse are presented in Fig. 4.11.

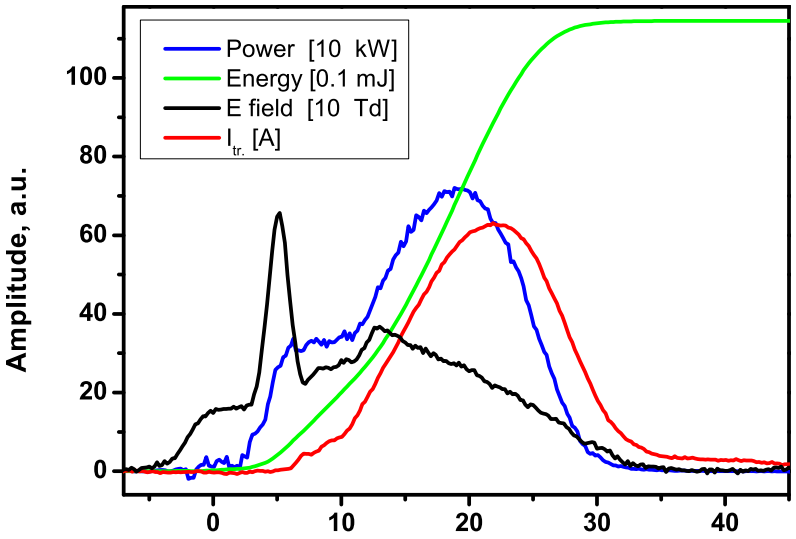

Figure 4.11 – The instantaneous power and energy deposited in the plasma with the current and electric field measured by CP as functions of time. First pulse, pure nitrogen, 27 mbar, $I_{tr} = 65$ A.

One can see that the instantaneous power is not zero from the moment when the FIW starts, while the transmitted current is still zero. The energy is deposited during the FIW with a high power (up to half of maximum value). However, the duration of the FIW stage is rather short and the most energy is deposited when the discharge gap is closed. Another way to calculate the energy deposition proposed in [63] is to calculate energy as

$$W_{dep} = \int_{t_0}^{t_{pulse}} E_{CP} \cdot l \cdot I_{tr} dt, \tag{4.11}$$

where E_{CP} is the electric field measured by capacitive probe and l is the inter-electrode distance. The results of measurements the with this technique are presented in Fig. 4.12 together with the results of BCS technique measurements (see, (4.10)). One can see that these techniques give different results with difference about 15%.

In [63] it was stated that this difference is caused by the following fact. During the discharge initiation some plasma is also created in the side tubes used for gas flow. The plasma in the side tubes was detected by ICCD imaging, and it is also visible even by eyes. It was proposed that CP method is more accurate, since it allows to measure the energy deposition exactly in the inter-electrode region, not taking into account the side tubes. In this case the difference in energies measurements is spent on "parasitic" plasma production. It was concluded that up to 20% of energy is spent on plasma generation in the side tubes. However, it seems that the

CP technique underestimates the energy deposition in the discharge development stage. Capacitive probe technique does not take into account the energy deposited during FIW propagation, since the transmitted current value is equal to zero at this stage, while the current in the plasma is closed by the displacement current. An alternative way to use the current flowing from the HV electrode $(U_{ref.vac} - U_{ref})/Z$ for energy deposition calculations (4.11) is not correct neither, since the electric field at this stage has a high radial component, and so the field measured by CP data is underestimated. Moreover, the electric power is determined by voltage drop, not by the field value: $P = I \cdot \Delta U$, and even if the absolute value of the electric field is known (based on spectroscopic data, for example), the field lines are still unknown, i.e. l value in (4.11) is not constant in time and space, has a complex dependence on discharge cell geometry, and so should be calculated based on at least 2D numerical calculations. Thus, it can be concluded that the results of energy calculations (4.11) can be considered as lower estimate of the deposited energy, while the method (4.10) has a clear physical sense and follows from the energy conservation law. The calculation of the exact value of the part of energy going to the side tubes requires additional study, but it is seen from Fig. 4.12 and the reasoning done above that this part of energy deposition is significantly lower than 15%. Further all deposited energies are calculated by (4.10).

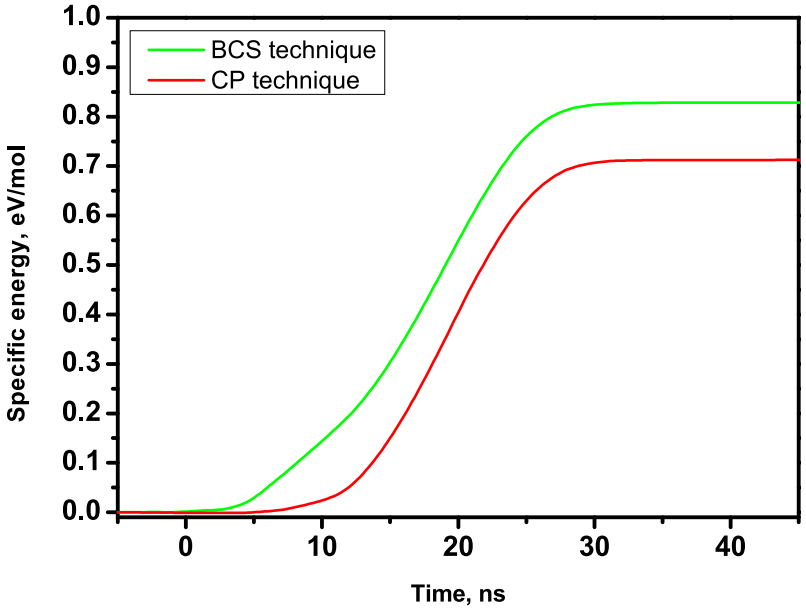

Figure 4.12 – The instantaneous power and energy deposited in the plasma measured by two different techniques (see the text). First pulse, pure nitrogen, 27 mbar, $I_{tr} = 65$ A.

The total, W, and specific, ω, deposited energy values for different transmitted currents and pressure values are presented in Fig. 4.13 (a) and Fig. 4.13 (b),

respectively. It is clearly seen that the energy deposition strongly depends on the transmitted current. At fixed I_{tr}, the total energy deposition increases with pressure, since the plasma density (the number of charge carriers) increases with the gas density, Fig. 4.13 (a). On the other hand, the increase of the gas density leads to reducing of the specific energy deposition at constant volume of the discharge tube, since the total number of particles increases, see Fig. 4.13 (b). Finally, the specific energy deposition only slightly increases with pressure, which can be important for nanosecond capillary discharge applications. It should be emphasized one more time that the dependence of ω upon the transmitted current value is much more significant.

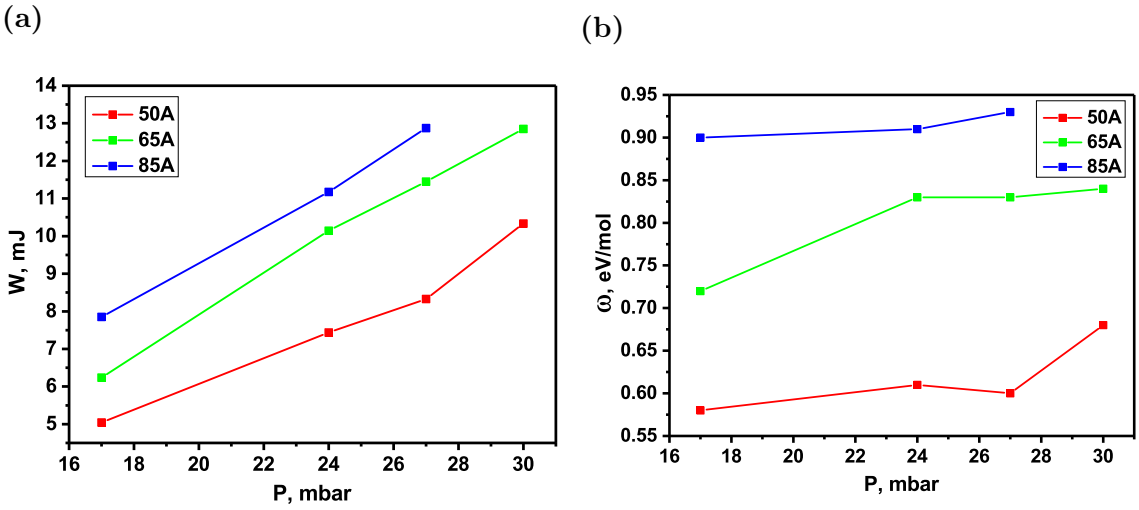

Figure 4.13 – The total (a) and specific (b) deposited energy for different transmitted currents and pressures of pure nitrogen.

4.2 Optical emission from the discharge

Typical spectrum of the optical emission of the nanosecond capillary discharge in pure nitrogen at $P = 27$ mbar is presented in Fig. 4.14 and Fig. 4.15. The signal is collected during the entire first discharge pulse. The electronic-vibrational transitions are denoted as $(v' - v'')$, where v' is a vibrational level of the upper electronic state and v'' is a vibrational level of the lower electronic state. The transitions corresponding to the first negative system of molecular nitrogen $N_2^+(B^2\Sigma_u^+, v') \rightarrow N_2^+(X^2\Sigma_g^+, v'')$ are denoted as $N_2^+(v' - v'')$. The transitions corresponding to the second positive system of nitrogen $N_2(C^3\Pi_u, v') \rightarrow N_2(B^3\Pi_g, v'')$ are denoted as $(v' - v'')$. The transitions corresponding to the first positive system (FPS) of molecular nitrogen $N_2(B^3\Pi_g, v') \rightarrow N_2(A^3\Sigma_u^+, v'')$ are highlighted by a blue frame in Fig. 4.15(b).

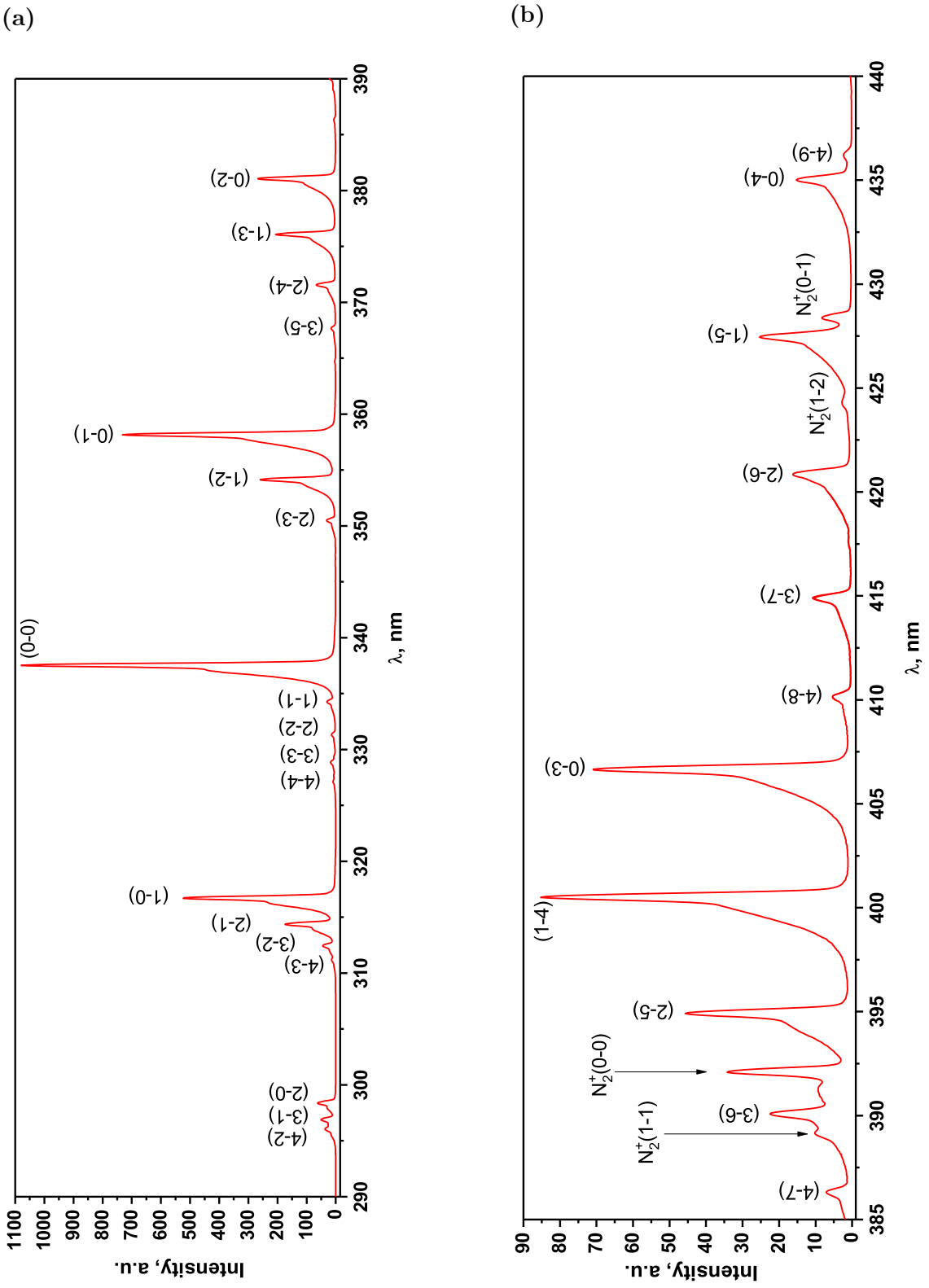

Figure 4.14 – Typical spectrum of the nanosecond capillary discharge in wavelength range (a) 290-390 nm, (b) 385-440 nm. For notations see text. The signal is collected during the first pulse, pure nitrogen, 27 mbar, $I_{tr} = 65$ A.

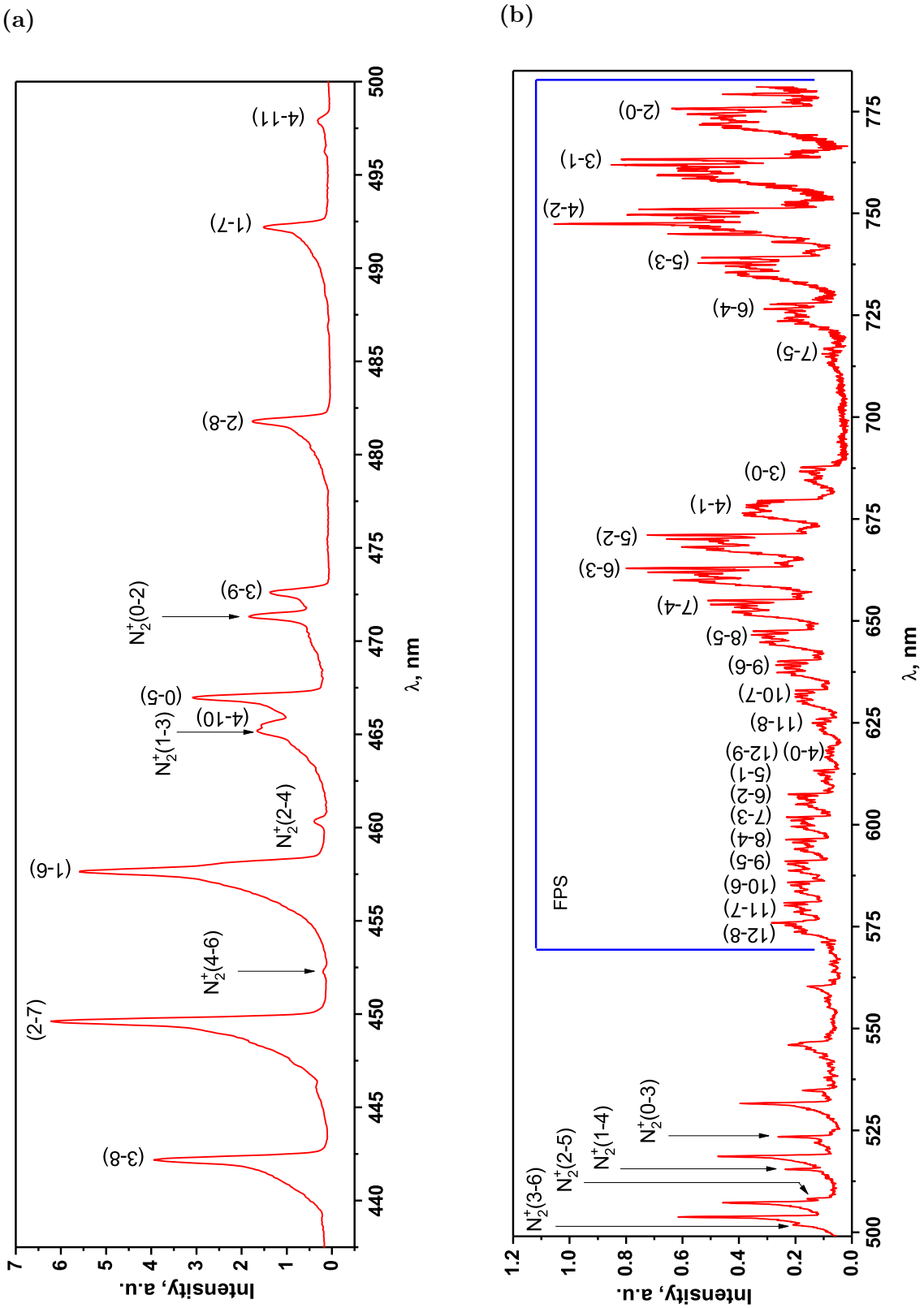

Figure 4.15 – Typical spectrum of the nanosecond capillary discharge in wavelength range (a) 440-500 nm, (b) 500-780 nm. For notations see text. The signal is collected during the first pulse, pure nitrogen, 27 mbar, $I_{tr} = 65$ A.

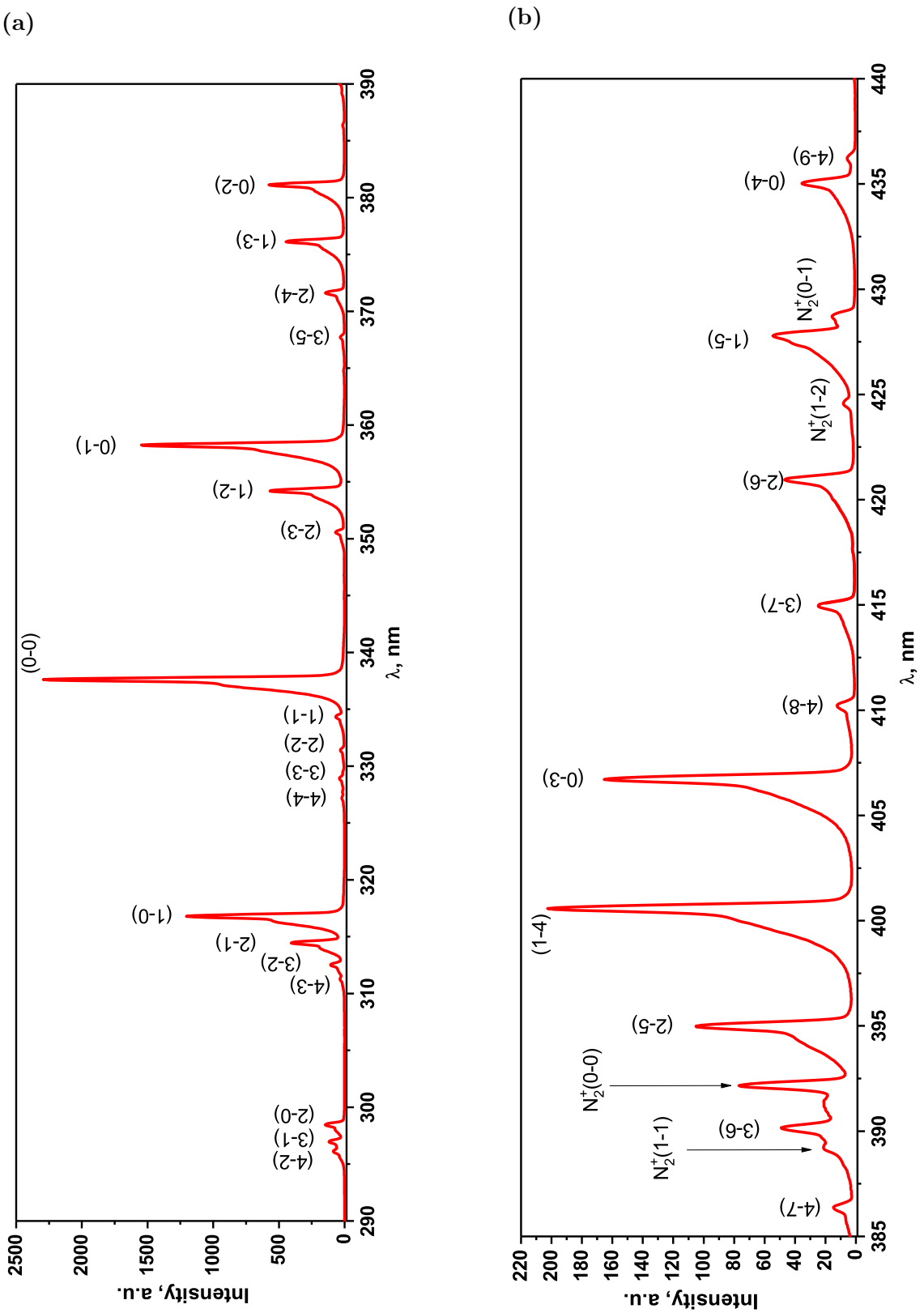

Figure 4.16 – Typical spectrum of the nanosecond capillary discharge in wavelength range (a) 290-390 nm, (b) 385-440 nm. For notations see text. The signal is collected during the first pulse, synthetic air, 27 mbar, $I_{tr} = 65$ A.

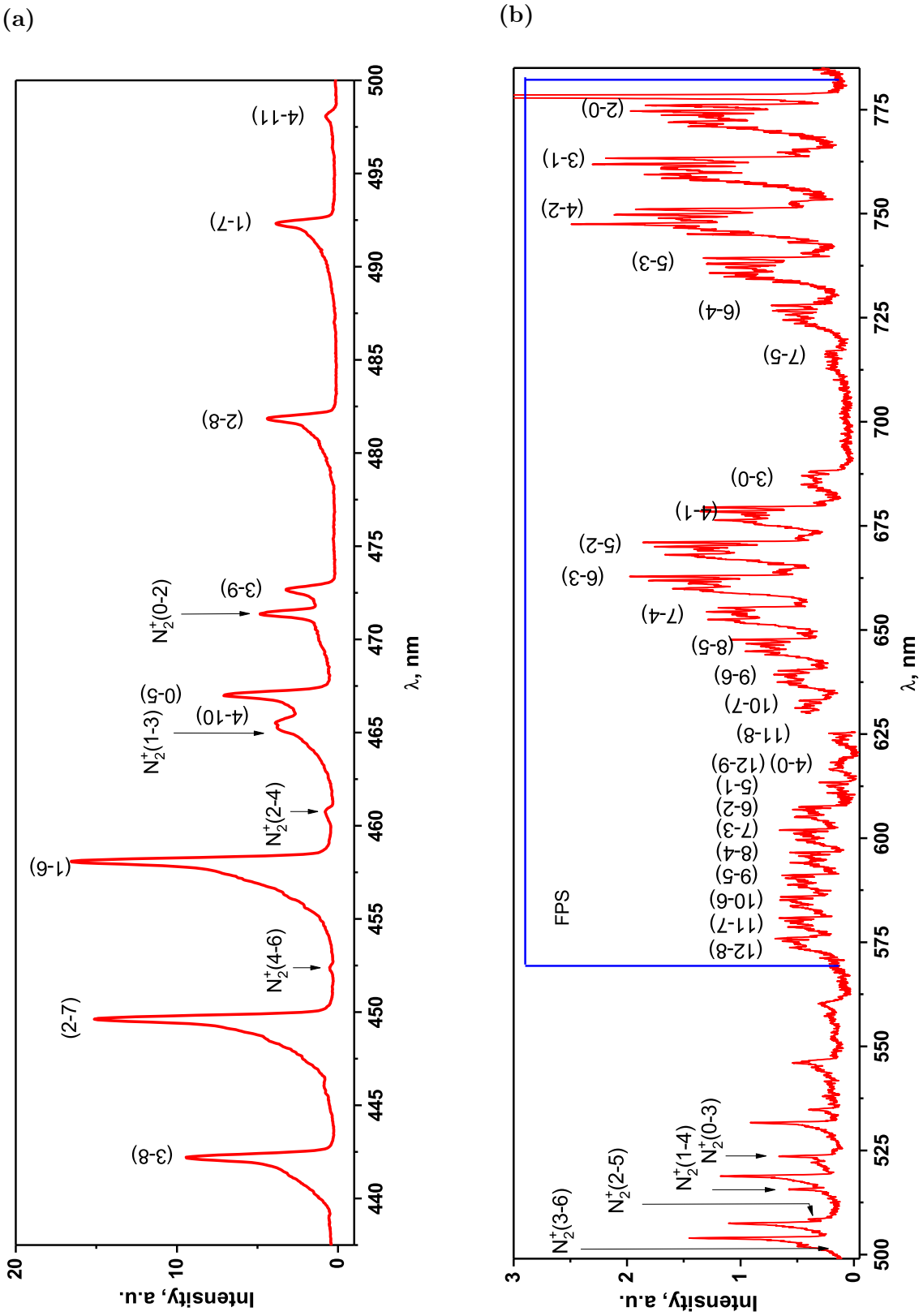

Figure 4.17 – Typical spectrum of the nanosecond capillary discharge in wavelength range (a) 440-500 nm, (b) 500-780 nm. For notations see text. The signal is collected during the first pulse, synthetic air, 27 mbar, $I_{tr} = 65$ A.

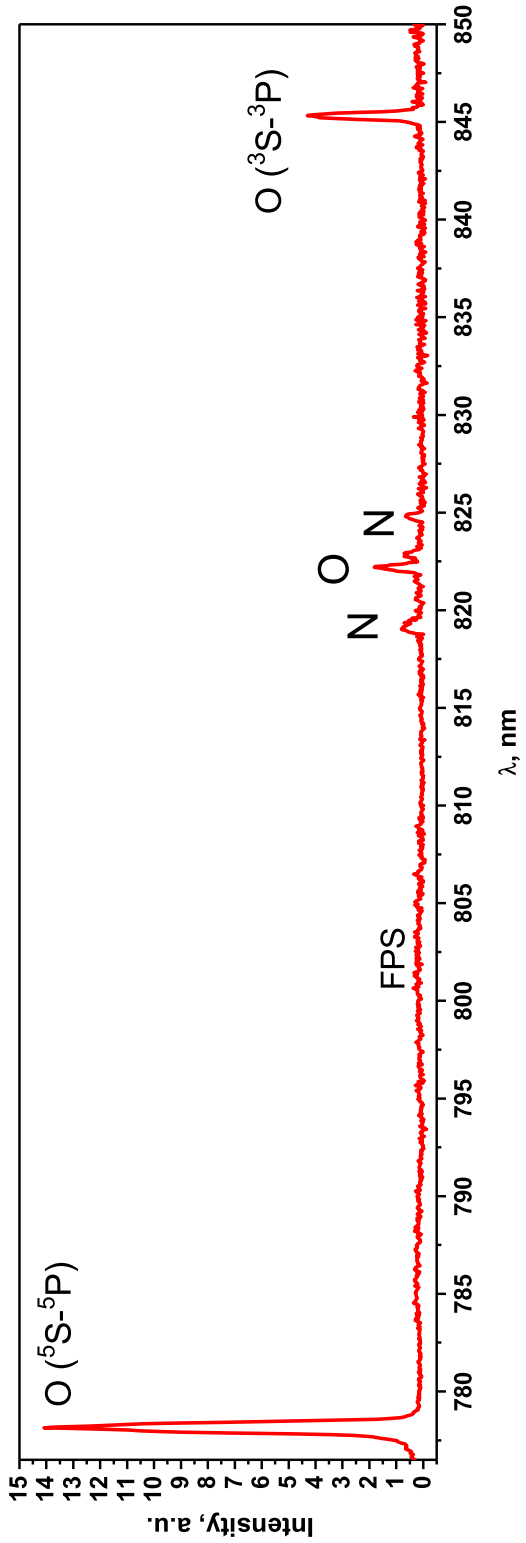

Figure 4.18 – Typical spectrum of the nanosecond capillary discharge in wavelength range 767-850 nm. For notations see text. The signal is collected during the first pulse, synthetic air, 27 mbar, $I_{tr} = 65$ A.

The spectra are corrected according to the spectral sensitivity of the combination of the spectrometer Acton SP-2500i with 600 l/mm grating and the ICCD camera PI-MAX 4 1024i, see Fig. 3.6(c), and the sensitivity of the 400 nm long-pass colored glass filter FGL400 (Thorlabs) used to avoid the second order of diffraction in measurements at wavelengths higher than 400 nm. The matching of the sensitivity levels of two parts of the spectrum (measured with and without the filter) was controlled by superimposition of the spectra overlapping at region 400-420 nm. It should be noted that intensity scales are different in the plots since the intensities of the transitions varies significantly.

The spectrum of the optical emission of the nanosecond capillary discharge in synthetic air at $P = 27$ mbar is presented in Fig. 4.16, Fig. 4.17 and Fig. 4.18. In this case, the emission of exited atomic oxygen and atomic nitrogen (denoted as O and N, respectively) is observed besides SPS, FPS and FPS nitrogen bands.

One can see that the emission of SPS dominates in the spectrum of the light collected during the entire discharge pulse (the camera gate is 60 ns). The highest amplitude of the signal corresponding to the SPS(0-0) transition is about 1080 a.u., while the highest amplitude corresponding to the FNS(0-0) transition is about 34 a.u. However, even this low intensity is can be detected and analyzed. This provides a possibility to use the emission of the transitions to measure the electric field value.

The main idea, as it was mentioned in Chapter 1, is the following. The rates of the population by electron impact $Y(x,t)$ defined as

$$Y(x,t) = \frac{\partial I}{\partial t} + k_q[\mathrm{N_2}]\mathrm{I} + \frac{\mathrm{I}}{\tau}, \tag{4.12}$$

where I is the intensity of the transition, k_q is the quenching rate constant, τ is the lifetime of the energetic level, $[\mathrm{N_2}]$ is the background gas density, are calculated based on the experimental results for FNS and SPS. Following [74] it is assumed that there is no self-absorption and the densities of the excited states are proportional to the intensities of corresponding optical transitions. The reduced electric field value is calculated based on the equation

$$\frac{Y_B(x,t)}{Y_C(x,t)} = \frac{k^B(E/N)}{k^C(E/N)}, \tag{4.13}$$

where $k^B(E/N)$ and $k^C(E/N)$ are the rate constants of the excitation by the electron impact for the $\mathrm{N_2^+}(\mathrm{B^2\Sigma_u^+}, v = 0)$ and $\mathrm{N_2}(\mathrm{C^3\Pi_u}, v = 0)$ states, respectively. The ratio between the rate constants $k^B(E/N)$ and $k^C(E/N)$ as function of E/N calculated using BOLSIG+ [3] software is presented in Fig. 4.19. The cross-sections were taken from [108]. One can see that high $k^B(E/N)/k^C(E/N)$ corresponds to high reduced electric field.

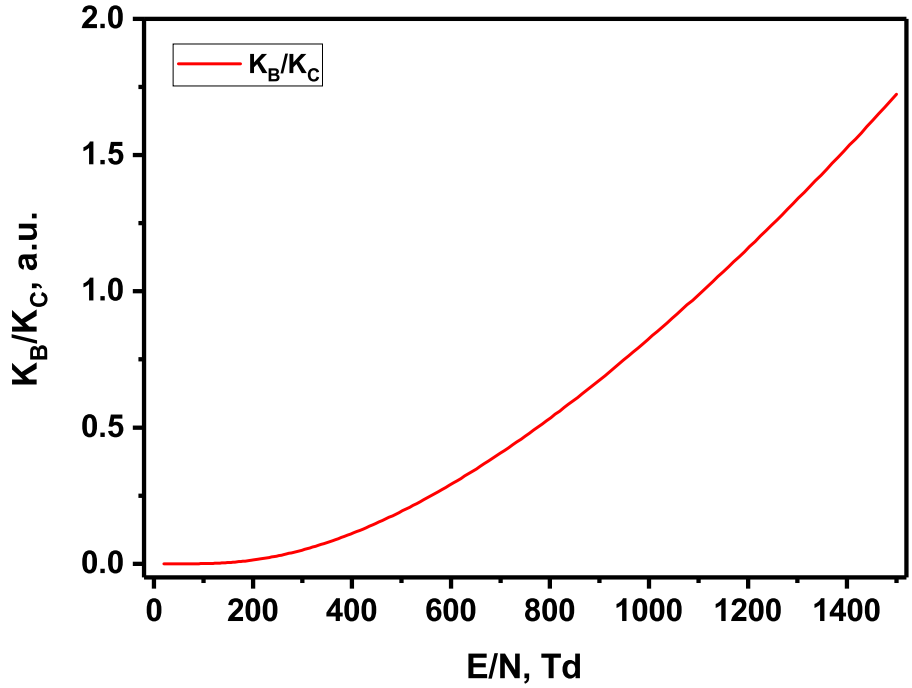

Figure 4.19 – The ratio between the rate constants of the excitation by the electron impact for the $N_2^+(B^2\Sigma_u^+, v = 0)$ and $N_2(C^3\Pi_u, v = 0)$ states as function of E/N calculated using BOLSIG+ [3] software.

There is another technique of reduced electric field measurements [101,102] using spectral measurements. In [101, 102] the ratios between intensities of the SPS(2-5), FNS(0-0) and SPS(0-0) bands were experimentally obtained as a function of the reduced electric field using non-self-sustaining discharge. The following relations were obtained [101, 102]:

$$R_{391/394}\left(\frac{E}{N}, N_0\right) = 46exp\left[-89\left(\frac{E}{N}\right)^{-0.5}\right], \tag{4.14}$$

$$R_{394/337}\left(\frac{E}{N}, N_0\right) = 0.065exp\left[-402\left(\frac{E}{N}\right)^{-1.5}\right], \tag{4.15}$$

$$R_{391/337}\left(\frac{E}{N}, N_0\right) = R_{391/394}\left(\frac{E}{N}, N_0\right) \cdot R_{394/337}\left(\frac{E}{N}, N_0\right), \tag{4.16}$$

where $R_{391/394}$ is the ratio between intensities of the FNS(0-0) and SPS(2-5) bands, $R_{394/337}$ is the ratio between intensities of the SPS(2-5) and SPS(0-0) bands, $R_{391/337}$ is the ratio between intensities of the FNS(0-0) and SPS(0-0) bands, N_0 is gas density at standard conditions (P = 100 kPa and T = 273 K). To use the formulas at conditions different from the standard ones the following equation was introduced

$$R_{i/j}\left(\frac{E}{N}, N\right) = R_{i/j}\left(\frac{E}{N}, N_0\right)\frac{g_i(N)g_j(N_0)}{g_i(N_0)g_j(N)}, \tag{4.17}$$

where i and j denote chosen transitions, and

$$g_i(N) = \frac{1}{1 + \tau_0^i N\left(\sum\limits_l n_l k_{ql}^i\right)}, \tag{4.18}$$

where τ_0^i is the radiative lifetime of the upper state of the transition i, l is the component with mole fraction n_l leading to the quenching of the upper state of the transition i with rate constant k_{ql}^i. Since the ratios (4.14)-(4.15) were obtained for non-self-sustaining stationary discharge, this technique can be applied to the nanosecond discharge for estimations of the reduced electric field value only at time instant when emission from excited species reach the local maximum, i.e. when the time derivative of emission are equal to zero. The results a this one particular time instant can be compared with the method using the ratio (4.13).

To obtain temporal electric field profile, the time-resolved spectroscopic measurements of the SPS(2-5), FNS(0-0) and SPS(0-0) transitions are required. In the present Thesis the measurements were performed for the first 55 ns of the first discharge pulse with 1 ns time resolution. The spectrum corresponding to the first nanosecond is presented in Fig. 4.20.

It is seen that during first nanosecond of the discharge, the intensity of the FNS(0-0) transition is much higher than the intensity of the SPS(2-5) transition in contrast to Fig. 4.14(b), where the signal was accumulated during the entire discharge pulse. The intensity of the FNS(0-0) transition even dominates the intensity of the SPS(0-0) transition in the beginning of the discharge pulse, see Fig. 4.21. It should be noted one more time, that in Fig. 4.14, where the spectrum collected during 60 ns is presented, the intensity of the SPS(0-0) transition is 30 times higher than the intensity of the FNS(0-0) transition.

One can see that the amplitudes of the FNS(0-0) and SPS(0-0) transitions become comparable after 3 ns. After 4 ns the amplitude of the SPS(0-0) transition is much higher than one of the FNS(0-0) transition. If it is assumed that both $N_2(C^3\Pi_u)$ state (11.03 eV) and $N_2^+(B^2\Sigma_u^+)$ state (18.75 eV) are populated by direct electron impact from the ground state of molecular nitrogen, the high ratios $R_{391/394}$ and $R_{391/337}$ indicates that E/N is rather high.

The spectra of the FNS(0-0) and SPS(2-5) bands at time instants 1-55 ns are presented in Fig. 4.22, Fig. 4.23. One can see that amplitude of the FNS(0-0) transition increases first two nanoseconds, after it decreases before 6 ns and increases again after. It is also seen that emission of the FNS(0-0) transition dominates the one of the SPS(2-5) transition first ten nanoseconds, see Fig. 4.22(a) and Fig. 4.22(b).

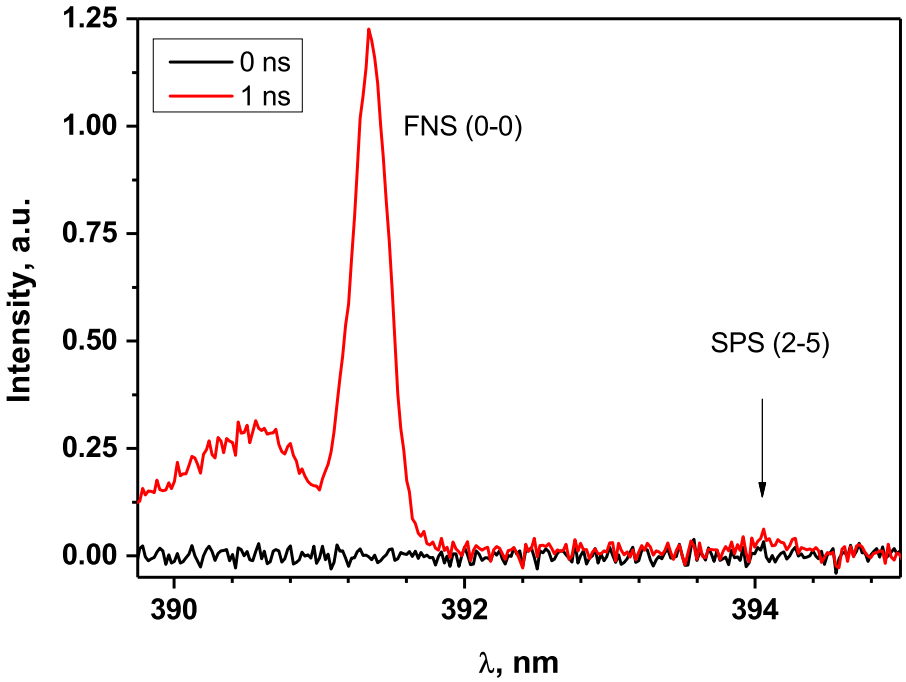

Figure 4.20 – SPS(2-5) and FNS(0-0) transitions during the first nanosecond of the discharge (red curve). The signal corresponding to the one nanosecond before the discharge (noise) is given for comparison (black curve). First pulse, pure nitrogen, 27 mbar, $I_{tr} = 65$ A.

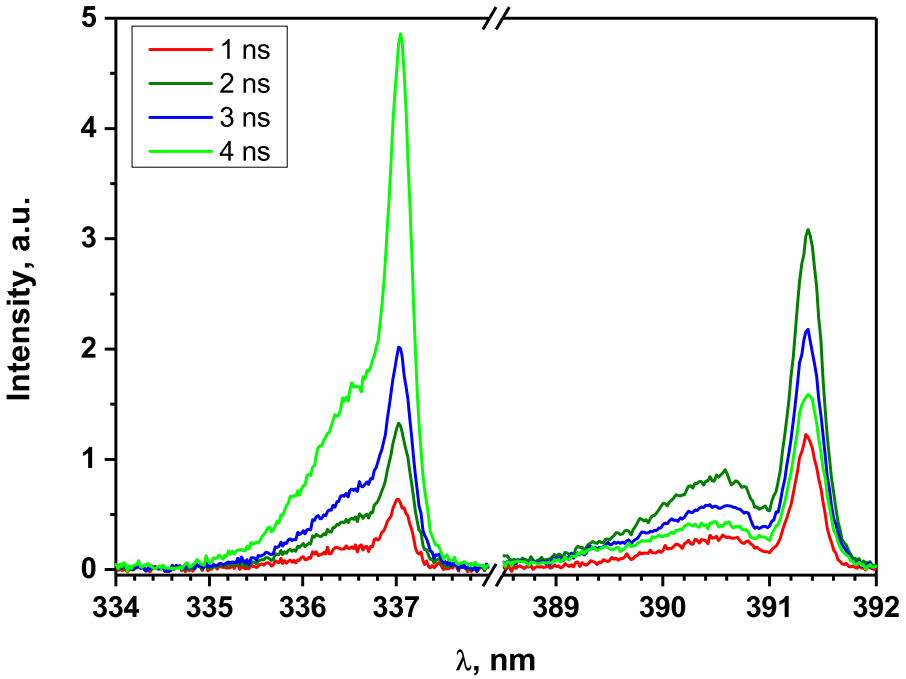

Figure 4.21 – SPS(0-0) and FNS(0-0) transitions during first four nanoseconds of the discharge. First pulse, pure nitrogen, 27 mbar, $I_{tr} = 65$ A.

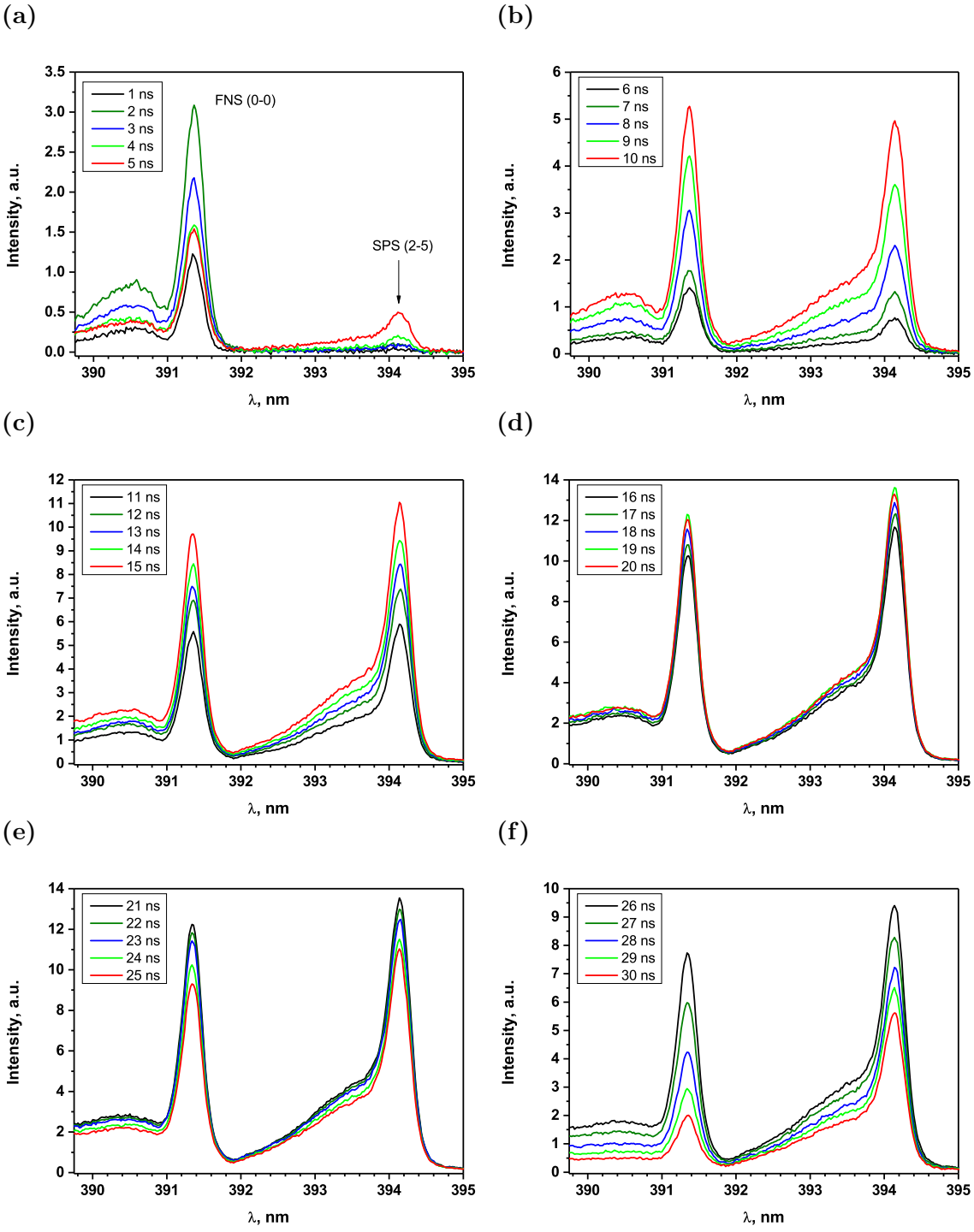

Figure 4.22 – The SPS(2-5) and FNS(0-0) transitions during time instants 1-30 ns. First pulse, pure nitrogen, 27 mbar, $I_{tr} = 65$ A.

Only at 10-11 ns the emission of the FNS(0-0) and SPS(2-5) bands become comparable. Then, the signals increase synchronously with almost constant ratio before 21 ns, see Fig. 4.22(c) and Fig. 4.22(d). Starting from 21 ns the decay of the both bands is observed. The emission of the FNS(0-0) band decays faster than the emis-

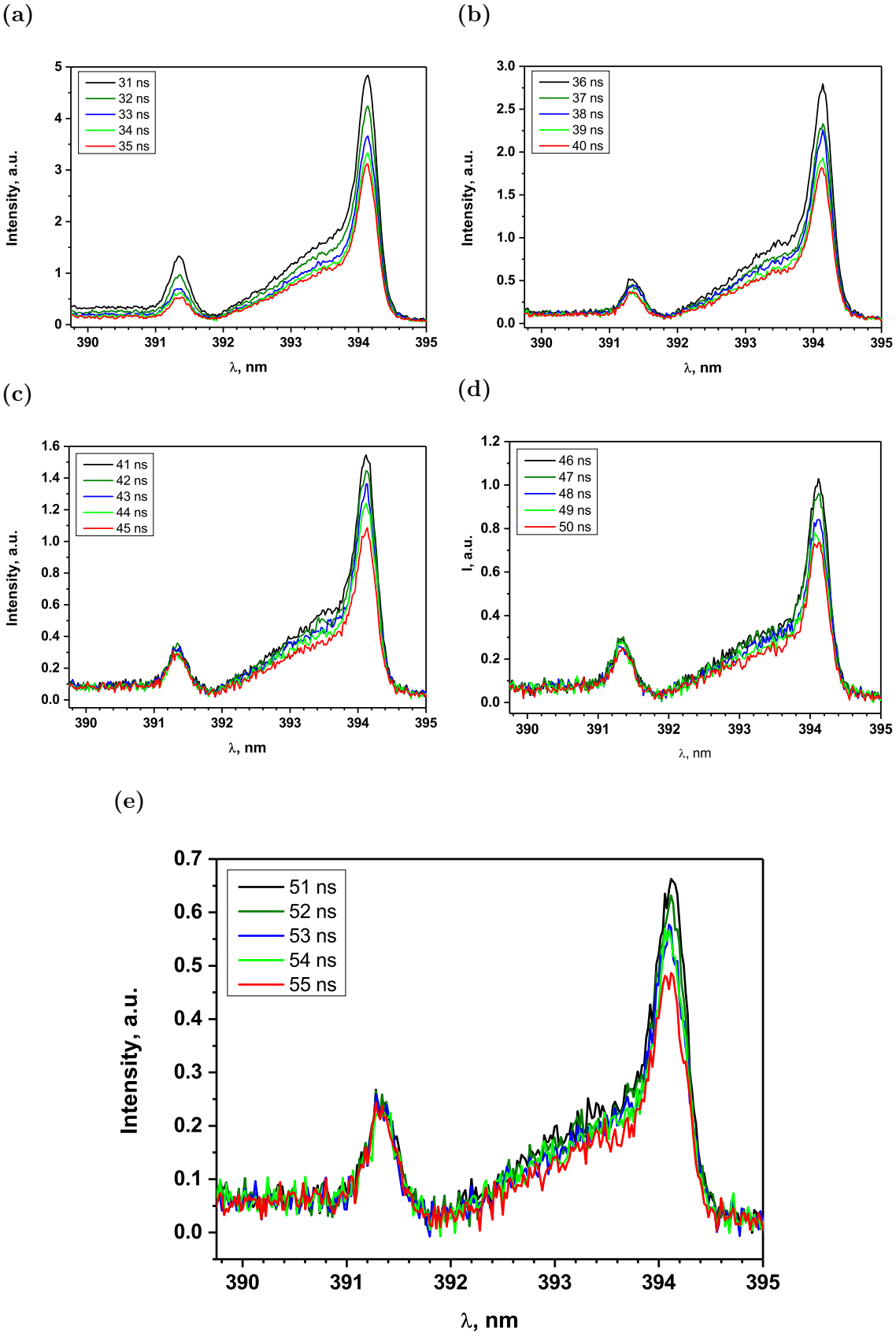

Figure 4.23 – The SPS(2-5) and FNS(0-0) transitions during time instants 31-55 ns. First pulse, pure nitrogen, 27 mbar, $I_{tr} = 65$ A.

sion of the SPS(2-5) band, see Fig. 4.22(f), Fig. 4.23(a) and Fig. 4.23(b). However, at 40 ns decay of the FNS(0-0) transition slows down dramatically, while the decay of the SPS(2-5) transition is still observed, see Fig. 4.23(c), Fig. 4.23(d) and Fig. 4.23(e).

Above the amplitudes of the signals were discussed. To obtain the value of the electric field using the relations (4.14) and (4.16) the ratio of the band intensities is required. It is not possible to obtain the intensities of the FNS(0-0) and SPS(2-5) bands by the direct integration of the spectrum over the wavelength, since the bands are overlapped. Thus, an additional procedure is required. To obtain the intensities, each band was fitted by SPECAIR software [54] separately. To fit the FNS(0-0) transition the spectra unaffected by the SPS(2-5) band were used, see Fig. 4.20 and Fig. 4.22(a), where the intensity of the SPS(2-5) band is low. To fit the SPS(2-5) transition any spectrum with its high amplitude can be used, since a significant part of the band is at higher wavelengths than the FNS(0-0) transition. The synthetic spectra were integrated to obtain intensities I^0_{391} and I^0_{394} of the FNS(0-0) and SPS(2-5) transitions with unit amplitude of the band head. Thus, the intensity $I_i(t)$ of the transition i at time instant t can be calculated as

$$I_i(t) = I^0_i \cdot A_i(t), \tag{4.19}$$

where $A_i(t)$ is the amplitude of the band head. It is valid, since during the discharge pulse the spectra of the bands have the fixed shapes. It was checked by the normalization of the spectra to unit at different time instants separately for the FNS(0-0) and SPS(2-5) bands.

For the SPS(0-0) and SPS(2-5) transitions, the values of the amplitude can be obtained directly from the spectrum. Since the band of the FNS(0-0) transition is overlapped with the tail of the SPS(2-5) band, the experimentally measured amplitude of the band head $A^{exp}_{391}(t)$ should be corrected by the amplitude $A^{\lambda=391}_{394}(t)$ of the SPS(2-5) band at wavelength corresponding to the band head of the FNS(0-0) transition:

$$A_{391}(t) = A^{exp}_{391}(t) - A^{\lambda=391}_{394}(t). \tag{4.20}$$

The results of the intensities measurements are presented in Fig. 4.24. It is seen that despite the fact that the maximum intensity of the SPS(0-0) transition is 20 times higher than the maximum intensity of the FNS(0-0) transition, the intensity of the FNS(0-0) transition dominates in the beginning of the discharge. Also, it is seen that decay of the upper state of the FNS(0-0) transition ($N_2^+(B^2\Sigma_u^+, v' = 0)$ state) slows down in the late afterglow significantly and becomes even slower (effective life time is about 28 ns) than the decay predicted theoretically based on the quenching

rate constants measured in [90] (effective life time is 6.4 ns at 27 mbar). This indicates that an additional population of the $N_2^+(B^2\Sigma_u^+, v' = 0)$ state takes place in the afterglow. The high density of the electrons and sufficient electron temperature are required to provide population of the $N_2^+(B^2\Sigma_u^+, v' = 0)$ state. The electron density in the afterglow will be measured and discussed in Chapter 6. The electron temperature in the afterglow will be discussed in Chapter 7. The slowing down of the decay of the $N_2^+(B^2\Sigma_u^+, v' = 0)$ state due to additional population indicates a deviation from classical plasma kinetics.

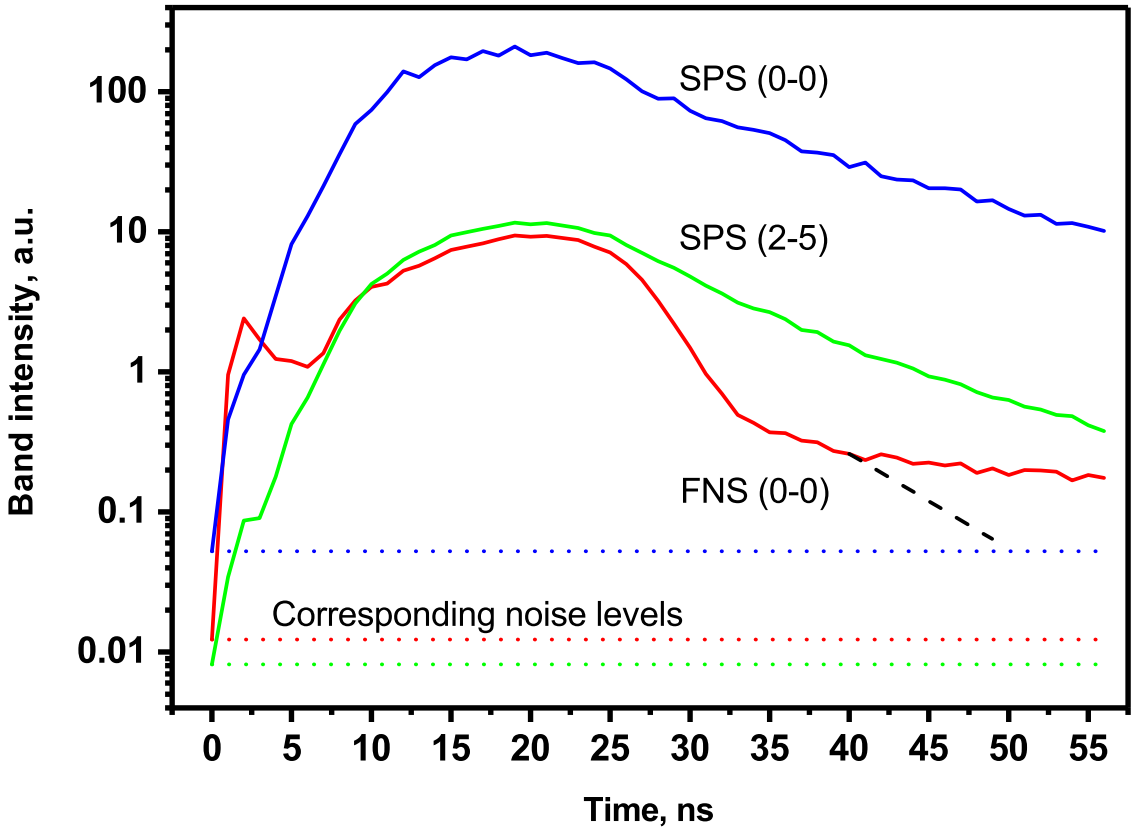

Figure 4.24 – The intensities of the SPS(0-0), FNS(0-0) and SPS(2-5) transitions during time instants 1-55 ns. The dash line corresponds to the decay of the $N_2^+(B^2\Sigma_u^+, v' = 0)$ state calculated based on the quenching rate constants measured in [90]. The horizontal dot lines indicate the corresponding noise levels defined as the signal intensity at 0 ns. First pulse, pure nitrogen, 27 mbar, $I_{tr} = 65$ A.

In this case, the spectroscopic method of the electric field measurements, (4.12) and (4.13), should give the electric field value different from the value measured by capacitive probe even after the FIW propagation, when discharge gap is closed, and the electric field is longitudinal. However, the significant changes in plasma kinetics are clearly seen even from the rates of the population by electron impact $Y_B(x, t)$

and $Y_C(x,t)$ calculated based on data from Fig. 4.24 using (4.12), see Fig. 4.25. The negative value of $Y_C(x,t)$ is seen starting from 20 ns, while $Y_B(x,t)$ reaches negative value at FIW stage. The negative values of $Y_B(x,t)$ and $Y_C(x,t)$ indicates that there is additional depopulation mechanism of the considered excited levels, which is not taken into account in classical plasma kinetics. The nature of this depopulation will be discussed in details in Chapter 7. Additional process leads to inapplicability of the spectroscopic technique of reduced electric field measurements, (4.12) and (4.13), at the considered conditions of high specific energy deposition at high reduced electric fields.

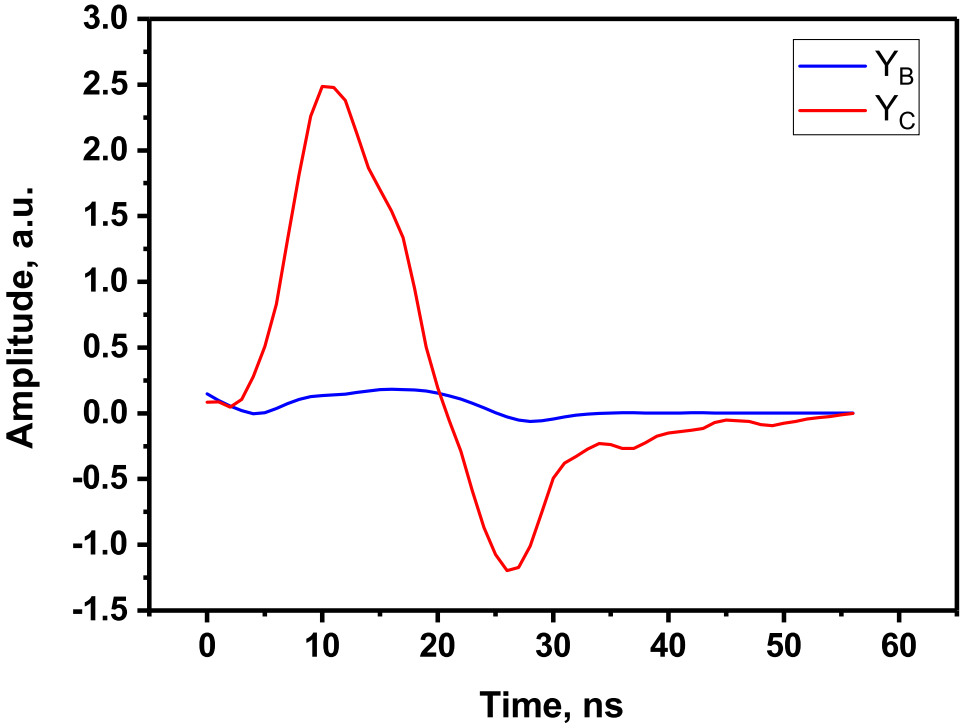

Figure 4.25 – The rates of the population by electron impact $Y_B(x,t)$ and $Y_C(x,t)$ of the $N_2^+(B^2\Sigma_u^+, v=0)$ and $N_2(C^3\Pi_u, v=0)$ states, respectively. First pulse, pure nitrogen, 27 mbar, $I_{tr}=65$ A.

To check applicability of the second spectroscopic method of the electric field measurements based on the ratios $R_{391/394}$ and $R_{391/337}$, they were calculated, using the electric field profile experimentally measured by the capacitive probe (CP), see Fig. 4.7, and the formulas (4.14)-(4.18). The ratios calculated based on the experimentally measured E/N profile are compared with the ratios of the emission intensities measured experimentally by OES, see Fig. 4.24. The results of the comparison are presented in Fig. 4.26, where the region of interest with time derivatives of the emission intensities are close to zero, when the method can be applied, is denoted by green rectangle.

(a)

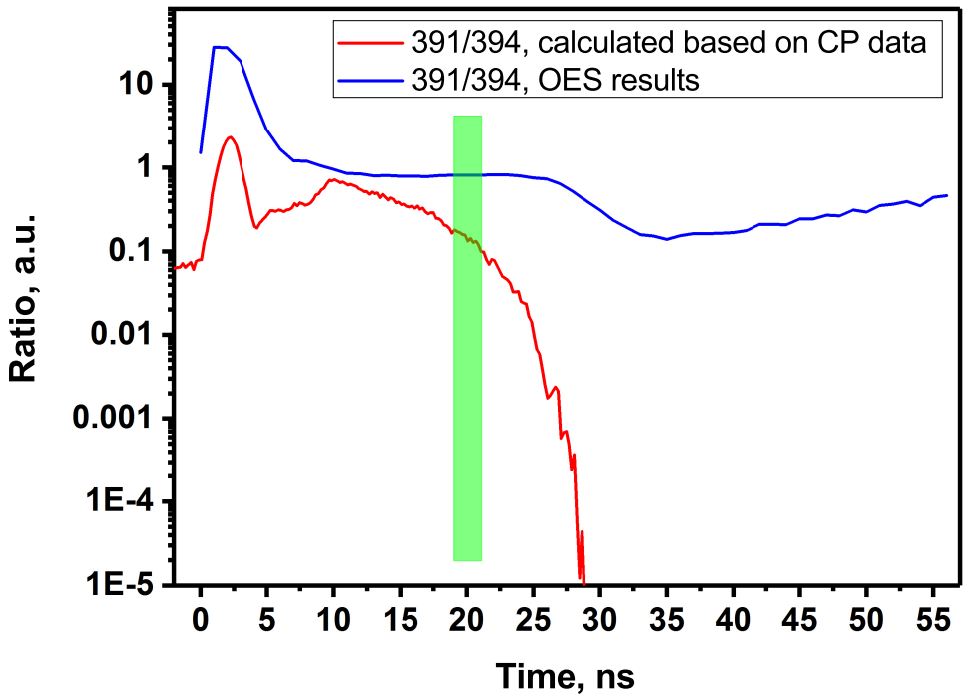

(b)

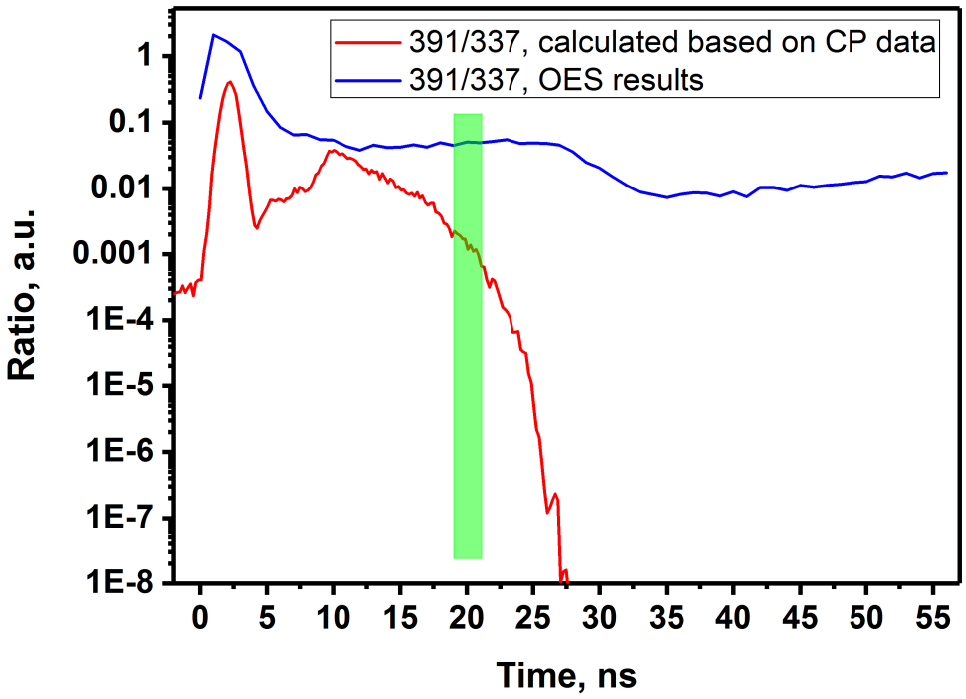

Figure 4.26 – Calculated from E/N profile measured by capacitive probe and measured experimentally by OES ratios of the intensities of the (a) FNS(0-0) and SPS(2-5) transitions, (b) FNS(0-0) and SPS(0-0) transitions. First pulse, pure nitrogen, 27 mbar, $I_{tr} = 65$ A.

One can see that the calculated ratios $R_{391/394}$ and $R_{391/337}$ do not agree with the experimental results. The experimentally measured ratios (OES) are much higher than the ones calculated using the formulas (4.14)-(4.18) and E/N profile measured by CP. The difference is significant: about 43 times for $R_{391/337}$ and about 6 times for $R_{391/394}$ at 20 ns, see Fig. 4.26. It shows that the spectroscopic method [101,102] can not be used at the conditions of the nanosecond capillary discharge with high specific energy deposition at high reduced electric field even at zero time derivatives of the emission intensities. As it was mentioned above, the relations (4.14)-(4.16) were obtained experimentally using non-self-sustaining discharge. The discharge at these conditions is described by the classical plasma kinetics. The deviation from the predictions of the spectroscopic method, see Fig. 4.26, shows one more time that plasma kinetics changes dramatically in the considered nanosecond capillary discharge. Overestimated ratio between intensities of the FNS and the SPS can be caused either by additional population of the $N_2^+(B^2\Sigma_u^+, v' = 0)$ state or by the additional depopulation of the $N_2(C^3\Pi_u)$ state. The additional population of the $N_2^+(B^2\Sigma_u^+, v' = 0)$ state in the afterglow was shown above, see Fig. 4.24. The additional depopulation of the considered excited states was also indicated above as reason of negative values of $Y_B(x,t)$ and $Y_C(x,t)$. Thus, both spectroscopic techniques can not be used at the considered conditions of high specific energy deposition at high reduced electric fields.

Since the emission of the second positive system of molecular nitrogen will be used for the gas temperature measurements during the fast gas heating studies in Chapter 9, further corresponding spectral data are presented. In Chapter 1 it was mentioned that the $N_2(C^3\Pi_u)$ state can be produced not by the direct electron impact, but also by the pooling reaction between metastable states of molecular nitrogen [55,56]

$$N_2(A^3\Sigma_u^+, v) + N_2(A^3\Sigma_u^+, v') \rightarrow N_2(C^3\Pi_u) + N_2. \quad (4.21)$$

Thus, it is required to check that the emission of the $N_2(C^3\Pi_u)$ state in the discharge pulses is not affected by the pooling reaction. The results of the measurements of the intensity of the SPS(0-0) band in the main discharge pulses and between them are presented in Fig. 4.27. One can see that emission intensity before the main pulses is about 220 times less than emission in the second discharge pulse and is about 95 times less than emission in the third discharge pulse. In oxygen containing mixtures the emission intensity before the main pulses are significantly suppressed due to efficient quenching of the excited states participating in the pooling reaction, $N_2(A^3\Sigma_u^+, v')$, and the $N_2(C^3\Pi_u)$ state as well, by molecular oxygen. Thus, the influence of the pooling reaction on the rotational structure of the SPS(0-0) band measured in the discharge pulses can be neglected in N_2 and N_2:O_2 mixtures.

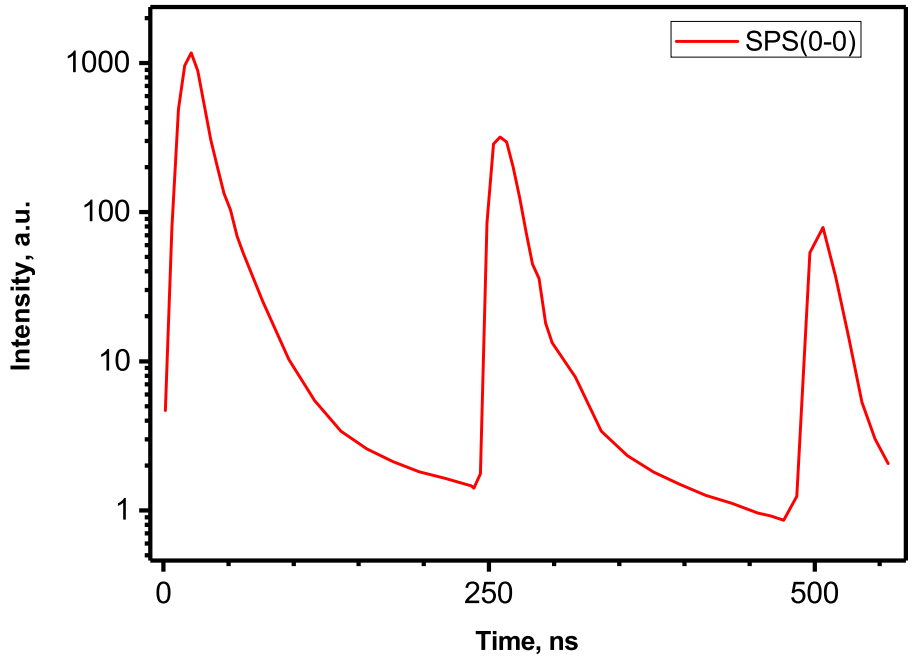

Figure 4.27 – The intensity of the SPS(0-0) band in the main discharge pulses and between them. Pure nitrogen, 27 mbar, $I_{tr} = 65$ A in the first pulse.

The temporal evolution of the intensity of the first positive system (FPS) of molecular nitrogen, $N_2(B^3\Pi_g, v') \rightarrow N_2(A^3\Sigma_u^+, v'')$, will also be required for the fast gas heating studies. The intensity of the FPS was obtained at each time instant by integration of the spectrum in the corresponding wavelength range denoted by blue frame in Fig. 4.15(b). The measured transitions correspond to the sequences of the electronic-vibrational transitions with $\Delta v = 2$, $\Delta v = 3$ and $\Delta v = 4$. The results are presented in Fig. 4.28. The decay times of the $N_2(B^3\Pi_g)$ state are determined for the three main discharge pulses and in the late afterglow of the first and the second pulses. In the late afterglow the decay of the $N_2(B^3\Pi_g, v')$ state corresponds to the decay with time 147 ns caused by the radiative decay with $1/\tau_0 = 1.5 \cdot 10^5$ s^{-1} [109] and the quenching of the $N_2(B^3\Pi_g)$ state by molecular nitrogen

$$N_2(B^3\Pi_g) + N_2 \rightarrow N_2(A^3\Sigma_u^+, v) + N_2(v) \qquad (4.22)$$

with the rate constant $k_{(4.22)} = 10^{-11}$ cm^{3}s^{-1} [27]. In the early afterglow the characteristic decay time is much shorter, which means that there is additional process of the depopulation of the $N_2(B^3\Pi_g)$ state. This will be discussed additionally in Chapter 7, where the quenching of the excited species is discussed, and in Chapter 9, where the fast gas heating is studied. The fast decay of the $N_2(B^3\Pi_g, v')$ state confirms one more time that the plasma kinetics changes at the present conditions.

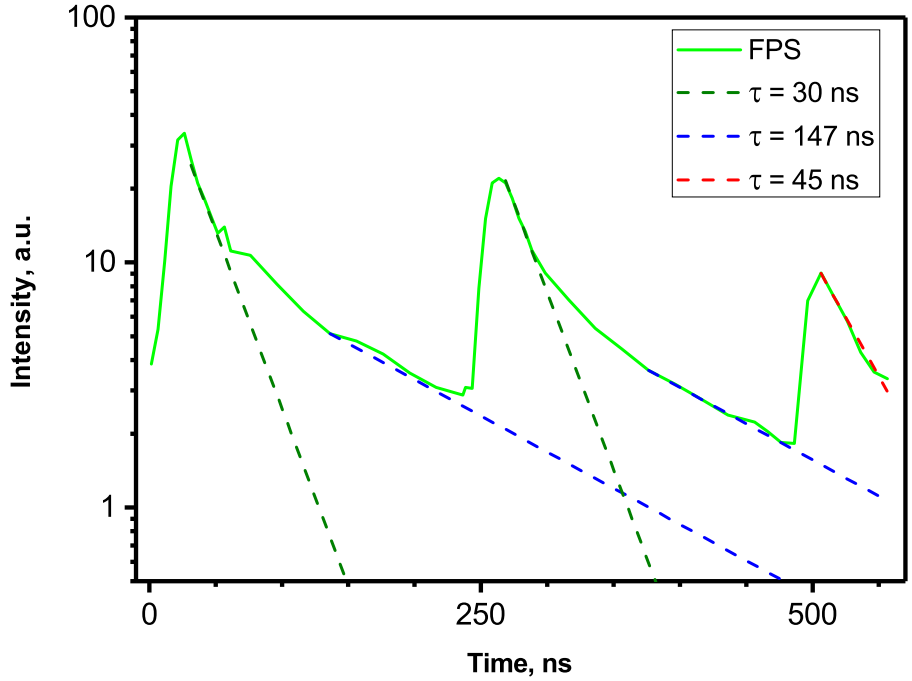

Figure 4.28 – The intensity of the FPS in the main discharge pulses and between them. The exponential decays with different characteristic lifetimes τ are given for comparison. Pure nitrogen, 27 mbar, $I_{tr} = 65$ A in the first pulse.

The temporal evolution of the intensity of the first positive system (FPS) of molecular nitrogen in the discharge in synthetic air is presented in Fig. 4.29.

(a) **(b)**

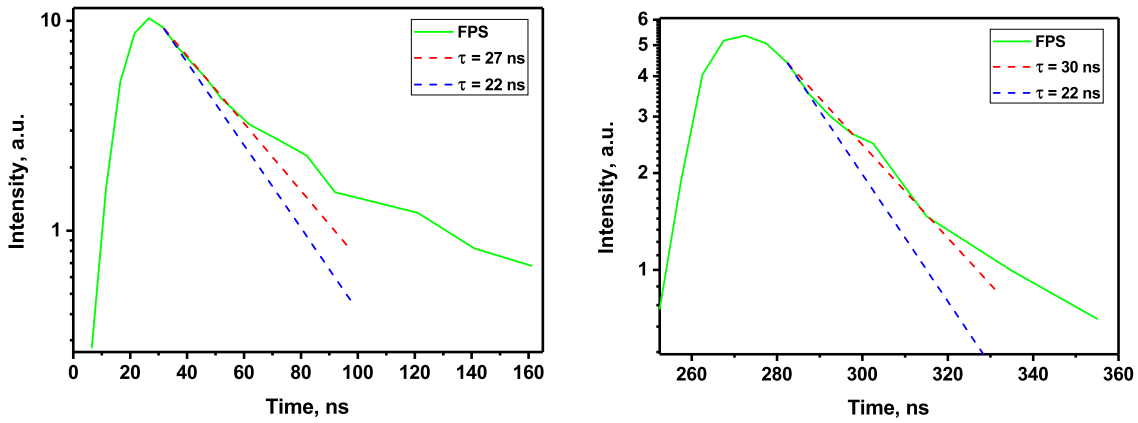

Figure 4.29 – The intensity of the FPS in the first (a) and the second (b) discharge pulses. The exponential decays with different characteristic lifetimes τ are given for comparison. Synthetic air , 27 mbar, $I_{tr} = 65$ A in the first pulse.

The lifetime of the $N_2(B^3\Pi_g)$ state in both pulses is close to the effective lifetime (22 ns) determined by radiative decay, quenching by molecular nitrogen (4.22) and quenching by molecular oxygen

$$N_2(B^3\Pi_g) + O_2 \rightarrow N_2(v) + 2O(^3P) \tag{4.23}$$

with rate constant $k_{(4.23)} = 3 \cdot 10^{-10}$ cm^{3}s^{-1} [109]. The slight difference is caused by the population of the $N_2(B^3\Pi_g)$ state due to radiative decay and quenching of the upper states (for example, the $N_2(C^3\Pi_u)$ state) to the $N_2(B^3\Pi_g)$ state. From comparison of Fig. 4.28 and Fig. 4.29 it can be concluded that additional process of the depopulation of the $N_2(B^3\Pi_g)$ state observed in the discharge in pure nitrogen is absent or significantly suppressed at presence of the molecular oxygen.

The results of the spectral measurements can be used to estimate the evolution of the relative population of the excited species from pulse to pulse. Knowledge of the relative population of the excited species can be important for correct interpretation of the results of the gas temperature measurements based on the analysis of the rotational structure of the molecular bands. For example, if the gas temperature is measured based on the rotational temperature of the $N_2(C^3\Pi_u)$ state, it is important to know, from which state the $N_2(C^3\Pi_u)$ state is populated. If the density of the $N_2(B^3\Pi_g)$ state, for example, is rather high and $E/N \leq 100$ Td, the population of the $N_2(C^3\Pi_u)$ state from the $N_2(B^3\Pi_g)$ state can be significant [110]. Using the results presented in Fig. 4.27 and Fig. 4.28, it is possible to trace the trend of the relative population of the $N_2(C^3\Pi_u)$ and $N_2(B^3\Pi_g)$ states. If there is no reabsorption, the intensity of the light $I_X(t)$ emitted by the excited specie X in transition $i \rightarrow j$ is proportional to the density of the excited specie $[X](t)$:

$$I_X(t) = A_{ij} \cdot [X](t), \tag{4.24}$$

where A_{ij} is the Einstein coefficient of the transition $i \rightarrow j$. Consequently,

$$[X] = \frac{I_X}{A_{ij}}. \tag{4.25}$$

The relation between the intensity of the SPS(0-0) band and the density of the $N_2(C^3\Pi_u, v = 0)$ state can be easily obtained by (4.25). However, for the $N_2(B^3\Pi_g)$ state it is not possible, since the intensity of the FPS measured in the experiments was obtained as the sum of the intensities of the transitions corresponding to the sequences of the electronic-vibrational transitions with $\Delta v = 2$, $\Delta v = 3$ and $\Delta v = 4$, totally 26 $(v' - v'')$ transitions, see Fig. 4.15(b). Each transition is characterized by its own Einstein coefficient [111] and its own intensity, which can not be determined precisely at low signals (compare the SPS(0-0) and the FPS in Fig. 4.14(a) and

Fig. 4.15(b), for example). Moreover, the ratio between the amplitudes of the different FPS($v' - v''$) transitions and their rotational structure change in time, because the vibrational and rotational temperatures evolve in time. Thus, even the "effective Einstein coefficient" can not be obtained, and (4.25) is not applicable for the FPS. However, the comparison of the intensities of the SPS(0-0) transition and the FPS can give a qualitative behavior of the relative populations of the $N_2(C^3\Pi_u, v = 0)$ and the $N_2(B^3\Pi_g)$ states from pulse to pulse. In Fig. 4.30 the ratio between the intensities of the SPS(0-0) transition and the FPS of molecular nitrogen is presented.

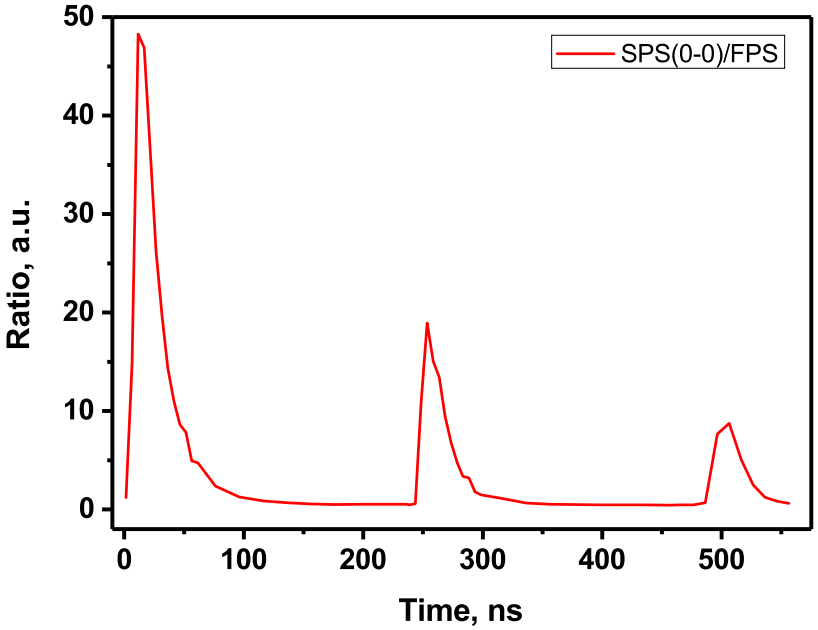

Figure 4.30 – The ratio of the intensities of the SPS(0-0) transition and the FPS in the main discharge pulses and between them. Pure nitrogen, 27 mbar, $I_{tr} = 65$ A in the first pulse.

This ratio does not correspond precisely to the ratio of the densities of the $N_2(C^3\Pi_u, v = 0)$ and $N_2(B^3\Pi_g)$ states, as it was shown above. Nevertheless, it is clearly seen that the density of the $N_2(B^3\Pi_g)$ state increases relatively the density of the $N_2(C^3\Pi_u, v = 0)$ state from pulse to pulse.

4.3 Conclusion

In this Chapter the main electric parameters of the discharge were determined. It was shown that the train of three high voltage pulses is applied on the discharge cell. The first main pulse is produced by the high voltage generator, and each of two other pulses is caused by the successive reflections of the high voltage pulse from the discharge cell and from the high voltage generator. The amplitudes, rise times and

durations of the pulses were determined by the back current shunt (BCS) technique. For the first pulse the amplitude is 9.3 kV, the rise time is 4 ns, the pulse width is 30 ns FWHM. The transmitted current parameters were measured as well. The synchronization of the incident, reflected and transmitted pulses were performed.

The longitudinal electric field temporal profiles were obtained by the capacitive probe (CP) technique and by BCSs. The synchronization of the electric field profile and incident, reflected and transmitted pulses was performed. It was shown that reduced electric field is high during the main energy deposition in all main discharge pulses: up to 350 Td in the first pulse, 275 Td in the second pulse and 175 Td in the third pulse.

Deposited energy was measured based on the BCS data. It was shown that specific deposited energy is high and depends mostly on the transmitted current value: about 0.9 eV/molecule at $I_{tr} = 85$ A and about 0.6 eV/molecule at $I_{tr} = 50$ A.

The analysis of the optical emission from the discharge showed that the second positive system (SPS) of molecular nitrogen dominates in the average emission of the discharge. However, it was demonstrated by the time resolved spectral measurements, that the first negative system (FNS) of the molecular nitrogen dominates in the beginning of the discharge. The analysis of the temporal behavior of SPS and FNS intensities showed that there is additional mechanism of depopulation of the excited species, that indicates that there is strong deviation of the discharge from the classical plasma kinetics. The abnormally fast decay of the first positive system (FPS) of molecular nitrogen was also observed in the early afterglow of the main discharge pulses in pure nitrogen. In the synthetic air this phenomenon is absent. Thus, it can be summarized that high values of the reduced electric field and specific deposited energy cause the plasma kinetics changes, as it was assumed.

Chapter 5

Description of the kinetic model

In Chapter 4 it was shown that nanosecond capillary discharge is characterized by a high value of the reduced electric field E/N and high specific energy deposition ω. This combination of high E/N and high ω is extremely interesting for plasma kinetics. At low E/N, the electronic excitation degree $\beta = N_{excited}/N$ is rather low, since the high energies of electrons are required for efficient electronic excitation [6, 112], see Fig. 1.2. The processes between the excited species are unlikely, since their rates are proportional to β^2 at least. At high E/N, the energy "threshold" can be overcome, but low ω means that β is still low. Only combination of high E/N and high ω provides rather high values of β and, consequently, high probability of interaction of electronically excited species between each other, which changes the plasma kinetics dramatically.

The efficient way to study plasma kinetics is numerical calculations. The simplest case is 0D kinetics, when there is no any spatial dimension, and all species densities are function of time only. In this case, there is no species/energy transport. This assumption implies that plasma is spatially uniform, all parameters are equal throughout the volume. However, as it was discussed in the Literature Review (Chapter 1), the non-uniform radial distribution of the electron density in the cross-section of the tube is quite common phenomenon for fast ionization waves and discharges in the thin tubes. It will be shown in Chapter 8 experimentally, that there are non-uniform radial distributions of excited species and electron density in the cross–section of the capillary tube used in the present work. To adequately describe plasma kinetics, the radial distribution of electrons and exited species must be taken into account. In this case it is required to introduce radius of the tube as a

spatial coordinate. It assumes 1D–approximation describing the values as functions of radius r over the cross–section of measurements at axial symmetry. The validity of suggested approximation for nanosecond capillary discharge is proved by the fact that radial gradients of the discharge parameters are much higher than the axial gradients in the direction between the electrodes [9].

The kinetic calculations were performed in 1D–approximation by co-supervisor of the present thesis Dr.Sc. Nikolay Popov. The transmitted current temporal profile is used as an input data. As it was mentioned above, at the early stage of the discharge, during the FIW propagation from the high–voltage to low–voltage electrode, current flowing through plasma can not be registered by BCS2 installed in the low-voltage cable, since this current closes to the metal screen by displacement current. To take this fact into account in the numerical calculations, the synthetic electric current for the first 10 ns was used. It was obtained as $U_{ref.vac}(t) - U_{ref}(t)$ taking into account the finite velocity of the FIW propagation.

The following main neutral species were considered by the model for nitrogen: $N_2(X^1\Sigma_g^+)$, $N_2(A^3\Sigma_u^+)$, $N_2(B^3\Pi_g)$, $N_2(W^3\Delta_u)$, $N_2(B'^3\Sigma_u^-)$, $N_2(C^3\Pi_u)$, $N_2(a'^1\Sigma_u^-)$, $N_2(a^1\Pi_g)$, $N(^4S)$, $N(^2D)$, $N(^2P)$. Three levels $N_2(B^3\Pi_g)$, $N_2(W^3\Delta_u)$ and $N_2(B'^3\Sigma_u^-)$ were considered and designated as a single $N_2(B)$ level. The following main neutral species were considered by the model for oxygen: $O_2(X^3\Sigma_g^-)$, $O_2(a^1\Delta_g)$, $O_2(b^1\Sigma_g^+)$, $O(^3P)$, $O(^1D)$, $O(^1S)$. The set of the reactions and the rate constants are available in [26, 110].

The $e-e$ processes were taken into account in the calculations, since at the end of the one of the main pulses or in low-amplitude diagnostic pulses, at relatively high electron densities and low electric fields, $E/N < 100$ Td, electron–electron collisions become important for EEDF formation, electron drift velocity and rates of excitation for considered electronically excited states. The following equation was solved for the electron density:

$$\frac{\partial N_e}{\partial t} = \frac{1}{r}\frac{\partial}{\partial r}(rD_a\frac{\partial N_e}{\partial r}) + N_e\nu_{ion} - Q_{rec} + Q_{as} - Q_{att} + Q_{det}. \qquad (5.1)$$

Here D_a is the ambipolar diffusion coefficient, ν_{ion} is the frequency of ionization by electron impact (a function of $E(t)/N$), Q_{rec} is the rate of electron–ion recombination, and Q_{as} describes additional production of electrons due to associative ionization, Q_{att} and Q_{det} are the rates of electron attachment and detachment, respectively. Similar balance equations have been written for positive N_2^+, N_3^+, N_4^+, O_2^+, $O_2^+{\cdot}N_2$, O_4^+, NO^+ and negative O^-, O_2^-, O_3^-, O_4^- ions. As far as the impurities in the system did not exceed 5.5 ppm, no other ions have been taken into account and kinetics was restricted by chemistry of pure nitrogen and oxygen. The density of excited species, ions and electrons were calculated in each time instant as a function of radius of the tube. The results of measurements of radial distribution

of excited species in the discharge were used to construct the initial radial distribution of the electron density, since it is assumed that during first nanoseconds of the discharge development the profile of excited species copies the distribution of the electron density. The measurements of the radial distribution of the excited species are discussed in details in Chapter 8.

Ionization and excitation rates were calculated for each time instant as a function of reduced electric field on the basis of the solution of the Boltzmann equation in a two–term approximation, see Chapter 1, using BOLSIG+ code [3] with the imported [4] cross–sections. It should be noted that the two–term approximation is valid [4, 5, 43] for the considered experimental conditions, because the reduced electric field in the region of significant energy input does not exceed a few hundreds of Td, see Chapter 4.

In Chapter 1 it was mentioned, see Fig. 1.16, that EEDF non-locality behind the wave front is possible at high E/N, especially, at positive polarity high voltage pulses. Since the local approximation is used, the estimations of the EEDF relaxation are required. The local approximation is valid, if the number of non-elastic collisions of electrons during a typical time of E/N change is much higher than unit:

$$\Theta = \nu_u \left(\frac{1}{E} \frac{dE}{dt} \right)^{-1} \gg 1, \tag{5.2}$$

where ν_u is the effective frequency of relaxation of energy of electrons. The value of ν_u can be estimated using BOLSIG+ software [3]. It gives $\nu_u/N \approx 2.5 \cdot 10^{-14}$ m^{3}s^{-1} or $\nu_u \approx 16.6$ ns^{-1} for $E/N \approx 650$ Td (FIW stage) and $\nu_u/N \approx 7.5 \cdot 10^{-15}$ m^{3}s^{-1} or $\nu_u \approx 5$ ns^{-1} for $E/N \approx 200$ Td (at the maximum of the electric current). The typical time of E/N change can be estimated using the temporal profile of E/N measured by the capacitive probe, see Fig. 4.7. It gives $\frac{1}{E}\frac{dE}{dt} = 0.315$ ns^{-1} for FIW front and $\frac{1}{E}\frac{dE}{dt} = 0.09$ ns^{-1} at the maximum of the electric current. Finally, one can obtain $\Theta_{FIW} \approx 53 \gg 1$ for FIW front and $\Theta_{I_{max}} \approx 56 \gg 1$ for the discharge stage at high current flowing. Thus, local approximation is valid for both stage of the discharge. It should be noted that real change of E/N in FIW can be faster than measured one, since the peak electric field in FIW front is not well resolved by the capacitive probe. However, the estimation showed that $\Theta_{FIW} \gg 1$ with large safety factor.

To verify the results of the calculation, the experimentally measured reduced electric field was compared with $E(t)/N$ dependence calculated using the equation

$$E(t) = \frac{I(t)}{2\pi e \int_0^R N_e(r,t)\mu_e(t) r dr}, \tag{5.3}$$

where $N_e(r)$ is the electron density, μ_e is the electron mobility (considered as a

function of reduced electric field E/N), R is internal radius of the discharge tube. The gas density N is assumed to be constant, since the time scale of considered processes (≈ 1.5 μs) is much less than a characteristic time of gas extension (≈ 40 μs for characteristic dimensions of the discharge cell), see Chapter 9. The calculated and measured electric field waveforms are presented in Fig. 5.1. Calculated electric field and measured one are in good agreement. This means that the kinetic model used in the calculations is valid.

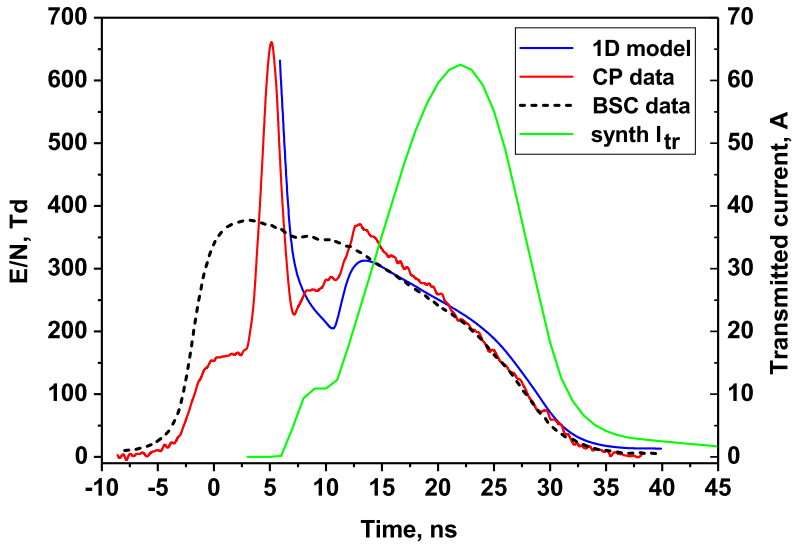

Figure 5.1 – Calculated electric field as a function of time and the synthetic electric current used as input data. Measured profile of the longitudinal electric field from Fig. 4.7 is given for comparison. First pulse (65 A), pure nitrogen, 27 mbar.

Using the validated kinetic model, it is possible to investigate the plasma not only qualitatively, but quantitatively. For example, comparison of the experimental results with the results of numerical calculations can be used for determination of the values of rate constants or energy effects of new reactions proposed in the present work. To do so one can perform calculations with different values of an adjustable parameter (value of the rate constant of new process, for example) until the results of the numerical results are in good agreement with the experiments. This method will be widely used in the present Thesis. Using the 1D model increases precision of such comparison, since the experiments usually provide values averaged over cross-section, and the results of averaging of calculated values with uniform distribution (0D) and with some radial profile (1D) can differ by a few times. Moreover, the processes involving two excited or charged particles, for example pooling reaction or electron-ion recombination, strongly depend on the densities of reagents and, thus, different distributions with the same average value give different total reaction rate.

The 1D numerical calculations based on validated kinetic scheme provide information about the plasma composition: the time evolution of the species densities and their radial distribution. The densities of the main species calculated numerically are presented in Fig. 5.2.

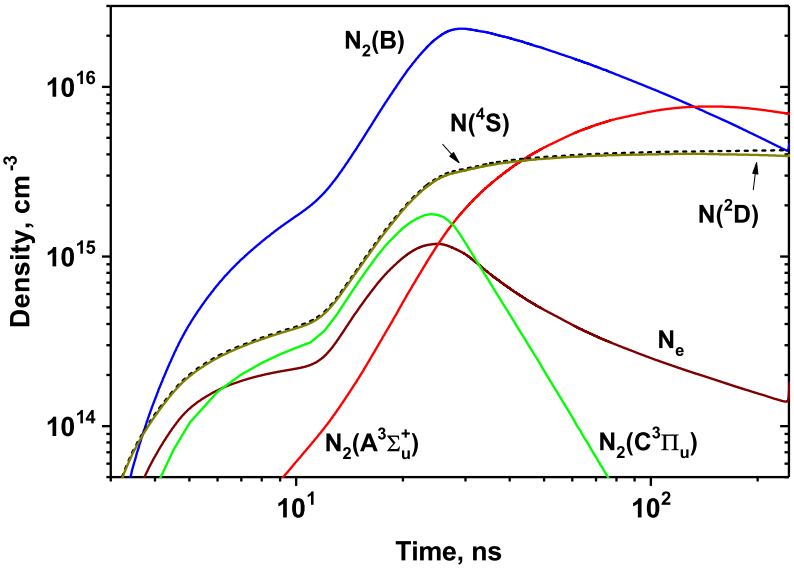

Figure 5.2 – The averaged over cross-section of the tube densities of the main nitrogen species and electron density calculated with 1D validated kinetic model at the same conditions as for Fig. 5.1.

One can see that, as it was predicted based on the results of the main discharge parameters measurements, the electronic excitation degree is high. The maximum total density of the excited atomic and molecular nitrogen states in the first pulse is 4.8% of the initial nitrogen density, $\beta \approx 0.048$. The peak electron density in the discharge reaches $N_e \approx 1.2 \cdot 10^{15}$ cm^{-3}, which means that ionization degree is also high, $\alpha = 1.8 \cdot 10^{-3}$. The recombination with main ion N_4^+ at electron density $N_e \approx 2.5 \cdot 10^{14}$ cm^{-3} (at 100 ns) is fast $\tau_{rec} \approx 9$ ns at $T_e = 0.5$ eV (the electron temperature at 100 ns according to the numerical calculations), however it is clearly seen in Fig. 5.2 that the electron density decay is much slower. It confirms that high α and β at high E/N change the plasma kinetics. Slow decay of the electron density will be discussed in details in Chapter 6. The behavior of the radial distribution of electrons and the excited species will be discussed in details in Chapter 8.

Chapter 6

Electron density measurements. Long-lived plasma

As was shown in Fig. 5.2, the electron density and ionization degree in the discharge are high. It was also shown that the electron density only slightly decays in the afterglow, which means that long-lived plasma is observed in nanosecond capillary discharge. In this Chapter these numerical results are confirmed experimentally.

6.1 Electron density in the discharge pulses

The electron density average over the tube cross–section can be determined based on the results of electrical parameters measurements of the discharge. The average current density can be written as

$$j = eN_e v_{dr.} = eN_e \mu E, \tag{6.1}$$

where e is the elementary charge value, N_e is the average electron density, $v_{dr.} = \mu E$ is the drift velocity with the mobility of electrons $\mu = \mu(E/N)$ and the electric field E. In the same time

$$j = \frac{I_{tr}}{S} \tag{6.2}$$

with the tube cross–section area S. This assumes that ions do not contribute in the total current value, since the mobility of ions is much lower than the mobility of electrons. From (6.1) and (6.2) it follows that temporal profile of the average

electron density can be calculated as

$$N_e(t) = \frac{I_{tr}(t)}{eS\mu E(t)}. \tag{6.3}$$

The mobility of electrons as a function of reduced electric field E/N can be calculated using BOLSIG+ software [3] for the given E/N range taking into account the high ionization degree. For N_e calculation the value of the mobility $\mu(t)$ is obtained by interpolation of pre-calculated values $\mu(E/N)$ at each time instant in accordance with experimentally measured reduced electric field profile, $E/N(t)$. The results of the electron density measurements are presented in Fig. 6.1. The measured peak electron density in the discharge reaches $N_e \approx 1.2 \cdot 10^{15}$ cm^{-3}, which is a good agreement with the value calculated numerically, see Fig. 5.2. It should be noted one more time, that this value is the electron density averaged over the cross-section of measurements.

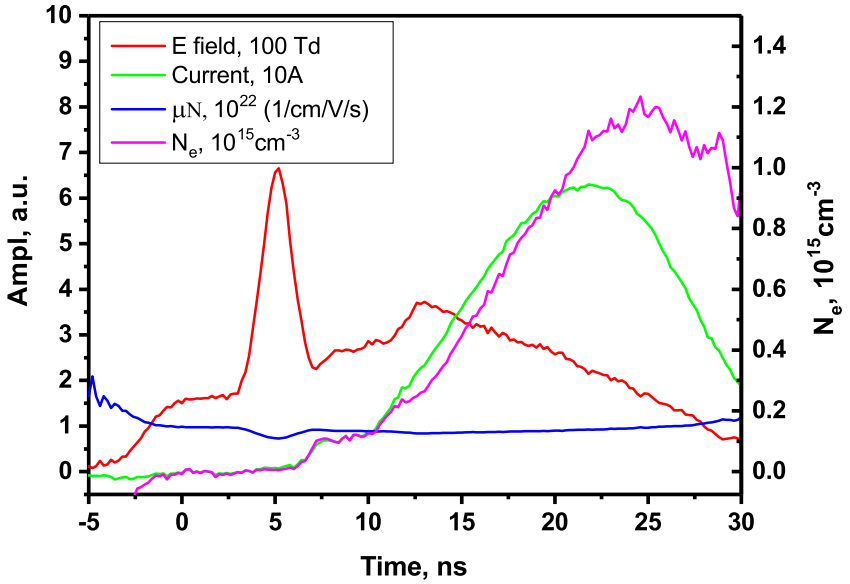

Figure 6.1 – The averaged over the tube cross–section electron density as a function of time (magenta curve) calculated by (6.3) with the electric field (red curve) and the corresponding electron mobility (blue curve). First pulse, pure nitrogen, 27 mbar, $I_{tr.} = 65$ A (green curve).

The same calculations can be performed for the second and the third main pulses. The results are presented in Fig. 6.2 and Fig. 6.3. The maximum averaged over the tube cross–section electron densities in these pulses are $\approx 1.5 \cdot 10^{15}$ cm^{-3} and $\approx 1.1 \cdot 10^{15}$ cm^{-3}, respectively.

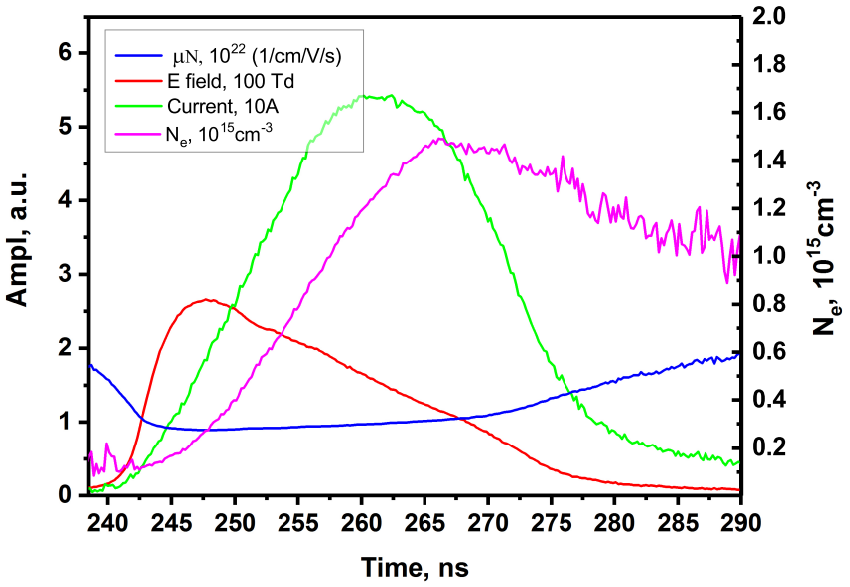

Figure 6.2 – The averaged over the tube cross–section electron density as a function of time (magenta curve) calculated by (6.3) with the electric field (red curve) and the corresponding electron mobility (blue curve). Second pulse, pure nitrogen, 27 mbar, $I_{tr.} = 65$ A in the first pulse.

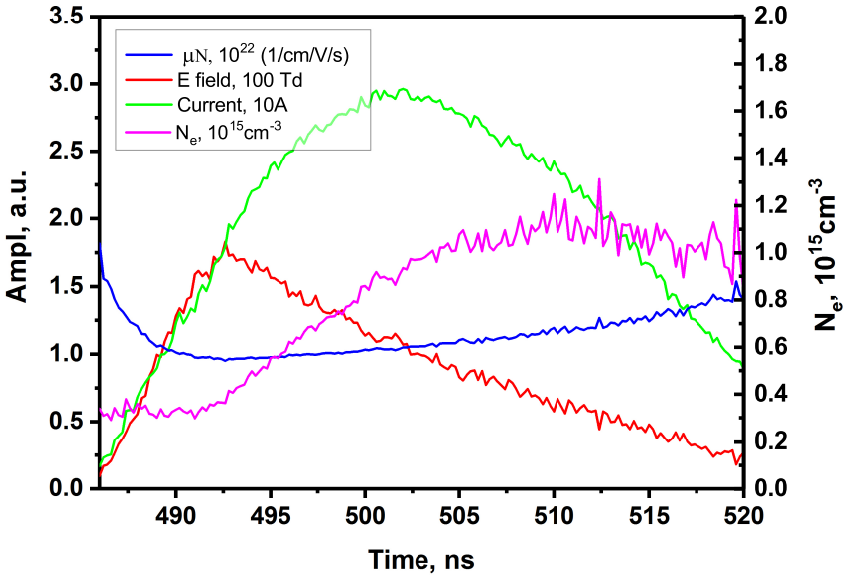

Figure 6.3 – The averaged over the tube cross–section electron density as a function of time (magenta curve) calculated by (6.3) with the electric field (red curve) and the corresponding electron mobility (blue curve). Third pulse, pure nitrogen, 27 mbar, $I_{tr.} = 65$ A in the first pulse.

6.2 Electron density in the afterglow of the discharge. Long-lived plasma

6.2.1 Plasma decay in pure nitrogen

The high measured electron densities in the main pulses itself do not mean that the long-lived plasma exists in the afterglow of the nanosecond capillary discharge. To check experimentally the behavior of $N_e(t)$ in the afterglow, the measurements between main high voltage pulses are required.

The main idea of the measurements in the afterglow is that N_e should be extracted from the measurements of the electric current and the electric field in a non-self-sustained pulsed discharge with duration of pulse shorter than a typical time of $N_e(t)$ dependence and variable time delay. The most elegant way to solve given technical problem was to use a reflection of the signal transmitted through the plasma from the end of the LV cable as a probe pulse. The duration of the reflected pulse is approximately equal to the duration of the pulse transmitted through the plasma, excepting some variation of the pulse duration caused by dispersion in the high voltage cable, see Fig. 4.2 and corresponding discussion in the text. This duration is shorter than a typical time of $N_e(t)$ decay in the afterglow observed in the experiments. The delay was adjusted varying the length of the LV cable. Finally, the amplitude of the reflected pulse was kept low enough by selecting a proper value of the load resistance R at the end of the cable. The majority of the experiments was performed at $R = 0$. The absence of the electron production was verified by controlling of the form of the electron density temporal profile in the probe pulse. The flat profile shape without electron density rise was interpreted as an absence of the ionization.

Variation of the length of the LV cable provided operation in the broad range of time. For example, if the length of the cable is changed by 1 m, the diagnostic time instant is shifted by 10 ns, since the velocity of the voltage pulse propagation is equal to 0.2 m/ns and the pulse propagates 1 m twice: to the end of the cable and back after reflection. The waveform of the current in plasma caused by the probe pulse was obtained by comparison of the signals from BCS1 for two cases: with and without the diagnostic pulse. The last one was measured at the matched end load, equal to the impedance of the used high-voltage cable ($R = Z = 50$ Ohm). Subtracting the reference signal from the measured one at the presence of the diagnostic pulse directly gives the value of the current induced by the probe pulse. Another way to obtain the reference signal is to solder an additional cable to the given LV cable, to delay the reflection from the end load.

The example of the diagnostic pulses and corresponding electric field with measured electron density in the afterglow is presented in Fig. 6.4.

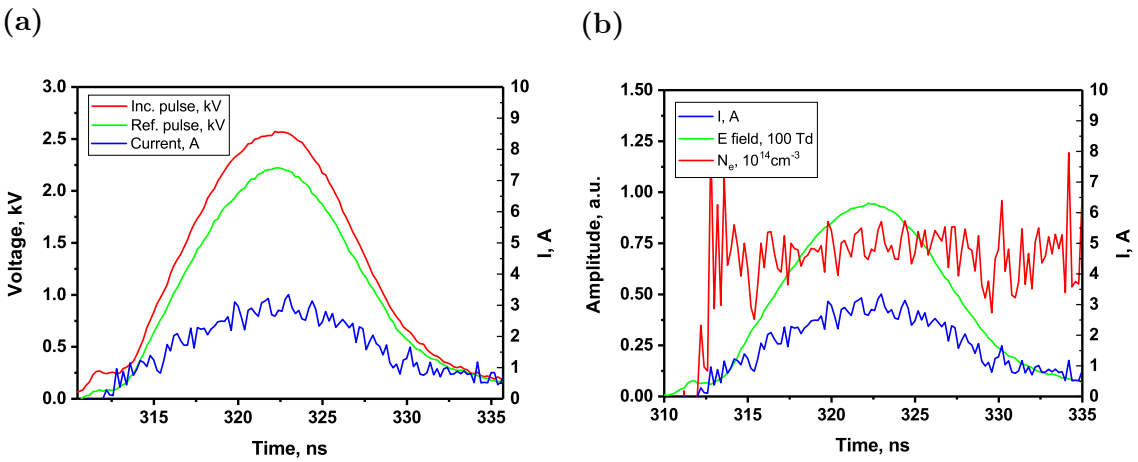

Figure 6.4 – (a) The incident (red curve), reflected (green curve) diagnostic pulses and corresponding transmitted current (blue curve) for electron density measurements in the afterglow. (b) Transmitted diagnostic current (blue curve) with the electric field (green curve) and the electron density (red curve). Pure nitrogen, 27 mbar, $I_{tr.} = 58$ A in the main pulse produced by 10 kV positive polarity high voltage pulse with 20 ns FWHM.

Here the electric field is measured by BCS technique (4.2), since plasma already exists and BCS technique is in a good agreement with CP technique due to absence of the FIW stage, see Fig. 4.8. One can see that the electron density profile in the probe pulse is rather flat, which means that no additional ionization in the probe pulse takes place.

Described technique provides a point on the N_e dependence upon time. To get the next point, the experiments are repeated with another length of the LV cable.

The electron density profile in the afterglow of the nanosecond capillary discharge in pure nitrogen at 27 mbar is presented in Fig. 6.5. Experimental results clearly demonstrate that nanosecond capillary discharge produces the long-lived plasma, as it was predicted by the kinetics model, see Fig. 5.2.

Typically in the discharges with main ion N_4^+, as in the present work, the rate of electron–ion recombination [5]

$$N_4^+ + e \rightarrow N_2(B^3\Pi_g, C^3\Pi_u) + N_2, \tag{6.4}$$

is high [109]

$$k_{(6.4)} = 2 \cdot 10^{-6} \cdot (300/T_e)^{0.5} \text{ cm}^3\text{s}^{-1}. \tag{6.5}$$

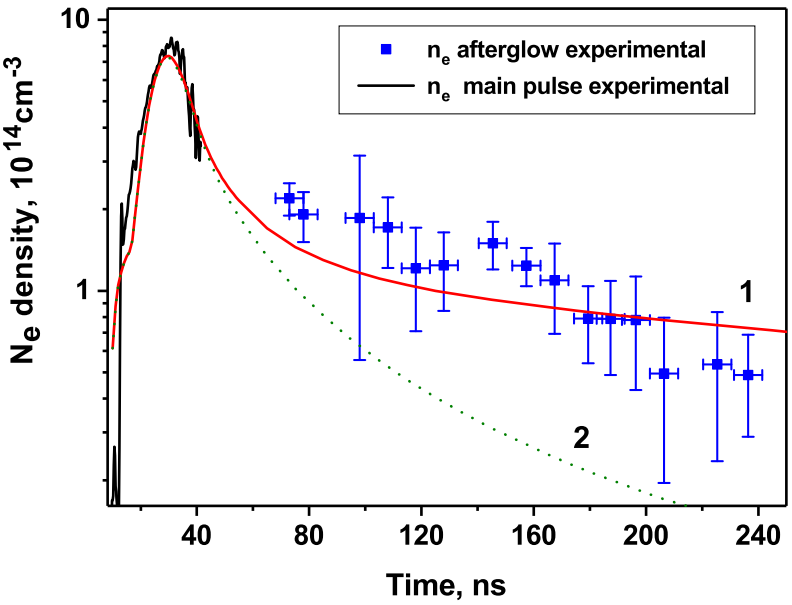

Figure 6.5 – Calculated and measured electron density averaged over cross-section of the capillary tube in the afterglow for 27 mbar pure nitrogen and transmitted current 40 A. Calculations are performed with (curve 1) and without (curve 2) taking into account the associative ionization.

It is assumed that the electron temperature T_e in the afterglow tends to the vibrational temperature of molecular nitrogen $T_{vib}^{N_2}$. According to the numerical calculations $T_{vib}^{N_2}$ is equal to 4000 K. However, in early afterglow electron temperature is still high. For example, at 100 ns the electron temperature is almost 1.5 times higher: $T_e \approx 0.5$ eV at $N_e \approx 2 \cdot 10^{14}$ cm^{-3}, thus the plasma should decay rapidly with characteristic time $1/(k_{(6.4)}N_e) \approx 10$ ns. The experimentally observed presents of the long-lived plasma clearly demonstrates that at conditions of high specific deposited energy at high reduced electric fields the plasma kinetics changes due to processes between excited species, which have negligible probability at low β. In particular, the electron density can be sustained by reactions of associative ionization [113] included in the kinetic model:

$$N_2(A^3\Sigma_u^+) + N_2(a'^1\Sigma_u^-) \rightarrow N_4^+ + e \tag{6.6}$$

and

$$N_2(a'^1\Sigma_u^-) + N_2(a'^1\Sigma_u^-) \rightarrow N_4^+ + e, \tag{6.7}$$

which can be extremely efficient at high excitation degree specific for considered capillary discharge.

To prove that exactly these process are responsible for high electron density in the afterglow corresponding reactions were excluded from the model. The results

of numerical calculations with and without reactions of associative ionization are presented in Fig. 6.5. One can see that a good agreement with the experimental results is achieved only if (6.6) and (6.7) are included in the kinetic model. Without these reactions plasma decay is much faster (curve 2 in Fig. 6.5) than experimentally observed one.

Typical time of $N_2(A^3\Sigma_u^+)$ and $N_2(a'^1\Sigma_u^-)$ decay at 27 mbar is comparable with the time between the first and the second pulses, $\Delta t \approx 250$ ns (see Fig. 5.2). This gives a unique possibility of the additional experimental check of the effect of associative ionization. The reactions of associative ionization (6.6) and (6.7) determine the residual electron density N_e in the afterglow, in particular, in the beginning of the second pulse at 250 ns after the first main pulse. The calculations of the electric field in the second pulse are sensitive to this value, which can be used as another method to check the effect of associative ionization. The calculations for the second pulse were carried out in two different assumptions: with and without the reactions of associative ionization. The results, presented in Fig. 6.6, prove the importance of the associative ionization in the afterglow of nanosecond discharge with high specific deposited energy in molecular nitrogen. When reactions (6.6) and (6.7) are taken into account, the waveform for the electric field calculated from the experimentally measured waveform for electric current at initial electron density determined by kinetics between pulses, is in good agreement with $E(t)$ dependence measured experimentally by the capacitive probe (see, Fig. 6.6). No agreement is observed if the reactions of the associative ionization (6.6) and (6.7) are neglected.

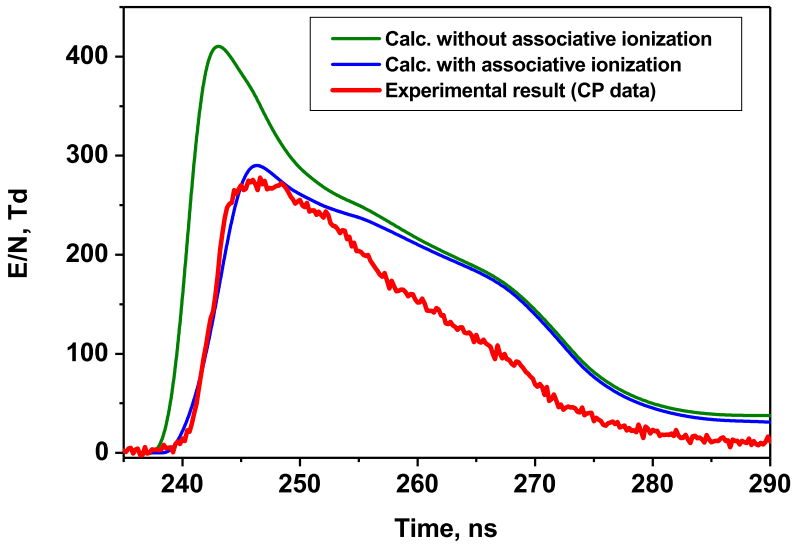

Figure 6.6 – Measured electric field compared with calculated electric field in two assumptions concerning the associative ionization, see text. Second pulse, pure nitrogen, 27 mbar, $I_{tr.} = 65$ A in the first pulse.

Thus, it can be concluded that at conditions of high specific energy deposition at high reduced electric field in nanosecond capillary discharge, the long-lived plasma is observed in pure nitrogen. The electron density in the afterglow is sustained by the reaction of associative ionization between $N_2(A^3\Sigma_u^+)$ and $N_2(a'^1\Sigma_u^-)$ states.

The observed long-lived nitrogen plasma can be used in the applications. However, the nitrogen/oxygen mixtures or the nitrogen flow in the ambient air are more frequently used in plasma applications than pure nitrogen. It was shown above that in pure nitrogen the long-lived plasma is observed due to reactions between metastable states of nitrogen. The presence of oxygen can suppress these processes, since the oxygen molecule is extremely efficient quencher of nitrogen excited states. For example, the total rate constant for quenching of the $N_2(A^3\Sigma_u^+)$ state to the ground one by molecular oxygen is equal to $3.9 \cdot 10^{-12}$ cm^{3}s^{-1} [109], while the quenching of the $N_2(A^3\Sigma_u^+)$ state by molecular nitrogen has the rate constant $3 \cdot 10^{-18}$ cm^{3}s^{-1} [109]. However, the values of mentioned rate constants are rather low, and the most important role is played by quenching of upper states of nitrogen to the ground one. The reason is that significant part of the $N_2(A^3\Sigma_u^+)$ metastable state is produced by cascade of non-radiative transitions and sum of $N_2(C^3\Pi_u) \rightarrow N_2(B^3\Pi_g)$ and $N_2(B^3\Pi_g) \rightarrow N_2(A^3\Sigma_u^+)$ radiative transitions from the upper states. The processes of the quenching of the $N_2(C^3\Pi_u)$ and $N_2(B^3\Pi_g)$ states are much faster when molecular oxygen is a quenching partner, instead of molecular nitrogen. The rate constant of quenching of $N_2(C^3\Pi_u)$ state by molecular nitrogen is equal to $0.13 \cdot 10^{-10}$ cm^{3}s^{-1}, while quenching of $N_2(C^3\Pi_u)$ by molecular oxygen has rate constant equal to $3 \cdot 10^{-10}$ cm^{3}s^{-1} [91]. The quenching of $N_2(B^3\Pi_g)$ state by molecular oxygen is also intensive: $3 \cdot 10^{-10}$ cm^{3}s^{-1} [109], while for molecular nitrogen the quenching rate constant is only $2 \cdot 10^{-12}$ cm^{3}s^{-1} [114, 115]. Moreover, molecular oxygen leads to quenching of the $N_2(C^3\Pi_u)$ and $N_2(B^3\Pi_g)$ to $N_2(X^1\Sigma_g^+)$, in contrast to the quenching by molecular nitrogen leading to population of the $N_2(A^3\Sigma_u^+)$ state. Thus, molecular oxygen can inhibit the reactions of the associative ionization (6.6) and (6.7) reducing the density of the metastable states of molecular nitrogen.

From the other hand side, the ion composition of the plasma can be affected by molecular oxygen due to reaction of the charge exchange

$$N_4^+ + O_2 \rightarrow O_2^+ + N_2 + N_2 \tag{6.8}$$

with a rather high rate constant [109]

$$k_{(6.8)} = 2.5 \cdot 10^{-10} \text{ cm}^3\text{s}^{-1}. \tag{6.9}$$

Therefore, N_4^+ is rapidly converted to O_2^+ ion. The recombination of O_2^+ ion

$$O_2^+ + e \rightarrow O + O \tag{6.10}$$

has the rate constant equal to [116]

$$k_{(6.10)} = 2 \cdot 10^{-7} \cdot (300/T_e)^{0.7} \text{ cm}^3\text{s}^{-1}, \tag{6.11}$$

that is about 17 times slower than (6.4) at $T_e = 0.5$ eV. Thus, the oxygen admixture can decrease decay of the plasma significantly.

As a result, the influence of the oxygen on the plasma decay in N_2:O_2 mixtures is not evident a priori and should be investigated additionally. This is the subject of the next subsection.

6.2.2 Plasma decay in nitrogen:oxygen mixtures

The measurements of the electron density in the discharge afterglow for N_2:O_2 mixtures with 5, 10, 15 and 20% of oxygen has been performed using the method described above. The results of the measurements are presented in Fig. 6.7. The plasma decay measured in pure nitrogen for the experimental conditions close to the ones for N_2:O_2 mixtures is given for comparison.

Direct comparison of the electron densities in the afterglow of the discharge in different mixtures is complicated due to the fact that the maximum electron density values are different in different mixtures, see Fig. 6.8(a), because transmitted current amplitude slightly varies with the oxygen fraction as well as the specific deposited energy, see Fig. 6.8(b). Nevertheless, it is seen in Fig. 6.7 that the electron density in the afterglow is rather high during investigated 650 ns for all mixtures and comparable with the electron density in the afterglow of the discharge in nitrogen.

To investigate the mechanism of plasma decay in nitrogen:oxygen mixtures the numerical calculations have been done. The calculated electron density and ion composition in the discharge and its afterglow in dry air are presented in Fig. 6.9 together with electron density measured experimentally. One can see that after 100 ns the main positive ion is O_2^+, thus, the plasma decay in the afterglow is completely controlled by the slow ion-electron recombination (6.10) involving this ion, as it was assumed above. Therefore, the character of the plasma decay in the late afterglow in the N_2:O_2 mixtures is the same despite the oxygen fraction. Oxygen density impacts only the time instant, when O_2^+ becomes dominate. It should be noted that under present conditions (27 mbar, $T_e = 4000$ K) the character time of complex ion O_4^+ formation is higher than 10 μs [109]. Thus, the role of O_4^+ ion is negligible.

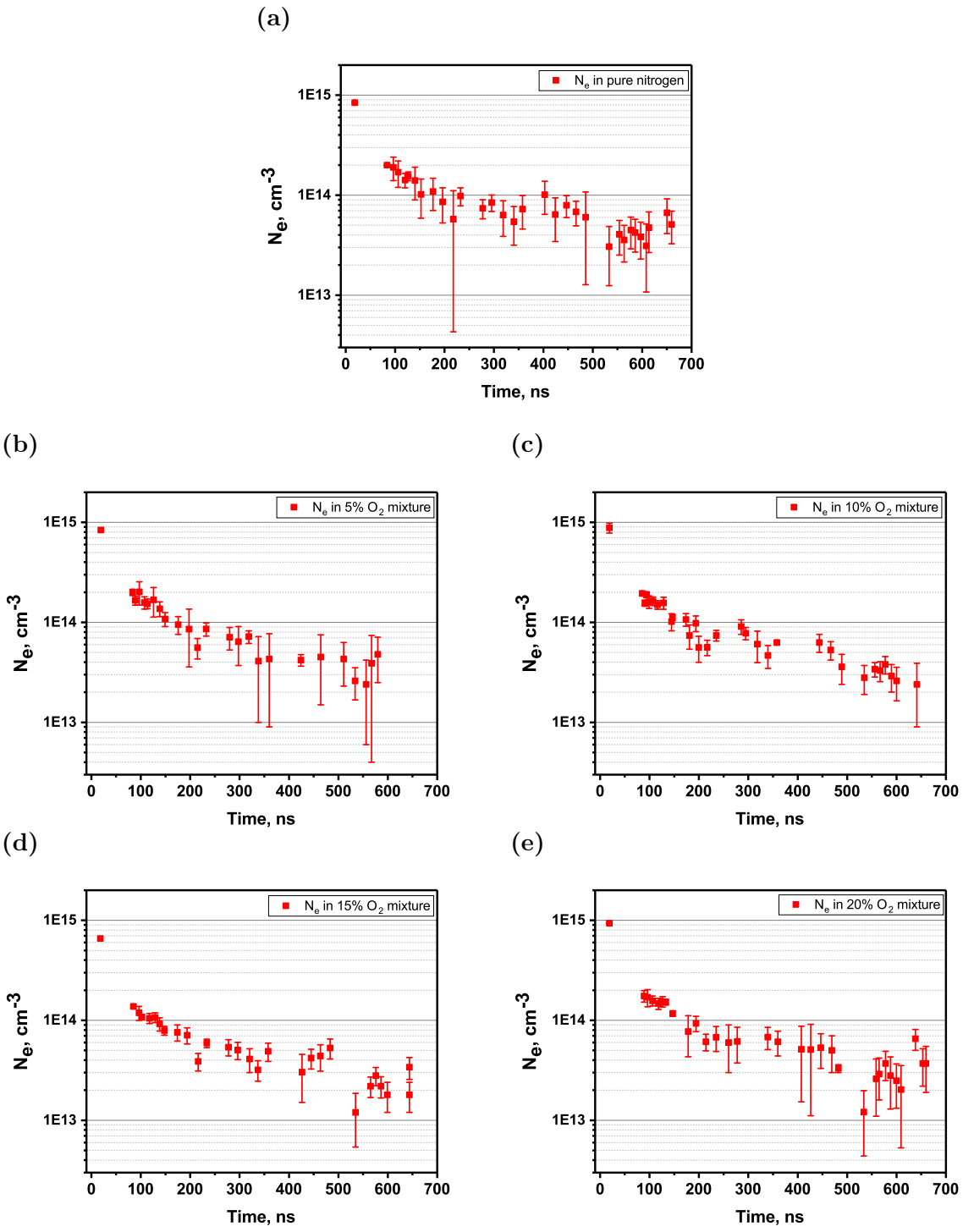

Figure 6.7 – The averaged over the tube cross–section electron density as a function of time experimentally measured in the afterglow of the nanosecond capillary discharge (a) in pure nitrogen, $I_{tr.} = 58$ A, and the N_2:O_2 mixtures (b) with 5% of oxygen, $I_{tr.} = 60$ A (c) with 10% of oxygen, $I_{tr.} = 62.5$ A (d) with 15% of oxygen, $I_{tr.} = 64$ A (e) with 20% of oxygen, $I_{tr.} = 67$ A; at 27 mbar, the discharge pulse produced by 10 kV positive polarity high voltage pulse with 20 ns FWHM.

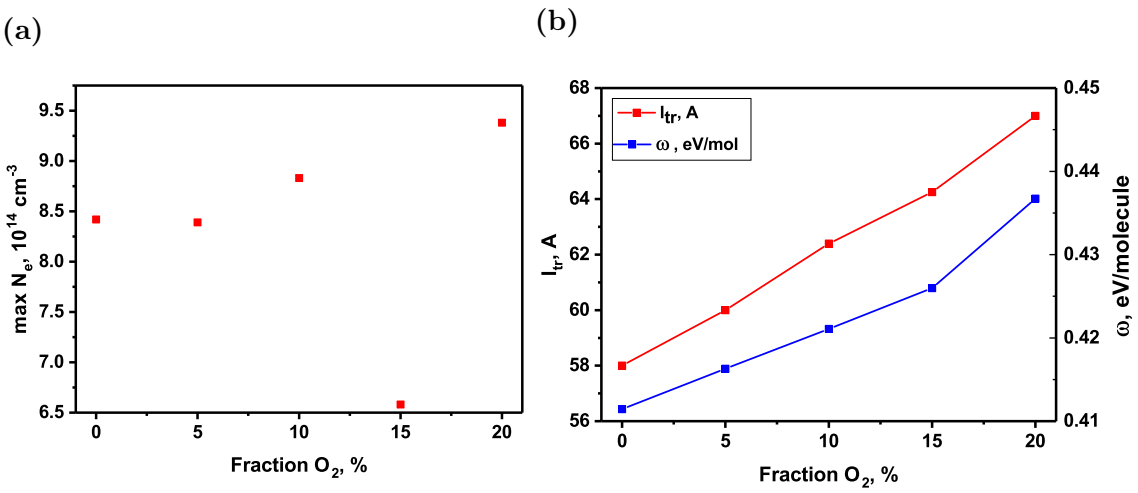

Figure 6.8 – (a) the maximum electron density, (b) the transmitted current amplitude and the specific deposited energy in the discharge pulse as functions of the oxygen fraction in the N_2:O_2 mixtures at 27 mbar, the main pulse produced by 10 kV positive polarity high voltage pulse with 20 ns FWHM.

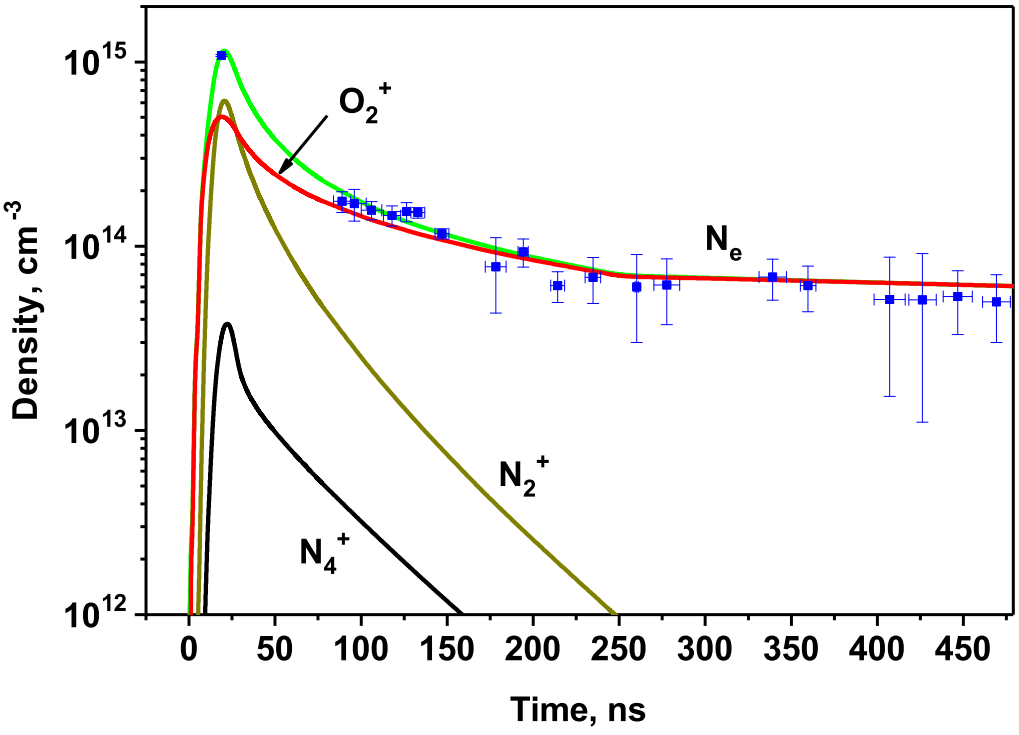

Figure 6.9 – The calculated electron density and ion composition in the discharge and its afterglow (solid curves) and the experimentally measured electron density (symbols) in dry air, 27 mbar, $I_{tr.} = 67$ A in the first pulse.

6.3 Conclusion

The electron density was measured in the main discharge pulses and in the afterglow of the nanosecond capillary discharge by electric measurements. The high electron densities were observed in the main pulses: $1.2 \cdot 10^{15}$ cm^{-3}, $1.5 \cdot 10^{15}$ cm^{-3} and $1.1 \cdot 10^{15}$ cm^{-3}. Despite the fast recombination rate constant for the main ion N_4^+ and high electron densities leading to the recombination with characteristic time about 10 ns, the high electron density at time scales of hundreds of nanosecond was observed numerically and experimentally in the late afterglow of the nanosecond capillary discharge in pure nitrogen. It was shown by the comparison of the experimental and numerical results that the reactions of the associative ionization between metastable states of molecular nitrogen sustain the high electron density in the afterglow. These reactions are efficient only at high density of the excited species. Thus, it was demonstrates one more time that the plasma kinetics changes significantly under present conditions. For the nitrogen:oxygen mixtures the same behavior of the electron density in the afterglow was observed. The slow plasma decay in this case is caused by the slow ion-electron recombination involving O_2^+, which is main positive ion. This was confirmed by numerical calculations.

Chapter 7

Depopulation of the excited species

Different optical methods, such as time-resolved actinometry, optical emission spectroscopy, Laser-Induced Fluorescence (LIF) and Two Photon Absorption Laser Induced Fluorescence (TALIF) are widely used to study plasma of discharges with high specific deposited energies. At pressures higher than a few tens of Torr, detailed analysis of collisional quenching becomes important [117]. In recent review [118] devoted to physics, chemistry and diagnostics of microplasmas and atmospheric pressure discharges, it is underlined that any advanced optical diagnostics requires a detailed understanding of plasma kinetics, in particular understanding of population and depopulation mechanisms of main excited states.

To be sure in the results of diagnostics potentially sensitive to the decay rates of the excited species, depopulation of excited molecules on the example of $N_2(C^3\Pi_u)$ state of molecular nitrogen is studied in N_2:O_2 mixtures. This electronic state with high threshold of excitation $\varepsilon = 11.03$ eV [4] is effectively excited in the discharges at high electric fields.

7.1 Decay of optical emission of the second positive system in the discharge and the near afterglow

Transition $N_2(C^3\Pi_u, v' = 0) \rightarrow N_2(B^3\Pi_g, v'' = 0)$ at $\lambda = 337.1$ nm is the most intensive band of emission of the second positive system of molecular nitrogen. The band was chosen for studying the decay rates at high specific deposited energy. The decay rates were measured based on emission profiles obtained with PMT (Hama-

matsu H6610 with a typical rise time of 0.7 ns and transit time spread of 0.16 ns; with high voltage supply Hamamatsu C9727) as a slope of the profile in semi-logarithmic scale.

The theory predicts that in the simplest case of low specific deposited energy and low densities of both electrons and excited species, the population/depopulation process of the upper, $N_2(C^3\Pi_u, v' = 0)$ state, is described by three processes [91]. They are population by direct electron impact from the ground state of molecular nitrogen,

$$N_2(X^1\Sigma_g^+) + e \rightarrow N_2(C^3\Pi_u, v' = 0) + e, \tag{7.1}$$

spontaneous emission,

$$N_2(C^3\Pi_u, v' = 0) \rightarrow N_2(B^3\Pi_g, v'') + h\nu, \tag{7.2}$$

and collisional deactivation by background gas,

$$N_2(C^3\Pi_u, v' = 0) + M_i \rightarrow \text{products}. \tag{7.3}$$

In the afterglow in, so called, current free regime, the first process (7.1) is absent. Thus the total balance for $N_2(C^3\Pi_u, v' = 0)$ is

$$\frac{d[N_2(C)]}{dt} = -[N_2(C)]\Big(1/\tau_0 + \sum_i k_i[M_i]\Big), \tag{7.4}$$

with the radiative lifetime τ_0, and the rate constants k_i for quenching by the background gas component M_i. The square brackets denote concentration. The solution of this equation is

$$[N_2(C)]|_t = [N_2(C)]|_{t=0} exp(-t/\tau_{eff.}) \tag{7.5}$$

with the effective decay time

$$\tau_{eff.} = \Big(1/\tau_0 + \sum_i k_i[M_i]\Big)^{-1}. \tag{7.6}$$

So, the theory predicts that the emission profile decays exponentially with the effective time $\tau_{eff.}$, which can be calculated based on the quenching rate constants. The rate constants for $N_2(C^3\Pi_u, v' = 0)$ quenching by molecular nitrogen are well–known [91,119–121] and in a good correlation in the papers of different authors [122].

The peculiarity of the nanosecond discharge in a capillary tube is that the specific deposited energy can be significantly changed by varying just configuration of the system. Increase of the tube diameter and disconnecting the low voltage cable (the load on the LV electrode is $R = \text{inf}$ in this case) result in decrease of the specific deposited energy from ≈ 1 eV/molecule to ≈ 0.1 eV/molecule. Fig. 7.1 presents the emission profile of $N_2(C^3\Pi_u, v' = 0)$ for the discharge in the tube of 4 mm diameter

filled by pure nitrogen at pressure 20.5 mbar at 13 kV negative polarity pulse. The deposited energy at this configuration is about 0.1 eV/molecule. However, it is clearly seen from Fig. 7.1, that even at $\omega = 0.1$ eV/molecule the decay is noticeably different: 29 ns instead of the theoretically predicted 33 ns (the rate constants are taken from [91]).

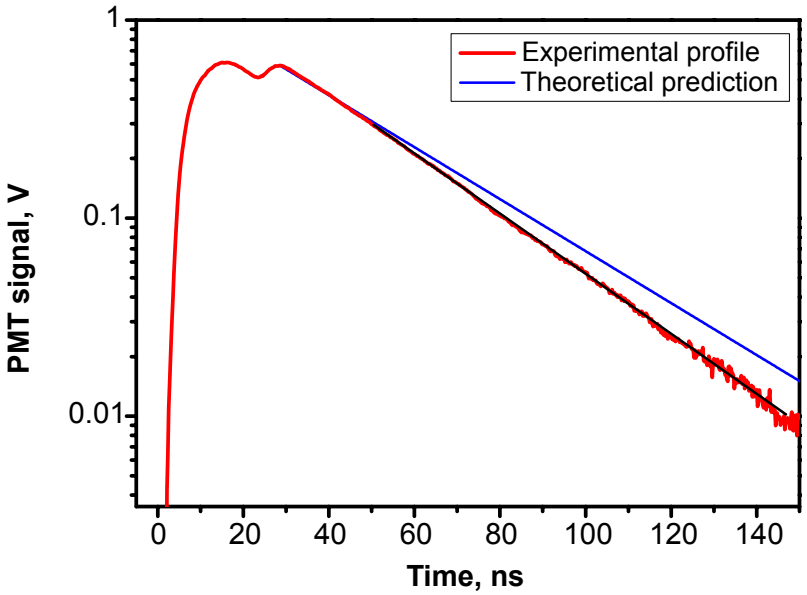

Figure 7.1 – PMT signal of $N_2(C^3\Pi_u, v' = 0)$ emission in pure N_2 at 20.5 mbar in 4 mm tube at low specific deposited energy (about 0.1 eV/molecule) at 13 kV negative polarity pulse. Dashed line corresponds to quenching by ground state of N_2 and radiative decay [91].

Specific deposited energy $\omega = 0.1$ eV/molecule can easily be reached in nanosecond plasmas at atmospheric pressure. Indeed, if total deposited energy W is about 5 mJ, and the volume of the plasma $V = 0.1$ mm $\times$ 0.1 mm $\times$ 1 cm $= 10^{-2}$cm^3, the specific deposited energy in assumption of uniform distribution of energy in space, is equal to $\omega = W/(V \cdot N) = 0.1$ eV/molecule, where $N = 2.5 \cdot 10^{19}$cm^{-3} is a number of molecules at atmospheric pressure at 300 K. In reality, in microdischarges at high electric field the specific deposited energy can be even higher.

If the deposited energy is high, the difference between experiment and theory is much more significant, see Fig. 7.2. Here the experimental profiles decays not only much faster then theory predicts, but also, become non-exponential: measured decay times are equal to 9 ns and 17 ns instead of calculated based on [91] 31 ns.

Observed phenomenon takes place not only in pure nitrogen, but also in nitrogen:oxygen mixtures, see Fig. 7.3. The decay rate of $N_2(C^3\Pi_u, v' = 0)$ state is presented as a function of O_2 mole fraction in N_2:O_2 mixtures. Two experimental curves correspond to slopes in the beginning and in the end of decay of PMT signal.

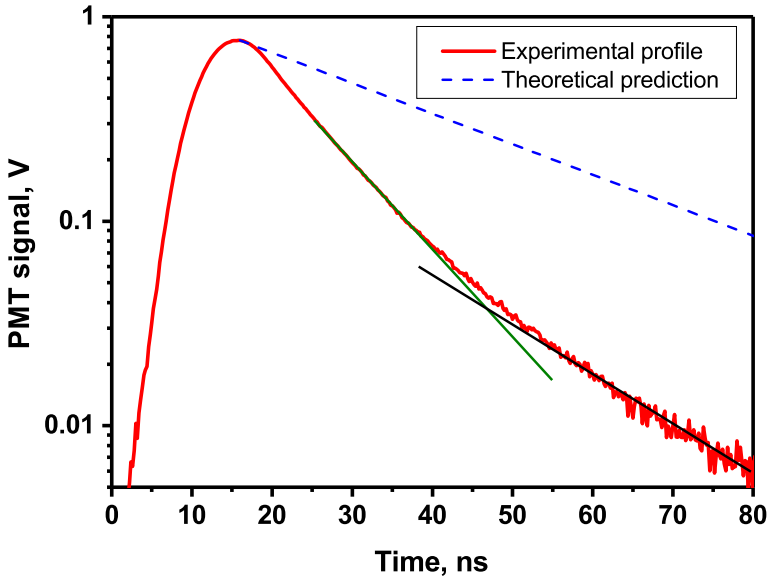

Figure 7.2 – PMT signal of $N_2(C^3\Pi_u, v' = 0)$ emission in pure N_2 at 27 mbar in 1.5 mm tube at high specific deposited energy (about 1 eV/molecule) at 13 kV negative polarity pulse. Dashed line corresponds to quenching by ground state of N_2 and radiative decay [91].

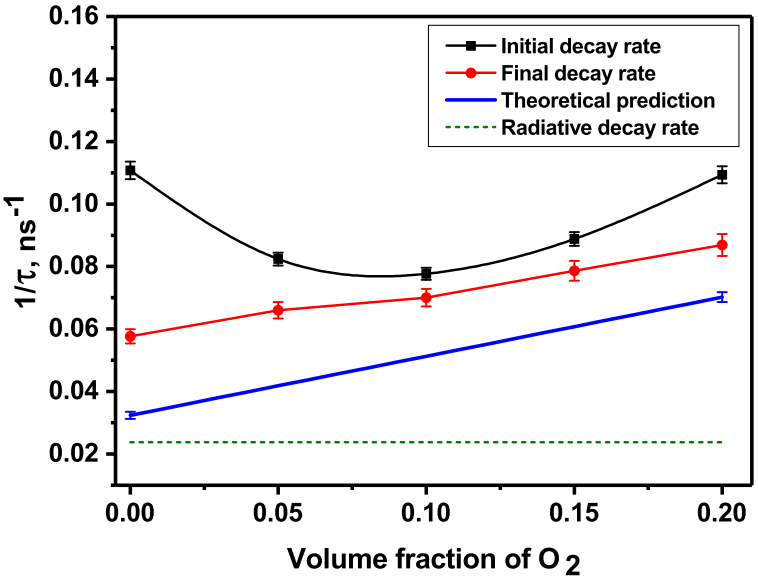

Figure 7.3 – Reverse decay times of $N_2(C^3\Pi_u, v' = 0)$ state in N_2:O_2 mixtures at 27 mbar in 1.5 mm tube as a function of the mole fraction of O_2. Negative polarity discharge. Black squares and red circles correspond to slopes in the beginning and in the end of decay of PMT signal, respectively. Blue curve is the decay rate predicted theoretically based on data from [91], olive dashed curve is radiative decay value [91].

One can see that non-radiative decay observed in the experiments is much higher than the theory predicts: up to 10 times for pure nitrogen, and about 2 times for air. In nitrogen the effect is the most intensive due to relatively low quenching by N_2 molecules. Also the system consisting of one gas is less complex. Thus further investigations are performed for pure nitrogen.

It can be concluded from Fig. 7.1 and Fig. 7.2, that different specific energy deposition causes different decay. To test this hypothesis, the experiments should be performed at identical conditions (pressure, voltage, pulse polarity), but for different ω values. In practice, this was realized using the electrode system providing non-stable start of the FIW (and so different transmitted currents and different specific deposited energy from pulse to pulse). The statistical analysis of the transmitted current has been made, and the data collected during the same experiment were averaged over a preliminary selected narrow range of transmitted electric current with a standard deviation not exceeding 5% of the central value by a custom made Fortran code. The results are presented in Fig. 7.4.

It is clearly seen that the experimental curves (i) have much faster decays; (ii) demonstrate two exponential slopes, τ_1 and τ_2. The theoretically predicted decay time is 31 ns, while the observed decay time is equal τ_1=10.4 ns at the beginning of the pulse and τ_2 =15.26 ns at the end of the pulse with transmitted current 65 A.

It is important to repeat one more time that both decays, τ_1 and τ_2, correspond to a zone free from electric current, where the excitation by direct electron impact (7.1) is not significant anymore. Another important remark is that the observed sharp decrease of the emission decay can not be caused by small non–controlled additions of molecular oxygen. Indeed, to get the presented in Fig. 7.4(a) decay $\tau_1 = 10.4$ ns for 27 mbar it would be necessary to have 33.3% of molecular oxygen in the gas mixture.

Additional plots presented in Fig. 7.4(a), taken at different values of electric current, clearly demonstrate the dependence of the decay upon the transmitted current, and so, upon the energy deposited to the discharge. Corresponding lifetimes are presented in Table 7.1. It is clearly seen that increase of the deposited energy enhances both depopulation of $N_2(C^3\Pi_u)$ and the relative difference between the decay rates at the beginning and at the end of the pulse, defined here as $(\tau_2 - \tau_1)/\tau_2$.

Fig. 7.4(b) presents the dependence of the observed reverse decay, τ_1^{-1}, on the gas pressure. Dashed line shows the theoretical value of τ^{-1} calculated from the processes (7.2) and (7.3) with the quenching rate constant taken from [91]. To check the limit case of significantly decreasing specific deposited energy, a few experiments in a capillary tube 4 mm in diameter with different end loads have been done. A specific deposited energy decreases sequentially in three series of experiments, see Fig. 7.4(b), namely: (i) curves (1)–(3) for a 1.5 mm diameter capillary, cable load,

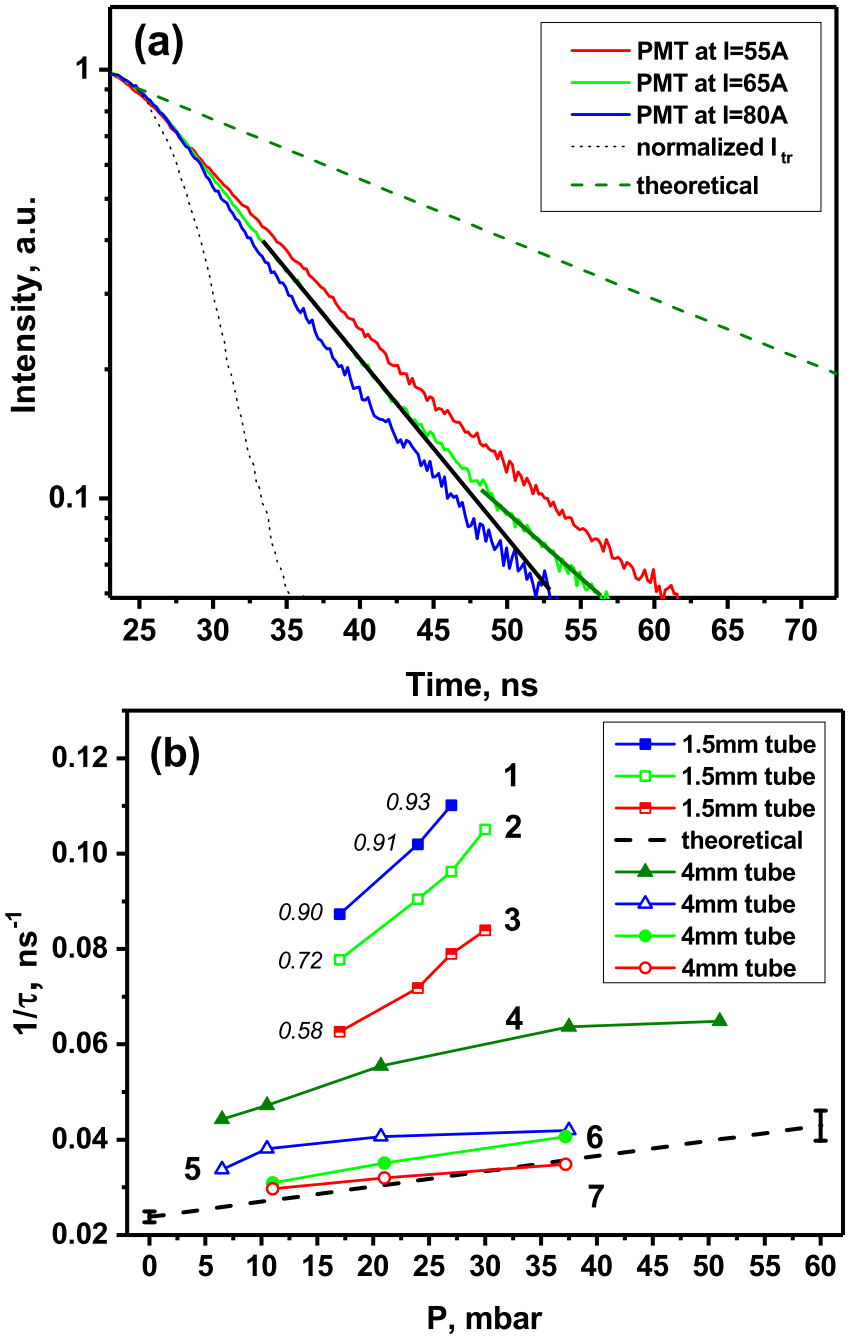

Figure 7.4 – Experimental results for $N_2(C^3\Pi_u, v' = 0)$ quenching in a capillary tube in pure nitrogen: (a) experimentally measured emission at 27 mbar for different discharge current; dashed line represents nitrogen emission calculated on the basis of quenching by N_2 with rate constant from [91]; dot line shows a normalized waveform for electric current; (b) reverse decay time τ_1 as a function of pressure for different specific deposited energies. Specific deposited energy decreases with the number of curve, see detailed explanations in the text. Dashed curve is for theoretical prediction.

9.3 kV positive polarity pulse; (ii) curves (4), (5) for a 4 mm diameter capillary, cable load; (iii) curve (6), (7) for a 4 mm diameter capillary, end load equal to infinity ($R = \infty$), that is disconnected low voltage electrode and the grounded screen, the experiments are performed at 12.6 kV negative polarity pulses. The values of the specific deposited energies corresponding to some of the observed decay rates are presented in Fig. 7.4 b in the units of eV/molecule. With the decrease of the specific deposited energy in the discharge, the τ_1^{-1} approaches to the theoretically predicted value, and the emission waveform changes to a single-exponential decay.

Table 7.1 – Measured $N_2(C^3\Pi_u)$ life times at the beginning (τ_1) and a the end (τ_2) of the pulse for different transmitted currents in pure nitrogen at 27 mbar in 1.5 mm inner diameter tube.

Transmitted current, A	τ_1, ns	τ_2, ns	$(\tau_2 - \tau_1)/\tau_2$
55	11.93	16.56	0.28
65	10.39	15.26	0.32
80	9.08	14.01	0.35

7.2 Analysis of possible reasons of abnormally high decay rate of $N_2(C^3\Pi_u)$

A few possible reasons of extra–high quenching rate for $N_2(C^3\Pi_u)$ were analyzed, namely: (i) stimulated emission in the case if conditions for laser transition are fulfilled for $N_2(C^3\Pi_u) \rightarrow N_2(B^3\Pi_g)$ emission; (ii) variation of quenching rate with gas temperature; (iii) additional collision quenching process.

7.2.1 Stimulated emission

At condition of high population of radiative energy level and low quenching, the spontaneous emission can be extremely intensive. Density of produced photons becomes high enough to efficiently stimulate emission from the levels with the same energy [103], that enhances this effect further (produced emission become laser in one pass without any resonator [8, 69–72]). Thus, stimulated emission results to depopulation of considered level, which can be observed as decreasing of the lifetime τ of this excited specie or, in other words, as increasing of the decay rate $1/\tau$. It can be a reason of the observed abnormally high decay of $N_2(C^3\Pi_u, v' = 0)$ state. Moreover, it is known [69, 70] that laser radiation can be produced by nanosecond

discharge under certain conditions in a long capillary tube in molecular nitrogen. Thus, it was experimentally checked that emission observed in the present work is not a laser emission.

To do this, time–resolved emission has been measured for a set of wavelengths in the rotational structure of SPS(0-0) transition, namely 337.0, 336.8, 336.4, 336.0 and 335.8 nm. In spite of the fact that absolute emission values decrease by a factor of 25 through this manifold, the shape of the emission curve remains identical (see Fig. 7.5). As far as stimulated emission should strongly increase with light intensity, it was concluded that no stimulation emission is observed within the rotational band. Slower decay for 336 and 335.8 nm in Fig. 7.5 can be explained by slight rotational redistribution of $N_2(C^3\Pi_u, v' = 0)$ state.

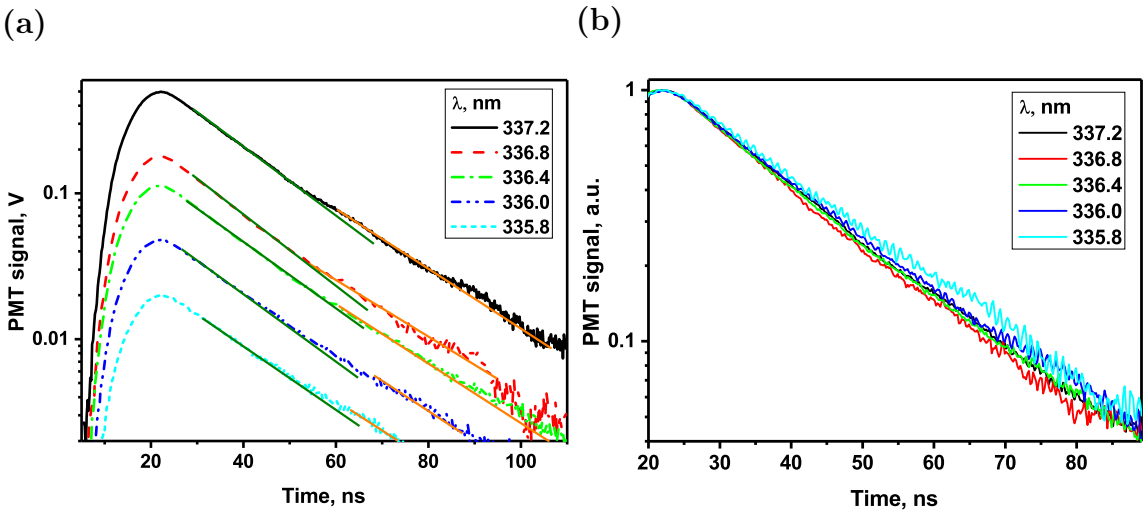

Figure 7.5 – Time–resolve $N_2(C^3\Pi_u, v = 0) \rightarrow N_2(B^3\Pi_g, v' = 0)$ emission for the different wavelengths: 337.0, 336.8, 336.4, 336.0 and 335.6 nm at 20.5 mbar pure nitrogen in 4 mm inner diameter tube. (a) The PMT signal in volts, (b) The same PMT signal profiles normalized to unit.

7.2.2 Variation of quenching rate with gas temperature

Gas temperature in the near afterglow of a nanosecond discharge can rise significantly because of energy relaxation from electronically excited molecules. This is so–called effect of a fast gas heating described in the Literature Review. As it will be shown in Chapter 9, in the nanosecond capillary discharge in nitrogen, the temperature rise in the afterglow at 60 ns is only ≈230 K. So, increase of the gas temperature can not be considered as a reason of a strong decay of $N_2(C^3\Pi_u)$ radiation.

7.2.3 Additional collisional quenching

After elimination of laser and temperature effect, the most probable scenario for the observed fast decay of $N_2(C^3\Pi_u, v = 0)$ emission is a collisional quenching. The collisional partner can be atomic nitrogen or excited (electronically or vibrationally) state of molecular nitrogen.

Bi–exponential decay of the emission (decay time τ_1 is changed by a slower decay time τ_2, both are much faster than the theoretically predicted one, τ_0, see Fig. 7.2 and Fig. 7.4 a.) is observed in the times of the order of 30 ns. Short time scale indicates that the collisional partner has a lifetime of the order of tens of nanoseconds. Thus, this can be neither metastable atom/molecule, nor vibrationally excited ground states of molecular nitrogen.

The calculations show that the densities of other excited species and atomic nitrogen in the discharge do not exceed 10% of the total gas density (see Fig. 5.2). To obtain a typical decay time about 10^{-8} s in collisions with such a partner, it is necessary to take a rate constant higher than $2 \cdot 10^{-9}$ cm^3s^{-1}, which is one order of magnitude higher than a gas kinetic rate constant, so seems to be not reasonable. Thus, we believe that heavy particles are unlikely to be a collisional partner responsible for the observed high decay rates.

However, as it was shown in Chapter 6, one of the distinctive features of the nanosecond capillary discharge at high specific energy deposition is a high ionization degree with the electron density of the order of $10^{15}cm^{-3}$. It is possible that super-elastic collisions between electrons and $N_2(C^3\Pi_u, v' = 0)$ depopulate $N_2(C^3\Pi_u, v' = 0)$ to lower energetic levels of nitrogen molecule:

$$N_2(C^3\Pi_u) + e \rightarrow N_2(X^1\Sigma_g^+, A^3\Sigma_u^+, B^3\Pi_g, ...) + e. \tag{7.7}$$

The probability of this process is discussed in the next subsection.

7.2.4 Quenching by electrons

To estimate the probability of quenching of $N_2(C^3\Pi_u, v' = 0)$ due to super-elastic collisions with electrons, it is necessary to know corresponding cross-section. Unfortunately, there is no this data in the literature. Another way to estimate influence of super-elastic collisions is to calculate their cross-sections based on the data on direct excitation of $N_2(C^3\Pi_u, v' = 0)$ from lower energetic levels by the electron impact using formula [2]

$$\sigma_-(\varepsilon) = \sigma_+(\varepsilon + w)\frac{g^-}{g^+}\frac{\varepsilon + w}{\varepsilon}, \tag{7.8}$$

where σ_+ and σ_- are the cross–sections of direct and reverse processes respectively, g^-/g^+ is a ratio of statistical weights of lower and upper states, w is a threshold for the direct process, and ε is energy of the electron (variable).

To the best of our knowledge there is only one publication [123], where the cross-sections of direct processes are available. This publication was used as a data source. There the cross-sections were calculated theoretically for the excitation of $N_2(C^3\Pi_u)$ from $(X^1\Sigma_g^+)$, $(A^3\Sigma_u^+)$, $(B^3\Pi_g)$, $(a'^1\Sigma_u^-)$ and $(a^1\Pi_g)$ at temperature 300 K.

The example of the cross-section of reverse process calculated using (7.8) is presented in Fig. 7.6. The cross-sections of reverse processes for de-excitation to other lower energy states are presented in Fig. 7.7.

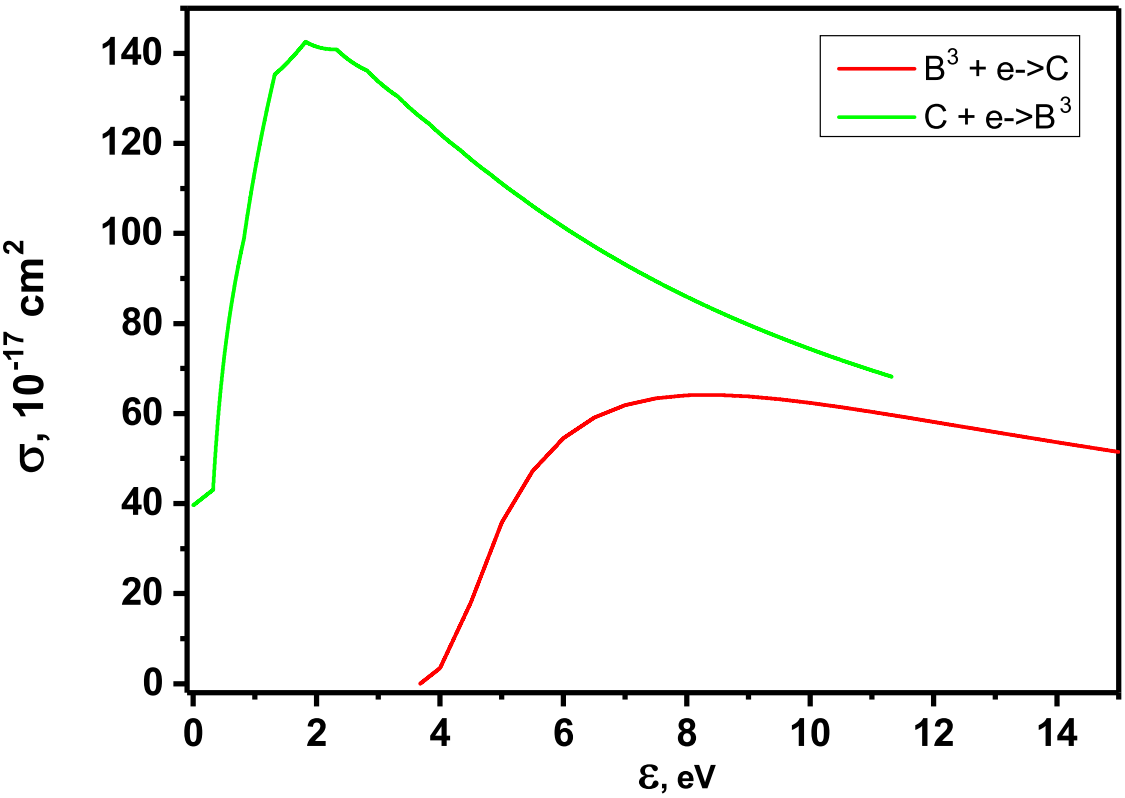

Figure 7.6 – Cross-section of excitation of $N_2(C^3\Pi_u)$ state from $N_2(B^3\Pi_g)$ state by direct electron impact [123] and cross-section for reverse process of super-elastic collisions with electrons calculated using (7.8).

The cross-sections of reversed processes presented in Fig. 7.6 and Fig. 7.7 were convoluted with Maxwellian electron energy distribution function calculated as

$$f_\varepsilon = 2\sqrt{\frac{\varepsilon}{\pi T_e^3}} exp\Big(-\frac{\varepsilon}{T_e}\Big), \tag{7.9}$$

with electron energy ε and electron temperature T_e.

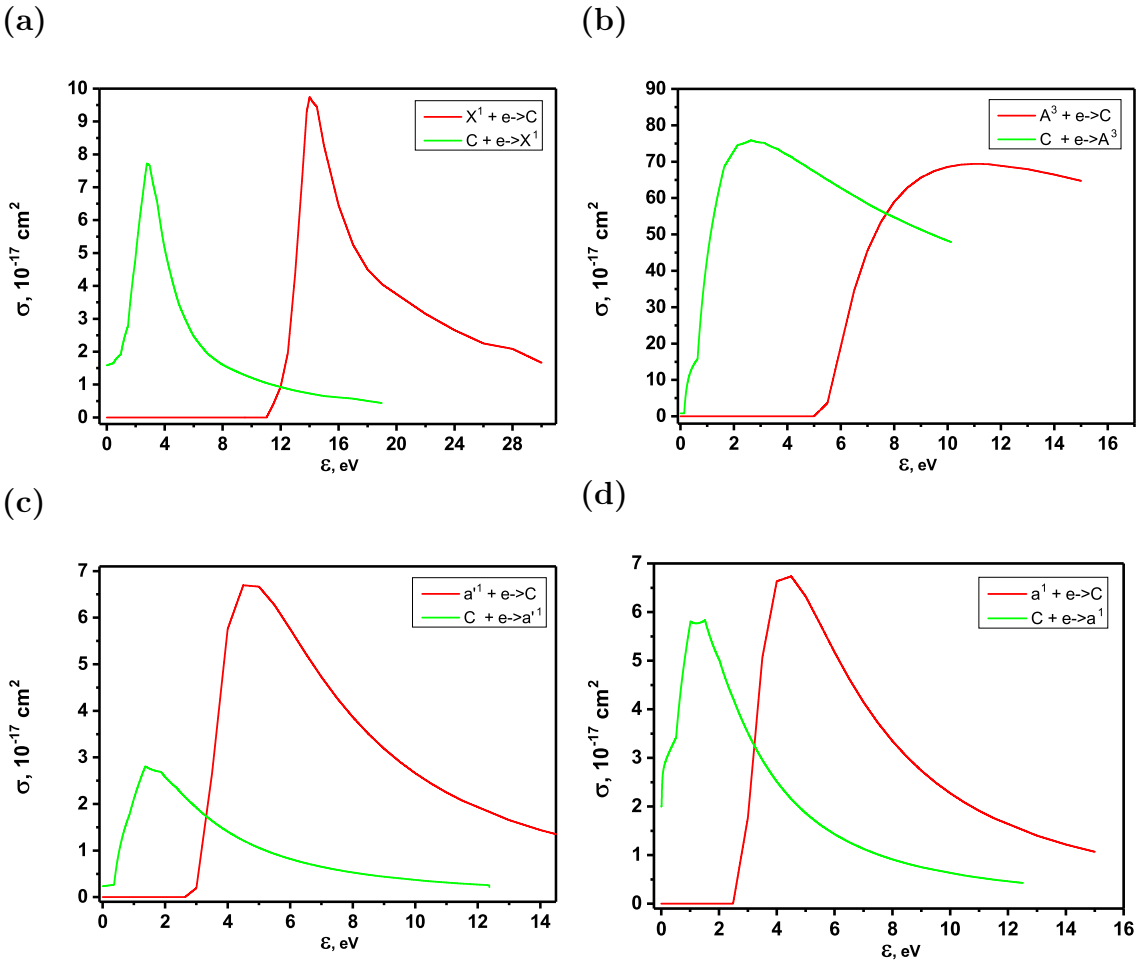

Figure 7.7 – Cross-section of excitation of $N_2(C^3\Pi_u)$ state from lower energy levels by direct electron impact [123] and cross-section for reverse processes of de-excitation of $(C^3\Pi_u)$ state to (a) $(X^1\Sigma_g^+)$, (b) $(A^3\Sigma_u^+)$, (c) $(a'^1\Sigma_u^-)$ and (d) $(a^1\Pi_g)$ due to super-elastic collisions with electrons calculated using (7.8).

The corresponding rate constants were calculated as

$$K(\varepsilon) = \sqrt{\frac{2}{m_e}} \int_0^\infty \varepsilon^{0.5} \sigma(\varepsilon) f_\varepsilon d\varepsilon, \tag{7.10}$$

here $\sigma(\varepsilon)$ is the cross-section of the considered process. In the calculations by (7.10) it is not necessary to integrate over ε up to infinity, since the integral value become almost constant at relatively low electron energies, because f_ε approaches zero rather fast, see Fig. 7.8, where Maxwellian EEDF and results of its convolution with cross-section of de-excitation from Fig. 7.6 are presented. It should be noted that for these figures calculations were performed without the normalization factors present in (7.9) and (7.10).

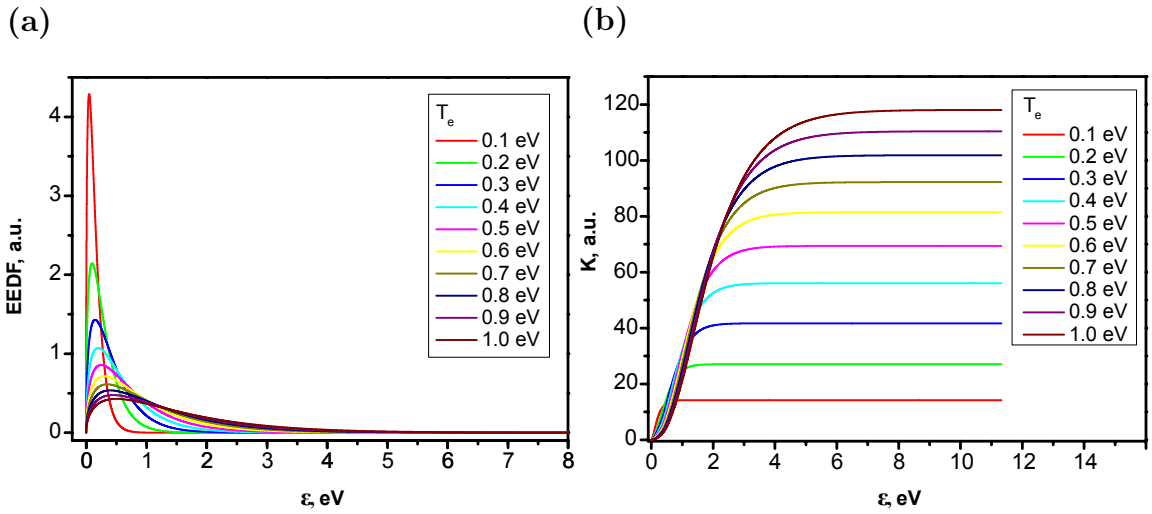

Figure 7.8 – (a) Maxwellian EEDFs used for the calculation of the quenching rate constants. (b) Value of the integral (7.10) with cross-section of de-excitation presented in Fig. 7.6.

The electron temperature in the afterglow is calculated numerically using

$$\frac{dT_e}{dt} = -\nu_u \cdot (T_e - T_v^{N_2}), \tag{7.11}$$

where ν_u is frequency of electron energy relaxation and $T_v^{N_2}$ is nitrogen vibrational temperature. The calculated dynamics of the electron temperature in the afterglow is presented in Fig. 7.9.

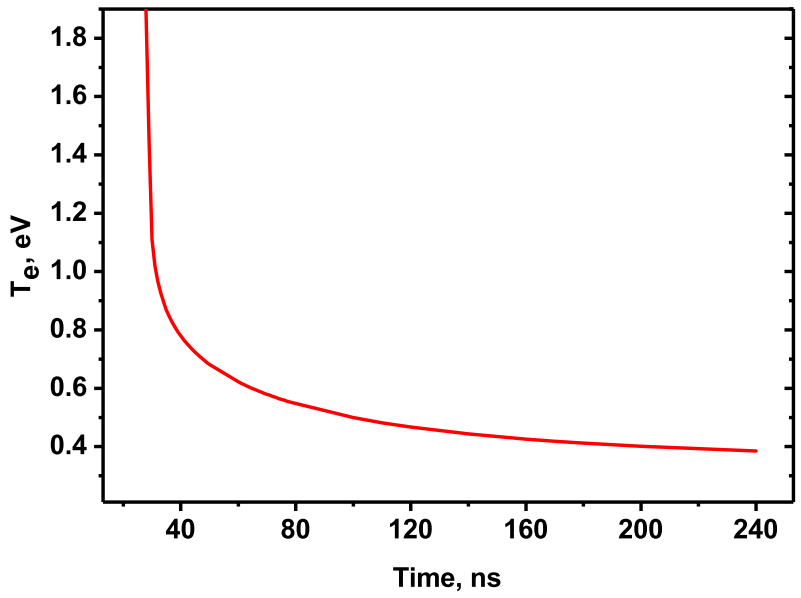

Figure 7.9 – The temporal evolution of the electron temperature in the afterglow. First pulse, pure nitrogen, 27 mbar.

The influence of the uncertainty in the initial cross-sections of excitation near the threshold on the rate constant should be discussed. The problem is that in [123] the cross-sections are presented with a rather coarse mesh in electron energy. The linear approximation near the threshold region can be not correct, since it is known from quantum mechanics [124] that near the threshold the behavior of the cross-section of excitation is proportional to $\sqrt{\varepsilon - w}$. Thus, real cross-section can be higher than the linear approximation, which can affect the results of calculations of the cross-sections of reverse process and, consequently, the resulting rate constant value. A maximum possible influence of this uncertainty can be estimated by setting the cross-section of excitation equal to some non-zero value in the threshold: $\sigma_+(w) = \sigma_0 \neq 0$. For example, the cross-section of excitation in the threshold can be artificially set equal to first known value $\sigma_+(\varepsilon_1) = \sigma_1$ from initial data table [123], or equal to some part of σ_1. The linear approximation of σ_+ between $\sigma_+(w)$ and $\sigma_+(\varepsilon_1)$ is much higher than real $\sqrt{\varepsilon - w}$ behavior for sure in this case. Therefore, the effect of this artificial overestimation of the σ_+ near the threshold is much higher than the error due to initial uncertainty in $\sigma_+(\varepsilon)$ behavior near w. In Fig. 7.10 the results of such overestimation are presented.

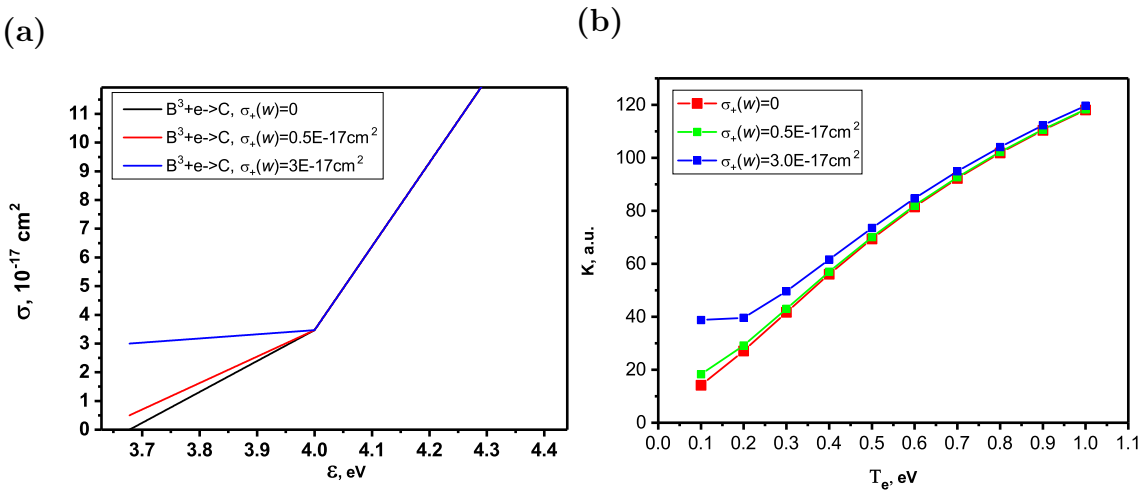

Figure 7.10 – (a) Modified threshold region of the cross-section of excitation presented in Fig. 7.6. (b) Value of the rate constant of quenching by electrons to lower electronic state calculated at different behavior of the excitation cross-section in the threshold region.

The initial cross-section from Fig. 7.6 was modified by setting $\sigma_+(w) = 0.5{\cdot}10^{-17}$ cm^2 and $\sigma_+(w) = 3 \cdot 10^{-17}$ cm^2, see Fig. 7.10 (a). This is extremely high overestimate leads to a relatively low difference (3% at $T_e = 0.3$ eV) in the rate constant, see green line in Fig. 7.10 (b). The blue line corresponds to absolutely unrealistic overestimate, but even in this case at relatively high electron temperatures (starting from 0.3 eV)

the difference with the results obtained using original data (red line) is lower than 20% and decreases further with T_e . Thus it can be stated that the influence of the uncertainty in the behavior of $\sigma_+(\varepsilon)$ near the threshold can be neglected.

The results of calculation of the rate constant of de-excitation of $N_2(C^3\Pi_u)$ to different electronic states are presented in Fig. 7.11.

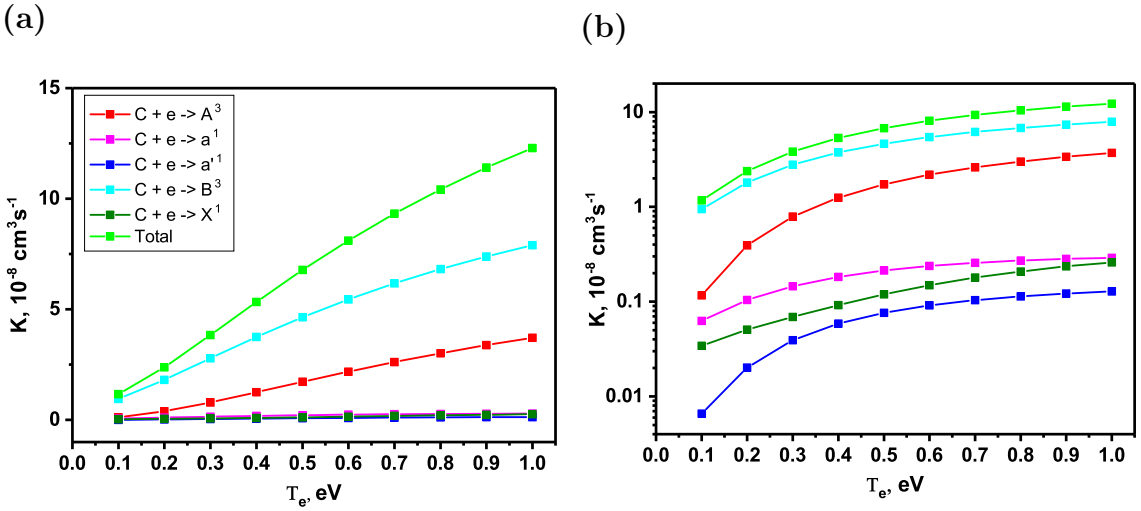

Figure 7.11 – (a) The results of the calculation of the rate constant of quenching of the $N_2(C^3\Pi_u)$ state by electrons to the different lower electronic states. (b) The same plot in the semi-logarithmic scale.

The total rate constant was calculated by summation of rate constants for quenching to $N_2(X^1\Sigma_g^+)$, $N_2(A^3\Sigma_u^+)$, $N_2(a'^1\Sigma_u^-)$, $N_2(a^1\Pi_g)$ and $N_2(B^3\Pi_g)$ states

$$K_{total} = K^{(X^1\Sigma_g^+)} + K^{(A^3\Sigma_u^+)} + K^{(a'^1\Sigma_u^-)} + K^{(a^1\Pi_g)} + K^{(B^3\Pi_g)}. \qquad (7.12)$$

One can see that the most intensive contribution in the total rate constant is given by de-excitation to $N_2(B^3\Pi_g)$ and $N_2(A^3\Sigma_u^+)$ states. De-excitation to the $N_2(W^3\Delta_u)$ and $N_2(B'^3\Sigma_u^-)$ states with energies close to the energy of the $N_2(B^3\Pi_g)$ state was not taken into account, since there are not available data for corresponding cross-section. However, in first approximation it was assumed that these cross-sections are much lower than the one for the $N_2(B^3\Pi_g)$ state, since the probability of $N_2(C^3\Pi_u) \rightarrow N_2(B^3\Pi_g)$ transition is significantly higher than for transitions to the $N_2(W^3\Delta_u)$ and $N_2(B'^3\Sigma_u^-)$ states.

In [91] a slight effect of increase, less than 10%, of the reverse decay time, has already been observed in nitrogen in nanosecond discharge at $P = 2$ Torr in the tube 2 cm in diameter. Quenching of the $N_2(C^3\Pi_u)$ state by electrons has been suggested there as an explanation. Drawin's semiempirical model [125] on the basis of Bethe–Born approximation with corrections [126] and the principle of detailed balance

were used to estimate the cross–section and finally, to calculate the rate constant. The estimate resulted in 10^{-7} cm^{3}s^{-1}. From Fig. 7.11 it follows that at electron temperature $T_e = 0.8$ eV, typical for the early afterglow in present conditions, the value of rate constant is equal to $1.04 \cdot 10^{-7}$ cm^{3}s^{-1}. Thus, the results of calculations obtained above, see Fig. 7.11, are in rather good agreement with results of [91]. Quenching of the $N_2(C^3\Pi_u)$ state by electrons was also mentioned in [127], where the rate constant was estimated as $\leq 10^{-7}$ cm^{3}s^{-1}.

To verify if the high electron density can be a reason of observed abnormally fast non-exponential decay of $N_2(C^3\Pi_u)$ emission, the experimental temporal behavior of emission of SPS(0-0) transition $N_2(C^3\Pi_u, v' = 0) \rightarrow N_2(B^3\Pi_g, v'' = 0)$ at $\lambda =$ 337.1 nm was compared with the density of $N_2(C^3\Pi_u)$ calculated under different assumptions about the value of the rate constant of the quenching by electrons.

To adequately describe quenching of electronically excited molecules by electrons, the radial distribution of electrons and exited species must be taken into account. Indeed, the highest frequency of quenching will take place in the areas with the highest density of electrons. In the most of the gas discharges, the electron density profile in the near afterglow is flatter than in the considered discharge due to efficient recombination in the areas with high charge density. However, at the considered conditions additional ionization in the afterglow is extremely important and the radial electron density distribution significantly depends on the distribution of excited molecules involved in the reactions of associative ionization (6.6) and (6.7). The averaging with different radial profiles (flat, picked or tubular distributions) also influences the results. So, all the calculations were performed in one-dimensional axisymmetric approximation. In more details the radial distributions of electrons and excited species are discussed in Chapter 8, where they are measured experimentally and compared with the results of the numerical calculations. Here, the calculations of density of $N_2(C^3\Pi_u)$ are performed with initial electron density distribution obtained in Chapter 8. The results are presented in Fig. 7.12. To verify that observed abnormally high decay of $N_2(C^3\Pi_u)$ emission is not caused by the malfunction of the experimental equipment (PMT), the results of the numerical calculations are compared both with the measurements by PMT and by measurements performed using spectrometer and ICCD camera, see Fig. 4.24. Additionally, the ICCD camera allows to increase dynamic range of the measurements by one order of magnitude in comparison with PMT. It is clearly seen that the results of numerical calculations assuming the fixed rate constant close to 10^{-7} cm^{3}s^{-1} agree with the experimental curves. Thus, it has been shown that high quenching rate of $N_2(C^3\Pi_u)$ in capillary discharge in nitrogen at high specific deposited energy is provided by quenching in collisions with electrons. The high electron density in the afterglow is sustained by reactions of associative ionization (6.6) and (6.7) described in Chapter 6.

(a)

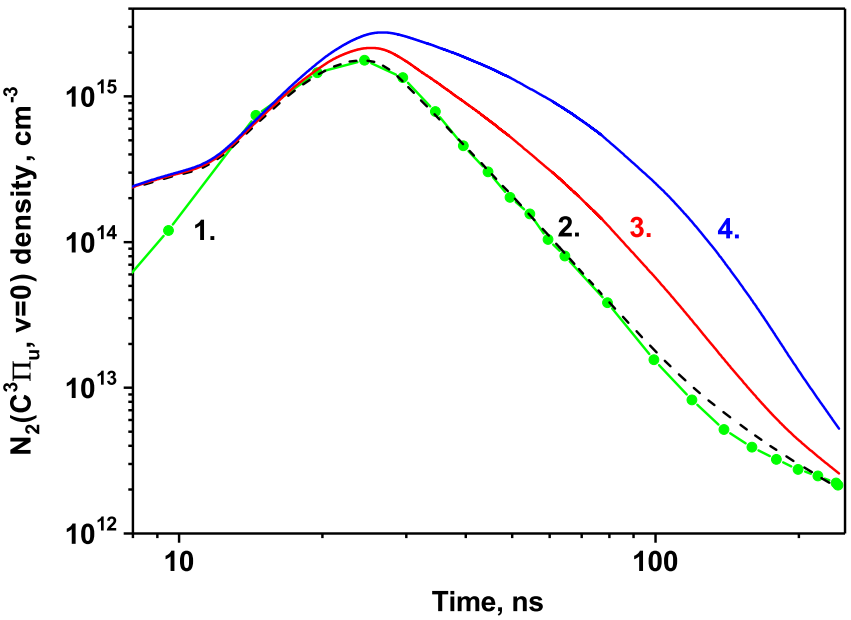

(b)

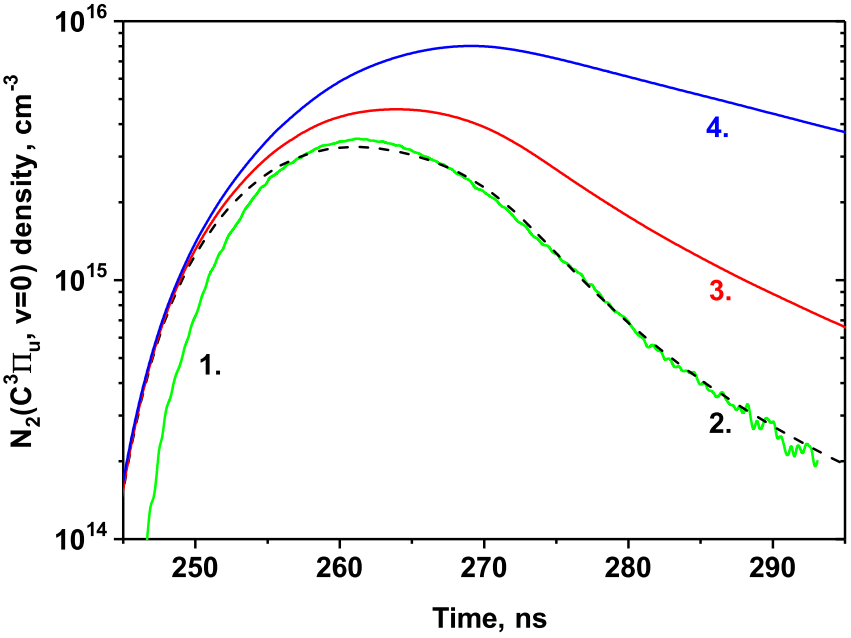

Figure 7.12 – Calculated density of $N_2(C^3\Pi_u)$ state averaged over the cross-section of the capillary tube compared to measured temporal emission profile for the first pulse coming to the capillary tube in pure nitrogen at 27 mbar with transmitted current 65 A. Curve (1) emission of SPS(0-0) in arbitrary units: (a) ICCD camera, (b) PMT; curves (2) – (4) correspond to numerical calculations with the quenching rate constant equal to 10^{-7} cm^3s^{-1}, $5 \cdot 10^{-8}$ cm^3s^{-1} and 0, respectively.

It should be noted here that the quenching of the $N_2(C^3\Pi_u)$ state by electrons is most likely the reason for the negative value of the rate of the population by electron impact $Y_C(x,t)$ calculated based on data from Fig. 4.24 using (4.12), see Fig. 4.25, since the quenching by electrons is not taken into account in (4.12).

For the $N_2^+(B^2\Sigma_u^+)$ state the quenching by electrons is also pronounced in the afterglow, since the rate constant value close to the one for the $N_2(C^3\Pi_u)$ state at $T_e = 0.8$ eV, see Fig. 7.13. The cross-section of the direct process was taken from [123].

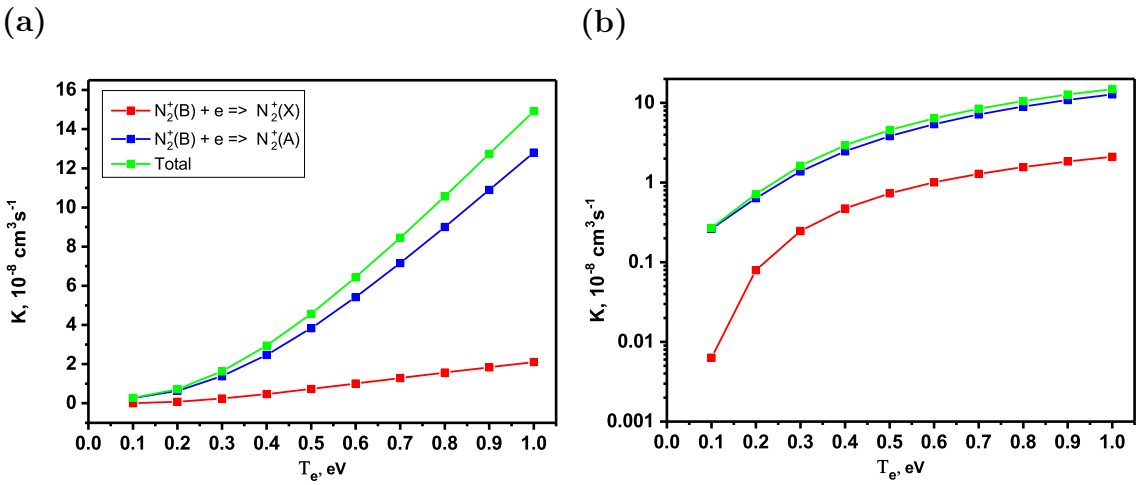

Figure 7.13 – (a) The results of the calculation of the rate constant of quenching of the $N_2^+(B^2\Sigma_u^+)$ state by electrons to the different lower electronic states. (b) The same plot in the semi-logarithmic scale.

The characteristic lifetime of the $N_2^+(B^2\Sigma_u^+)$ state is equal to 4.9 ns, if the quenching by electrons is taken into account even with high density $N_e = 5\cdot10^{14}$ cm^{-3}. The radiative decay and the quenching by molecular nitrogen provides effective lifetime equal to 6.4 ns, which is slightly higher. The additional depopulation is noticeable both in FIW and in the early afterglow and leads to the negative value of the rate of the population by electron impact $Y_B(x,t)$ calculated using (4.12), see Fig. 4.25.

It should be noted that under conditions different from the discharge studied in present Thesis, quenching of the $N_2^+(B^2\Sigma_u^+)$ state by electrons also can be noticeable. For example, in [128], where OES of nitrogen was used in studies of the laser oblation of metals, quenching of the $N_2^+(B^2\Sigma_u^+)$ state by electrons was the reason of the decay of FNS(0-0) band faster than predicted based on the rates of quenching by the background gas.

The quenching of other excited states of molecular nitrogen by electrons is also possible. The rate constants of the quenching of the $N_2(B^3\Pi_g)$ and $N_2(A^3\Sigma_u^+)$ states by electrons were calculated using the same technique. The cross-sections of the

direct processes were taken from [123] and [4, 129], respectively. The results are presented in Fig. 7.14 and Fig. 7.15.

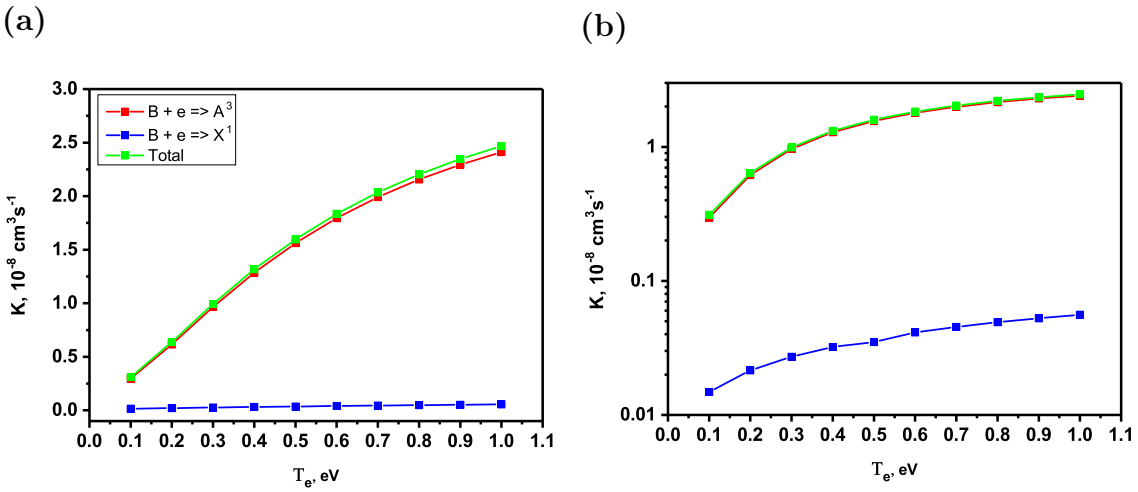

Figure 7.14 – (a) The results of the calculation of the rate constant of quenching of the $N_2(B^3\Pi_g)$ state by electrons to the different lower electronic states. (b) The same plot in the semi-logarithmic scale.

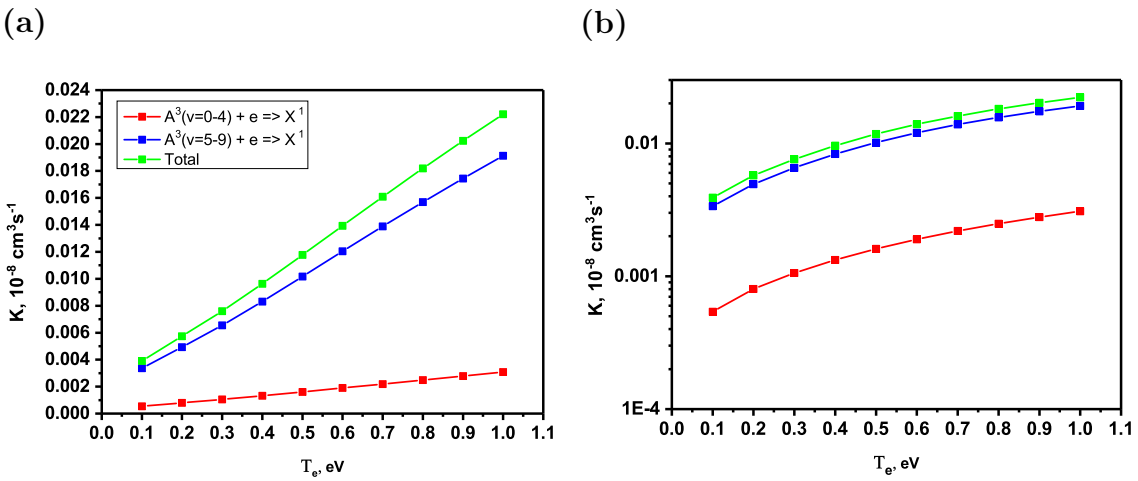

Figure 7.15 – (a) The results of the calculation of the rate constant of quenching of the $N_2(A^3\Sigma_u^+)$ state by electrons to the ground state of the molecular nitrogen. (b) The same plot in the semi-logarithmic scale.

At the electron temperature $T_e = 0.8$ eV the rate constant of the quenching of the $N_2(B^3\Pi_g, v')$ state by electrons is equal to $2.2 \cdot 10^{-8}$ cm^{3}s^{-1}, which is 4.5 times lower than for the $N_2(C^3\Pi_u)$ state. However, if the quenching by electrons with density $N_e = 5 \cdot 10^{14}$ cm^{-3} is taken into account, the effective lifetime of the $N_2(B^3\Pi_g, v')$ state is reduced to 56 ns, while the radiative decay and the quenching by molecular nitrogen provide effective lifetime equal to 147 ns, see blue lines in

Fig. 4.28. Nevertheless, the observed effective lifetime of 30 ns is about 2 times lower than quenching by electrons taken into account provides. Thus, there is an additional process depopulating the $N_2(B^3\Pi_g, v')$ state. It will be discussed in Chapter 9.

7.3 Conclusion

The decay of optical emission of the second positive system of molecular nitrogen was studied experimentally in pure nitrogen and nitrogen:oxygen mixtures. It was observed that decay of the $N_2(C^3\Pi_u, v = 0)$ state is abnormally fast and demonstrate bi-exponential behavior. The detailed studies for pure nitrogen demonstrates that the additional collision process, which is not taken into account usually in kinetics models, is responsible for the quenching of the $N_2(C^3\Pi_u, v = 0)$ state. It was proposed that additional quenching process is super-elastic collisions with electrons. The estimation of the corresponding cross-sections of de-excitation of the $N_2(C^3\Pi_u, v = 0)$ state to the lower energy levels of N_2 was performed based on the principle of the detailed balance and the cross-section of the excitation from the lower states to the $N_2(C^3\Pi_u, v = 0)$ state available in the literature. The good agreement between the experimentally measured emission profile of the SPS(0-0) and density of the $N_2(C^3\Pi_u, v = 0)$ state calculated numerically using the estimated rate constant value was obtained. Thus, it was proved that quenching of the $N_2(C^3\Pi_u, v = 0)$ state by electrons is responsible for its abnormally fast decay.

The estimations of the rate constants of the quenching of the $N_2^+(B^2\Sigma_u^+)$ state and the $N_2(B^3\Pi_g, v')$ state by electrons were performed. It was shown that the quenching of the $N_2^+(B^2\Sigma_u^+)$ state is almost not pronounced. It was demonstrated that quenching of the $N_2(B^3\Pi_g, v')$ state by electrons is significant, however, it is not high enough to explain abnormally fast decay of the $N_2(B^3\Pi_g, v')$ state presented in Chapter 4. Thus, it was concluded that there is an additional collisional process of the $N_2(B^3\Pi_g, v')$ state depopulation , which will be discussed in Chapter 9.

Observed depopulation of the $N_2(C^3\Pi_u, v = 0)$ state due to quenching by electrons with high density sustained by the reactions of the associative ionizations in the afterglow confirms that plasma kinetics under the conditions of the high energy deposition at high reduced electric fields changes dramatically.

Chapter 8

Radial distribution of excited species

Optical emission from the discharge can be used not only for measurement of temporal evolution of total density of a given excited specie, but also for investigation of the spatial distribution of the species in the discharge and the afterglow. Measuring the light from the fast discharges, the experimentalist should make a choose between the photomultiplier tube (PMT) and the ICCD camera. Both provide high temporal resolution (0.6–0.7 ns for modern PMTs, and 0.2–0.5 ns for modern ICCD cameras). The gain of the PMTs based on "traditional" system of separated dynodes, typically reaches $10^5 - 10^6$, while for the ICCDs, using the micro-channel plates (MCP) for amplification of electrons, the gain is on order $10^4 - 10^5$. So, the gain of the PMTs are higher and they are efficiently used to measure the time-resolved signals. However, all information about spatial distribution of elementary light sources (excited molecules, atoms, etc.) is lost, in this case. To measure the spatial distribution of the light sources the ICCDs are used.

If the electric field is uniform and high enough (to neglect the decay processes), the radial distribution of the excited species copies the radial distribution of electron density. Thus, the spatial distribution of excited species can give extremely important information about initial electron density distribution formed after FIW propagation. The further discharge development and energy deposition are determined by the initial electron density profile, which affects the main observed effects, for example, the fast gas heating. Moreover, the knowledge of the distribution of excited species is required for the correct comparison of the results of 1D numerical calculations and the experiment results presenting integral and averaged values, for example, the emission intensity discussed above, see Fig. 7.12 and the rotational

structure of the molecular band transition (i.e. the rotational temperature of the gas), see Section 9.1, respectively.

In this Chapter, the experimental and mathematical techniques for measuring of the distribution of excited species are presented. The validity of these techniques is discussed. The experimental results and the results of numerical 1D calculations are presented.

8.1 Applicability of the technique used for reconstruction of the electron density profile

As it was mentioned above, the radial distribution of the excited species copies the radial distribution of electron density, only if the electric field is uniform and high enough to neglect the decay processes. In this subsection, the validity of these assumptions are discussed.

In [9,63] it was shown for the same discharge geometry that the electric field has complex structure in the FIW front only, while in the current stage it is uniform and directed along the main axis of the tube. The electric field in FIW is higher than at current stage. However, the electron density profile determining the further discharge development is formed during the current stage of the discharge, since it is much longer than FIW stage. Thus, it can be assumed that E/N is uniform.

The behavior of the density of the $N_2(C^3\Pi_u)$ state used for electron density profile reconstruction is described by

$$\frac{d}{dt}[\mathrm{N_2(C)}](r) = k^e_{exc} N_e(r)[\mathrm{N_2}] - k^e_q N_e(r)[\mathrm{N_2(C)}](r) - \\ -k^{\mathrm{N_2}}_q[\mathrm{N_2}][\mathrm{N_2(C)}](r) - [\mathrm{N_2(C)}](r)/\tau_0, \tag{8.1}$$

where $[X](r)$ denotes density of the specie X at point with radius r, $N_e(r)$ is the electron density, k^e_{exc} is the rate constant of the excitation by electron impact, k^e_q is the rate constant of the quenching by electrons, $k^{\mathrm{N_2}}_q$ is the rate constant of the quenching by nitrogen, τ_0 is the radiative lifetime. The decay described by the last two terms in the right hand side of (8.1) does not change shape of the radial distribution of the $N_2(C^3\Pi_u)$ state, since $k^{\mathrm{N_2}}_q[\mathrm{N_2}]$ and τ_0 are constant over tube radius. Moreover they are less intensive than quenching by electrons, as it was shown in Chapter 7. Thus, the excitation term $k^e_{exc} N_e(r)[\mathrm{N_2}]$ should be compared with $k^e_q N_e(r)[\mathrm{N_2(C)}](r) \propto k^e_q N_e(r)^2$, which leads to transformation of the profile shape. The ratio between these two terms is presented in Fig. 8.1. The ratio is calculated using the profile of the electric field value shown in Fig. 4.7 and the $N_2(C^3\Pi_u)$ state density presented in Fig. 7.12 (a). One can see that two terms become comparable

only at 18 ns. The reasonable threshold $k^e_{exc}N_e(r)[\mathrm{N_2}]/k^e_qN_e(r)[\mathrm{N_2(C)}](r) = 10$ corresponding to noticeable profile transformation is reached only at 12 ns. Thus, it can be concluded that during first $\approx$ 12 ns the radial distribution of the $\mathrm{N_2(C^3\Pi_u)}$ state can be used to reconstruct initial electron density profile.

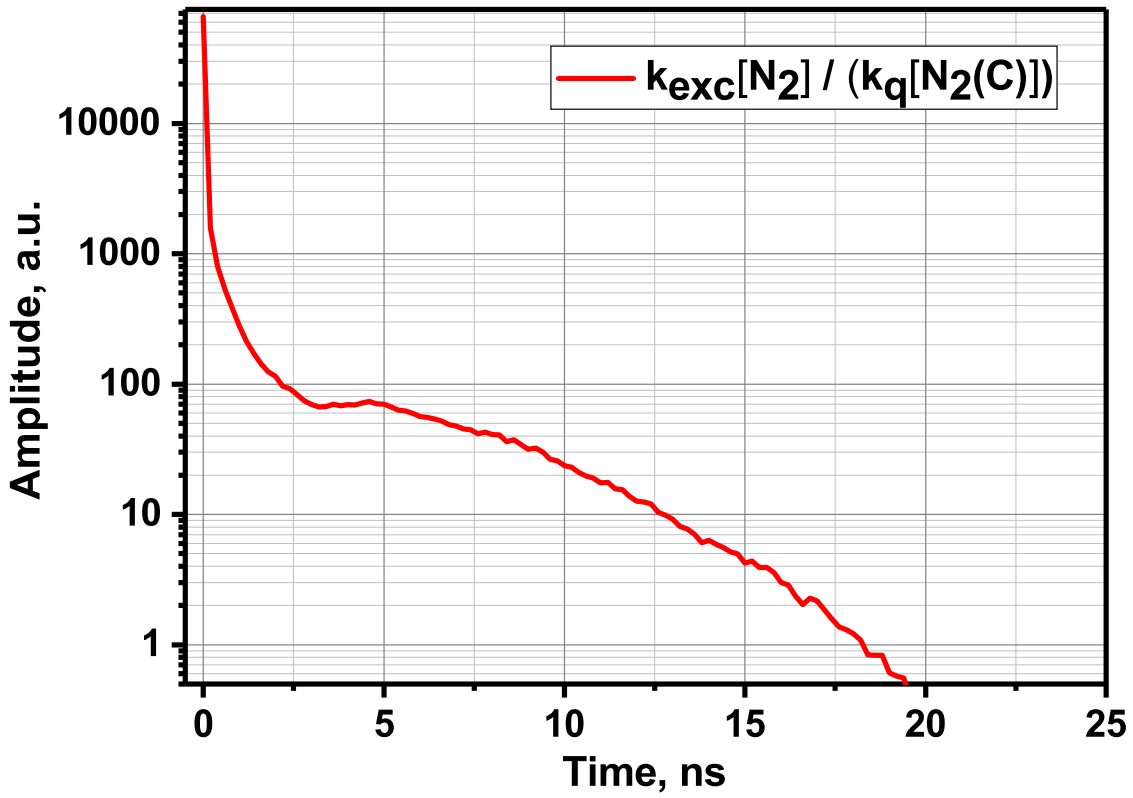

Figure 8.1 – The ratio between intensity of population of the $\mathrm{N_2(C^3\Pi_u)}$ state and depopulation due to quenching by electrons leading to the profile shape transformation. The ratio is calculated based on data from Fig. 4.7 and Fig. 7.12 (a).

8.2 Experimental results

To check the optical system adjustment, the image of the capillary tube illuminated by a LED lamp was acquired without a narrow band filter. The image is presented in Fig. 8.2. This image was also used to identify the pixels corresponding to the outside boundaries of the tube. The pixels corresponding to the internal walls of the tube were determined from external boundary coordinates and known geometry of the tube (internal and external radii). Thus, the external diameter (3.0 mm) corresponds to 130 pixels on ICCD image, and 75 pixels are related to the internal diameter (1.75 mm), consequently. The image of the tube is located in the center region of the ICCD matrix to avoid the influence of the edge effects.

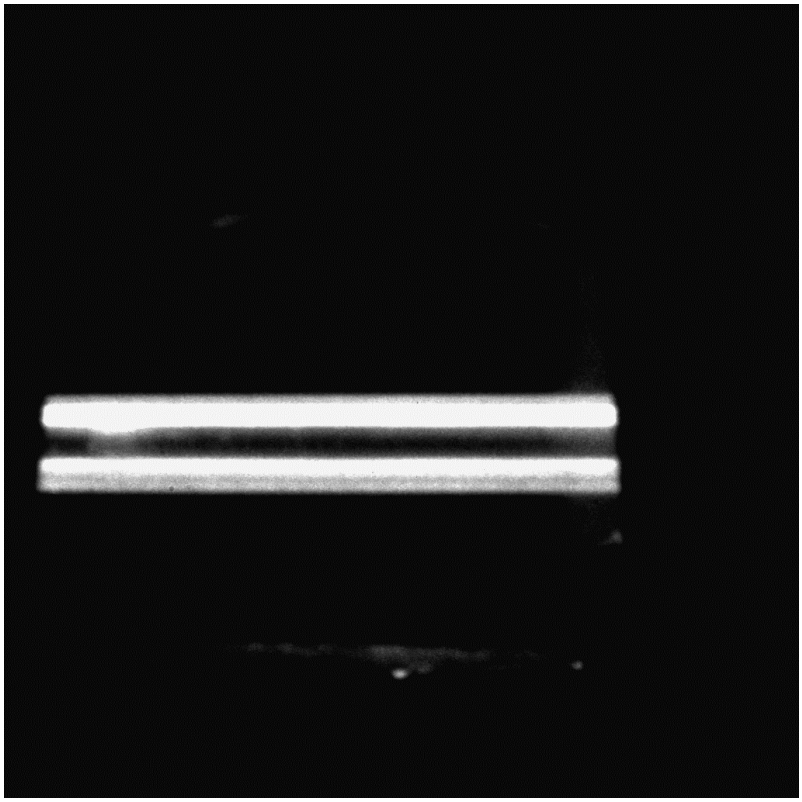

Figure 8.2 – The image of the capillary tube illuminated by LED lamp acquired with the optical system used to measure radial distribution of $\mathbf{N_2(C^3\Pi_u, v' = 0)}$ state.

The data collected by ICCD camera were treated by the code created using LabView package. After background subtraction, the cross-section was constructed by averaging of 500 columns of pixels in the central part of the image of the tube. Further, the obtained profile was split into two symmetrical parts, which were averaged to decrease the influence of a random noise. However, to use the mathematical procedure described in Section 3.2.4 successfully, the noise should be decreased additionally. To decrease the noise, smoothing using Savitzky-Golay method [130, 131] with 3rd polynomial order at 18 points of the window was performed. The results of smoothing of a few experimental profiles are presented in Fig. 8.3. It is seen that the smoothed profiles repeat the behavior of the experimental profile.

In Fig. 8.4 one of the obtained profiles is presented (blue line). The gray transparent line denotes the position of the boundary of the volume of the plasma (the inner diameter of the quartz wall). One can see that emission in this point is not zero. This in contradiction with the discussion in Section 3.2.4, where it was concluded that the capillary discharge emission parallel to the optical axis can be considered as emission from the plasma channel fixed in the free space without any wall, which means that emission intensity should be zero at $r \geq r_{internal}$.

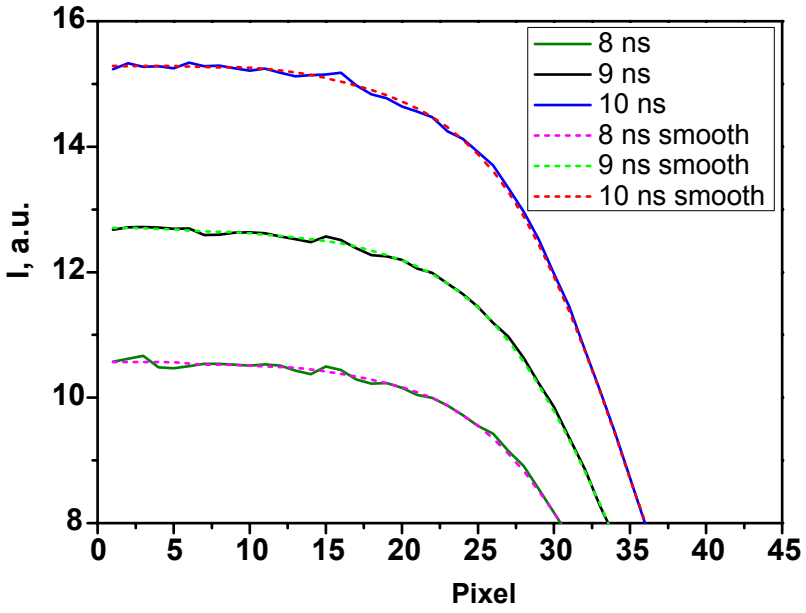

Figure 8.3 – The example of the experimental profiles with results of smoothing performed to decrease noise.

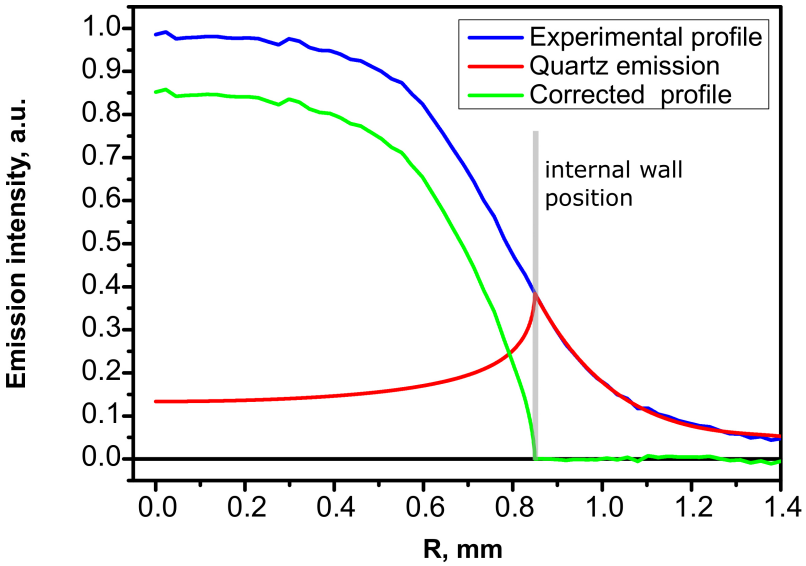

Figure 8.4 – Emission profile correction using manually defined distribution of emission caused by light scattering in the quartz wall. Blue line is the experimental profile, red line is the result of Abel transform (3.12) **of the distribution of emission due to light scattering defined by** (8.2)**. Green line corresponds to resulting corrected emission profile.**

In Section 3.2.4 the quartz was considered as a perfectly transparent medium without any light scattering. However, it is known that quartz diffuses light even without any defects and inhomogeneities in the volume [132]. The scattered light is not negligible, because the volume of the quartz wall filled by the photons is

comparable with the volume of the plasma. Moreover, the required optical system is constructed so that it cuts dramatically the emission of the plasma, selecting the parallel beams only. On the contrary, each elementary volume of quartz diffuses a large number of beams traveling in the quartz wall (see Fig. 3.14), thus total diffused light from any point in the quartz is comparable with direct emission from the plasma. In addition, the diffused emission is caused not only by beams lying in the cross-section of the capillary, but by the light traveling along the capillary tube with a non-zero angle to the axis.

The beams traveling along the capillary tube with a non-zero angle to the axis are partially reflected on the boundaries of the wall and go back in the volume many times before the light leaves the quartz volume. This distributes diffused light along the tube uniformly. Therefore, for each of 500 columns of pixels averaged to obtain the intensity profile the contribution of the light scattering is the same, since the region of interest is much shorter than the entire capillary tube and located far away from the ends of the tube, where the homogeneity is impaired.

If the distribution of the light scattered by quartz along the tube can be assumed as uniform, its radial distribution is unknown and can not be calculated directly. However, one can make an assumption about the radial distribution of the scattered light and compare the result of its Abel transform (3.12) with the part of the experimental profile at $r \geq r_{internal}$.

Finally, it was assumed that the intensity of the scattered light is described by a sum of the two exponential decays with the same decay rates from the boundary plasma-quartz and from the boundary quartz-air to the internal volume. This distribution can be written as

$$I_{quartz}(r) = A_1 \cdot \theta(r - r_{int})\theta(r_{ext} - r)\left(e^{\frac{-|r-r_{int}|}{\alpha}} + A_2 e^{\frac{-|r-r_{ext}|}{\alpha}}\right). \tag{8.2}$$

Here r_{int} and r_{ext} are internal and external radii, respectively, A_1 is amplitude of the scattered light determined from the intensity at r_{int}, A_2 is weight of the second exponential decay, α is decay rate, and $\theta(r - r_0)$ is a Heaviside step function defined as

$$\theta(r - r_0) = \begin{cases} 0 & r < r_0, \\ 1 & r \geq r_0. \end{cases} \tag{8.3}$$

The Abel transform (3.12) of the distribution described by (8.2) gives a red curve in Fig. 8.4. The values A_2 and α determined from this figure are

$$\begin{aligned} A_2 &= 0.175, \\ \alpha &= 0.175. \end{aligned} \tag{8.4}$$

The model distribution of the scattered light intensity is presented in Fig. 8.5.

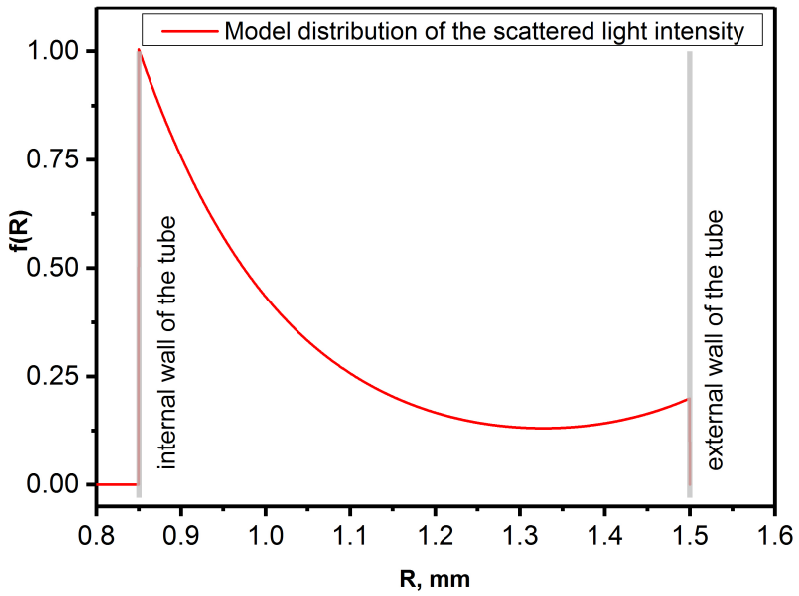

Figure 8.5 – The model distribution of the scattered light intensity described by (8.2) **with parameters** (8.4)**.**

One can see that these values give a rather good agreement between the results of Abel transform of (8.2) and the experimental emission profile at $r \geq r_{internal}$. It is extremely important that these values are the same for all experimentally measured profiles, see Fig. 8.6. This confirms the validity of the proposed correction of experimental profiles.

The profiles prepared as described above (smoothed and corrected) were used to reconstruct the distribution of $N_2(C^3\Pi_u, v' = 0)$ state of molecular nitrogen. The results of reconstruction of radial distribution of $N_2(C^3\Pi_u, v' = 0)$ state are shown below. The experiment was performed for negative polarity high voltage pulse with amplitude 13.5 kV in the cable and 20 ns FWHM at average transmitted current value equal to 65 A in pure nitrogen at 55.5 mbar. The normalized profiles for first ten nanosecond (with 1 ns time resolution) demonstrate that at first ten nanoseconds the profiles have the same shape, see Fig. 8.7 (profiles for 1 ns and 2 ns are omitted because of high noise). As it was shown in Section 8.1, at this timescale electric field is high enough to neglect decay processes and distribution of the $N_2(C^3\Pi_u, v' = 0)$ state is determined by radial electron density profile. One can see that the initial profile of $N_2(C^3\Pi_u, v' = 0)$ (i.e. electron density profile) increases with radius and has a maximum near the periphery of the tube. The profile confirms that the inverse Abel transform (3.13) is not valid here, as was assumed in Section 3.2.4.

The measurements for the pressure of 27 mbar of pure nitrogen and positive polarity high voltage pulses with amplitude 9.3 kV in the cable and 30 ns FWHM

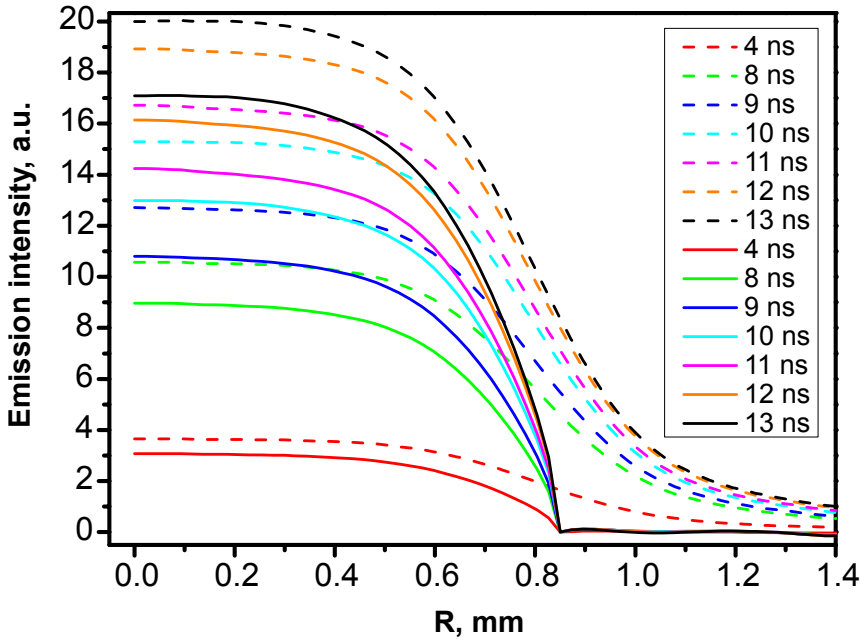

Figure 8.6 – Emission profiles correction at different time instants. Solid lines are the experimental profiles, dashed lines are the corrected emission profiles. Correction of all profiles is performed with the same values of parameters of the model distribution of scattered light intensity (8.2).

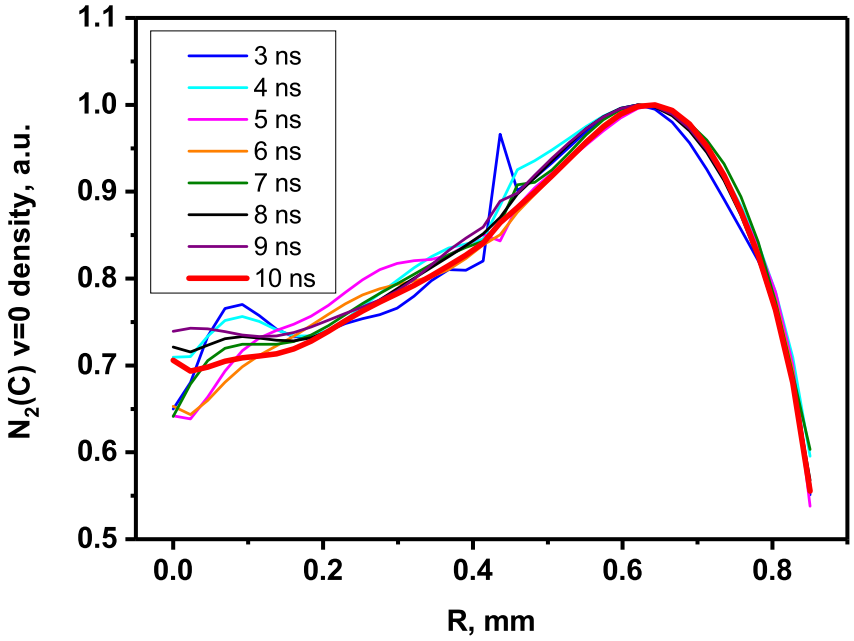

Figure 8.7 – Normalized experimentally measured radial distribution profiles of $N_2(C^3\Pi_u, v' = 0)$ state during first 10 nanoseconds in pure nitrogen at 55.5 mbar, negative polarity high voltage pulses (amplitude 13.5 kV in the cable, 20 ns FWHM).

at the same transmitted current value, demonstrate the same behavior of the radial distribution of the $N_2(C^3\Pi_u, v' = 0)$ state. During first twelve nanoseconds (with 2 ns time resolution) the radial distribution profiles of $N_2(C^3\Pi_u, v' = 0)$ state are similar to each other, see Fig. 8.8.

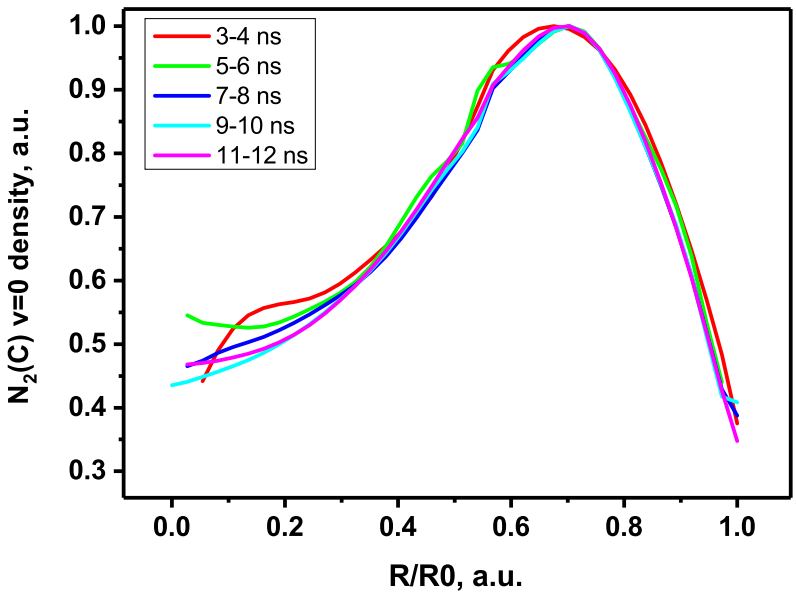

Figure 8.8 – Normalized experimentally measured radial distribution profiles of the $N_2(C^3\Pi_u, v' = 0)$ state during first 12 nanoseconds in pure nitrogen at 27 mbar, positive polarity high voltage pulses (amplitude 9.3 kV in the cable, 30 ns FWHM).

During this time, according to Fig. 8.1, the excitation by direct electron impact is more than 10 times higher than depopulation process leading to the profile shape transformation. Thus, the obtained radial distribution profile of the $N_2(C^3\Pi_u, v' = 0)$ state emission measured during first few nanoseconds can be considered as initial electron density profile. One can see from Fig. 8.8 that at positive polarity pulses the distribution of electron density has the maximum on the periphery of the cross-section of the capillary tube similarly to negative polarity discharge.

As it was mentioned in Chapter 1, the maximum of the electron density on the periphery of the cross-section of the capillary tube can be explained by interaction of UV radiation emitted by excited nitrogen species with the quartz wall of the capillary tube [78, 80]. The quartz wall absorbs UV photons and emits electrons to the gas volume near the wall [133], which facilitates the discharge propagation and further electron production in this region. It was also mentioned in Chapter 1 that the tubular structure of the discharge can be caused by increasing of the electric field near the wall due to the jump in dielectric permittivity [78, 80]. However, as it was mentioned above, the electric field is uniform and longitudinal in the cross-section

of the capillary tube during electron density profile formation. So, it seems that the main mechanism of the tubular discharge formation is the UV irradiation of the quartz wall.

This assumption can be verified by addition of molecular oxygen in the pure nitrogen. It is well-known that photo-ionization of oxygen molecules by UV radiation from the nitrogen species is very efficient [134]. It can be very important for the discharge development in oxygen/nitrogen mixtures, for example, it plays the key role in the streamer head propagation in air [135, 136]. If pure nitrogen in the capillary tube is diluted by oxygen, there is an additional source of seed electrons ahead of the FIW front, it is photo-ionization of oxygen molecules. Photo-ionized oxygen is volumetric source of seed electrons, while quartz wall is surface one. Since the UV radiation from excited molecules is isotropic, the most intensive ionization takes place near tube axis, since in this region the solid angle, from which the radiation is collected by O_2 molecules, is higher than in the region, where the solid angle is limited by the presence of the quartz wall. The balance between intensities of two sources of seed electrons due to photo-ionization (surface of the quartz wall and oxygen molecules) determines the position of the maximum of electron density during the discharge development. It can be assumed that the maximum of the electron density shifts from the periphery of the cross-section of the capillary tube to the axis of the tube with the oxygen fraction increase. For example, the similar transformation of the discharge structure was observed in [79], when the molecular nitrogen has been replaced by dry air, see Fig. 1.19.

To verify the assumption the measurements of the initial radial distribution of the $N_2(C^3\Pi_u, v' = 0)$ state emission have been performed for the N_2:O_2 mixtures with oxygen volumetric fraction equal to 0.01, 0.05, 0.1 and 0.2. The results of the measurements are presented in Fig. 8.9.

One can see that even 1% of molecular oxygen leads to profile change. The maximum is still on the periphery of the discharge tube, however, the difference between $N_2(C^3\Pi_u, v' = 0)$ density (or electron density) on the axis and the maximum value on the periphery decreases. The profile became flatter. It is also clearly seen that at 5% of molecular oxygen admixture the maximum of electron density is on the tube axis. Further increase of the oxygen percentage leads to higher gradient of the electron density. Thus, the experimental results confirm the assumption about role of the photo-ionization in the initial electron density profile formation. The obtained initial electron density profiles will be used in the numerical calculations of fast gas heating in Chapter 9.

It was shown above that the shape of the radial distribution of $N_2(C^3\Pi_u, v' = 0)$ state emission does not change during the discharge development (first 12 ns), since the electric field is high enough to neglect the decay processes. When the electric

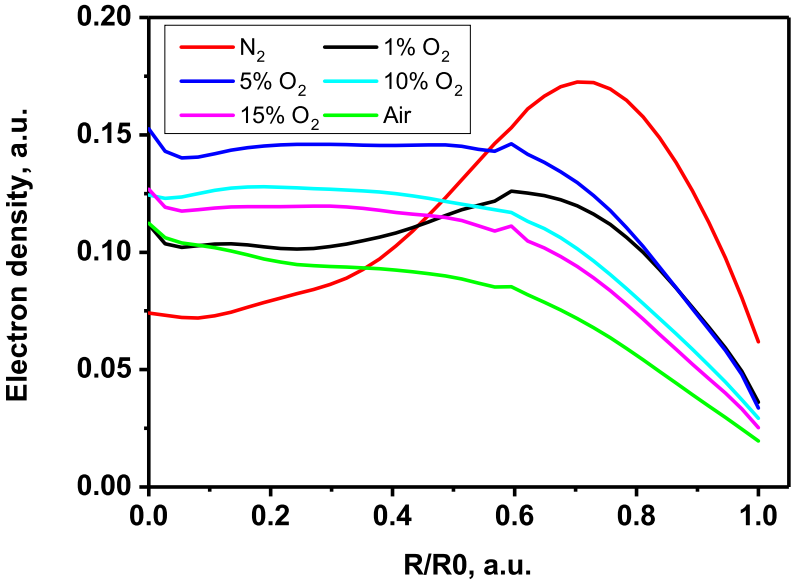

Figure 8.9 – Experimentally measured initial radial distribution profiles of $N_2(C^3\Pi_u, v' = 0)$ state at 27 mbar in different N_2:O_2 mixtures, positive polarity high voltage pulses (amplitude 9.3 kV in the cable, 30 ns FWHM).

field decrease, the decay processes become important and affect the $N_2(C^3\Pi_u, v' = 0)$ state population. In "classical" plasma kinetics (at low energy deposition) the decay rates of the excited species are constant in the tube cross-section, since the radiative decay is a constant value for given specie and since the density of quenchers, i.e. background gas, is uniform at time scale faster than gas dynamic time scale. As it was shown in Chapter 7, under the conditions of high specific energy deposition at high reduced electric field the additional collisional process leading to excited species decay takes place: the quenching by electrons. The decay rate due to this process depends on the electron density and the density of $N_2(C^3\Pi_u, v' = 0)$ state, which are not uniform in the cross-section of capillary tube from the very beginning of the discharge, as it was shown above, see Fig. 8.8. The maximums of the profiles in pure nitrogen are on the periphery of the cross-section of the capillary tube. Therefore, the quenching of $N_2(C^3\Pi_u, v' = 0)$ by electrons is more intense in this region. Consequently, the population of the $N_2(C^3\Pi_u, v' = 0)$ state decreases faster, see Fig. 8.10, where experimentally measured profiles are presented for pure nitrogen at positive polarity high voltage pulse. The profiles at 1 ns and 10 ns time instants have the same shape. The difference between the periphery and the axis of the tube is lower for the profile at 20 ns time instant than for the initial profile. At 30 ns profile this difference decrease further. At 40 ns one can see that central part of the profile is almost flat.

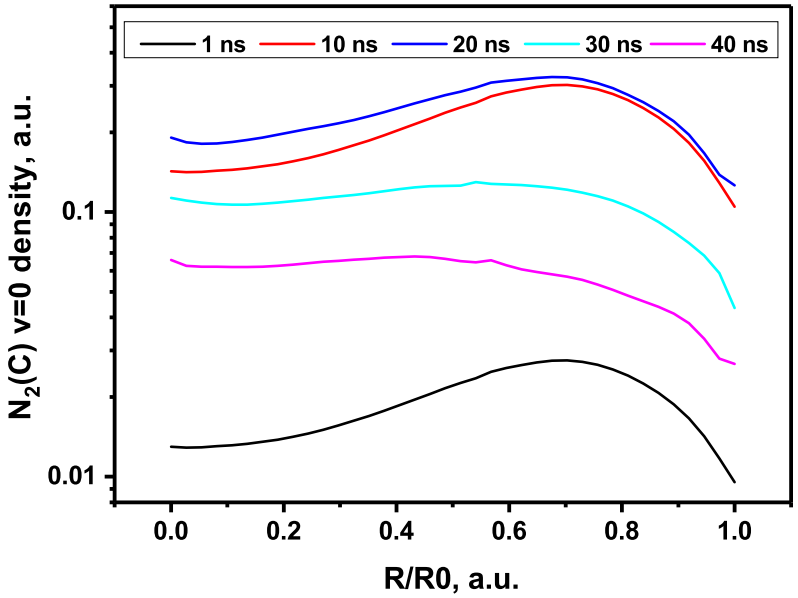

Figure 8.10 – Experimentally measured time evolution of the radial distribution profiles of the $N_2(C^3\Pi_u, v' = 0)$ state at 27 mbar in pure nitrogen, positive polarity high voltage pulses (amplitude 9.3 kV in the cable, 30 ns FWHM).

The same behavior of the profiles is observed at negative polarity high voltage pulse, see Fig. 8.11 and Fig. 8.12, where the experimentally measured profiles are presented for time instants 5-10 ns and 15-40 ns, respectively.

At the end of high voltage pulse, the radial profile of the $N_2(C^3\Pi_u, v' = 0)$ state becomes flatter, see green (20 ns) and blue (24 ns) curves in Fig. 8.12, with further more intense decay near the periphery of the tube cross-section. The evolution of the radial profiles of the $N_2(C^3\Pi_u, v' = 0)$ state was also studied numerically. The results of the numerical calculations are presented in Fig. 8.13. The calculated electron density profiles are also presented in Fig. 8.13. The calculations are performed for the discharge in pure nitrogen at 27 mbar initiated by positive polarity high voltage pulses with 9.3 kV amplitude and 30 ns FWHM.

One can see that time evolution of the calculated radial profiles of the density of the $N_2(C^3\Pi_u, v' = 0)$ state is similar to the evolution of the radial profiles of the $N_2(C^3\Pi_u, v' = 0)$ emission observed in the experiments, compare Fig. 8.10 and Fig. 8.13(a,b). The influence of quenching by electrons on the radial profile of the $N_2(C^3\Pi_u, v' = 0)$ state is clearly seen. The comparison of the radial profiles of the $N_2(C^3\Pi_u, v' = 0)$ density, Fig. 8.13(a,b), and the radial profiles of the electron density, Fig. 8.13(c,d), clearly demonstrate that decay of the $N_2(C^3\Pi_u, v' = 0)$ state is higher in the region with higher electron density. It is also seen that the electron density is sustained in this region by the reactions of associative ionization

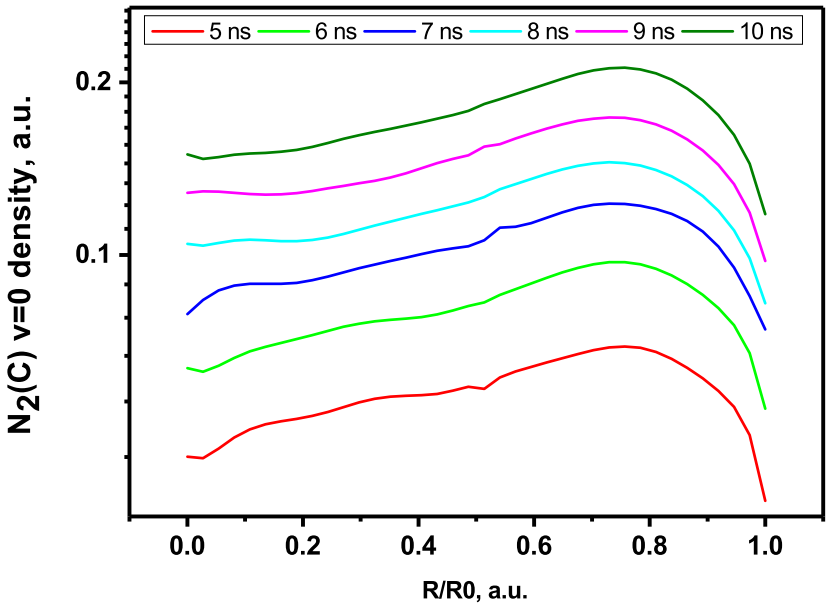

Figure 8.11 – Experimentally measured radial distribution of the $N_2(C^3\Pi_u, v' = 0)$ state at time instants 5-10 ns in pure nitrogen at 55.5 mbar, negative polarity high voltage pulses (amplitude 13.5 kV in the cable, 20 ns FWHM)

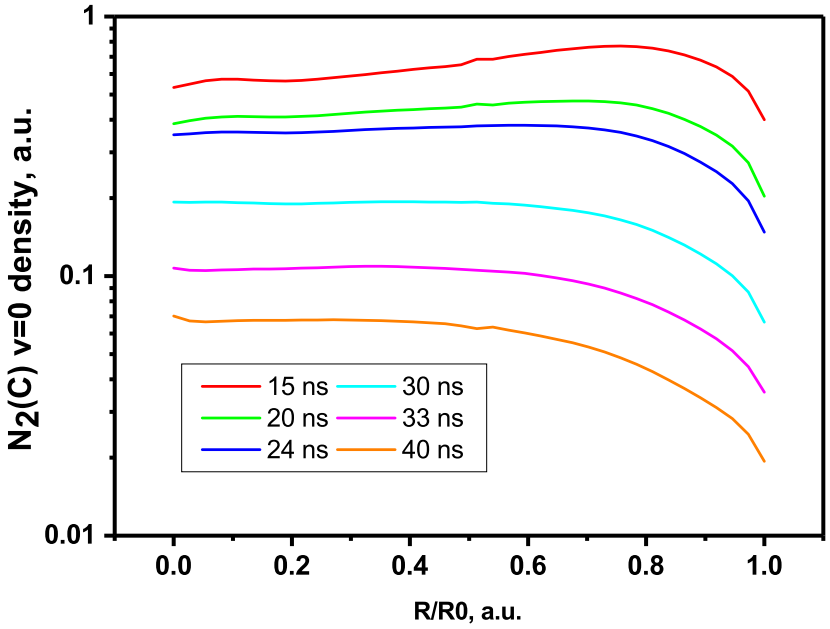

Figure 8.12 – Experimentally measured radial distribution of the $N_2(C^3\Pi_u, v' = 0)$ state at time instants 15-40 ns in pure nitrogen at 55.5 mbar, negative polarity high voltage pulses (amplitude 13.5 kV in the cable, 20 ns FWHM).

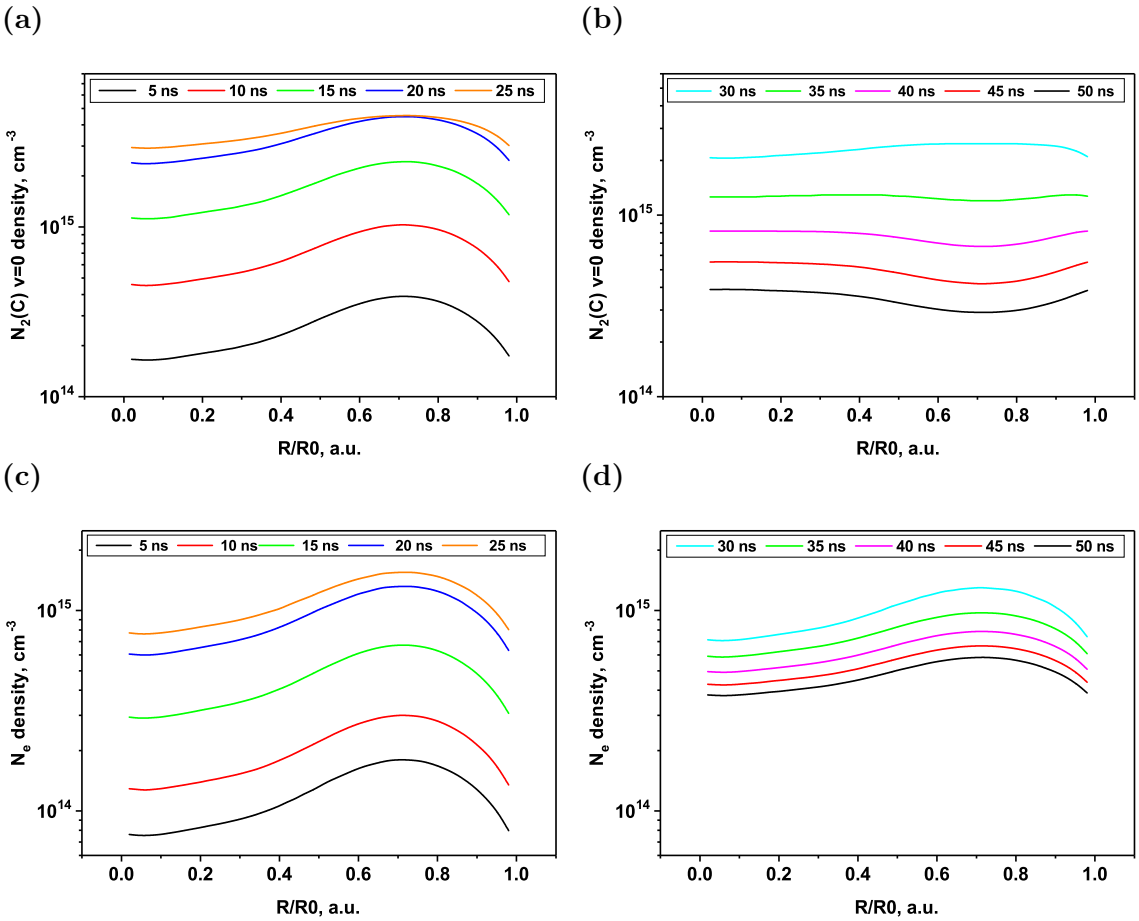

Figure 8.13 – Calculated numerically time evolution of the radial distribution profiles of the $N_2(C^3\Pi_u, v' = 0)$ state (a, b) and the electron density (c, d) in pure nitrogen at 27 mbar, positive polarity high voltage pulses (amplitude 9.3 kV in the cable, 30 ns FWHM).

between metastable states of nitrogen. The radial profile of the electron density copies the radial profile of the metastable states in the afterglow. The density of the metastable states has the distribution similar to the $N_2(C^3\Pi_u, v' = 0)$ state, since both distribution copies the initial electron density distribution.

However, it also is seen that near the wall of the capillary tube the decay of the $N_2(C^3\Pi_u, v' = 0)$ state observed experimentally after the discharge pulse is faster than numerical calculations shows. It is also seen from Fig. 8.10 and Fig. 8.13 that just after end of the discharge pulse the effect of more intensive quenching of the $N_2(C^3\Pi_u, v' = 0)$ state is intensive near the wall only. The effect becomes more noticeable in the plasma volume with time. Thus, one can say that effect is observed as a "wave" propagating from the wall to the plasma bulk with characteristic times about few nanoseconds. The fast propagation of the "wave" means that this perturbation does not have gas-dynamic nature, i.e. it is not a perturbation of the

density of nitrogen molecules leading to faster quenching of the $N_2(C^3\Pi_u, v' = 0)$ state. The effect is not noticeable during the discharge pulse. It is valid both for discharge pulses with 20 ns FWHM and 30 ns FWHM, see Fig. 8.14. Thus, there is a reliable correlation with the end of the discharge pulse.

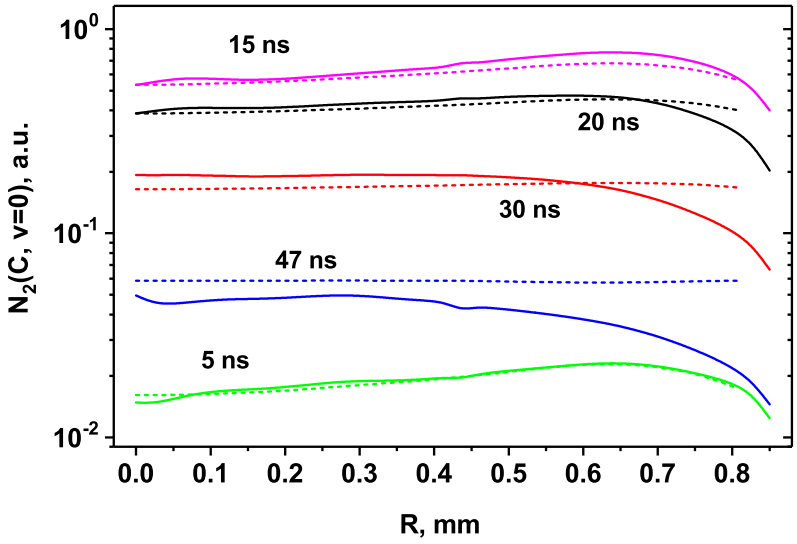

Figure 8.14 – Calculated numerically and measured experimentally time evolution of the radial distribution profiles of the $N_2(C^3\Pi_u, v' = 0)$ state in pure nitrogen at 55.5 mbar, negative polarity high voltage pulses (amplitude 13.5 kV in the cable, 20 ns FWHM).

The following mechanism is proposed to explain observed phenomenon. It is seen in Fig. 4.6, Fig. 4.9 and Fig. 4.10 that after the discharge pulse, when the electric field is zero already, the electric potential uniform along the tube is observed. This electric potential is caused by the electric charge accumulation on the internal wall surface. The electric charge on the wall surface causes the high electric field. This field is intensive in the thin layer near the wall only and not penetrate in the plasma bulk due to screening of the electric field in a plasma. As it was shown above, during the discharge the uniform longitudinal electric field dominates. Thus, the influence of the radial field due to surface charge is negligible both in the plasma bulk and near the wall. After the end of the discharge pulse the electric field is present near the wall only, while in the plasma bulk it is absent. Therefore, after the discharge pulse the electron temperature in the plasma bulk decrease fast, while in the thin layer near the wall the temperature of electrons is sustained by the rather high radial electric field. The electron temperature gradient leads to the diffusivity wave of the electron temperature. The wave of the electron temperature increase is followed by "wave" of more intensive quenching of the $N_2(C^3\Pi_u, v' = 0)$ state by electrons, since the rate constant of the process strongly depends on the electron temperature, see

Fig. 7.11. In the 1D numerical kinetics calculation this possible process can not be implemented. To check proposed assumption the 2D or 3D numerical calculations of the nanosecond capillary discharge and its afterglow is required. Nevertheless, one can verify a possibility of the proposed mechanism by estimations of the characteristic time of the diffusivity wave of the electron temperature propagation. If this time is fast enough to provide more intensive quenching of the $N_2(C^3\Pi_u, v' = 0)$ state by electrons near the wall, the assumption is reasonable.

In first approximation, the wall of the tube can be considered as flat and infinite, since the region of the interest is thin layer close to the wall. The simple 1D estimation can be used in this case. The time interval Δt, after which the temperature perturbation will be noticeable distance d can be estimated as

$$\Delta t = \frac{d^2}{\chi}, \tag{8.5}$$

with χ is the thermal diffusivity of electrons, which can be estimated [137] as

$$\chi = l_e \bar{u}/3, \tag{8.6}$$

with the mean free path l_e and the thermal velocity $\bar{u}$. Equation (8.6) can be rewritten as

$$\chi = \frac{kT}{m_e \nu_{ee}}, \tag{8.7}$$

where m_e is the mass of the electron and ν_{ee} is the electron-electron collision frequency. The electron-electron collision frequency can be calculated [2] as

$$\nu_{ee} = \frac{3.7 \cdot N_e \cdot ln\Lambda}{(T_e[K])^{3/2}}, \tag{8.8}$$

where $ln\Lambda = 7.45 + 1.5 \cdot lg(T_e[K]) - 0.5 \cdot lg(N_e[\mathrm{cm}^{-3}])$ is Coulomb logarithm [2] equal to 6 at $T_e \approx 1$ eV and $N_e \approx 10^{15}\mathrm{cm}^{-3}$ typical for the early afterglow of the considered capillary nanosecond discharge. Equation (8.8) gives $\nu_{ee} = 1.78 \cdot 10^{10}\ \mathrm{s}^{-1}$. Thus, one can obtain $\chi = 9.82\ \mathrm{m}^2\mathrm{s}^{-1}$. Finally, for $d = 0.25$ mm one can obtain $\Delta t = 6.4$ ns. The distance $d = 0.25$ mm corresponds to the distance from the wall surface at which more intensive quenching of the $N_2(C^3\Pi_u, v' = 0)$ state by electrons was observed in the experiment 10 ns after the end of the discharge, see curve "30 ns" in Fig. 8.14, for example. Thus, there is a good agreement between estimation of the thermal diffusivity wave propagation and the experimentally observed dynamics of more intensive quenching of the $N_2(C^3\Pi_u, v' = 0)$ state. It means that assumption about nature of the observed more intensive quenching of the $N_2(C^3\Pi_u, v' = 0)$ state near the wall is reasonable.

8.3 Conclusion

The radial distribution of the $N_2(C^3\Pi_u, v' = 0)$ state in the nanosecond capillary discharge was studied experimentally using optical scheme providing mathematically correct radial distribution reconstruction. The measured intensity profiles were analyzed numerically by the self-developed Fortran code. The reconstructed radial distributions of the emission sources showed that the noticeable part of the signal is the light scattered by the quartz wall. Thus, the light scattering was taken into account during the data treatment.

The initial electron density radial distributions were obtained assuming that the radial distributions of the $N_2(C^3\Pi_u, v' = 0)$ state copies the electron density distribution during the initial stage of the discharge. It was shown that the initial electron density radial profile is sensitive to the gas composition. In pure nitrogen the electron density radial profile with maximum out of axis of the tube was observed. It was demonstrated that even 1% admixture of the molecular oxygen changes the electron density radial profile, which becomes flatter. Further increase of oxygen admixture leads to the electron density radial distribution with the maximum on the tube axis. Observed radial profile transformation is explained by photo-ionization of molecular oxygen in the tube volume competing with the electron production near the wall surface due to quartz wall irradiation by UV.

The time evolution of the radial distribution of the $N_2(C^3\Pi_u, v' = 0)$ state was studied numerically and experimentally in pure nitrogen. Faster decay in regions with high electron density observed experimentally and numerically emphasizes one more time the role of quenching of the $N_2(C^3\Pi_u, v' = 0)$ state by electrons. More intensive quenching of the $N_2(C^3\Pi_u, v' = 0)$ state near the surface of the tube wall was observed experimentally in contrast to the numerical modeling results after the end of the discharge pulse. The observed difference was explained by thermal diffusivity wave of electron temperature leading to the higher rate constant of quenching by electrons. It was assumed that electrons are heated in the thin layer near the wall surface due to electric field of the electric charge deposited on the wall surface during discharge pulse. The estimations of characteristic times of the thermal diffusivity wave propagation has been performed. A good agreement between estimations and experimental results confirms the reasonability of the assumption.

Chapter 9

Fast gas heating in pure nitrogen and N_2:O_2 mixtures

In the previous Chapters it was shown that the high specific energy deposition can significantly change plasma kinetics in the discharge and in the afterglow. High density of electronically excited species is a reservoir of energy released in collisions during tens and hundreds of nanoseconds at a pressure of tens of Torr. For example, the energy of electronic excitation is spent on the production of electrons in the afterglow by the reactions of associative ionization between metastable states of molecular nitrogen. The electronic energy can be spent on fast heating of heavy species, i.e. fast gas heating. This Chapter is dedicated to the experimental and numerical study of processes responsible for this pathway of the energy relaxation in pure nitrogen and nitrogen/oxygen mixtures in the afterglow of the nanosecond capillary discharge.

9.1 Applicability of the technique used for temperature measurements

It is possible to measure the gas temperature by emission spectroscopy technique [53]. The idea is to measure the rotational temperature of the gas, which is equal to the translational one at thermodynamics equilibrium, using analysis of emission spectrum. In Chapter 8 it was shown that the initial electron density distribution is not uniform in the tube cross-section. This leads to the non-uniform

energy deposition and, consequently, the non-uniform fast gas heating. Thus, first of all, the relation between the measured value of the temperature averaged over the cross-section of the capillary tube and the real temperature distribution should be established. The relation is required for correct comparison of the results of the experimental measurements and the results of numerical calculations aimed at determining the main mechanisms of the fast gas heating in pure nitrogen and nitrogen:oxygen mixtures.

The emission spectroscopy technique is based on the analysis of the distribution of the intensities of the rotational lines of given optical transition. The distribution of the intensities of the rotational lines is characterized by the rotational distribution of the ensemble of the excited molecules. Typically the rotational distribution is described by a function $exp(-E/(kT_{rot}))$ (Boltzmann distribution) with rotational energy E, Boltzmann's constant k and rotational temperature T_{rot}. If there are number of the ensembles of excited molecules of the same type characterized by the different rotational temperatures, the observed distribution of the intensities of the rotational lines will be characterized by "effective temperature".

To derive the formula for the "effective temperature", let us consider the sum of the exponential distributions $a_i e^{-\frac{E}{kT_i}}$ with the same rotational energy E and different temperatures T_i with weights a_i (at restriction $\sum a_i = 1$). The rotational energy $E = J(J+1)B$ with rotational quantum number J and rotational constant B is much smaller than kT, since a typical value of B/k is few Kelvins ($B/k = 2.626$ K for the $N_2(C^3\Pi_u)$ state). Thus, it can be assumed that $E \ll kT$ even at room temperature. In this case one can write using the Taylor expansion

$$\sum a_i e^{-\frac{E}{kT_i}} \approx \sum a_i (1 - \frac{E}{kT_i}) = \sum a_i - \frac{E}{k} \cdot \sum \frac{a_i}{T_i} = 1 - \frac{E}{k} \cdot \sum \frac{a_i}{T_i} \approx e^{\frac{E}{kT_{eff}}} \quad (9.1)$$

with the effective temperature T_{eff} defined as

$$\frac{1}{T_{eff}} = \sum \frac{a_i}{T_i}. \quad (9.2)$$

Thus, it is shown that the sum of the exponential distributions can be considered as exponential distribution.

In the discharge the number of particles is large and the temperature varies continuously, thus the generalization of (9.1) and (9.2) is required. In the discharge the linear density of the emitting specie with density $N(r)$ in the ring with radius r and thickness dr is equal to $2\pi N(r)rdr$, the total linear density in the entire cross-section is $\int_0^{R_0} 2\pi N(r)rdr$, where R_0 is the radius of the plasma channel. Thus, the weight $a(r)$ of the ring with temperature $T_{rot}(r)$ can be written as

$$a(r) = \frac{2\pi N(r)rdr}{\int_0^{R_0} 2\pi N(r)rdr}. \quad (9.3)$$

Finally, for T_{eff} one can write generalization of (9.1) using (9.3)

$$\frac{1}{T_{eff}} = \frac{1}{\int_0^{R_0} 2\pi N(r) r dr} \int_0^{R_0} \frac{2\pi N(r) r dr}{T_g(r)} \tag{9.4}$$

or

$$T_{eff} = \frac{\int_0^{R_0} 2\pi N(r) r dr}{\int_0^{R_0} \frac{2\pi N(r) r dr}{T_g(r)}}. \tag{9.5}$$

This formula gives the value of the observed rotational temperature expressed through the radial distribution of the density of the emitting molecules and the radial distribution of the rotational temperature of the emitting molecules at given time instant. However, the optical emission is collected during some time interval (gate of the ICCD camera, or the time interval of the most intense emission) t_{emiss}. As was shown in Chapter 8, the radial distribution of the emitting specie is not fixed and changes in time during the pulse and the afterglow. It means that the rotational temperature value obtained by treatment of the signal collected during time t_{emiss} is averaged not only spatially, but temporally as well. To take it into account (9.5) can be rewritten as

$$T_{eff} = \frac{1}{t_{emiss}} \int_0^{t_{emiss}} \left(\frac{\int_0^{R_0} 2\pi N(r,t) r dr}{\int_0^{R_0} \frac{2\pi N(r,t) r dr}{T_g(r,t)}} \right) dt. \tag{9.6}$$

This formula gives value of the observed rotational temperature of the excited specie averaged spatially and temporally. The relation between the rotational temperature of the excited specie and the value of the gas temperature is discussed below.

The relation between the rotational temperature of the excited specie and the gas temperature depends on the discharge conditions. There are two limiting cases. The first case is when the lifetime of the excited species t_0 is much greater than a characteristic time of rotational-translational relaxation t_{RT}: $t_0 \gg t_{RT}$. In this case the radiative molecule is in the thermodynamics equilibrium with the background gas, and measured T_{rot}^{exc} is equal to the gas temperature. The second case corresponds to $t_0 \ll t_{RT}$. Here, there are no collisions perturbing the initial rotational distribution formed during excitation.

The relaxation time in pure nitrogen can be estimated through the rate of nitrogen-nitrogen gasdynamic collisions. The collisional rate constant k_{coll} defined by $\nu_{coll} = k_{coll} N$, where ν_{coll} collision frequency, can be calculated as

$$k_{coll} = \sqrt{2} \bar{V} \sigma = \sqrt{2} \sigma \sqrt{\frac{8RT}{\pi \mu}}, \tag{9.7}$$

where $\bar{V}$ is average thermal velocity, μ is molar mass, $R = 8.31$ J·mol^{-1}K^{-1} is universal gas constant and σ is collisional cross-section. For molecular nitrogen

with $\mu = 28$ g $\cdot$ mol^{-1} and $\sigma_{N_2} = 4.31 \cdot 10^{-15}$ cm^2 [2] equation (9.7) gives

$$k_{coll} = 0.16762 \cdot 10^{-10} \sqrt{T[K]} \text{ cm}^3 \cdot \text{s}^{-1}. \tag{9.8}$$

At $T = 300$ K the collisional rate constant k_{coll} is equal to $2.9 \cdot 10^{-10}$ cm^{3}s^{-1}, at $T = 3000$ K it is equal to $9.2 \cdot 10^{-10}$ cm^{3}s^{-1}. In the same time, the rate constant k_q for quenching of $N_2(C^3\Pi_u, v' = 0)$ state by molecular nitrogen is $0.13 \cdot 10^{-10}$ cm^{3}s^{-1} [91]. The radiative lifetime τ_0 of this state is equal to 42 ns [91]. Using these three values it is possible to estimate the range of applicability of the spectroscopic temperature measurements technique in the case of "classical" kinetics.

First of all, one can calculate the nitrogen density, at which the radiative decay is comparable with the self-quenching, using the equality $k_q[N_2] = 1/\tau_0$. It gives $[N_2] = 1.83 \cdot 10^{18}$ cm^3, which corresponds to pressure 75 mbar at $T = 300$ K. Thus, at pressures much higher than 75 mbar the radiative decay is negligible comparing with quenching by N_2. Under these conditions a simple comparison of k_{coll} and k_q shows that on each act of collisional quenching there are 22 collisions with nitrogen molecules leading to thermalization. To thermalize excited nitrogen, 5-20 collisions are typically required [103], more precise data show that at $T = 300$ K it is required about 5 collisions, and at $T = 3000$ K the required number of collision is the order of 10 [138]. In this case $N_2(C^3\Pi_u, v' = 0)$ state is always thermalized. Finally, it means that at pressures much higher than 75 mbar one can determine the gas temperature directly from the rotational temperature of the $N_2(C^3\Pi_u, v' = 0)$ state, they are equal.

In the opposite case, when the pressure is low enough to neglect collisional quenching in comparison with radiative decay, one can estimate the density of N_2, at which the radiative decay is comparable with the nitrogen-nitrogen collisions. The calculation gives the density equal to $0.8 \cdot 10^{17}$ cm^3, or pressure 3.3 mbar at $T = 300$ K. Thus, at pressures much lower than 3 mbar the radiative decay dominates on collisions between N_2 molecules. In this case there are no collisions perturbing the rotational distribution of the radiative specie. If the radiative state of the molecule is directly populated by the electron impact from the ground state, see (7.1), the rotational distribution of the excited state copies the rotational distribution of the ground state [139] according to the Franck-Condon principle. The ground state rotational temperature is equal to the translational one, thus the temperature of the gas can be calculated. Knowing the rotational temperature of the excited specie, the rotational temperature (and, consequently, translational one) of the ground state $N_2(X^1\Sigma_g^+)$ can be calculated as

$$T_{tr} = T_{rot}^X = (B_e^X / B_e^C) T_{rot}^C, \tag{9.9}$$

where T_{rot}^X is the rotational temperature of the ground state, T_{rot}^C is the rotational

temperature of the $N_2(C^3\Pi_u)$ state and $B_e^X/B_e^C = 1.998/1.825 = 1.095$ [140] is the ratio between rotational constants of the $N_2(X^1\Sigma_g^+)$ and $N_2(C^3\Pi_u)$ states, respectively.

In the present Thesis, the pressure is equal to 27 mbar for most of the experiments, in particular, in fast gas heating measurements. This pressure is lower than estimated limit 75 mbar in 3 times only. This means that radiative decay and collisional quenching are comparable. Moreover, as it was shown in Chapter 7, at condition of high specific energy deposition at high reduced electric field there is an additional collisional process, namely, quenching by electrons, which decreases the lifetime of the $N_2(C^3\Pi_u, v' = 0)$ state. It is equal to $t_1 = 10.4$ ns in the beginning of the decay and $t_2 = 15.3$ ns at the end of the decay at $P = 27$ mbar, $T = 300$ K. The characteristic time between two collisions calculated with (9.8) for the same conditions is equal to 5.2 ns. This means that during the lifetime $N_2(C^3\Pi_u, v' = 0)$ state undergoes 2-3 collision only, instead of 6 collisions during 31 ns lifetime predicted by theory due to radiative decay and quenching by nitrogen only. Thus, there are no enough collisions to thermalize the rotational distribution of the radiative species with background gas, especially at high temperatures, but it is possible that these two-three collisions perturb the rotational distribution. One can check it by comparison of the experimental spectrum with theoretically calculated one. If simulated spectrum fits the experimental one with rather good agreement, this means that influence of a few collisions during $N_2(C^3\Pi_u, v' = 0)$ lifetime at present conditions does not perturb initial Boltzmann rotational distribution formed by direct population by the electron impact from the ground state. In this case, the temperature can be calculated by (9.9). At higher temperatures, the balance of the collisions does not change. The number of the collisions with nitrogen increase: k_{coll} is 3 times higher at $T = 3000$ K. However, it is compensated by increase of the number of collisions required for thermalization by the same factor [138]. It is also should be noted that at "classical" kinetics the lifetime of $N_2(C^3\Pi_u, v' = 0)$ decreases additionally at presence of oxygen due to quenching by O_2 molecules with rate constant $3 \cdot 10^{-10}$ cm^{3}s^{-1} [91], which is 23 times higher than collisional quenching by nitrogen $0.13 \cdot 10^{-10}$ cm^{3}s^{-1} [91]. The influence of the molecular oxygen is observed at conditions of high specific energy deposition too, see Fig. 7.3. This figure demonstrates that the decay rate at the end of the pulse increases with oxygen volume fraction, see red squares. The decay rate in the beginning of the pulse, see black squares in Fig. 7.3, decreases at small oxygen admixtures (less than 10%), but increases with further increasing of oxygen fraction. This, probably, is due to electron attachment to the oxygen molecules and, consequently, less intense quenching by electrons. Nevertheless, the effect of the electron quenching is still significant, and the total decay rate is still higher than theory predicts. So, the number of the collisions is still not

enough to thermalize excited nitrogen molecule and the formula (9.9) can be used.

However, it should be noted that population of the $N_2(C^3\Pi_u)$ state from the ground state of molecular nitrogen is typical for $E/N > 100$ Td. If the density of the $N_2(B^3\Pi_g)$ state, is rather high and $E/N \leq 100$ Td, the population of the $N_2(C^3\Pi_u)$ state from the $N_2(B^3\Pi_g)$ state can be significant [110], see Fig. 9.1, where the ratio K_{BC}/K_{XC} of the rate constants of the electron impact excitation of the $N_2(C^3\Pi_u)$ state from the $N_2(B^3\Pi_g)$ state and from the ground state of molecular nitrogen are presented.

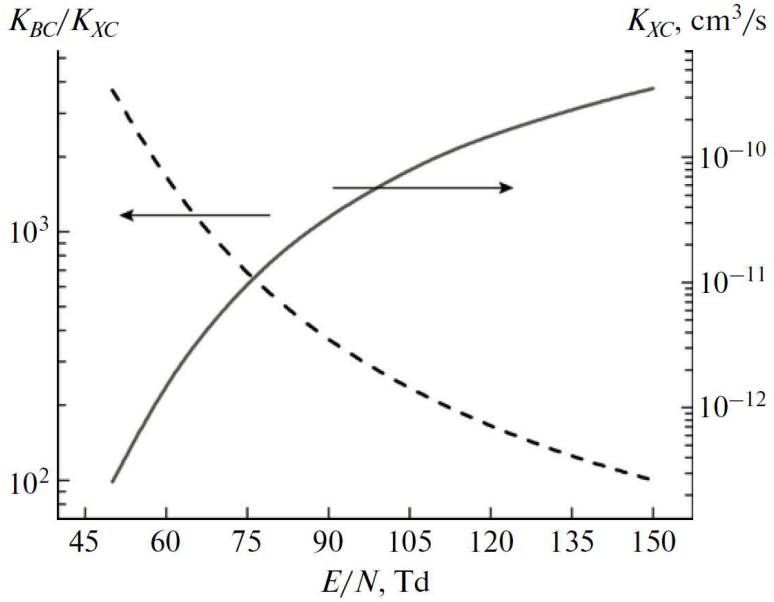

Figure 9.1 – The ratio K_{BC}/K_{XC} of the rate constants of the electron impact excitation of the $N_2(C^3\Pi_u)$ state from the $N_2(B^3\Pi_g)$ state and from the ground state of molecular nitrogen, respectively, and value of the rate constant K_{XC} as a function of the reduced electric field. The figure is taken from [110].

The reduced electric field value in the diagnostic pulses, which are reflections of the transmitted current pulses from the zero end load on the end of the LV cable, is rather low, see Fig. 6.4, for example. Moreover, in Chapter 4 it was shown for pure nitrogen that the density of the $N_2(B^3\Pi_g)$ state increases relatively the density of the $N_2(C^3\Pi_u, v = 0)$ state from pulse to pulse, see Fig. 4.30. The relatively slow decay of the $N_2(B^3\Pi_g)$ state (the lifetime is 147 ns, see Fig. 4.28) leads to the noticeable density of the $N_2(B^3\Pi_g)$ state after the main discharge pulses. Also, there is additional production of the $N_2(B^3\Pi_g)$ state in the pooling reaction between the $N_2(A^3\Sigma_u^+)$ states [42,56,141], see (9.11). Therefore, for the low-amplitude diagnostic pulses with $E/N < 100$ Td, see Fig. 6.4(b), arriving after the third main discharge

pulse it is reasonable to assume that the $N_2(C^3\Pi_u, v = 0)$ state is mostly populated from the $N_2(B^3\Pi_g)$ state. The $N_2(B^3\Pi_g)$ state in the thermal equilibrium with the background gas due to rather high the lifetime. In this case for pure nitrogen in low-amplitude diagnostic pulses after the third main discharge pulse

$$T_{tr} = T_{rot}^B = (B_e^B/B_e^C)T_{rot}^C, \tag{9.10}$$

where $B_e^B/B_e^C = 1.637/1.825 = 0.897$ [140] is the ratio between rotational constants of the $N_2(B^3\Pi_g)$ and $N_2(C^3\Pi_u)$ states, respectively. In the nitrogen:oxygen mixtures with noticeable oxygen fraction the $N_2(B^3\Pi_g)$ state is quenched efficiently by the molecular oxygen, and the $N_2(C^3\Pi_u)$ state is populated from the ground state always, thus, the formula (9.9) is used in this case.

Regardless from which electronic level the $N_2(C^3\Pi_u)$ state is populated, it is required that the $N_2(C^3\Pi_u)$ state has been excited by direct electron impact in the discharge pulse. Otherwise, observed emission is caused by the pooling reaction between metastable states of molecular nitrogen [55, 56] (9.12), which produces $N_2(C^3\Pi_u)$ state in the afterglow with the rate constant $k_{(9.12)} = 2.4 \cdot 10^{-10}$ cm^{3}s^{-1} estimated based on the data [55, 142]. The rotational distribution corresponding to the produced $N_2(C^3\Pi_u)$ state does not correspond to the rotational temperature of the gas. However, during the next discharge pulse emission due to electron impact excitation is much higher, and influence of process (9.12) on the temperature measurements can be neglected, which was checked experimentally in Chapter 4, see Fig. 4.27.

Another item, which should be checked, is the influence of the hydrodynamics. During nanosecond pulse, there is no any influence of gas dynamics, for example, cooling due to gas expansion. However, if the train of the pulses is considered at μs time scale, the use of isochoric approximation should be proved. A characteristic gas-dynamic times can be estimated as $t_{g.d.} = l/v_{sound}$, where $l = 40$ mm is the half length of the capillary tube, v_{sound} is the maximum expected sound speed in nitrogen at present conditions. It can be estimated as $v_{sound} = \sqrt{T/273\ \mathrm{K}}v_{sound}^{273}$ with sound speed at normal condition $v_{sound}^{273} = 334$ m/s. For $T = 2500$ K the estimation gives $t_{g.d.} = 40$ μs. Thus, the fast gas heating can be studied at time scale of a few μs at isochoric approximation.

9.2 Fast gas heating in pure nitrogen

9.2.1 Experimental results

The transition $N_2(C^3\Pi_u, v' = 0) \rightarrow N_2(B^3\Pi_g, v'' = 0)$ at $\lambda = 337.1$ nm was used for temperature measurements as the most intensive band in the discharge spectrum, see Section 4.2.

The rotational temperature of $N_2(C^3\Pi_u, v' = 0)$ state was determined by fitting of experimentally measured spectrum by SPECAIR [54] software. As it was shown in Section 3.2.1, the broadening can be considered as a constant function not depending on the gas temperature, since the broadening is determined by the apparatus function of the spectrometer. The measured mercury line was used as an apparatus function in the spectrum simulation, see Fig. 3.5.

For each initial pulse coming from the generator, typically 3 main pulses (30 ns FWHM) separated by ≈ 245 ns are observed because of the difference in impedance of the cable, the discharge tube and the generator. The sequence of the pulses is repeated at ≈ 1 μs due to reflection from the end-load of the delay cable. Thus, the following points at 15, 135, 260, 365, 505, 615, 1010, 1255 and 1500 nanoseconds are obtained in $T(t)$ dependence. The experimental conditions was the following: transmitted current in the first pulse was equal to 65 A, pressure of pure nitrogen is equal to 27 mbar.

An example of the experimentally measured spectrum is presented in Fig. 9.2 together with the spectra calculated by SPECAIR [54] software using the slit function from Fig. 3.5. The temperature of the $N_2(C^3\Pi_u, v' = 0)$ state in simulations is indicated in the legend. One can see that the simulated spectrum fits experimental one at the temperature of $N_2(C^3\Pi_u, v' = 0)$ state equal to $T = 350$ K. A good agreement between the calculated and the measured spectra means that 2-3 collisions during $N_2(C^3\Pi_u, v' = 0)$ state lifetime discussed in Section 9.1 do not perturb the rotational distribution. To obtain the gas temperature, the values of the rotational temperature of $N_2(C^3\Pi_u, v' = 0)$ state were multiplied by 1.095 for the pulses at 15-505 ns according to (9.9), and by 0.897 for the pulses after 505 ns according to (9.10), see discussion above. The evolution of the gas temperature in time is presented Fig. 9.3. The spectra for corresponding discharge pulses are given in Fig. 9.4. One can see that the fast gas heating in pure nitrogen is rather intense. The final temperature at 1500 ns is about 2100 K. The gas temperature reaches 2000 K during 600 ns after the first pulse, it means that the heating rate during first 600 ns is about 2800 K/μs.

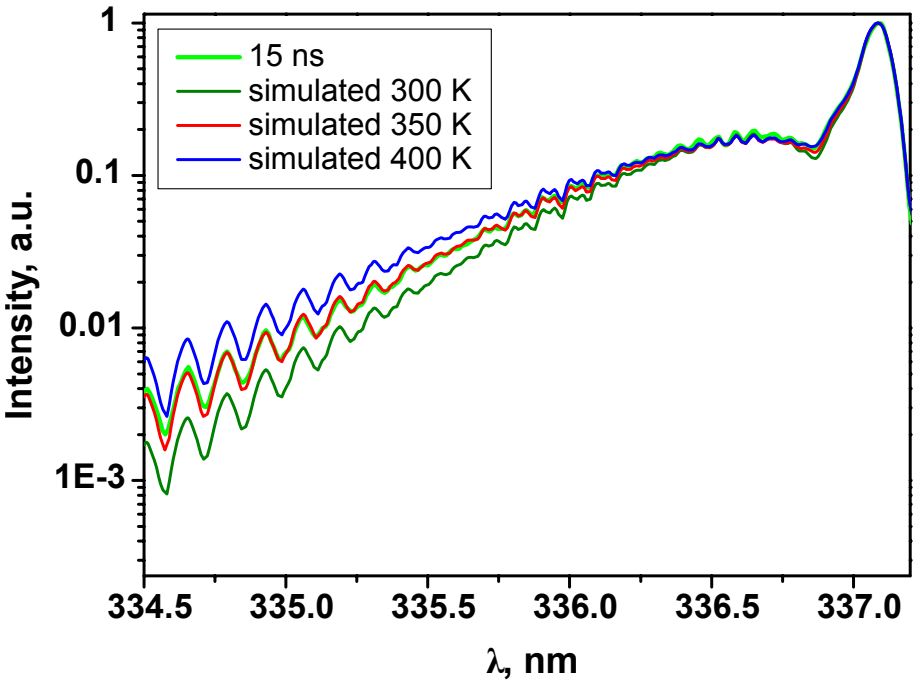

Figure 9.2 – Experimentally measured spectrum of (0-0) transition of 2^+-system of molecular nitrogen in pure nitrogen at 27 mbar in first discharge pulse (65 A) and the spectra at different temperatures calculated using SPECAIR [54] software.

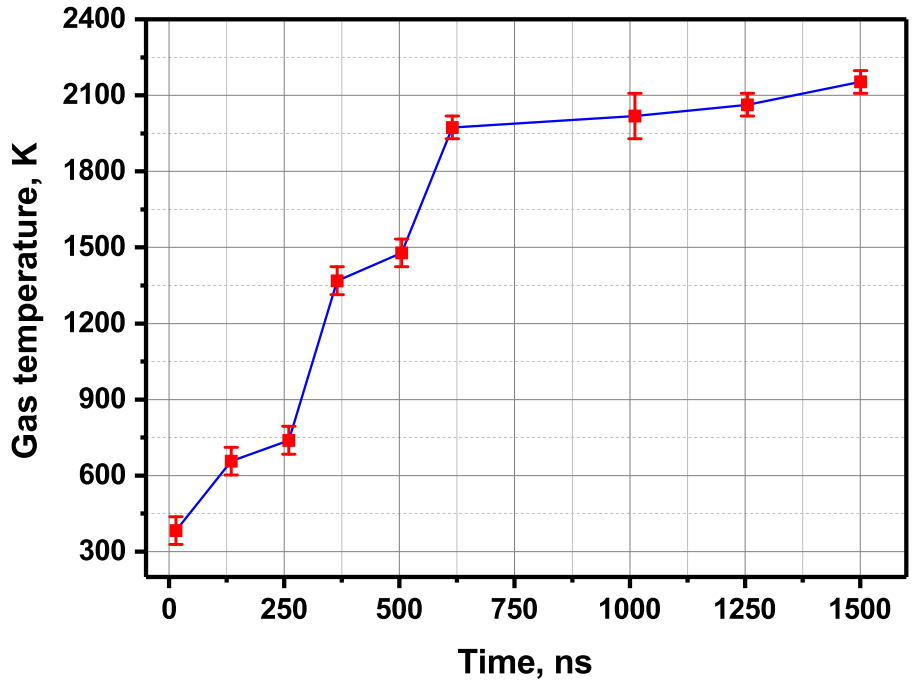

Figure 9.3 – The gas temperature temporal dynamics in pure nitrogen at 27 mbar and transmitted current 65 A.

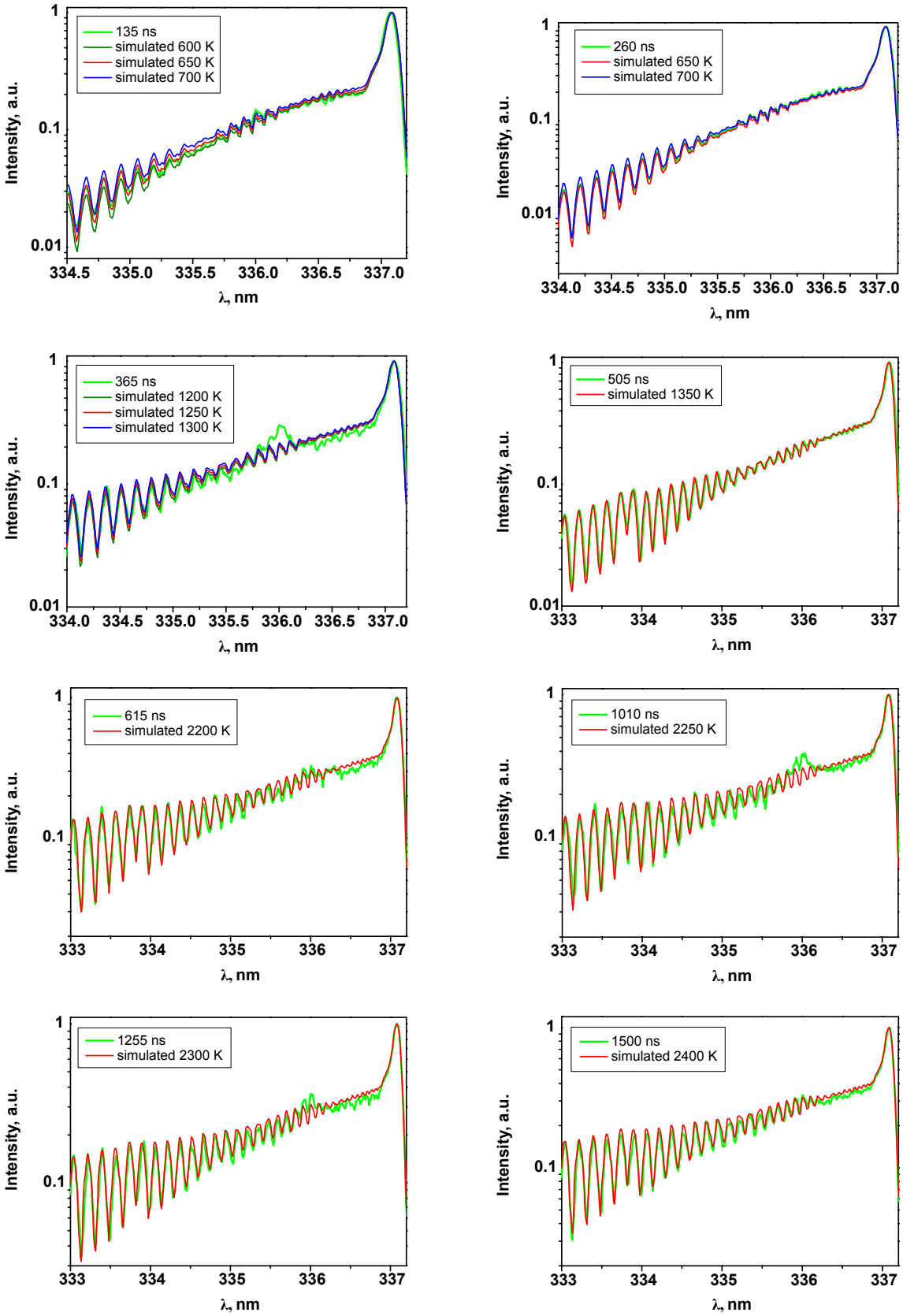

Figure 9.4 – Experimentally measured spectra and spectra calculated for different temperatures of the $N_2(C^3\Pi_u, v' = 0)$ state using SPECAIR [54] software. Conditions are the same as in Fig. 9.2.

9.2.2 Discussion

A good way to investigate the processes, responsible for the gas heating in pure nitrogen, is to compare the experimental results with the results of numerical calculations. Further, the key reactions in the kinetics model will be discussed.

One of the main process responsible for energy relaxation from the electronic degrees of freedom is the reaction of self-quenching of the $N_2(A^3\Sigma_u^+)$ states [42, 56, 141]:

$$N_2(A^3\Sigma_u^+) + N_2(A^3\Sigma_u^+) \rightarrow N_2(X^1\Sigma_g^+, v) + N_2(B^3\Pi_g, v') + \varepsilon_{(9.11)} \tag{9.11}$$

and

$$N_2(A^3\Sigma_u^+, v) + N_2(A^3\Sigma_u^+, v') \rightarrow N_2(X^1\Sigma_g^+, v) + N_2(C^3\Pi_u) + \varepsilon_{(9.12)}. \tag{9.12}$$

The measurements of the total rate constant of reactions (9.11) and (9.12) were presented in many papers, see [142, 143] and reference therein, however, almost all of them were performed at gas temperature $T = 300$ K. In the nanosecond capillary discharge the gas temperature increases up to 2100 K in the time interval of the interest, see Fig. 9.3. This means that an additional assumption about temperature behavior of the total rate constant of reactions (9.11) and (9.12) should be done. To do this, the experimental results from the paper [144] have been treated.

In [144], the investigation of the dynamics of nitrogen plasma decay was performed at atmospheric pressure and gas temperature $T_0 = 1600$ K. The gas was excited by pulsed nanosecond discharge. The CRDS method for (0-2) transition of 1^+-system of molecular nitrogen followed by data calibration was used for $N_2(A^3\Sigma_u^+,\ v = 0)$ density measurements in the afterglow. Gas temperature was determined from the rotational structure of the 2^+-system of molecular nitrogen. The results of these measurements are presented in Fig. 9.5 (dots). The total rate constant of reactions (9.11) and (9.12) obtained in [144] is $k_{(9.11)+(9.12)} = 1.1 \cdot 10^{-9}\mathrm{cm^3 s^{-1}}$ at $T = 1600$ K.

However, it was shown [145] that in high pressure nitrogen plasma the population of $v = 0$ vibrational level of $N_2(A^3\Sigma_u^+)$ can be less than 20% of total population of $N_2(A^3\Sigma_u^+)$ vibrational levels. If it is assumed that all vibrational levels of $N_2(A^3\Sigma_u^+, v)$ participate in the reactions (9.11) and (9.12), the modeling of the evolution of the vibrational distribution function of $N_2(A^3\Sigma_u^+, v)$ molecules is required for the determination of the total rate constant of reactions (9.11) and (9.12).

The results of numerical calculation for the conditions similar to [144] using the model from [145] are presented in Fig.9.5. It was assumed that the rate constant of the reactions (9.11) and (9.12) does not depend on the vibrational level number ($k_{(9.11)+(9.12)}(v) = const$). The evolution of the vibrational distribution function of

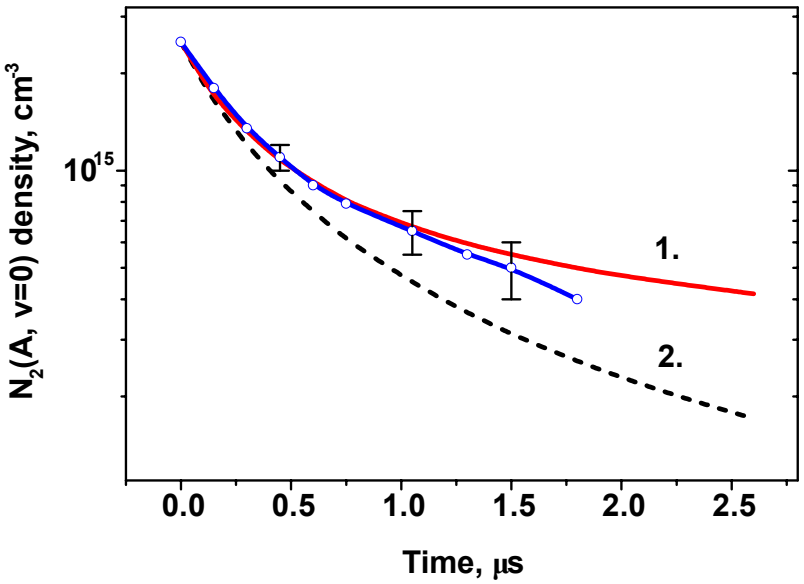

Figure 9.5 – The temporal dynamics of the population of $N_2(A^3\Sigma_u^+, v = 0)$ state in the afterglow for the conditions of the experiments [144]: $P =$ 760 Torr, $T = 1600$ K. Dots correspond to the results of the experimental measurements, curves correspond to the results of the numerical calculations at $k_{(9.11)+(9.12)} = 1.5 \cdot 10^{-10}$ cm^{3}s^{-1} with (curve 1) and without (curve 2) taking into account the reaction (9.13)**.**

$N_2(A^3\Sigma_u^+, v)$ due to collisions with nitrogen molecules was taken into account:

$$N_2(A^3\Sigma_u^+, v) + N_2(X^1\Sigma_g^+, v' = 0) \to N_2(A^3\Sigma_u^+, v - 2) + N_2(X^1\Sigma_g^+, v' = 1). \quad (9.13)$$

The dependence of the rate constant of the reaction (9.13) on the vibrational level number and on the gas temperature was determined in [145].

The results of the numerical calculations according to the described model are compared with the results of experimental measurements in Fig. 9.5. Curves 1 and 2 correspond to the results of numerical calculations with and without taking into account the reaction (9.13). It should be noted that the results of the modeling are very sensitive to $k_{(9.11)+(9.12)}$ and they are in a good agreement with the experimental data at $k_{(9.11)+(9.12)} = 1.5 \cdot 10^{-10}$ cm^{3}s^{-1} (the difference at $t > 1$ μs is most likely caused by additional quenching of $N_2(A^3\Sigma_u^+)$ by nitrogen atoms).

The obtained value of $k_{(9.11)+(9.12)}$ is close to the value obtained in [143] at $T =$ 300 K. Thus, in the present Thesis it was assumed that the total rate constant of reaction (9.11) and (9.12) does not depend on the gas temperature and equal to $k_{(9.11)+(9.12)} = 3.6 \cdot 10^{-10}$ cm^{3}s^{-1} with $k_{(9.11)}/k_{(9.12)} = 1/2$ (based on the data [142, 143]).

The value of energy ε_p released in the process (9.11) and converted to gas heating is not exactly defined in the literature, since it depends on the degree of vibrational

excitation of the produced $N_2(X^1\Sigma_g^+, v)$ molecules [5]. For numerical calculations performed for present conditions the value $\varepsilon_{(9.11)} = 3.5$ eV was taken according to estimations [5]. The same estimations based on the data [55] shows that heat release in the process (9.12) does not exceed $\varepsilon_{(9.12)} = 0.86$ eV.

Another process responsible for the fast gas heating at present conditions is quenching of $N(^2D)$ atoms produced in dissociation of N_2 by the electron impact:

$$N(^2D) + N_2 \rightarrow N(^4S) + N_2(v). \tag{9.14}$$

According to the results of calculations [59], the rate constant of this process significantly increases with the gas temperature

$$k_{(9.14)}(T) = 4.52 \cdot 10^{-14} \cdot T^{0.68} \cdot exp\Big(-\frac{1438}{T}\Big) \text{ cm}^3\text{s}^{-1}. \tag{9.15}$$

Moreover, if was shown [58] that up to 90% of excitation energy of $N(^2D)$ atoms (2.35 eV) goes to the gas heating and less than 10% goes to vibrational excitation of molecular nitrogen. These data were used in the present numerical calculations.

The next process leading to the fast gas heating has been introduced based on the analysis of the temporal behavior of the $N_2(B^3\Pi_g)$ state. It was demonstrated in Chapter 4 that in the early afterglow the decay of the $N_2(B^3\Pi_g)$ state is 5 times faster than the decay provided by the sum of radiative depopulation and quenching by the molecular nitrogen, see Fig. 4.30. It was also noted in Chapter 7 that observed additional process of the excited species depopulation, namely, quenching by electrons is not intensive enough for the $N_2(B^3\Pi_g)$ state to explain the difference between predicted and observed decay rates. Thus, it was concluded that there is additional collisional process responsible for the depopulation of the $N_2(B^3\Pi_g)$ state. In Chapter 4 it was concluded that the additional process of the depopulation of the $N_2(B^3\Pi_g)$ state observed in the discharge in pure nitrogen is absent or significantly suppressed in presence of the molecular oxygen, see Fig. 4.29. Thus, it can be assumed that the collisional partner leading to the depopulation of the $N_2(B^3\Pi_g)$ state is the excited nitrogen molecule or atom, which are quenched rapidly by the molecular oxygen in air. One can see in Fig. 4.30 that abnormally fast decay (lifetime is 30 ns) of the $N_2(B^3\Pi_g)$ state is followed by the decay agreeing with the theoretically predicted one (lifetime is 147 ns) in the late afterglow. Also, it is seen that the decay rate in the early afterglow slows down rather fast: during 25 ns, while the intensity of the emission decrease only in 3 times. Based on the listed facts it is assumed that fast decay of the $N_2(B^3\Pi_g)$ state is caused by self-quenching of $N_2(B^3\Pi_g)$ molecules. Indeed, self-quenching is fast, when the density of the $N_2(B^3\Pi_g)$ state is high. Then decay slows down significantly, since the reaction rate is proportional to the squared value of the density of the $N_2(B^3\Pi_g)$ state. The proposed process is the pooling

reaction

$$N_2(B) + N_2(B) \rightarrow N_2^* + N_2(X^1\Sigma_g^+, v) \rightarrow N_2(B, v) + N_2(X^1\Sigma_g^+, v) + \varepsilon_{(9.16)},$$
$$N_2(B) = N_2(B^3\Pi_g, W^3\Delta_u, B'^3\Sigma_u^-), \varepsilon_{(9.16)} = 5 \text{ eV}. \quad (9.16)$$

Here $\varepsilon_{(9.16)}$ is the thermalization energy. The process (9.16) can be efficient only under conditions of the high specific energy deposition at high reduced field, since it requires high excitation degree leading to the high density of the $N_2(B)$ state. To the best of our knowledge the rate constant $k_{(9.16)}$ of the process (9.16) is not available in the literature. Thus, it was assumed that the rate constant $k_{(9.16)}$ is the same as the total rate constant of the pooling reactions (9.11) and (9.12) of the $N_2(A^3\Sigma_u^+)$ state and equal to $3.6 \cdot 10^{-10}$ cm^{3}s^{-1}. The heat release in the process (9.16) is set to be equal 5 eV.

Results of numerical calculations using the kinetics model including the proposed process (9.16) demonstrates good agreement between temporal dynamics of $N_2(B^3\Pi_g)$ density and FPS emission profile, see Fig. 9.6. Thus, process (9.16) allows to explain decay of FPS emission faster than depopulation of $N_2(B^3\Pi_g)$ provided by the sum of radiative depopulation and quenching by the molecular nitrogen.

Another possible process between vibrationally excited $N_2(B^3\Pi_g, v)$ molecules leading to the $N_2(B^3\Pi_g)$ state depopulation is

$$N_2(B^3\Pi_g, v') + N_2(B^3\Pi_g, v'') \rightarrow N_4^+ + e. \quad (9.17)$$

However, produced in (9.17) ion N_4^+ recombines according to (6.4) with formation of the $N_2(C^3\Pi_u)$ state. The dynamics of the $N_2(C^3\Pi_u, v = 0)$ state calculated numerically without (9.17) and the dynamics of the SPS(0-0) emission measured experimentally demonstrate good agreement, see Fig. 9.6.

Test calculations showed that if the process (9.17) is included in the kinetic scheme, the good agreement is violated significantly. Thus, the dynamics of the $N_2(C^3\Pi_u)$ state in the late afterglow is controlled by the pooling reaction (9.12) between $N_2(A^3\Sigma_u^+)$ states only. In other words, the probability of the reaction (9.17) is relatively low. Following the same logic it is concluded that the $N_2(C^3\Pi_u)$ state is not one of the main products in the reaction (9.16). It was shown by the test numerical calculations that possible fraction the $N_2(C^3\Pi_u)$ state in the products is not higher than 1.5%, otherwise the dynamics of the $N_2(C^3\Pi_u)$ density does not agree the dynamics of SPS(0-0) emission, see Fig. 9.6, and the time evolution of the calculated radial distribution of SPS(0-0) emission does not agree experimentally measured one, see Chapter 8.

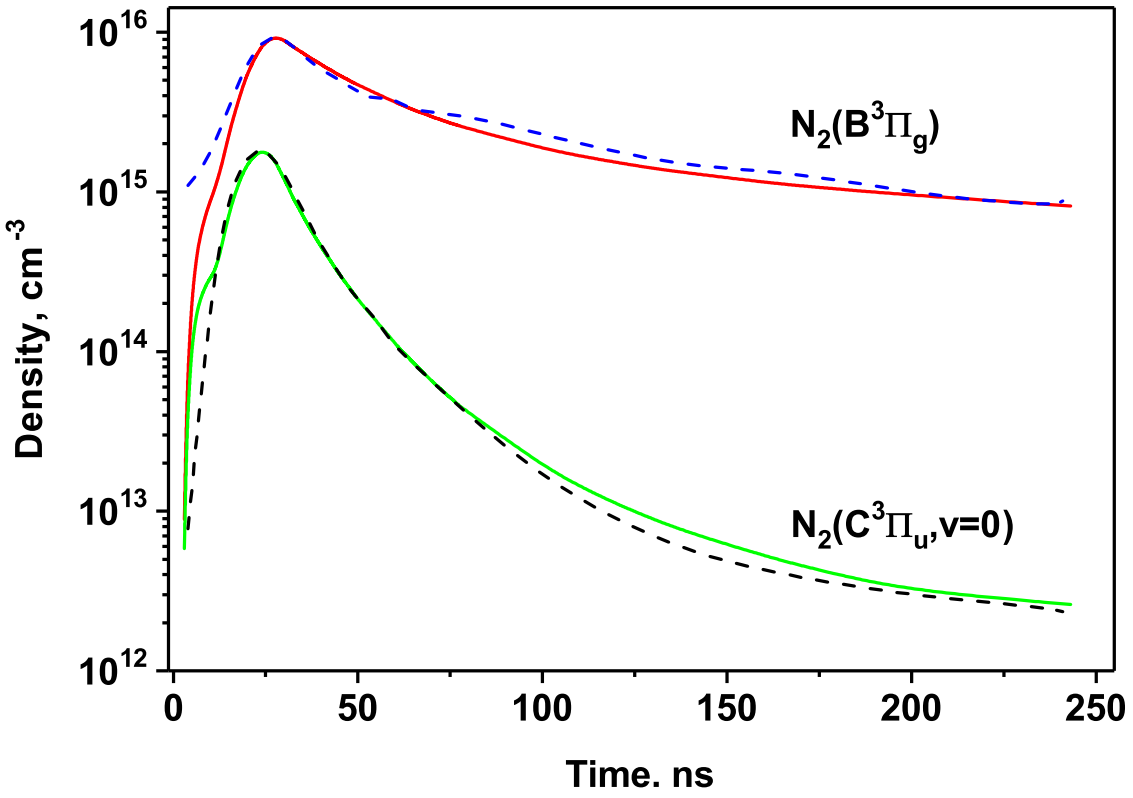

Figure 9.6 – The dynamics of the $N_2(B^3\Pi_g)$ and $N_2(C^3\Pi_u, v = 0)$ states calculated numerically (solid lines) and the dynamics of the emission intensity of FPS and SPS(0-0) measured experimentally (dashed lines).

To verify validity of the assumptions about main processes leading to the fast gas heating in pure nitrogen, the numerical modeling of the fast gas heating dynamics was performed. The results of the numerical calculations of the fast gas heating in pure nitrogen and the experimental results are presented in Fig. 9.7. The shape of initial radial distribution profile of the electron density for calculations was taken from Fig. 8.9. In the modeling the output temperature value is calculated using equation (9.6) taking into account radial distribution of the $N_2(C^3\Pi_u, v = 0)$ state.

One can see that good agreement with the experimental results is achieved. This means that modified kinetics scheme including the process (9.16) proposed above describes well the fast gas dynamics in pure nitrogen. If the proposed pooling process (9.16) is excluded from the model the numerical calculations underestimate gas heating significantly, the calculated temperature is 900 K less in this case. Thus, it is extremely important to take this process into account at conditions of high specific energy deposition at high reduced electric fields.

The sharp rise of the gas temperature is clearly seen after 0, 260 and 505 ns time instants in Fig. 9.7. These time instants correspond to the three main discharge pulses, where the energy is deposited and molecular nitrogen is excited efficiently.

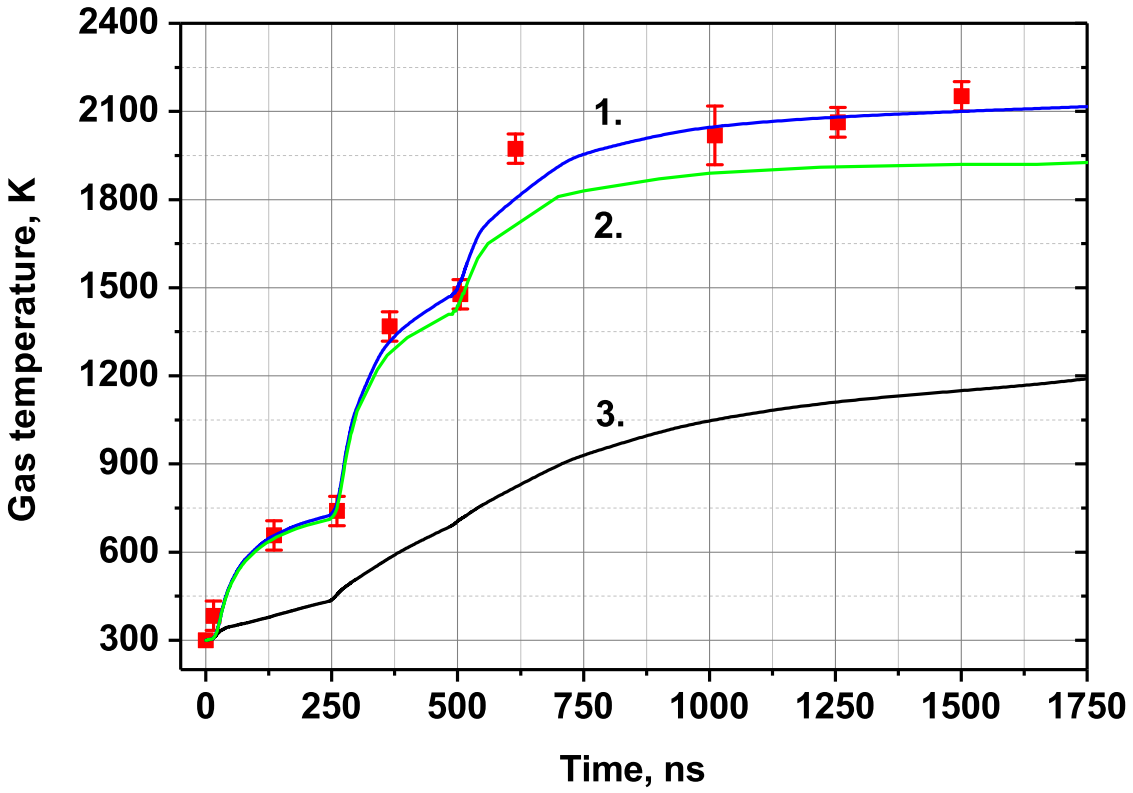

Figure 9.7 – Translational gas temperature in the nanosecond capillary discharge and its afterglow at 27 mbar in pure N_2, $I_{tr} = 65$ A in the first discharge pulse. Square symbols denote the experimental results from Fig. 9.3. Solid curves denote results of numerical calculations at different assumptions about the kinetics model: (1) with proposed pooling reaction (9.16) and with the heat release due to quenching of $N(^2D)$ atoms; (2) with proposed pooling reaction (9.16), but without the heat release due to quenching of $N(^2D)$ atoms; (3) with the heat release due to quenching of $N(^2D)$ atoms, but without proposed pooling reaction (9.16). The pooling reaction (9.11) is included in all calculations.

The fast energy relaxation from the electronic degrees of freedom in processes (9.11) and (9.16) is extremely intensive after the pulses due to high density of the excited nitrogen states. Then the energy release slows down, since the densities of the excited species decrease, and the slope of the tangent of the temporal profile of the gas temperature becomes lower. At time scale of 1 μs the exited species participating in the fast gas heating are almost used up and the temperature rise slows down significantly. It is illustrated by Fig. 9.8, where the temporal dynamics of the main nitrogen plasma species is presented.

One can see that effective production of atoms and excited nitrogen molecules during the main discharge pulses takes place. Concentrations of $N(^4S)$ and $N(^2D)$

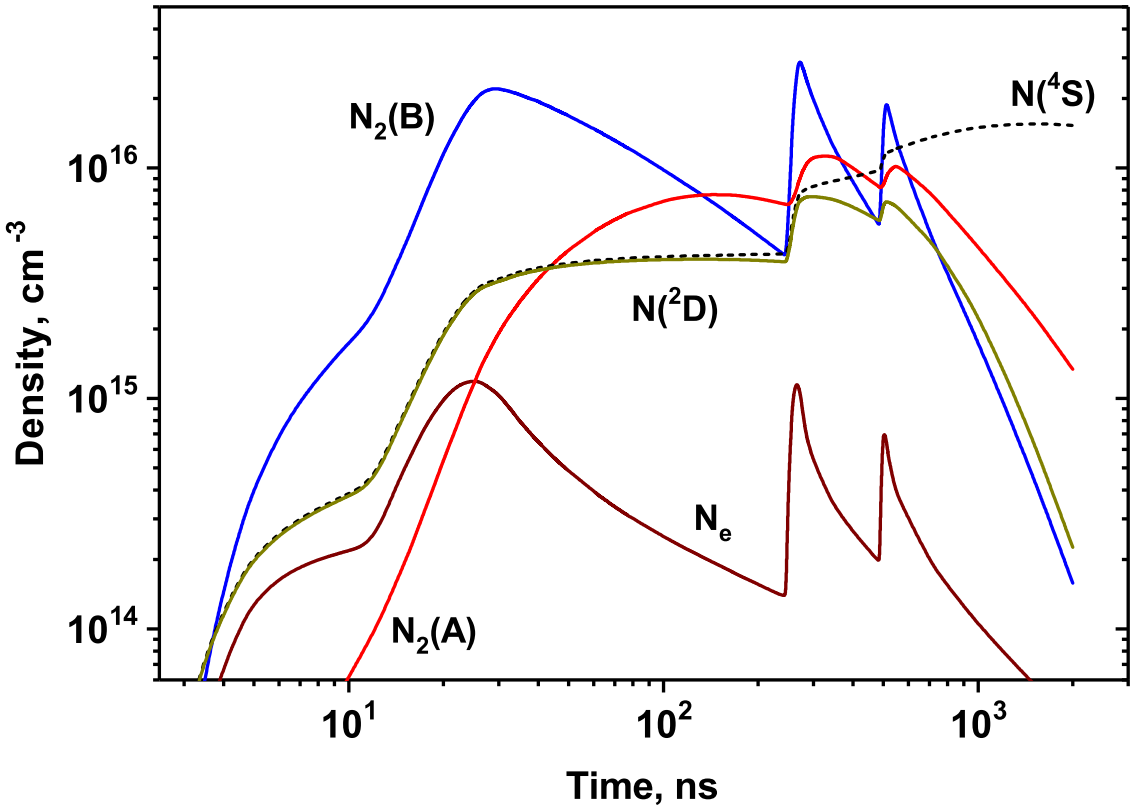

Figure 9.8 – The temporal evolution of the main nitrogen species averaged over the cross-section of the discharge tube for conditions of the Fig. 9.7.

atoms at $t < 20$ ns are comparable, since they are produced in the same process

$$e + \mathrm{N_2} \rightarrow \mathrm{N}(^4\mathrm{S}) + \mathrm{N}(^2\mathrm{D}). \tag{9.18}$$

Then $\mathrm{N}(^4\mathrm{S})$ atom density slightly decreases due to the reaction

$$\mathrm{N_2}(\mathrm{A}^3\Sigma_\mathrm{u}^+) + \mathrm{N}(^4\mathrm{S}) \rightarrow \mathrm{N_2} + \mathrm{N}(^2\mathrm{P}). \tag{9.19}$$

After the third discharge pulse, at times t > 500 ns, $\mathrm{N}(^2\mathrm{D})$ atoms density sufficiently decreases due to quenching by nitrogen molecules in the reaction (9.14) with the rate constant increasing at high temperatures [58], see (9.15).

The density of metastable electronically excited $\mathrm{N_2}(\mathrm{A}^3\Sigma_\mathrm{u}^+)$ molecules decreases only after 700 ns. It is caused by quenching in the pooling reaction (9.11) in the beginning, and further by quenching by atomic nitrogen. Rather high electron density in the afterglow (higher than 10^{14} cm^{-3} at times $t < 1$ μs) also can be noted one more time.

The $\mathrm{N_2}$(B) state is efficiently produced in the discharge pulses and reaches maximum density $2.88 \cdot 10^{16}$ cm^{-3} in the second discharge pulse. This is about 4.3% of initial nitrogen density, which is not typical for the nanosecond discharge at low

specific energy deposition, but can be easily achieved in at high specific energy deposition under the present conditions. So high density of the $N_2(B)$ state leads to the intensive fast gas heating due to proposed pooling process (9.16), which is not observed usually and was not mentioned in the kinetics schemes [5, 26–28, 60] validated and widely used for the description of the fast gas heating in nitrogen and nitrogen:oxygen mixtures.

The final temperature is high, about 2100 K, at an initial temperature of 300 K, see Fig. 9.7. In Chapter 1 it was mentioned that typical temperature rise in the fast gas heating studies is much lower, for example, 200 K in [60]. The almost one order magnitude higher temperature rise allows to demonstrate the role of quenching (9.14) of $N(^2D)$ atoms in the fast gas heating of pure nitrogen clearly. In Fig. 9.7 it is seen that a good agreement between the experimental results and the results of the numerical calculations is achieved only if the process (9.14) is taken into account. If the process (9.14) is excluded from the model, the final temperature value is about 200 K lower. It is also clearly seen that this channel of the heat release starts to play a significant role only at rather high temperature (at $t > 300$ ns, i.e. after the third current pulse), since the rate constant of the reaction (9.14) strongly depends on the gas temperature, see expression (9.15).

Strong temperature dependence of the rate constant of the process (9.14) together with significant impact to the final temperature rise, see Fig. 9.7, allow to validate the value the of the thermalization energy in the pooling reaction (9.16) between $N_2(B)$ molecules. Indeed, if the thermalization energy $\varepsilon_{(9.16)}$ is underestimated in the kinetics model, the temperature rise will be slower, and, consequently, the energy release due to quenching (9.14) of $N(^2D)$ atoms will be suppressed. The final temperature value in the numerical calculations will be much lower than the experimentally measured one. In opposite case, when the $\varepsilon_{(9.16)}$ is overestimated, the energy releases will be much faster, thus the process (9.14) will be much more intensive. The final temperature value in the numerical calculations will be much higher than the experimentally measured one in this case. Good agreement between experimental results and results of the numerical calculations shown in Fig. 9.7 demonstrate that $\varepsilon_{(9.16)} = 4 - 5$ eV is reasonable.

Another conclusion following from the strong temperature dependence of the rate constant of the process (9.14) was mentioned in Chapter 1. It was shown in [5, 26] that in nitrogen:oxygen mixtures the fraction of the discharge energy converted to the gas heating is the function of the reduced electric field only. One can conclude based on Fig. 9.7 that for pure nitrogen this value also depends on the specific deposited energy. Indeed, if the specific deposited energy is lower even at the same reduced electric field, the densities of the $N_2(A^3\Sigma_u^+)$ and $N_2(B)$ states are also lower. Thus, the heat release in the processes (9.11) and (9.16) decreases, and the tem-

perature rise is slower. At lower temperatures quenching of $N(^2D)$ atoms is less efficient, see (9.15), thus, the smaller fraction of energy stored in $N(^2D)$ atoms will be released to the gas heating comparing to the discharge at high specific deposited energy even at the same reduced electric field.

The new process playing significant role in the fast gas heating in pure nitrogen under present conditions (pooling reaction between $N_2(B)$ molecules) introduced above was not mentioned in the kinetics schemes [5, 26–28, 60] validated and widely used for the description of the fast gas heating in nitrogen and nitrogen:oxygen mixtures. So, it is important for modified model verification to compare experimental results and results of the numerical calculations by kinetics model including this process in nitrogen:oxygen mixtures under the same conditions as for pure nitrogen. This is the subject of the next section.

9.3 Fast gas heating in nitrogen:oxygen mixtures

The same experimental technique was used to study the fast gas heating in the nitrogen:oxygen mixtures. The only difference is that rotational temperature of the $N_2(C^3\Pi_u, v = 0)$ state is interpreted by the different manner: using (9.9) or (9.10) depending on the oxygen concentration.

Admixtures of molecular oxygen influence on the fast gas heating dynamics by two factors. First factor is the influence on the initial electron density distribution, see Fig. 8.9, which leads to different distribution of deposited energy in the cross-section of the tube and, consequently, different local excitation degree. Second factor is changes in the kinetics processes, since oxygen molecule is effective quencher of excited nitrogen states.

In Chapter 8 it was shown that even 1% of molecular oxygen changes the initial electron density distribution over the tube cross-section noticeably, see Fig. 8.9. The electron density radial profile is flatter in this case than in pure nitrogen, but the maximum of the electron density is still located out of axis. At the same time, molecular oxygen at low concentration does not affect the fast gas heating kinetics dramatically. Indeed, the ratio between the rate constants of the quenching of the $N_2(B^3\Pi_g, C^3\Pi_u)$ states by oxygen molecules and by nitrogen molecules is about 30. Thus, the oxygen admixture with $[O_2]/[N_2] = 1\% < 1/30$ is negligible. Thus, role the proposed pooling reaction (9.16) is significant even at 1% of molecular oxygen.

The temperature dynamics in N_2:O_2 mixture with 1% of O_2 calculated numerically and measured experimentally is presented in Fig. 9.9. The shape of initial radial distribution profile of the electron density for calculations was taken from Fig. 8.9. To obtain the gas temperature, the values of the rotational temperature of

$N_2(C^3\Pi_u, v' = 0)$ state were multiplied by 1.095 for the pulses at 15-505 ns according to (9.9), and by 0.897 for the pulses after 505 ns according to (9.10) as for pure nitrogen, since small oxygen admixture does not change lifetime of the $N_2(B^3\Pi_g)$ state significantly. The results of the numerical calculations and the experimentally measured gas temperature are in good agreement. The final temperature is slightly (about 150 K) lower than the final temperature in pure nitrogen. The difference is mostly caused by the differences in the local specific deposited energy due to initial electron density profile transformation, see Fig. 8.9. Flatter profile causes more uniform energy deposition in the cross-section of the tube and, consequently, lower local specific deposited energy. This leads to decrease of the peak values of the densities of excited nitrogen species and decrease of the fast gas heating. At 1% admixture only slightly changes radial profile of the initial electron density, thus the difference in the final temperature value is not high.

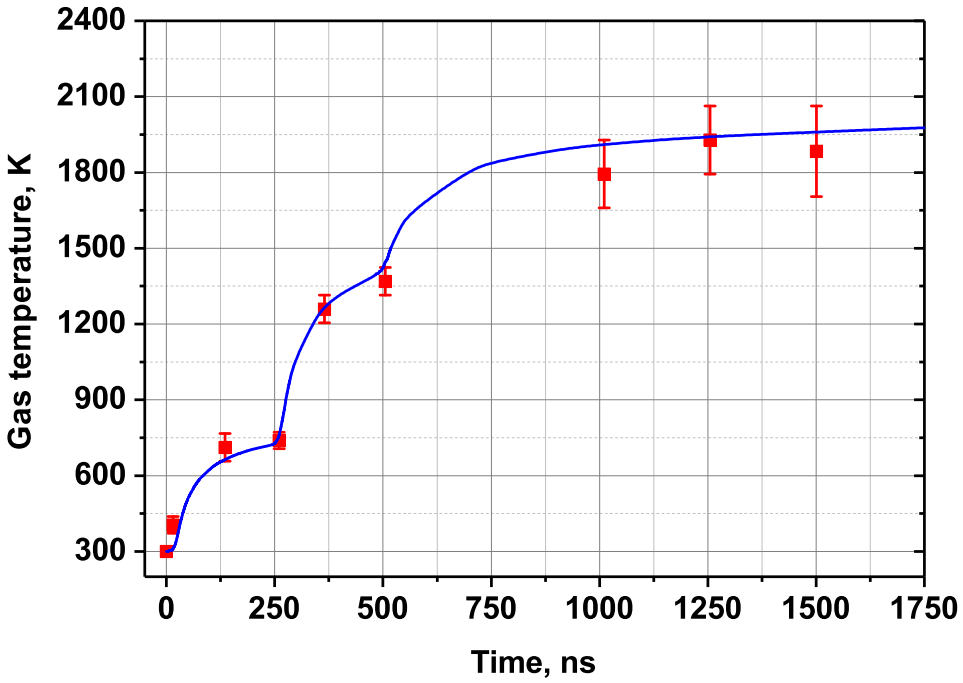

Figure 9.9 – Translational gas temperature in the nanosecond capillary discharge and its afterglow at 27 mbar in N_2:O_2 mixture with 1% of O_2, I_{tr} = 65 A on the first discharge pulse. Experimental results (square symbols) and results of numerical calculations (solid line).

More significant influence of the presence of molecular oxygen is expected in N_2:O_2 mixture with 10% of O_2. Firstly, the shape of the initial electron density in N_2:O_2 mixture with 10% of O_2 has the maximum on the tube axis in contrast to pure nitrogen and N_2:O_2 mixture with 1% of O_2. Secondly, the density of O_2 in this case is high enough and the interaction of excited nitrogen states with oxygen

becomes dominate.

The gas temperature in N_2:O_2 mixture with 10% of O_2 measured experimentally and calculated numerically is presented in Fig. 9.10. The shape of initial radial distribution profile of the electron density for calculations was taken from Fig. 8.9. To obtain the gas temperature, the values of the rotational temperature of $N_2(C^3\Pi_u, v' = 0)$ state were multiplied by 1.095 for all pulses according to (9.9), since rather high density of molecular oxygen leads to efficient quenching of the $N_2(B^3\Pi_g)$ state after the main pulses, thus, the $N_2(C^3\Pi_u, v' = 0)$ state is populated by direct electron impact mainly from the ground state of molecular nitrogen, despite the low reduced electric field in the low-amplitude diagnostic pulses.

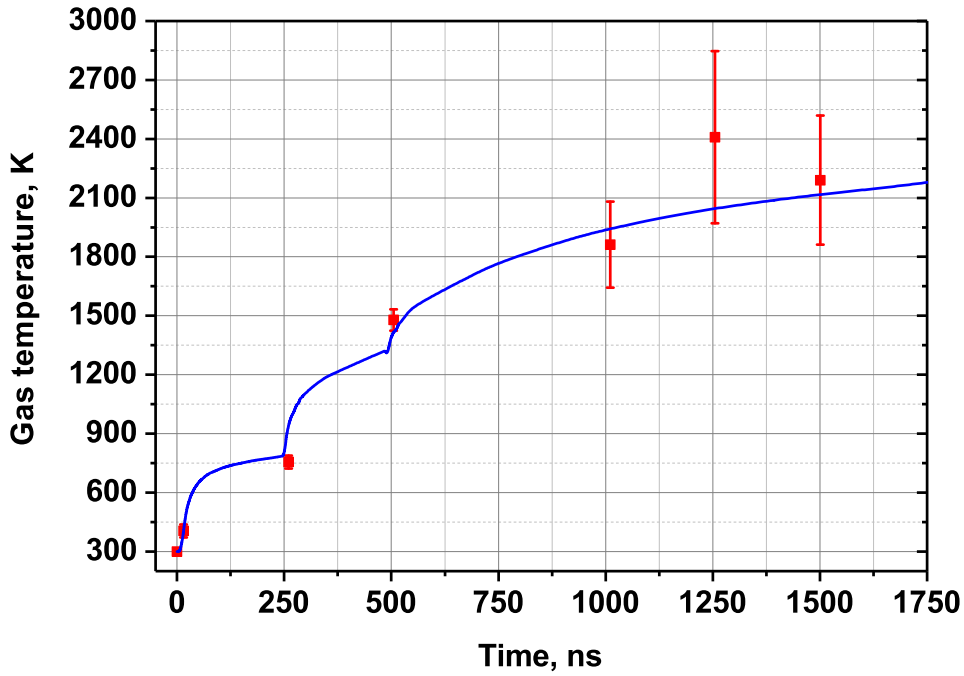

Figure 9.10 – Translational gas temperature in the nanosecond capillary discharge and its afterglow at 27 mbar in N_2:O_2 mixture with 10% of O_2, $I_{tr} = 65$ A on the first discharge pulse. Experimental results (square symbols) and results of numerical calculations with (solid line).

One can see that the results of numerical calculation agrees the experimentally measured gas temperature dynamics rather good. The test calculations showed that impact of the proposed pooling reaction (9.16) in this case is low. If this process is excluded from the model, the final temperature is less by 50 K only. However, the final temperature in N_2:O_2 mixture with 10% of O_2 is even higher than it is in pure nitrogen ($\Delta T = 60$ K at 1750 ns), since interaction of excited nitrogen species with oxygen is fast and effective channel of the thermalization of electronic degrees of freedom in nitrogen:oxygen mixtures [5, 26, 27].

In air the kinetic of the fast gas heating is determined by fast quenching of the excited nitrogen states by oxygen as well. The influence of the pair pooling processes (9.11) and (9.16) is negligible in this case. The fast gas heating dynamics in dry air measured experimentally and calculated numerically is presented in Fig. 9.11. The shape of initial radial distribution profile of the electron density for calculations was taken from Fig. 8.9. To obtain the gas temperature, the values of the rotational temperature of $N_2(C^3\Pi_u, v' = 0)$ state were multiplied by 1.095 for all pulses according to (9.9). Good agreement between experimentally measured gas temperature and the temperature calculated numerically is seen in Fig. 9.11. The final temperature is noticeably higher than in pure nitrogen ($\Delta T = 200$ K at 1750 ns) and higher than in N_2:O_2 mixture with 10% of O_2 due to high oxygen density.

Comparison of the results of numerical calculations with the experimental results demonstrates good agreement in the wide range of gas composition: from pure nitrogen to dry air. This confirms validity of the kinetic model and results of the measurements of the initial electron density distribution used as input data for the calculations.

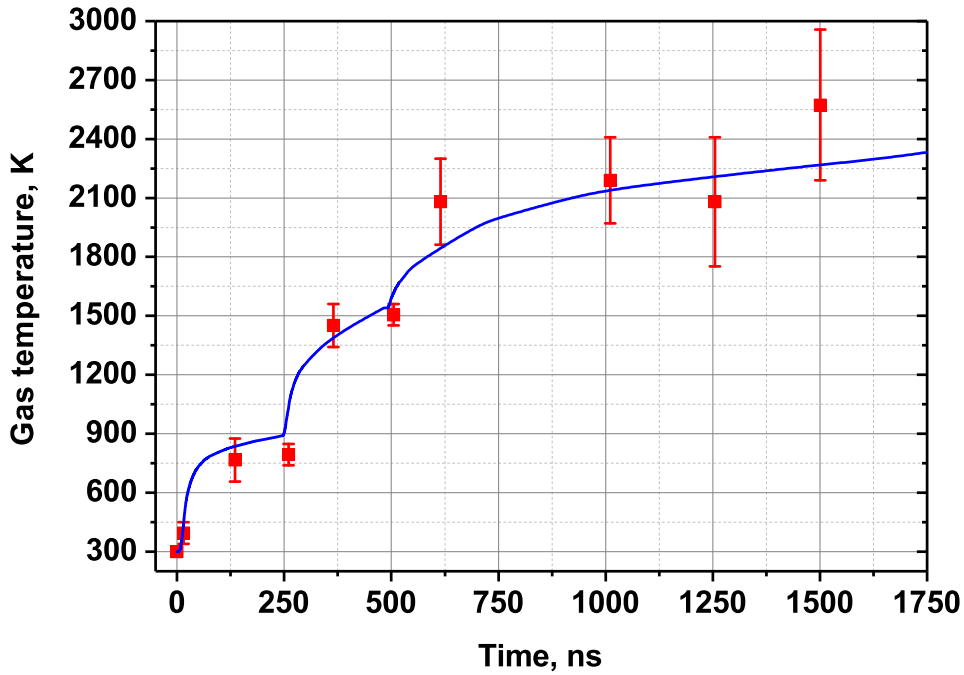

Figure 9.11 – Translational gas temperature in the nanosecond capillary discharge and its afterglow at 27 mbar in dry air, $I_{tr} = 65$ A on the first discharge pulse. Experimental results (square symbols) and results of numerical calculations with (solid line).

9.4 Conclusion

The fast gas heating in pure nitrogen was studied using nanosecond capillary discharge under conditions of high specific energy deposition at high reduced electric fields. The high temperature rise at microsecond time scale was obtained. The role of quenching of $N(^2D)$ atoms was clearly demonstrated. A new process leading to the fast gas heating has been proposed: pooling reaction between $N_2(B) = N_2(B^3\Pi_g, W^3\Delta_u, B'^3\Sigma_u^-)$ molecules. In spite of numerous kinetics schemes widely used for the description of the fast gas heating in nitrogen and nitrogen:oxygen mixtures, for example [5, 26–28, 60], this process has never been mentioned before. It was shown that at the conditions of high specific energy deposition at high reduced electric fields, the pooling reaction between $N_2(B)$ molecules plays key role in the fast gas heating in pure nitrogen. The numerical calculations of fast gas heating dynamics in 1D geometry for pure nitrogen and N_2:O_2 mixtures with 1, 10 and 20% of O_2 agree the experimental results of temperature measurements by optical emission spectroscopy technique. Thus, it was concluded that the proposed kinetics scheme modification including quenching of nitrogen excited species by electrons and pooling reaction between $N_2(B)$ molecules is reasonable. The results of measurements of the initial electron density distribution in the cross-section of the tube used as input data for the numerical calculation also can be considered as validated.

Chapter 10

General conclusions

Contributions of the present work

The work was focused on kinetics of nanosecond plasma at the conditions of high specific energy deposition at high reduced electric fields.

Measurements of the electric parameters of the nanosecond capillary discharge demonstrated that the major part of energy is deposited at high reduced electric fields, 100-350 Td. The total specific deposited energy is also high, up to 1 eV/molecule. It was shown by numerical kinetics modeling that the total fraction of excited nitrogen atoms and molecules is 5-7% of initial gas density. At these conditions, probability of interaction between excited and/or charged particles increases changing kinetics in the discharge and afterglow. In this case, applicability of any spectroscopic technique should be analyzed taking into account additional production and depopulation of the levels under study. In particular, it was shown that the technique of the electric field measurements based on relative population of the $N_2(C^3\Pi_u)$ and $N_2^+(B^2\Sigma_u^+)$ levels, is not valid under conditions of the capillary nanosecond discharge at moderate pressure.

Long-lived plasma was observed in pure nitrogen experimentally: at typical electron density $N_e = 9 \cdot 10^{14}$ cm^{-3} in the discharge pulse, the electron density values observed after the discharge, for example 200 ns and 600 ns later, are equal to 10^{14} cm^{-3} and $0.4 \cdot 10^{14}$ cm^{-3}, respectively. Similar decay was observed numerically. It was shown by comparison of the experimental results and the results of the numerical calculations that the reactions of the associative ionization between

excited states of molecular nitrogen sustain the high electron density in the afterglow. Therefore, the high electronic excitation degree due to high specific energy deposition was confirmed, since these reactions are efficient only at high density of the excited species. The long decay of the plasma was also observed experimentally and numerically in nitrogen:oxygen mixtures. In this case the existence of the long-lived plasma is explained by slow ion-electron recombination involving ion O_2^+, which is the dominant positive ion under given conditions according to the numerical calculations.

Depopulation of excited species in the early afterglow of the nanosecond capillary discharge in pure nitrogen and nitrogen:oxygen mixtures was studied. It was shown that the decay of the excited states, in particular of the $N_2(C^3\Pi_u, v = 0)$ and $N_2(B^3\Pi_g)$ states, is abnormally fast. The detailed studies for pure nitrogen demonstrated that the additional collision process, which is usually not taken into account in kinetics models developed for discharges at low specific energy deposition, is responsible for the quenching of the $N_2(C^3\Pi_u, v = 0)$ state. This process is superelastic collisions between $N_2(C^3\Pi_u, v = 0)$ and electrons:

$$N_2(C^3\Pi_u) + e \rightarrow N_2(X^1\Sigma_g^+, A^3\Sigma_u^+, B^3\Pi_g, ...) + e.$$

The estimations of the rate constants of quenching of the $N_2(C^3\Pi_u)$, $N_2(B^3\Pi_g)$, $N_2^+(B^2\Sigma_u^+)$ and $N_2(A^3\Sigma_u^+)$ states by electrons were performed. The estimated rate constants of quenching by electrons are $k_e^{N_2(C)} \approx 10^{-7}$ cm^{3}s^{-1}, $k_e^{N_2(B)} \approx 2.2 \cdot 10^{-8}$ cm^{3}s^{-1}, $k_e^{N_2^+(B)} \approx 10^{-7}$ cm^{3}s^{-1} and $k_e^{N_2(A)} \approx 1.8 \cdot 10^{-10}$ cm^{3}s^{-1} at the electron temperature $T_e \approx 0.8$ eV typical for the early afterglow according to the numerical calculations. A good agreement between the experimental results and the results of the kinetic modeling of the emission intensity decay using the suggested rate constants was demonstrated on the example of the $N_2(C^3\Pi_u, v = 0)$ state.

Radial distribution of excited species was studied experimentally to obtain initial profile of the electron density required for the reliable 1D numerical modeling of the nanosecond capillary discharge and correct comparison of the results of the numerical calculations with the experiment. It was demonstrated that the maximum of the electron density is located out of axis of the capillary tube in pure nitrogen. It was also observed that the initial electron density distribution is sensitive to gas composition: even 1% of oxygen admixture changes the initial radial profile of the electron density.

Fast gas heating in pure nitrogen and N_2:O_2 mixtures was studied experimentally and numerically using experimentally measured initial electron density profiles as input data. The high temperature rise at time scale of hundreds of nanoseconds was obtained. The significant role of quenching of $N(^2D)$ atoms in the fast gas heating in pure nitrogen was clearly demonstrated. On the basis of

comparison of the experimental results of gas temperature dynamics measurements and the results of numerical modeling, the new process leading to the intensive fast gas heating in pure nitrogen has been proposed: pooling reaction between $N_2(B)$ molecules

$$N_2(B) + N_2(B) \rightarrow N_2^* + N_2(X^1\Sigma_g^+, v) \rightarrow N_2(B, v) + N_2(X^1\Sigma_g^+, v) + \varepsilon,$$
$$N_2(B) = N_2(B^3\Pi_g, W^3\Delta_u, B'^3\Sigma_u^-), \varepsilon = 5 \text{ eV},$$

with the rate constant $k \approx 4 \cdot 10^{-10}$ cm^{3}s^{-1}. In spite of numerous kinetics schemes widely used for the description of the fast gas heating in pure nitrogen and nitrogen:oxygen mixtures, this process has never been mentioned before. The mechanism of gas heating in this process is assumed to be similar to the mechanism of heating in pooling reaction between $N_2(A^3\Sigma_u^+)$ molecules used in most models of the fast gas heating in nitrogen plasma.

It was shown that at the conditions of high specific energy deposition at high reduced electric fields, the pooling reaction between $N_2(B)$ molecules plays the key role in the fast gas heating in pure nitrogen. The agreement between the numerical calculations of the fast gas heating dynamics for N_2:O_2 mixtures with 1, 10 and 20% of O_2 and the experimental results of the gas temperature measurements was also demonstrated.

Finally, the following can be concluded: the obtained experimental data set – reduced electric field profile, deposited energy, plasma decay, time evolution of the radial profiles of the excited species, temporal dynamics of the $N_2(C^3\Pi_u, v = 0)$ density and dynamics of the gas temperature – is adequately described by the kinetics model including quenching of nitrogen excited species by electrons and pooling reaction between $N_2(B)$ molecules.

Perspectives and future work

The presented results proved that describing the plasma-chemical kinetics of nanosecond capillary discharges, it is necessary to take into account the appearance of a number of new important processes associated with the high specific energy deposition at high reduced electric field leading to the high electronic excitation degree. However, the high absolute density of excited species was demonstrated only by numerical modeling and by indirect measurements, for example, by observation of long-lived plasma and intensive fast gas heating. Taking this into account, the future work will consist of absolute density measurements of the main excited species. The following methods will be used: the absolute spectroscopy of the atomic and molecular species and the two-photon absorption laser-induced fluorescence (TALIF), including two-dimensional TALIF by so-called "laser knife" technique. The obtained

knowledge of the discharge characteristics will allow choosing the optimal experimental conditions for atomic species measurements. The particular interest is to measure the nitrogen dissociation degree in the present range of the reduced electric field. This continuation of the discharge studies will be a part of work of the ASPEN (ANR) project. An additional item here is to put into operation a new experimental setup, which was designed and constructed during the present work. This will allow to perform measurements varying specific deposited energy independently on gas pressure at given E/N.

The study of the dissociation of the other molecular gases will be done. For example, it is planned to study possibility of CO_2 dissociation by nanosecond capillary discharge, and to find the most optimal conditions for high yield of the process. The nanosecond capillary discharge is a perspective tool for the investigation of plasma chemical processes in gas mixtures of various compositions due to the combination of the high electric field, high density of atomic species and high temperature.

List of Figures

Bibliography

[1] Babich L P 2005 Analysis of a new electron-runaway mechanism and record-high runaway-electron currents achieved in dense-gas discharges *Physics-Uspekhi* **48** 1015

[2] Raizer Y P 1991 *Gas Discharge Physics* (New York: Springer)

[3] Hagelaar G J M and Pitchford L C 2005 Solving the Boltzmann equation to obtain electron transport coefficients and rate coefficients for fluid models *Plasma Sources Science and Technology* **14** 722

[4] Phelps A V and Pitchford L C 1985 Anisotropic scattering of electrons by N_2 and its effect on electron transport *Phys. Rev. A* **31**(5) 2932–2949

[5] Popov N A 2011 Fast gas heating in a nitrogen-oxygen discharge plasma: I. Kinetic mechanism *Journal of Physics D: Applied Physics* **44** 285201

[6] Starikovskiy A, Aleksandrov N and Rakitin A 2012 Plasma-assisted ignition and deflagration-to-detonation transition *Philosophical Transactions of the Royal Society of London A: Mathematical, Physical and Engineering Sciences* **370** 740–773

[7] Kosarev I N, Khorunzhenko V I, Mintoussov E I, Sagulenko P N, Popov N A and Starikovskaia S M 2012 A nanosecond surface dielectric barrier discharge at elevated pressures: time-resolved electric field and efficiency of initiation of combustion *Plasma Sources Science and Technology* **21** 045012

[8] Vasilyak L M, Kostyuchenko S V, Kudryavtsev N N and Filyugin I V 1994 Fast ionisation waves under electrical breakdown conditions *Physics-Uspekhi* **37** 247

[9] Klochko A V, Starikovskaia S M, Xiong Z and Kushner M J 2014 Investigation of capillary nanosecond discharges in air at moderate pressure: comparison

of experiments and 2D numerical modelling *Journal of Physics D: Applied Physics* **47** 365202

[10] Pancheshnyi S V, Starikovskaia S M and Starikovskii A Y 1999 Population of nitrogen molecule electron states and structure of the fast ionization wave *Journal of Physics D: Applied Physics* **32** 2219

[11] Petrishchev V, Leonov S and Adamovich I V 2014 Studies of nanosecond pulse surface ionization wave discharges over solid and liquid dielectric surfaces *Plasma Sources Science and Technology* **23** 065022

[12] Stepanyan S A, Starikovskiy A Y, Popov N A and Starikovskaia S M 2014 A nanosecond surface dielectric barrier discharge in air at high pressures and different polarities of applied pulses: transition to filamentary mode *Plasma Sources Science and Technology* **23** 045003

[13] Simeni M S, Goldberg B M, Zhang C, Frederickson K, Lempert W R and Adamovich I V 2017 Electric field measurements in a nanosecond pulse discharge in atmospheric air *Journal of Physics D: Applied Physics* **50** 184002

[14] Fridman G, Friedman G, Gutsol A, Shekhter A B, Vasilets V N and Fridman A 2008 Applied Plasma Medicine *Plasma Processes and Polymers* **5** 503–533

[15] Kong M G, Kroesen G, Morfill G, Nosenko T, Shimizu T, van Dijk J and Zimmermann J L 2009 Plasma medicine: an introductory review *New Journal of Physics* **11** 115012

[16] Dobrynin D, Fridman G, Friedman G and Fridman A 2009 Physical and biological mechanisms of direct plasma interaction with living tissue *New Journal of Physics* **11** 115020

[17] Heinlin J, Morfill G, Landthaler M, Stolz W, Isbary G, Zimmermann J L, Shimizu T and Karrer S 2010 Plasma medicine: possible applications in dermatology *JDDG: Journal der Deutschen Dermatologischen Gesellschaft* **8** 968–976

[18] Laroussi M 2014 From Killing Bacteria to Destroying Cancer Cells: 20 Years of Plasma Medicine *Plasma Processes and Polymers* **11** 1138–1141

[19] Graves D B 2014 Low temperature plasma biomedicine: A tutorial review *Physics of Plasmas* **21** 080901

[20] Song K, Li G and Ma Y 2014 A Review on the Selective Apoptotic Effect of Nonthermal Atmospheric-Pressure Plasma on Cancer Cells *Plasma Medicine* **4** 193–209

[21] Graves D B 2017 Mechanisms of Plasma Medicine: Coupling Plasma Physics, Biochemistry, and Biology *IEEE Transactions on Radiation and Plasma Medical Sciences* **1** 281–292

[22] Ayan H, Fridman G, Gutsol A F, Vasilets V N, Fridman A and Friedman G 2008 Nanosecond-Pulsed Uniform Dielectric-Barrier Discharge *IEEE Transactions on Plasma Science* **36** 504–508

[23] Jiang C, Chen M T, Gorur A, Schaudinn C, Jaramillo D E, Costerton J W, Sedghizadeh P P, Vernier P T and Gundersen M A 2009 Nanosecond Pulsed Plasma Dental Probe *Plasma Processes and Polymers* **6** 479–483

[24] Adamovich I V, Choi I, Jiang N, Kim J H, Keshav S, Lempert W R, Mintusov E, Nishihara M, Samimy M and Uddi M 2009 Plasma assisted ignition and high-speed flow control: non-thermal and thermal effects *Plasma Sources Science and Technology* **18** 034018

[25] Starikovskaia S M 2006 Plasma assisted ignition and combustion *Journal of Physics D: Applied Physics* **39** R265

[26] Popov N A 2001 Investigation of the mechanism for rapid heating of nitrogen and air in gas discharges *Plasma Physics Reports* **27** 886–896

[27] Popov N A 2016 Pulsed nanosecond discharge in air at high specific deposited energy: fast gas heating and active particle production *Plasma Sources Science and Technology* **25** 044003

[28] Aleksandrov N L, Kindysheva S V, Nudnova M M and Starikovskiy A Y 2010 Mechanism of ultra-fast heating in a non-equilibrium weakly ionized air discharge plasma in high electric fields *Journal of Physics D: Applied Physics* **43** 255201

[29] Popov N A 2007 The effect of nonequilibrium excitation on the ignition of hydrogen-oxygen mixtures *High Temperature* **45** 261–279

[30] Aleksandrov N L, Kindysheva S V and Kochetov I V 2014 Kinetics of low-temperature plasmas for plasma-assisted combustion and aerodynamics *Plasma Sources Science and Technology* **23** 015017

[31] Popov N A 2016 Kinetics of plasma-assisted combustion: effect of non-equilibrium excitation on the ignition and oxidation of combustible mixtures *Plasma Sources Science and Technology* **25** 043002

[32] Li T, Adamovich I V and Sutton J A 2016 Effects of non-equilibrium plasmas on low-pressure, premixed flames. Part 1: CH^* chemiluminescence, temperature, and OH *Combustion and Flame* **165** 50 – 67

[33] Kosarev I, Aleksandrov N, Kindysheva S, Starikovskaia S and Starikovskii A 2009 Kinetics of ignition of saturated hydrocarbons by nonequilibrium plasma: C_2H_6- to C_5H_{12}-containing mixtures *Combustion and Flame* **156** 221 – 233

[34] Leonov S B, Adamovich I V and Soloviev V R 2016 Dynamics of near-surface electric discharges and mechanisms of their interaction with the airflow *Plasma Sources Science and Technology* **25** 063001

[35] Starikovskii A Y, Nikipelov A A, Nudnova M M and Roupassov D V 2009 SDBD plasma actuator with nanosecond pulse-periodic discharge *Plasma Sources Science and Technology* **18** 034015

[36] Montello A, Yin Z, Burnette D, Adamovich I V and Lempert W R 2013 Picosecond CARS measurements of nitrogen vibrational loading and rotational/translational temperature in non-equilibrium discharges *Journal of Physics D: Applied Physics* **46** 464002

[37] Benard N, Zouzou N, Claverie A, Sotton J and Moreau E 2012 Optical visualization and electrical characterization of fast-rising pulsed dielectric barrier discharge for airflow control applications *Journal of Applied Physics* **111** 033303

[38] Rethmel C, Little J, Takashima K, Sinha A, Adamovich I and Samimy M 2011 Flow Separation Control Using Nanosecond Pulse Driven DBD Plasma Actuators. *International Journal of Flow Control* **3**

[39] Takashima K, Zuzeek Y, Lempert W R and Adamovich I V 2011 Characterization of a surface dielectric barrier discharge plasma sustained by repetitive nanosecond pulses *Plasma Sources Science and Technology* **20** 055009

[40] Unfer T and Boeuf J P 2009 Modelling of a nanosecond surface discharge actuator *Journal of Physics D: Applied Physics* **42** 194017

[41] Komuro A, Takashima K, Konno K, Tanaka N, Nonomura T, Kaneko T, Ando A and Asai K 2017 Schlieren visualization of flow-field modification over an

airfoil by near-surface gas-density perturbations generated by a nanosecond-pulse-driven plasma actuator *Journal of Physics D: Applied Physics* **50** 215202

[42] Berdyshev A, Vikharev A, Gitlin M, Deryugin A, Ivanov O, Kochetov I, Litvak A, Napartovich A, Polushkin I, Stepanov A and Shcherbakov A 1988 Heating of the molecular gas in pulsed microwave discharges *High Temperature* **26** 496–501

[43] Mintoussov E I, Pendleton S J, Gerbault F G, Popov N A and Starikovskaia S M 2011 Fast gas heating in nitrogen-oxygen discharge plasma: II. Energy exchange in the afterglow of a volume nanosecond discharge at moderate pressures *Journal of Physics D: Applied Physics* **44** 285202

[44] Pai D Z, Lacoste D A and Laux C O 2010 Nanosecond repetitively pulsed discharges in air at atmospheric pressure - the spark regime *Plasma Sources Science and Technology* **19** 065015

[45] Rusterholtz D, Pai D, Stancu G, Lacoste D and Laux C 2012 Ultrafast Heating in Nanosecond Discharges in Atmospheric Pressure Air *Aerospace Sciences Meetings* (American Institute of Aeronautics and Astronautics) pp 2012–0509

[46] Rusterholtz D L, Lacoste D A, Stancu G D, Pai D Z and Laux C O 2013 Ultrafast heating and oxygen dissociation in atmospheric pressure air by nanosecond repetitively pulsed discharges *Journal of Physics D: Applied Physics* **46** 464010

[47] Zuzeek Y, Choi I, Uddi M, Adamovich I V and Lempert W R 2010 Pure rotational CARS thermometry studies of low-temperature oxidation kinetics in air and ethene-air nanosecond pulse discharge plasmas *Journal of Physics D: Applied Physics* **43** 124001

[48] Lo A, Cessou A, Boubert P and Vervisch P 2014 Space and time analysis of the nanosecond scale discharges in atmospheric pressure air: I. Gas temperature and vibrational distribution function of N_2 and O_2 *Journal of Physics D: Applied Physics* **47** 115201

[49] Lempert W R and Adamovich I V 2014 Coherent anti-Stokes Raman scattering and spontaneous Raman scattering diagnostics of nonequilibrium plasmas and flows *Journal of Physics D: Applied Physics* **47** 433001

[50] Znamenskaya I A, Latfullin D F, Lutskiĭ A E and Mursenkova I V 2010 Energy deposition in boundary gas layer during initiation of nanosecond sliding surface discharge *Technical Physics Letters* **36** 795–797

[51] Bazhenova T V, Znamenskaya I A, Lutsky A E and Mursenkova I V 2007 An investigation of surface energy input to gas during initiation of a nanosecond distributed surface discharge *High Temperature* **45** 523–530

[52] Kamardin I, Kuchinskii A and Rodichkin 1985 Investigation of heating of molecular nitrogen in the pulsed self-sustained discharge by a method of holographic interferometry *High Temperature* **23** 518–521

[53] Bruggeman P J, Sadeghi N, Schram D C and Linss V 2014 Gas temperature determination from rotational lines in non-equilibrium plasmas: a review *Plasma Sources Science and Technology* **23** 023001

[54] Laux C O, Spence T G, Kruger C H and Zare R N 2003 Optical diagnostics of atmospheric pressure air plasmas *Plasma Sources Science and Technology* **12** 125

[55] Piper L G 1988 State-to-state $N_2(A^3\Sigma_u^+)$ energy-pooling reactions. I. The formation of $N_2(C^3\Pi_u)$ and the Herman infrared system *The Journal of Chemical Physics* **88** 231–239

[56] Boeuf J P and Kunhardt E E 1986 Energy balance in a nonequilibrium weakly ionized nitrogen discharge *Journal of Applied Physics* **60** 915–923

[57] Ono R, Teramoto Y and Oda T 2010 Gas density in a pulsed positive streamer measured using laser shadowgraph *Journal of Physics D: Applied Physics* **43** 345203

[58] Galvao B R L, Braga J P, Belchior J C and C V A J 2014 Electronic Quenching in $N(^2D)$ + N_2 Collisions: A State-Specific Analysis via Surface Hopping Dynamics *Journal of Chemical Theory and Computation* **5** 1872–1877

[59] Galvao B R L, Varandas A J C, Braga J P and Belchior J C 2013 Electronic Quenching of $N(^2D)$ by N_2: Theoretical Predictions, Comparison with Experimental Rate Constants, and Impact on Atmospheric Modeling *The Journal of Physical Chemistry Letters* **4** 2292–2297

[60] Shkurenkov I and Adamovich I V 2016 Energy balance in nanosecond pulse discharges in nitrogen and air *Plasma Sources Science and Technology* **25** 015021

[61] Cosby P C 1993 Electron-impact dissociation of nitrogen *The Journal of Chemical Physics* **98** 9544–9553

[62] Klochko A V, Lemainque J, Booth J P and Starikovskaia S M 2015 TALIF measurements of oxygen atom density in the afterglow of a capillary nanosecond discharge *Plasma Sources Science and Technology* **24** 025010

[63] Klochko A 2014 *Excited species chemistry in homogeneous nanosecond discharges with high specific energy deposition.* Ph.D. thesis Ecole Polytechnique

[64] Thomson J J 1893 *Notes on recent researches in electricity and magnetism: intended as a sequel to Professor Clerk-Maxwell's Treatise on electricity and magnetism* (Clarendon Press)

[65] Amirov R, Asinovskii E I and Samoilov I S 1991 Growth of a nanosecond discharge in a conical shell *High temperature* **29** 649–654

[66] Starikovskaia S M, Starikovskii A Y and Zatsepin D V 1998 The development of a spatially uniform fast ionization wave in a large discharge volume *Journal of Physics D: Applied Physics* **31** 1118

[67] Starikovskaya S 1995 On the energy branching in high-voltage nanosecond discharge: dissociation of molecular oxygen *Fizika Plazmy (in russian)* **21** 541–548

[68] Krasnochub A V and Vasilyak L M 2001 Dependence of the energy deposition of a fast ionization wave on the impedance of a discharge gap *Journal of Physics D: Applied Physics* **34** 1678

[69] Wladimiroff W W and Andersson H E B 1977 The construction and operational analysis of an interference-free, coaxial N_2 laser system *Journal of Physics E: Scientific Instruments* **10** 361

[70] Tokunov Y M, Asinovskii E I and M V L 1981 Lasing and the dynamics of a nanosecond discharge in nitrogen *High Temperature* **19** 347–351

[71] Abramov A G, Asinovskii E I and Vasilyak L M 1983 Investigation of the spatial and temporal dynamics of the pump and radiation waves in a nitrogen laser *Soviet Journal of Quantum Electronics* **13** 1203

[72] Vasilyak L M, Kostyuchenko S V, Kudryavtsev N N and Rodionov A S 1995 Pumping of a coaxial nitrogen laser by a high-speed ionisation wave *Quantum Electronics* **25** 1170

[73] Anikin N B, Pancheshnyi S V, Starikovskaia S M and Starikovskii A Y 1998 Breakdown development at high overvoltage: electric field, electronic level excitation and electron density *Journal of Physics D: Applied Physics* **31** 826

[74] Anikin N B, Starikovskaia S M and Starikovskii A Y 2002 Polarity effect of applied pulse voltage on the development of uniform nanosecond gas breakdown *Journal of Physics D: Applied Physics* **35** 2785

[75] Morgan W Kinema software (Software Solutions for Applied Physics and Chemistry) and Boeuf JP, Pitchford LC CPAT (Centre de Physique des Plasmas et Applications de Toulouse) *BOLSIG Boltzmann solver (freeware) http://www.kinema.com*

[76] Anikin N, Starikovskaia S and Starikovskii A 2004 Study of the oxidation of alkanes in their mixtures with oxygen and air under the action of a pulsed volume nanosecond discharge *Plasma Physics Reports* **30** 1028–1042

[77] Anikin N B, Zavialova N A, Starikovskaia S M and Starikovskii A Y 2008 Nanosecond-Discharge Development in Long Tubes *IEEE Transactions on Plasma Science* **36** 902–903

[78] Takashima K, Adamovich I V, Xiong Z, Kushner M J, Starikovskaia S, Czarnetzki U and Luggenhölscher D 2011 Experimental and modeling analysis of fast ionization wave discharge propagation in a rectangular geometry *Physics of Plasmas* **18** 083505

[79] Takashima K, Adamovich I V, Czarnetzki U and Luggenhölscher D 2012 Development of Fast Ionization Wave Discharges at High Pulse Repetition Rates *Plasma Chemistry and Plasma Processing* **32** 471–493

[80] Jansky J, Tholin F, Bonaventura Z and Bourdon A 2010 Simulation of the discharge propagation in a capillary tube in air at atmospheric pressure *Journal of Physics D: Applied Physics* **43** 395201

[81] Delliou P L, Tardiveau P, Jeanney P, Bauville G and Pasquiers S 2011 Nanosecond Pulsed Discharge Phenomenology in Micrometer-Sized Radially Confined Air Gap *IEEE Transactions on Plasma Science* **39** 2686–2687

[82] Jansky J, Delliou P L, Tholin F, Tardiveau P, Bourdon A and Pasquiers S 2011 Experimental and numerical study of the propagation of a discharge in a capillary tube in air at atmospheric pressure *Journal of Physics D: Applied Physics* **44** 335201

[83] Jansky, J and Bourdon, A 2011 Surface charge deposition inside a capillary glass tube by an atmospheric pressure discharge in air *Eur. Phys. J. Appl. Phys.* **55** 13810

[84] Robert E, Barbosa E, Dozias S, Vandamme M, Cachoncinlle C, Viladrosa R and Pouvesle J M 2009 Experimental Study of a Compact Nanosecond Plasma Gun *Plasma Processes and Polymers* **6** 795–802

[85] Karakas E and Laroussi M 2010 Experimental studies on the plasma bullet propagation and its inhibition *Journal of Applied Physics* **108** 063305

[86] Robert E, Sarron V, Ries D, Dozias S, Vandamme M and Pouvesle J M 2012 Characterization of pulsed atmospheric-pressure plasma streams (PAPS) generated by a plasma gun *Plasma Sources Science and Technology* **21** 034017

[87] Lu X, Laroussi M and Puech V 2012 On atmospheric-pressure non-equilibrium plasma jets and plasma bullets *Plasma Sources Science and Technology* **21** 034005

[88] Ji L, Xia Y, Bi Z, Niu J and Liu D 2015 The density and velocity of plasma bullets propagating along one dielectric tube *AIP Advances* **5** 087181

[89] Dilecce G 2014 Optical spectroscopy diagnostics of discharges at atmospheric pressure *Plasma Sources Science and Technology* **23** 015011

[90] Pancheshnyi S, Starikovskaia S and Starikovskii A 1998 Measurements of rate constants of the $N_2(C^3\Pi_u,\ v\,' = 0)$ and $N_2^+(B^2\Sigma_u^+,\ v' = 0)$ deactivation by N_2, O_2, H_2, CO and H_2O molecules in afterglow of the nanosecond discharge *Chemical Physics Letters* **294** 523 – 527

[91] Pancheshnyi S, Starikovskaia S and Starikovskii A 2000 Collisional deactivation of $N_2(C^3\Pi_u,\ v = 0,\ 1,\ 2,\ 3)$ states by N_2, O_2, H_2 and H_2O molecules *Chemical Physics* **262** 349 – 357

[92] Lepikhin N D, Klochko A V, Popov N A and Starikovskaia S M 2016 Long-lived plasma and fast quenching of $N_2(C^3\Pi_u, v)$ by electrons in the afterglow of a nanosecond capillary discharge in nitrogen *Plasma Sources Science and Technology* **25** 045003

[93] Qayyum A, Zeb S, Naveed M A, Ghauri S A and Zakaullah M 2007 Optical actinometry of the N-atom density in nitrogen plasma *Plasma Devices and Operations* **15** 87–93

[94] Pagnon D, Amorim J, Nahorny J, Touzeau M and Vialle M 1995 On the use of actinometry to measure the dissociation in O_2 DC glow discharges: determination of the wall recombination probability *Journal of Physics D: Applied Physics* **28** 1856

[95] Henriques J, Villeger S, Levaton J, Nagai J, Santana S, Amorim J and Ricard A 2005 Densities of N- and O-atoms in N_2-O_2 flowing glow discharges by actinometry *Surface and Coatings Technology* **200** 814 – 817

[96] Booth J P, Joubert O, Pelletier J and Sadeghi N 1991 Oxygen atom actinometry reinvestigated: Comparison with absolute measurements by resonance absorption at 130 nm *Journal of Applied Physics* **69** 618–626

[97] Donnelly V M 2004 Plasma electron temperatures and electron energy distributions measured by trace rare gases optical emission spectroscopy *Journal of Physics D: Applied Physics* **37** R217

[98] Marco A Gigososa Manuel A Gonzalez V C 2003 Computer simulated Balmer-alpha, -beta and -gamma Stark line profiles for non-equilibrium plasmas diagnostics *Spectrochimica Acta Part B: Atomic Spectroscopy* **58** 1489 – 1504

[99] Lisitsa V S 1977 Stark broadening of hydrogen lines in plasmas *Soviet Physics Uspekhi* **20** 603

[100] Lo A, Cessou A, Lacour C, Lecordier B, Boubert P, Xu D A, Laux C O and Vervisch P 2017 Streamer-to-spark transition initiated by a nanosecond overvoltage pulsed discharge in air *Plasma Sources Science and Technology* **26** 045012

[101] Paris P, Aints M, Laan M and Valk F 2004 Measurement of intensity ratio of nitrogen bands as a function of field strength *Journal of Physics D: Applied Physics* **37** 1179

[102] Paris P, Aints M, Valk F, Plank T, Haljaste A, Kozlov K V and Wagner H E 2005 Intensity ratio of spectral bands of nitrogen as a measure of electric field strength in plasmas *Journal of Physics D: Applied Physics* **38** 3894

[103] Ochkin V N 2009 *Spectroscopy of low temperature plasma* (John Wiley & Sons)

[104] Roper Scientific SAS Z.I. Petite Montagne Sud - Lisses - 8 Rue Du Forez - CE 1702 - 91017 Evry Cedex - France *Specifications of the Princeton Instruments equipment*

[105] Bracewell R N 2000 *The Fourier Transform and its Applications* third edition ed

[106] Wolfram|Alpha 2016 https://www.wolframalpha.com/ *Wolfram Alpha LLC*

[107] Wolberg J 2006 *Data analysis using the method of least squares: extracting the most information from experiments* (Springer Science & Business Media)

[108] Skubenich V and Zapesochnyi I 1975 Excitation of diatomic molecules in collisions with monoenergetic electrons *High Energy Chemistry (in russian)* **9** 387

[109] Kossyi I A, Kostinsky A Y, Matveyev A A and Silakov V P 1992 Kinetic scheme of the non-equilibrium discharge in nitrogen-oxygen mixtures *Plasma Sources Science and Technology* **1** 207

[110] Popov N A 2011 Kinetic processes initiated by a nanosecond high-current discharge in hot air *Plasma Physics Reports* **37** 807

[111] Piper L G, Holtzclaw K W, Green B D and Blumberg W A M 1989 Experimental determination of the Einstein coefficients for the N_2(B-A) transition *The Journal of Chemical Physics* **90** 5337–5345

[112] Aleksandrov N L and Son E E 1980 *Plasma Chemistry* (*Plasma Chemistry* vol 7) (Atomizdat Publushing)

[113] Guerra V and Loureiro J 1997 Electron and heavy particle kinetics in a low-pressure nitrogen glow discharge *Plasma Sources Science and Technology* **6** 361

[114] Heidner R, Sutton D and Suchard S 1976 Kinetic study of $N_2(B^3\Pi_g, v)$ quenching by laser-induced fluorescence *Chemical Physics Letters* **37** 243 – 248

[115] Gordiets B, Ferreira C M, Pinheiro M J and Ricard A 1998 Self-consistent kinetic model of low-pressure N_2 - H_2 flowing discharges: I. Volume processes *Plasma Sources Science and Technology* **7** 363

[116] Florescu-Mitchell A and Mitchell J 2006 Dissociative recombination *Physics Reports* **430** 277 – 374

[117] Zhang S, van Gessel A F H, van Grootel S C and Bruggeman P J 2014 The effect of collisional quenching of the O 3p ^3P_J state on the determination of the spatial distribution of the atomic oxygen density in an APPJ operating in ambient air by TALIF *Plasma Sources Science and Technology* **23** 025012

[118] Bruggeman P and Brandenburg R 2013 Atmospheric pressure discharge filaments and microplasmas: physics, chemistry and diagnostics *Journal of Physics D: Applied Physics* **46** 464001

[119] Chen C H, Payne M G, Hurst G S and Judish J P 1976 Kinetic studies of N_2 and N_2-SF_6 following proton excitation *The Journal of Chemical Physics* **65** 3863–3868

[120] Millet P, Salamero Y, Brunet H, Galy J, Blanc D and Teyssier J L 1973 De-excitation of $N_2(C^3\Pi_u;\ v'=0$ and 1) levels in mixtures of oxygen and nitrogen *The Journal of Chemical Physics* **58** 5839–5841

[121] Albugues F, Birot A, Blanc D, Brunet H, Galy J, Millet P and Teyssier J L 1974 Destruction of the levels $C^3\Pi_u$, ($v'=0$, $v'=1$) of nitrogen by O_2, CO_2, CH_4, and H_2O *The Journal of Chemical Physics* **61** 2695–2699

[122] Valk F, Aints M, Paris P, Plank T, Maksimov J and Tamm A 2010 Measurement of collisional quenching rate of nitrogen states $N_2(C^3\Pi_u, v = 0)$ and $N_2^+(B\,^2\Sigma_g^+, v = 0)$ *Journal of Physics D: Applied Physics* **43** 385202

[123] Bacri J and Medani A 1982 Electron diatomic molecule weighted total cross section calculation: III. Main inelastic processes for N_2 and N_2^+ *Physica B+C* **112** 101 – 118

[124] Landau L D and Lifshitz E M 1958 *Quantum mechanics: non-relativistic theory* Course of theoretical physics (London: Pergamon)

[125] Drawin H and Emard F 1976 Instantaneous population densities of the excited levels of hydrogen atoms and hydrogen-like ions in plasmas *Physica B+C* **85** 333 – 356

[126] Chernyi G, Losev S, Macheret S, Potapkin B, Gerasimov G and et al 2004 *Physical and Chemical Processes in Gas Dynamics: Physical and Chemical Kinetics and Thermodynamics* (AIAA Reston, Virginia) ISBN 1-56347-519-7

[127] Berkeliev B M, Dolgikh V A, Rudoi I G, Sevast'yanov A E and Soroka A M 1990 Laser utilizing the 2 + nitrogen system with excitation powers up to 20 kW/cm 3 *Soviet Journal of Quantum Electronics* **20** 1045

[128] Ratynskaia S, Dilecce G and Tolias P 2014 Nitrogen optical emission during nanosecond laser ablation of metals: prompt electrons or photo-ionization? *Applied Physics A* **117** 409–413

[129] SIGLO database, http://www.lxcat.laplace.univ-tlse.fr, retrieved June 4, 2013

[130] Savitzky A and Golay M J E 1964 Smoothing and Differentiation of Data by Simplified Least Squares Procedures. *Analytical Chemistry* **36** 1627–1639

[131] Steinier J, Termonia Y and Deltour J 1972 Smoothing and differentiation of data by simplified least square procedure *Analytical Chemistry* **44** 1906–1909

[132] Krishnan R S 1953 The scattering of light in fused quartz and its Raman spectrum *Proceedings of the Indian Academy of Sciences - Section A* **37** 377–384

[133] Gosho Y and Saeki M 1989 Photoelectron Emission from the Quartz Surface of an Ultraviolet Lamp under Atmospheric Conditions *Japanese Journal of Applied Physics* **28** 1939

[134] Pancheshnyi S 2015 Photoionization produced by low-current discharges in O_2, air, N_2 and CO_2 *Plasma Sources Science and Technology* **24** 015023

[135] Pancheshnyi S V, Starikovskaia S M and Starikovskii A Y 2001 Role of photoionization processes in propagation of cathode-directed streamer *Journal of Physics D: Applied Physics* **34** 105

[136] Nudnova M M and Starikovskii A Y 2008 Streamer head structure: role of ionization and photoionization *Journal of Physics D: Applied Physics* **41** 234003

[137] Braginsky S 1963 Transport phenomena in plasma (in russian) *Problems of Plasma Theory, Gosatomizdat, Moscow* **1** 183–272

[138] Brau C A and Jonkman R M 1970 Classical Theory of Rotational Relaxation in Diatomic Gases *The Journal of Chemical Physics* **52** 477–484

[139] Park C 1989 *Nonequilibrium hypersonic aerothermodynamics* (New York, Chichester: J. Wiley and sons) ISBN 0-471-51093-9

[140] Radtsig A and Smirnov B 1980 Handbook on atomic and molecular physics *Atomizdat, Moscow* 240

[141] Guerra V, Sa P A and Loureiro J 2001 Role played by the $N_2(A^3\Sigma_u^+)$ metastable in stationary N_2 and N_2 -O_2 discharges *Journal of Physics D: Applied Physics* **34** 1745

[142] Herron J T 1999 Evaluated Chemical Kinetics Data for Reactions of $N(^2D)$, $N(^2P)$, and $N_2(A^3\Sigma_u^+)$ in the Gas Phase *Journal of Physical and Chemical Reference Data* **28** 1453–1483

[143] Piper L G 1988 State-to-state $N_2(A^3\Sigma_u^+)$ energy pooling reactions. II. The formation and quenching of $N_2(B^3\Pi_g, v = 1 - 12)$ *The Journal of Chemical Physics* **88** 6911–6921

[144] Stancu G D, Janda M, Kaddouri F, Lacoste D A and Laux C O 2010 Time-Resolved CRDS Measurements of the $N_2(A^3\Sigma_u^+)$ Density Produced by Nanosecond Discharges in Atmospheric Pressure Nitrogen and Air *The Journal of Physical Chemistry A* **114** 201–208

[145] Popov N A 2013 Vibrational kinetics of electronically-excited $N_2(A\,^3\Sigma_u^+, v)$ molecules in nitrogen discharge plasma *Journal of Physics D: Applied Physics* **46** 355204

Titre : Relaxation rapide de l'énergie dans la post-luminescence d'une décharge capillaire nanoseconde

Mots clés : cinetique, nanosecondes, plasma

Résumé : L'objectif principal du travail présent était d'étudier, comment la cinétique du plasma change dans le condition de dépôt d'énergie spécifique élevé dans les champs électriques réduits élevées. La décharge capillaire nanoseconde a été utilisée comme un outil expérimental. Les mesures sont effectuées dans l'azote pur et dans les mélanges azote/oxygène. Les paramètres électriques de la décharge ont été mesurés : la tenson applique, le dépôt de l'énergie, le champ électrique et le courant électrique. Les spectres de l'émission optique de la décharge sont obtenus. La densité électronique dans les impulsions de la décharge a été mesurée. La décroissance du plasma a été étudiée par les mesures de la densité électronique dans la post-luminescence de la décharge. Les processus contrôlant la décroissance du plasma ont été déterminés. La dépopulation des espèces excitées sur l'exemple de l'état $N_2(C)$ de l'azote moléculaire a été étudié dans l'azote pur et les mélanges azote/oxygène. Les processus responsables de la dépopulation de espèces excitées lors de la post-luminescence de la décharge nanoseconde aux conditions de dépôt de l'énergie spécifique élevée dans les champs électrique réduit élevés ont été examinés. La distribution radiale des espèces excitées pour les différentes compositions de gaz a été étudiée et comparée. L'études expérimentale et numérique des processus responsables du chauffage rapide du gaz dans l'azote pur et dans les mélanges azote/oxygène dans la post-luminescence de la décharge capillaire nanoseconde ont été effectués. Les particularités de chauffage rapide du gaz dans les conditions de la décharge nanoseconde à de dépôt d'énergie spécifique élevé dans les champs électrique réduits élevées ont été étudies. La modification du schéma cinétique actuellement utilise est proposée.

Title : Fast energy relaxation in the afterglow of a nanosecond capillary discharge in nitrogen/oxygen mixtures

Keywords : kinetics, nanoseconds, plasma

Abstract : The main object of the present work was to study how the plasma kinetics changes at condition of high specific energy deposition at high reduced electric fields. The nanosecond capillary discharge was used as an experimental tool. The measurements were performed in pure nitrogen and nitrogen/oxygen mixtures. The electric parameters of the discharge were measured: the applied voltage, the deposited energy, the electric field and the electric current. The spectra of the optical emission of the discharge were obtained. The electron density was measured in the discharge pulses. The plasma decay was studied by electron density measurements in the afterglow of the discharge. The processes controlling the decay of the plasma were determined. The depopulation of excited species on the example of $N_2(C)$ state of molecular nitrogen was studied in pure nitrogen and nitrogen/oxygen mixtures. The processes responsible for the depopulation of the excited species at conditions of high specific energy deposition at high reduced electric fields were investigated. The experimental and numerical studies of the process responsible for the fast gas heating in pure nitrogen and nitrogen/oxygen mixtures were performed. The peculiarities of the fast gas heating at conditions of high specific deposited energy at high reduced electric fields were studied. The modification of the currently used kinetic scheme is proposed.

Université Paris-Saclay
Espace Technologique / Immeuble Discovery
Route de l'Orme aux Merisiers RD 128 / 91190 Saint-Aubin, France